
Delft University of Technology | Van Oord

*Modelling the immediate penetration of rock particles in soft clay
during subsea rock installation, using a flexible fallpipe vessel*

Final v1.0



*“There are known knowns; there are things
we know we know.*

*There are known unknowns; that is to say,
we know there are things we do not know.*

*But there are also unknown unknowns —
The ones we don't know we don't know.”*

Donald Rumsfeld (2002)

Contact details

T.N. (Dirk) Beemsterboer
Master student Geo-Engineering
1362194
Koornmarkt 38a
2611 EH Delft
E: tnbeemsterboer@gmail.com

Delft University of Technology
Faculty of Civil Engineering & Geosciences (CiTG)
Stevinweg 1
2628 CN Delft

Van Oord
Schaardijk 211
3063 NH Rotterdam
<http://www.vanoord.com>

Graduation committee

Chairman
Prof. ir. A.F. (Frits) van Tol
Foundation Engineering
Section Geo-Engineering
Delft University of Technology

Supervision
Dr. ir. K.J. (Klaas Jan) Bakker
Hydraulic Structures and Flood Risk
Section Hydraulic Engineering
Delft University of Technology

Daily supervision Van Oord
Ir. W. (Wouter) Karreman
Engineering specialist
Estimating and Engineering
Van Oord Dredging and Marine Contractors

Ing. M. (Mike) Hermans
Senior Estimator
Estimating and Engineering Offshore
Van Oord Offshore BV

Acknowledgement

This thesis forms the final result of the master Geo Engineering at the Delft University of Technology and was executed in collaboration with Van Oord Dredging and Marine Contractors. During the past eight months I have studied the influence of immediate rock penetration in soft clays during subsea rock installation. This graduation has mostly been an individual process, nevertheless several people contributed to the realization of the final result, for which I am very grateful.

First and foremost I would like to express my gratitude to all the members of my committee, their support and knowledge proved very valuable. Special gratitude goes to W. Karreman for his enthusiastic daily support and to M. Hermans for providing the opportunity to join a SRI project aboard Van Oord's FFPV Stornes. Recognition goes to the Stornes crew, who provided me with helpful data and answered my numerous questions.

Furthermore I would like to thank L.A. van Paassen and M.G. Ottolini for their help during the experiments and J.J. de Visser for his assistance in creating the test setup.

Lastly my gratitude goes to my fellow graduate students both at the university and at Van Oord for their welcome distraction when needed and the elaborate discussions during coffee breaks.

T.N. Beemsterboer,

Rotterdam 25 October 2013

Abstract

Subsea rock installation is often used in offshore engineering. With offshore activities in increasing water depths a flexible fallpipe is currently used to accurately install the rock particles. The total required volume of rock material during installation can be determined by summing the geometrical volume, the operational losses and the displacements of the seabed. Accurate knowledge of the volume loss during installation is needed to ensure proper project management and cost estimation. This thesis provides insight in the processes which influence the volume loss during subsea rock installation and focusses specifically on immediate particle penetration. During installation the following processes affect volume loss:

- Immediate deformation of the seabed
- Loss of fine particles due to deep sea currents
- Immediate particle penetration in the seabed
- Flow of cohesive material in to the pores of the rock fill
- Long term settling of the berm due to consolidation
- Possible erosion of the seabed
- Stones deposited outside the theoretical perimeter of the construction

With a lot of oil and gas activity offshore Norway the problem of large volume losses becomes more important since this seabed consists of very soft clay. Additionally, since the rocks are installed in deeper waters using a flexible fallpipe, the impact velocity at the bottom is high (~ 3 m/s). Due to the high velocity and the low strength of the soil, the particles are thought to penetrate relatively deep into the soil (~ 0.1 m). In this thesis a model is presented to predict single stone penetration in very soft clay. This model is developed based on existing static bearing capacity formulae and validated using laboratory experiments. The results agree well with the theoretical formulation.

Field tests on board of FFPV Stornes are performed in the northern part of the North Sea to define all relevant processes and corresponding magnitude. Based on calculations performed seabed deformation due to consolidation forms the largest individual factor of volume loss. With one fifth of the complete loss single stone penetration embodies another important factor. However its influence is smaller than initially expected. Multi stone penetration causes the particles to penetrate even deeper into the soft soil. The stone penetration processes combined represent almost half of the average expected volume loss.

Based on the validated single stone model and the described supplementary processes the total volume loss is modelled. A fit between the field results and the modelled penetration is determined to check if all processes are described and to validate their magnitude. The match between the measured and calculated processes suggests that all the right processes are taken into account. However to be able to predict the volume loss, accurate derivation of each process will have to be optimised. So far no clear conclusion can be drawn. The measurement accuracy currently used to obtain height deficits lacks the precision to undoubtedly state the influence of all separate processes. Important factors such as seabed erosion and the presence of sludge on top of the seabed, let alone the inaccuracy of the provided low stress soil properties, cause a lot of uncertainty in the determination of the individual process influence.

Content

Acknowledgement	II
Abstract	IV
Content	V
1 Introduction	1
1.1 Problem description	1
1.2 Demarcation	2
1.3 Objectives	3
PART I – THEORY	5
2 Subsea rock installation	6
2.1 Application	6
2.2 Equipment	8
3 Relevant properties	11
3.1 Soil properties	11
3.2 Rock properties	13
3.3 Bathymetry	15
4 Volume loss	16
4.1 Single stone penetration	16
4.2 Impact velocity	21
4.3 Additional processes	24
4.4 Remarks on the theory	31
PART II – DATA GATHERING	34
5 Introduction	35
6 Experimental measurements	36
6.1 Setup	36
6.2 Clay properties	37
6.3 Undrained shear strength determination	39
7 Experimental results	41
7.1 Single stone penetration	41
7.2 High speed camera tests	45
8 Subsea rock installation project	49
8.1 Project description	49
8.2 Seabed properties	51
8.3 Rock properties	53

9	Field measurements	55
9.1	Approach	55
9.2	Accuracy	56
10	Field results	60
10.1	Volume loss	60
10.2	In-situ density	61
10.3	Consolidation	63
PART III – MODELLING		64
11	Single stone penetration model	65
11.1	Validation	65
11.2	Sensitivity analysis	68
12	Volume loss determination	71
12.1	Single stone penetration	71
12.2	Multi stone penetration	71
12.3	Loss of fines	72
12.4	Immediate deformation	73
12.5	Consolidation	75
12.6	Material flow into pores	77
12.7	Results	78
PART IV – CONCLUSIONS		82
13	Conclusions	83
14	Recommendations	85
14.1	Future research	85
14.2	Data gathering	86
14.3	Future data gathering	87
PART V – APPENDICES		89
15	Appendices	90
15.1	Bibliography	90
15.2	Nomenclature	94
15.3	List of tables	96
15.4	List of figures	97
15.5	Flexible Fallpipe Vessel – Stornes	101
15.6	Bearing capacity models	103
15.7	Brinch Hansen	105
15.8	Staged descent of a group of rock through water	106
15.9	Flexible fallpipe forces	107
15.10	Shield parameter	109
15.11	Derivation of clay penetration in a rock fill	110
15.12	Images of experiments	115
15.13	Additional experimental results	122

15.14	Berm dimensions	123
15.15	Construction drawing Knarr project	124
15.16	Soil profile	127
15.17	Fugro soil profile	128
15.18	Volume calculation	129
15.19	Phased subsea rock installation	130
15.20	In-situ densities of Norwegian rock material	131
15.21	Input file for Single Stone Penetration model	133
15.22	Sensitivity analysis input	134
15.23	Factors with negligible influence	134
15.24	Plaxis input parameters	136
15.25	Plaxis mesh	137
15.26	D-settlement calculation	138
15.27	Volume determination results	139
15.28	Quarry density tests	142

1 Introduction

Over the past decades the world's energy consumption has increased significantly. This relentless rise in energy demand combined with the fact that natural onshore resources have become harder to retrieve, has led to offshore hydrocarbon exploration. Offshore activity has not only increased, but also tends to take place in greater water depths. The offshore related subsea rock fills often used to protect pipelines, prevent upheaval buckling and provide support for offshore structures, were consequently forced to be installed in increasing water depths. In these deeper circumstances the accuracy of rock placement using conventional rock dumping methods decreased. A new type of subsea rock installation vessel was therefore developed. This vessel used a flexible fallpipe to guide the rocks towards the seabed, allowing it to accurately install rock berms up to great depths.

During subsea rock installation (SRI) a number of processes occur, for example surface erosion, seabed deformation and rock penetration. These effects all influence the amount of rock material required to successfully fulfil the designed rock fill. Especially with an increasing amount of offshore activity in the Northern part of the North Sea, which is characterised by its soft fine grained glaciomarine sediments, rock penetration is believed to cause a significant rock loss during installation.

1.1 Problem description

Accurate knowledge of the amount of rock material required to complete a rock fill according to its original design is needed to ensure proper project management and cost estimation. The total volume of rock used during installation can be determined by summing the geometrical volume, the operational losses and the displacements of the seabed. The geometrical volume can accurately be determined using Digital Terrain Models (DTM) and CAD drawings of the design. However precise estimation of the operational losses and losses due to the displacement of the seabed is challenging since numerous processes influence these losses. Currently the magnitude of these losses is based on previous projects, experience and consequently lacks physical background and theoretical or experimental confirmation. By creating a model to calculate these losses a more accurate prediction of the additional volume necessary to complete the fill can be made. This will benefit both the client and Van Oord.

Figure 1.1 shows the processes which can influence the required rock volume during subsea rock installation. In this thesis the processes which influence the volume loss during subsea rock installation will be described.

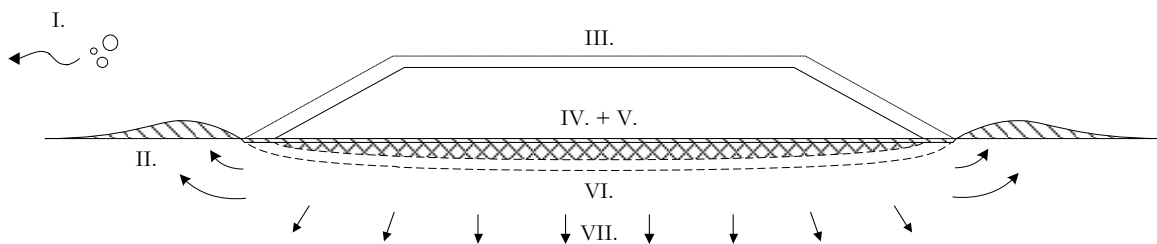





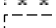
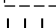


Figure 1.1: Processes that affect the volume installed during the subsea rock installation

I.	Loss of fine particles due to currents	
II.	Immediate deformation of the seabed	
III.	Stones deposited outside the theoretical perimeter of the construction	
IV.	Immediate particle penetration in the seabed	
V.	Erosion of the seabed	
VI.	Flow of cohesive material in to the pores of the rock fill	
VII.	Long term settling of the berm due to consolidation and creep	

However since the immediate penetration is the biggest unknown and most of the other contributors can be modelled rather well, the main focus of the thesis is to determine the immediate penetrations of rocks in the seabed. At the moment there is no proven formulation available to compute the penetration of a falling stone into the seabed, due to the lack of such a formula alternative calculation methods will have to be studied.

With a lot of oil and gas activity offshore Norway the problem of large penetrations becomes more important since the losses in the very soft clays can be significant. Additionally since the rock fills in these deeper water are installed using a flexible fallpipe vessel, the impact velocity at the bottom is particularly high. The final speed is higher than the terminal velocity of the particle in stagnant water, due to the fact that the velocity of the rock-water mixture is the summation of the water velocity plus the equilibrium fall velocity of the rock. This causes the velocity of the particles inside the fallpipe to reach about 6 m/s. Due to the high velocity and the low strength of the soil, the particles can penetrate relatively deep into the soil.

Van Oord currently possesses an in-house model which estimates the immediate rock penetration, based on a static bearing capacity equation. The penetration depth obtained from this model has not been validated and might differ from the penetration encountered during real projects. Therefore the model should be reevaluated and adjusted where necessary. Hence the main topic of this graduation thesis can be defined as follows:

“Modelling the immediate penetration of rock particles in soft clay during subsea rock installation, using a flexible fallpipe vessel.”

1.2 Demarcation

Because of the extent of this subject, the numerous variables influencing volume losses during installation and since time for this graduation research is limited, it is important to clearly define the boundaries and limitations of the research. Henceforth the detailed scope of this research is indicated here.

As described earlier several processes influence the volume loss during installation and these processes will be described including their relative influence. Subsea rock installation frequently occurs in deep waters, in this specific environment the seabed often consists of soft fine grained soil with low undrained shear strength. Hence it is expected that the volume losses during installation are mainly influenced by immediate particle penetration. This research will therefore emphasise the processes which determine the extent of the immediate penetration.

This penetration is primarily examined from a geotechnical point of view. Problems related to fluid mechanics will only be explained briefly in case a connection is required to improve the penetration model. Other possible hydraulic influences, for instance inside the flexible pipe, will not be taken into account. Additionally offshore and maritime influences during installation also fall outside the scope of this research (see Figure 1.2).

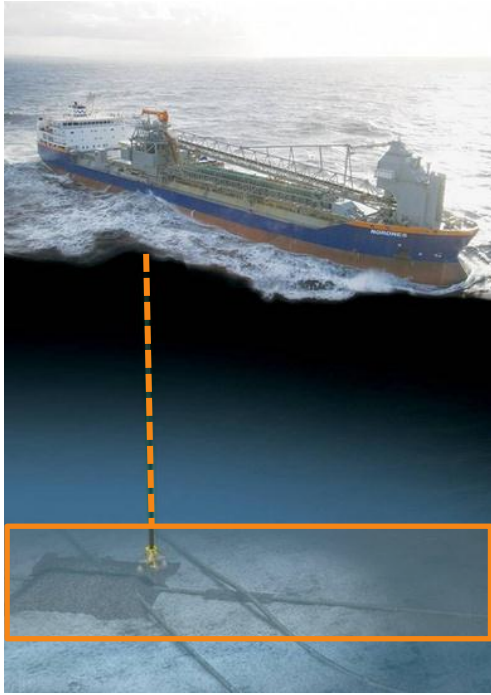


Figure 1.2: Boundaries of the research (Visser & Van der Meer, 2008)

The effect of immediate particle penetration is present in both clay and sandy soils. The current modelled penetration is expected to deviate from reality for both soil types. Namely the penetration determined using the existing model for clay is thought to be too progressive, i.e. the penetration is smaller than estimated. On the other hand for sand the model is thought to produce conservative values. However since the amount of penetration in soft clays is more severe and consequently the potential losses are higher, this thesis will only focus on penetration in clay.

Since it is impossible to investigate the influence of all individual variables separately, the most promising parameters will be selected based on a literature survey. The effect of these governing variables is explored using the newly developed model. This model will be based on a single stone model (SSM) and only address single stone immediate penetration. Clearly the effect of many stones penetrating at the same time will affect the amount of energy and the properties of the soil and consequently the penetration depth. One stone can be pushed deeper into the soil as a result of on-going impact of new stones. Furthermore part of the stone's kinetic energy will dissipate during the interaction with the other stones during the descent from the ship to the seabed. All these aspects significantly complicate the already complex dynamic problem and will not be incorporated in the model. Additionally since the installation project duration is short, long term effects such as creep will not be considered.

1.3 Objectives

Purpose of this thesis is to get more insight in the governing parameters that will influence the volume loss during subsea rock installation using a flexible fallpipe in general and immediate penetration in particular. The final objective of this study is to produce a quick decision tool, which can be used on site as well as in the office, to predict the immediate penetration of particles in soft clays depending on different soil strengths, particle sizes and production rates. The model will be based on the existing theory which describes a set of kinematic equations to obtain the penetration. The created physical and mathematical formulation will be validated using laboratory tests.

Additionally the remaining processes influencing the volume losses during rock installation will be described and their magnitude will be assessed. The description of these processes will be based on theory as well as practice. Practical experience of the SRI process will be obtained during field work. The data

collected during this fieldwork will be used as reference for the estimation of the order of magnitude of all separate installation processes. A summary of the approach used for this thesis is given in the flow chart below.

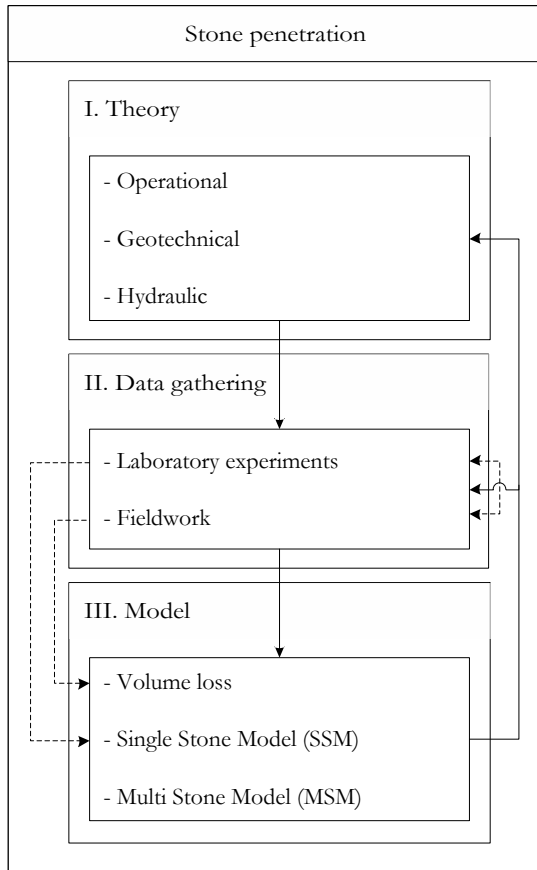


Figure 1.3: Flowchart indicating the approach of this thesis

Part I – Theory

2 Subsea rock installation

Rock dumping has historically been used for scour protection of dikes and breakwaters. At first this protection was installed by hand from ashore or from a pontoon. Later so called side-stone dumping vessels were used to mechanically install large amounts of rock by simply shoving the rocks over the side of the vessel (Figure 2.1a). However with increasing water depths this type of dumping could no longer provide the required accuracy due to dispersion of the rock material in water and current influences. Hence, for deeper rock dumping a new solution had to be found, therefore the telescopic fallpipe was introduced (Figure 2.1c). This pipe provided guidance during the drop of rocks from the hull of the vessel towards the seabed.

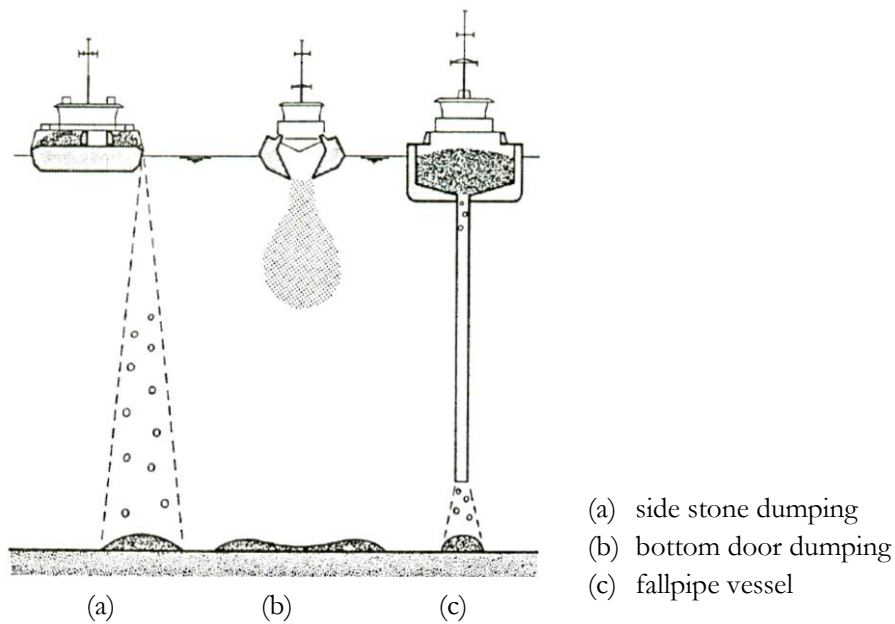


Figure 2.1: Different rock installation vessels (CUR, 1995)

When offshore projects demanded even deeper rock fills the pipe was modified to a flexible fallpipe, consisting of hundreds of separate open ended buckets attached together by steel chains. At the end of the pipe a Remote Operating Vehicle (ROV) ensures the correct location of the pipe mouth and keeps this end in position under the influence of currents. The current state of the art flexible fallpipe vessels (FFPV) can install rocks up to a water depth of 1350 m. Because of the increased feasible depth and higher accuracy the original term rock dumping is changed to subsea rock installation. This chapter will further explain the process and purpose of subsea rock installation.

2.1 Application

As stated before, historically rock dumping is used in hydraulic engineering for scour protection. Currently subsea rock installation can be used for a variety of reasons in a range of different conditions. In this section the most common application are described briefly.

2.1.1 Pipeline engineering

Subsea pipelines are used for a number of purposes in the development of subsea wells and the extraction hydrocarbon resources, as shown in Figure 2.2. Additionally an increasing amount of subsea cables, pipelines and umbilicals is used in the development of new offshore wind parks. These lines can span between installations or form a connection with the mainland and have to be protected against various forces.

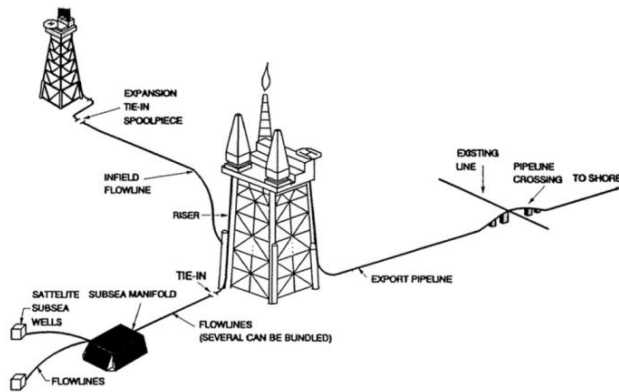


Figure 2.2: Applications of subsea pipelines (Palmer & King, 2008)

Loads can be induced both by the natural and human influences. Natural circumstance can cause severe loading due to, for instance, underwater currents or large height differences in the bathymetry. In undulating terrain large free spans can occur in the pipeline trajectory which results in large tension forces. Moreover human interference can also provoke high loading, for example due to physical impact because caused by trailing fishing nets and anchors.

All these forces will have to be mitigated to prevent the pipe from damaging or even failing. To mitigate these forces, rocks can be installed underneath the pipeline (pre-lay) or on top of the pipeline (post lay), depending on the nature of the force (Figure 2.3a - b). Other possible reasons for SRI occur during usage and installation of the pipeline. During production the pipe expands due to a difference in temperature between the inside of the pipe and the ambient water temperature. This expansion can cause buckling of the pipeline, if this buckling occurs locally failure of the pipeline can be the result (i.e. upheaval buckling). To prevent this buckling – both in horizontal and vertical direction – an additional weight is put on top of the pipe in the form of rocks. Moreover when pipelines cross each other it is possible to cover one of the pipes with rock, in order to prevent abrasion of the pipeline's outer layer (see Figure 2.3c).



(a) The basic design of supports (brown) and counter fills (grey) (b) Free span mitigation supports (brown) including counter fills (grey) (c) Support for a pipeline crossing (brown) and counter fill (grey)

Figure 2.3: Different reasons for subsea rock installation (Visser & Van der Meer, 2008)

2.1.2 Foundation engineering

Another purpose for subsea rock installation is the creation of a suitable foundation for an offshore structure. With a lot of activity in locations with soft clays soil properties are not particularly suitable for large offshore structures. In these areas rock fills are used to ensure the level placement of a structure. Especially structures such as pipeline end manifolds and towheads might have to be placed on top of rock fills to ensure a lower friction during expansion movements of the system and to meet certain workability requirements concerning the level placement of the structure.

Furthermore if a stronger layer of soil lies on top of a soft clay layer, punch through of the foundation forms a risk. This is often encountered with the installation of spudcan foundations for a jackup platform. By creating a large rock fill underneath the spudcan the forces working on the foundation can be distributed over a larger area reducing the risk of punch through.

2.1.3 Ballast and scour protection

Some offshore installations, for example bottom founded structures, require additional ballasting after installation to obtain sufficient stability, often this is done using rock material. In this case FFPVs can be used to fill the ballast compartments of these structures. In case of high wave- and current forces around offshore structures, subsea rock installation can be applied to minimize scouring near pillars and foundations. This type of scour protection is lately been applied a lot surrounding offshore windmills due to the increase in offshore wind parks.

2.2 Equipment

While historically the first flexible fallpipe vessel was a bulk carrier equipped with a fallpipe, Van Oord currently owns three vessels which are fully optimized for accurate rock installation, more information about their latest and biggest FFPV “Stornes”, please refer to Appendix 15.5. The equipment needed to install rocks on the seabed up on to great depths is described in this paragraph.

2.2.1 Vessel

Figure 2.4 shows a cross section of Van Oord’s flexible fallpipe vessel “Stornes” capable of carrying and installing 25.500 tons of aggregate. Using this cross section the process during rock installation can be explained.

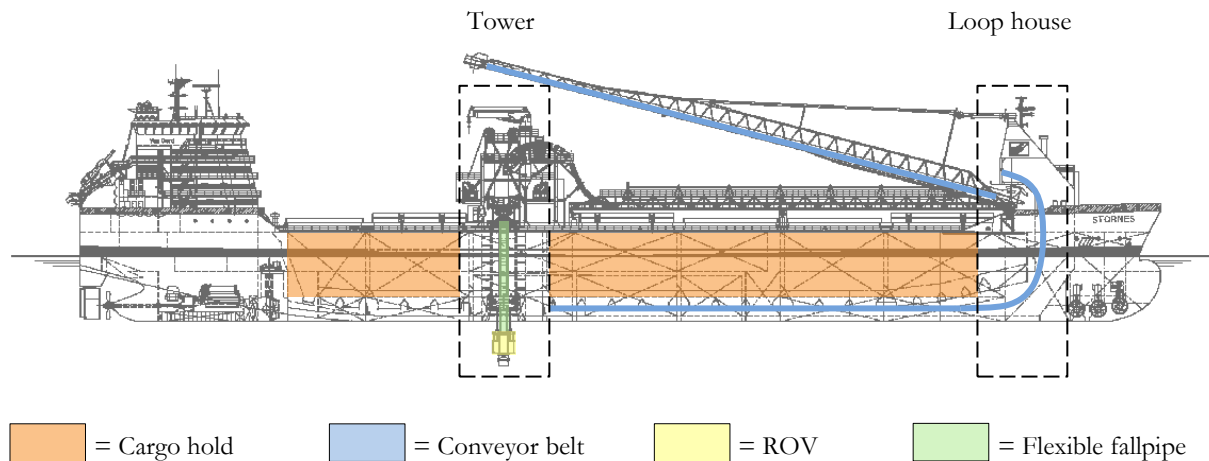


Figure 2.4: Cross section FFPV Stornes

First, rock particles are loaded from an onshore quarry on to the ship and into the cargo hold (indicated with the orange colour). The cargo hold is subdivided into a number of separate storage rooms. If necessary each storage room can contain different size rock particles. When the vessel has reached the location where the rock needs to be installed, the ship switches to dynamic positioning (DP). This system enables the vessel to accurately maintain its position at sea under challenging weather conditions. Then the flexible fallpipe is deployed through a hole in the middle of the hull, called the moon pool (see Figure 2.5) (or over the side in case of the FFPV Tertnes). When the fallpipe reaches its final length, ~10 m above the seabed, the dumping of rock particles can commence. By activating the conveyor belt underneath the cargo hold and opening the hold’s hatches, rocks will fall on the conveyor belt and be transported towards the bow of the vessel (shown in blue). Here the rocks are elevated onto the boom with help of the so called C-Loop located in the loophouse. The boom is the movable part of the conveyor belt which can swing over the deck to allow the different holds to be filled from ashore. The boom transfers the rocks into the feeder, which is located in the middle of the vessel at the tower. This feeder acts as a huge funnel which ensures the right amount of rock is dumped into the fallpipe at a constant rate. From the feeder the rock falls onto the shuttle conveyor and into the fallpipe and makes its way down to the seabed (indicated in green). At the end of the fallpipe a remotely operated vehicle is attached (as shown in yellow). This

ROV controls the mouth of the pipe and ensures the rocks are dumped at the right location. Moreover the ROV is equipped with all the survey equipment.

2.2.2 Fallpipe

A more detailed view of the composition of the complete fallpipe is given in Figure 2.6 and in Appendix 15.5. As stated before the flexible fall pipe consist of hundreds of cone shaped bottomless buckets, also referred to as vlutters. One vlutter is typically about 2 m long and has a diameter of 1.1 m. Figure 2.6 shows the vlutters as they are guided from the bucket storage container down through the moon pool towards the seabed. As indicated in this figure the first set of buckets is made out of steel, this also applies to the last set of buckets. All intermediate buckets are made out of composite to limit the weight of the complete string on the supporting chains. Evidently the steel buckets are heavier but less prone to wear compared to the composite buckets. That is why these buckets are used in the beginning and end of the pipe, where the particles tend to hit the side more frequently. The final connection between the flexible pipe and the ROV is made using a steel telescopic pipe. Due to this section the length of the complete flexible fall pipe can change slightly during dumping (<9 m), creating a tolerance in case the seabed is inclined.

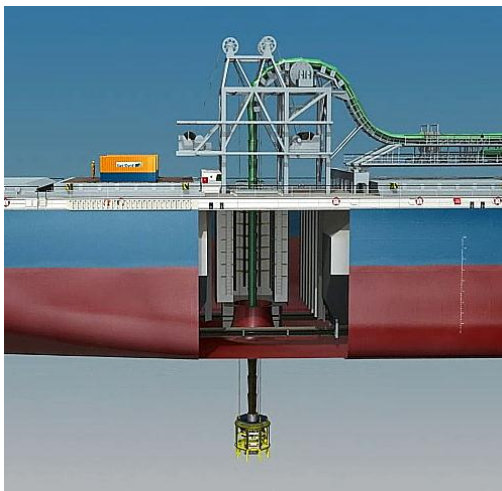


Figure 2.5: Moon pool and fallpipe installation

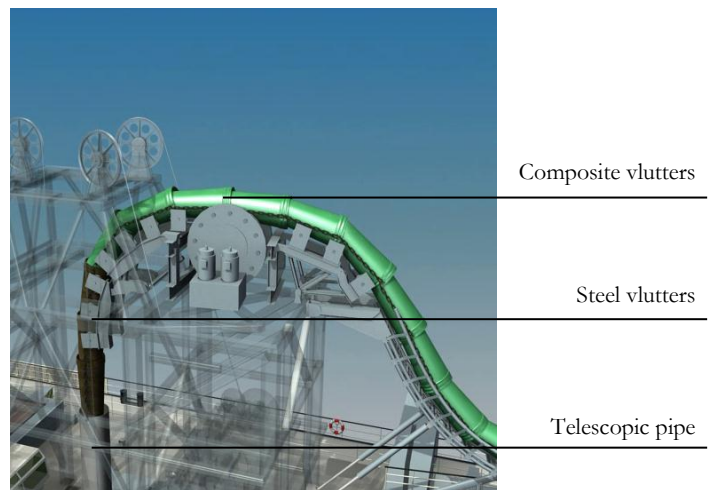


Figure 2.6: Composition of the flexible fallpipe system

2.2.3 Remote Operated Vehicle

Figure 2.7 shows the self-propelled remotely operated vehicle, this is an essential piece of technology at the end of the fallpipe. Using its integrated thrusters this machine can accurately control the location where the rocks are dumped, even if the pipe is deflected by the subsea currents. Moreover the ROV is equipped with two hydraulic arms which accommodate all survey equipment. This equipment, such as multibeam echo sounders (MBES), side-scan sonars and underwater cameras, is used to accurately determine the initial local bathymetry, monitor the intermediate developments and verify final result of the dumping process. The ROV also contains the splitter, which is located at the end of the pipe. The splitter consist of a set of steel flaps which can be opened and rotated to influence the direction and fall speed of the particles.

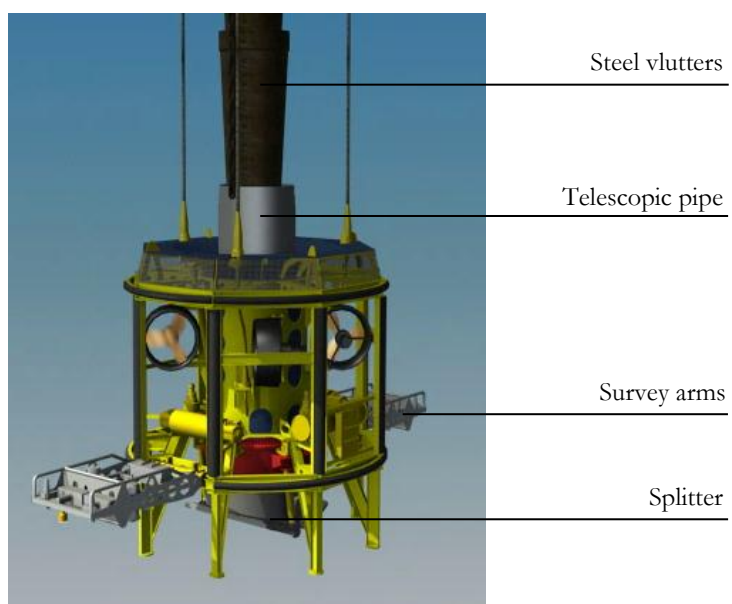


Figure 2.7: Self-propelled remotely operated vehicle

3 Relevant properties

As described by Verruijt (2006) the properties of soils are usually strongly non-linear, with the material exhibiting irreversible plastic deformations when loaded and unloaded even at low stress levels. Moreover soil often behaves anisotropic and may show distinctive effects such as dilatancy; volume increase during shearing. Specific soil behaviour is difficult to predict due to heterogeneity of the soil structure and can often not be determined using laboratory tests or in-situ. The behaviour of soils is further complicated by the presence of water in the pores; this fluid may prevent or retard volume deformations. All this uncertainty in property characterisation causes that soil properties are often adapted to a particular type of problem under consideration. Hence for an undrained penetration problem properties are quite different from those for a stability problem. Thus in soil mechanics the range of applicability of a certain parameter is often restricted to a special type of problem. Some properties cannot be used outside their intended field of application. In this chapter the relevant properties for the immediate penetration of particles will be discussed together with their possible range of values. The chapter does not only cover the important soil properties; the characteristics of the installed aggregate and bathymetry are also briefly addressed.

3.1 Soil properties

For immediate penetration of soil particles into the seabed the properties of top layer of the seafloor are most relevant. At these shallow depths existing stresses are low, hence the in-situ determination of soil properties using common methods such as a cone penetration test (CPT) is difficult. These instruments are more appropriate to determine properties of deeper layers. Often obtained values are situated within the accuracy of the instrument and are therefore less reliable. More about the limitation of offshore soil investigation (SI) and recent developments in this field is found in chapter 8.

In deep water the top layer is often characterised by soft fine sediment. Especially on the Norwegian continental shelf, which is of particular interest because of the huge quantity of offshore activity, the seabed conditions are characterized by very soft clay deposits ((De Vries, et al., 2007), (Rise, et al., 1984)). The properties of these sediments greatly affect possible penetration. In the following paragraphs the range of expected soil properties which should be included in the model, is illustrated.

3.1.1 Deposition

Depositional environment and history determines the properties of a soil type to a large extent. A relevant example is given by defining the depositional environment and history of the northern North Sea. Although the top layer might only consist of very soft normally consolidated clay, the depositional history can reveal much more and given insight in the properties which can be expected.

During the Quaternary period (2.3 Myr before present (BP) until today) glacial and interglacial conditions have been a dominant influence on soil deposits. Alternating periods of significant erosion, deposition and rapid sea level changes characterise this geological time period. Consequently the geological formations on the Norwegian continental shelf are characterised by a glaciomarine depositional environment. Glaciomarine sediments are characterised by soil with low undrained shear strength and a small proportion of coarse material (Sejrup, et al., 1989).

Extensive soil investigations revealed two important formations: the Norwegian trench formation and the Kleppe senior formation (Fugro Geoconsulting Ltd., 2012). The deeper (>10 m) Norwegian trench formation consist of grey to dark grey very silty to sandy clay with fragments of gravel including chalk. It is believed that the formation was deposited during late Weichselian (25 kyr BP) and therefore may have been influenced by ice movement. The clay may be weakly overconsolidated where advancing ice touched the ground. In the deepest parts of the trench, the ice may have been buoyant enabling deposition of normally consolidated glaciomarine clay (Rise, et al., 1984). The top Kleppe senior formation which

covers the Norwegian trench formation and forms the seabed, consist of soft plastic silty clays of up to 40 m thick in some places and is interspersed with lenses of sand and silt. This formation may show an uneven bathymetry due to erosion of the underlying Norwegian trench formation. Moreover iceberg plough marks may be present. For soil properties regarding particle penetration this formation is governing.

3.1.2 Strength

In soils two types of shear strength can be recognized; drained and undrained. If water in a soil is able to flow out of the pores during shearing, the soil behaves drained. The total stress in a soil then equals the effective stress since the pore water pressure is zero. However if this water is prevented to drain from the pores, because the soil has been sealed off, the soil will behave undrained. During undrained shearing of the soil the total pressure is equal to the sum of the effective pressure and the pore water pressure. The specific response is dependent on the shearing rate. The transition between drained and undrained response is shown in Figure 3.1. At extremely low shearing rates there is time for the developed pore pressures to fully dissipate causing the soil to behave drained. As the strain rate increases the time for drainage reduces, resulting in increasing pore pressures. That is why lower shear strengths are observed in the partially drained region. As the strain rates further increase the soil response becomes almost fully undrained, the pore pressures are at their maximum. After this point viscous effects cause the shear strength to increase with strain rate up to a potential viscous limit (Quinn & Brown, 2011). Since the permeability of clay is low and the penetration of the single rock particle is very fast (~ 50 ms) water will not be able to flow from the pores. Therefore the soil is assumed to behave fully undrained during the penetration of rock particles (Chung, et al., 2006).

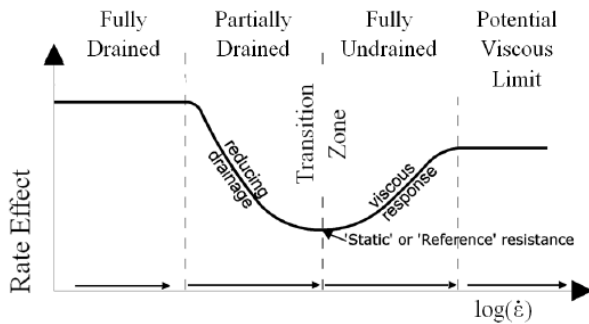


Figure 3.1: Curve showing the idealized variation of rate effect with strain rate (Quinn & Brown, 2011)

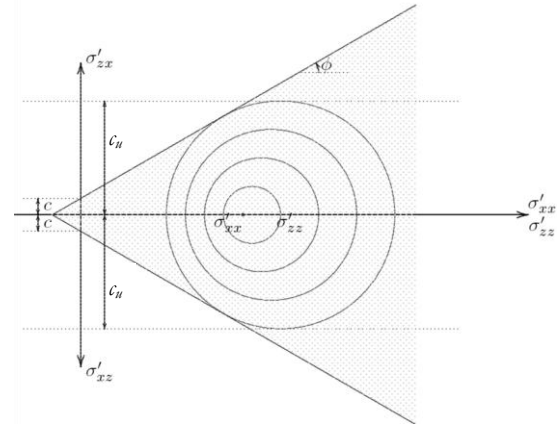


Figure 3.2: Mohr circles for undrained shear strength (Verruijt, 2005)

During undrained behaviour the shear strength of the material (τ_f), normally found using $\tau_f = c + \sigma \tan \varphi$, changes. The undrained shear strength parameter (c_u) can be estimated based on the basic shear strength parameters c and φ , using:

$$c_u = \frac{\sigma'_1 - \sigma'_3}{2} = c \frac{\cos \varphi}{1 - \frac{1}{3} \sin \varphi} + \sigma'_0 \frac{\sin \varphi}{1 - \frac{1}{3} \sin \varphi} \quad (3.1)$$

Here σ'_1 and σ'_3 are the effective principal stresses, σ'_0 is the initial average effective stress and φ is the internal friction angle of the soil. Based on this formula it can be derived that $c_u = c$ if $\varphi = 0^\circ$ and if $\varphi > 0^\circ$ the undrained shear strength c_u increases with the average effective stress σ'_0 . This can also be seen in Figure 3.2. Here a number of effective stress Mohr circles are shown, all based on the assumption that the average effective stress (σ'_0) remains constant. The total stress always differs from the effective stress by the value of the pore water pressure. The location of the total stress circles is not known, and in this case

not relevant (Verruijt, 2005). As will later be explained in more depth, undrained shear strength primarily depends on the initial void ratio or the initial water content of the soil. Unlike the angle of friction, the undrained shear strength is not a fundamental soil parameter. Its value depends on the effective confining stress. An increase in effective confining stress causes a decrease in void ratio and hence an increase in undrained shear strength. This thesis focusses on very soft clay deposits with an undrained shear strength between 0 - 20 kPa.

3.1.3 Stiffness

The stiffness of a material indicates the resistance of that material to an imposed deformation. Many materials used in engineering behave linear elastically, i.e. when the stresses on the material double the deformations become twice as large. However this behaviour does not apply for soil, in fact soil can be described as highly nonlinear (see Figure 3.3).

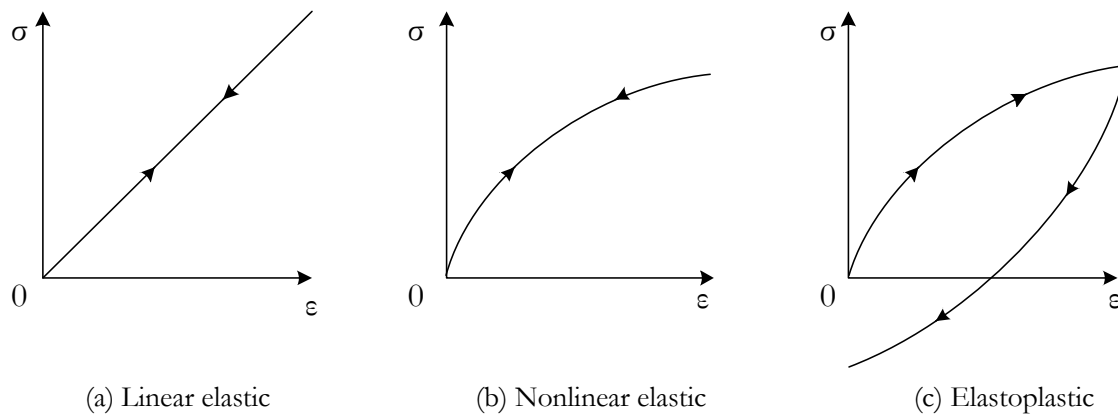


Figure 3.3: Schematic representation of different types of stress strain behaviour

During penetration water cannot drain from the pores and the soil behaves undrained. In case of undrained behaviour the stiffness of the soil depends on both the stiffness of the soil material as well as water stiffness. Since water can only be compressed, the deviatoric stresses or shear will be completely taken by the solid material. The extent of the compressibility of the clay is dependent on the saturation of the material. A lower saturation will cause a drop in the compressibility of the material. Yet the material on the bottom of the sea is fully saturated (Brinkgreve, 2007). Therefore the confining pressure of the soil is more important for its stiffness. The stiffness of a soil is dependent on the stress level, i.e. if the stress level in the soil is high the soil mass will behave stiff (Verruijt, 2005). Since the penetration losses in clay material occur in the top layer of the seabed stress levels can be presumed to be small and hence the stiffness of the deforming material is small as well. During laboratory tests of the seabed material found in Norway the secant stiffness (E_{50}) lay between 1.0 and 1.5 MPa (Fugro Geoconsulting Ltd., 2012).

3.2 Rock properties

Understandably the properties of the dumped rock can influence the penetration. For example the size, shape and density of the rock material influence the velocity during falling and mass together with the velocity influence the impulse balance used to determine penetration.

The density of the material is important since this determines the mass of an individual stone with equal size. Often rock with a higher density is preferred, since less material is needed to prevent upheaval buckling in case of pipe fixation. Common stone type is granite, which is widely available along the Norwegian coast, with a particle density of $\sim 2600 \text{ kg/m}^3$.

The shape of the stones is relevant since this influences operational aspects during dumping and loading. Preferred material is highly angular with equal dimensioned sides, a so called equant shape. The angularity

enhances particles interlocking and the equal dimensions improve durability, that is to say these stones are stronger and less likely to break during instalment.

The size of the material is governed by demands in stability and practical requirement. In SRI projects most particles used lie in the range of 1 to 5". These stones are large enough to withstand the current forces, but can still be handled easily by the ship's machinery. Bigger stones (>9") are possible but increase wearing of the conveyor belt which transports the stones from the hold to the fallpipe. Smaller stones are prone to be carried away by bottom currents and will therefore increase volume losses.

Besides the size and shape, the particle size distribution of the rock particles is important. This distribution is used to determine the hydraulic stability and filter selection of the berm. Figure 3.4 indicates the particle size distribution for two different samples of rock material. The distributions do not only show differences in size but also in size gradient. A steeper slope indicates that the material is more uniformly graded and consist mainly of stones with the same size (Figure 3.4a). This causes the porosity of the material to increase, since the inter particle voids will not be filled by smaller material. In contrast, a gentler slope indicates a better graded material with a lower porosity (Figure 3.4b). With the same material density, porosity influences the bulk density of the installed material and consequently the additional volume loss due to immediate deformation, plastic flow through pores and consolidation.

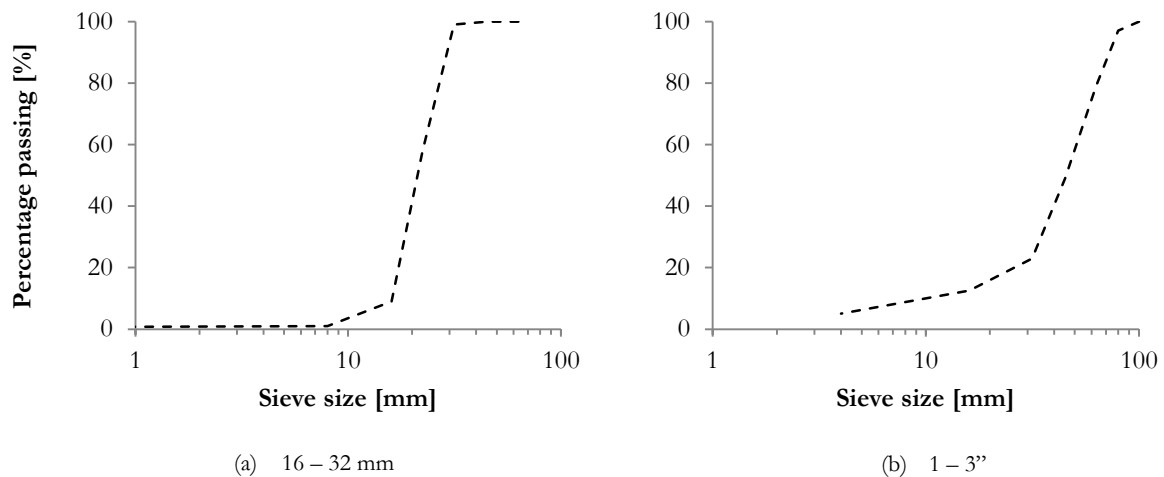


Figure 3.4: Particle size distributions for the Knarr Surf project

Since the installed rock particles are non-spherical and slightly differ from each other in shape and size, it is sometimes difficult to determine representative dimensions of a rock sample. Non-spherical stones can be described using multiple ratios such as length-to-thickness (LT), blockiness (BLc) and multiple horizontal and vertical projections (Figure 3.5).

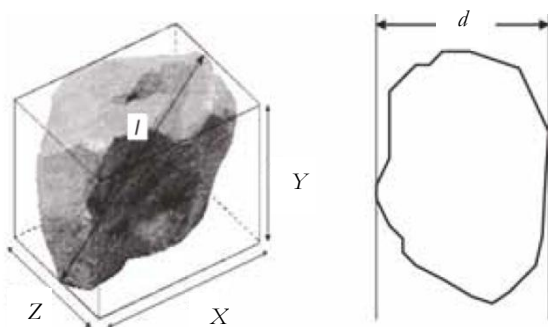


Figure 3.5: Particle shape measurement system (CUR, 1995)

These descriptions provide greater accuracy, but also greater complexity. Therefore it is common to assume that every particle is a sphere. The Rock Manual (CUR, 1995) provides formulae to calculate the

equivalent median sphere diameter (D_{s50}). This value is based on the median diameter (D_{50}) derived from the particle size distribution. Using formulae (3.2) till (3.4) the equivalent median sphere diameter and mass are determined:

$$D_{n50} = 0.84 \cdot D_{50} \quad (3.2)$$

$$D_{s50} = \frac{D_{n50}}{\left(\frac{\pi}{6}\right)^{\frac{1}{3}}} \quad (3.3)$$

$$m_{50} = \frac{\pi}{6} \cdot D_{s50}^3 \cdot \rho_s \quad (3.4)$$

3.3 Bathymetry

Most offshore – and related fall pipe – activity is carried out in a marine zone called the continental terrace, which itself consist of the continental shelf and the continental slope (Figure 3.6). The continental shelf is often characterised by the gently dipping smooth seafloor in water depths of less than 200 m. Geological processes such as currents, waves, tides and outflow of rivers have influence on the seabed conditions, however this influence is limited. The seabed conditions on the Norwegian continental shelf specifically, distinguish themselves by many outcrops of rock as well as very soft clay deposits (De Vries, et al., 2007)

The dipping continental slope often consists of complex seafloor topography and with large gradients. The typical water depth for this region lies between the 200 and 2000 m. The geology is complex because of possible geological processes such as submarine sliding, slope failures and turbidity currents. These processes limit the lateral continuity of soil layers present in this irregular seafloor (Peuchen & Raap, 2007).

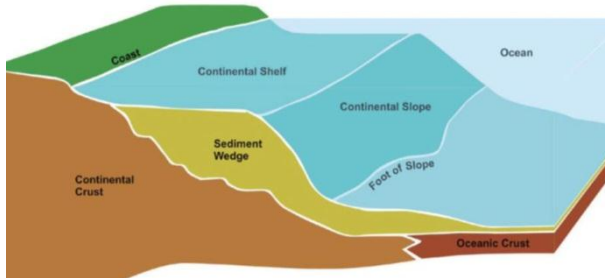


Figure 3.6: Marine zones (Fugro Geoconsulting Ltd., 2012)

4 Volume loss

In order to predict the penetration of rock particles into the seabed, it is first necessary to understand what happens to a single stone when it falls through water. The forces which act on a single stone are explained in the following paragraph. Subsequently additional penetration due to multi stone influence is assessed. Finally all other relevant processes to determine the total volume loss during subsea rock installation using a flexible fallpipe vessel are described. To simplify the problem the particles are modelled as spheres.

4.1 Single stone penetration

Several theories have been created in order to predict the penetration of a particle into soft soil, varying from the cavity expansion theory ((Hill, 1950), (Russell & Khalili, 2006)) to experimental research performed on high speed particle impact for military purposes ((Bernard, 1978), (Kumano & Goldsmith, 1982), (Young, 1981)). After having reviewed these theories it is decided that as a first reconnaissance of penetration theory for rock installation purposes, a more straightforward approach might be suitable as well. Mainly because the practical accuracy during a project is in the order of centimetres and simplified penetration problems already are very challenging (Einav & Randolph, 2004). Using the soil resistance for static problems, i.e. bearing capacity, an impression for the highly dynamic penetration problem can be created. This model can easily be created and validated, and forms the first step in assessing the penetration of particles in soft soil.

Research describing the behaviour of a single stone in water is performed extensively ((Van Rhee, 2002) (Wal, 2002), (Vrijling, et al., 1995), (Ravelli, 2012)) and a great deal is known about the forces and processes influencing this behaviour. The different forces are explained below. In addition to the hydraulic forces on a single stone in water a link is made with the geotechnical processes. This relation is used in the model to assess the penetration of a single stone in soft soil.

4.1.1 Vertical forces

When an object is submerged in a fluid there are always two forces acting on this object simultaneously, namely gravity and buoyancy. If the object is moving through the fluid it also experiences resistance in the form of drag, this force is always directed opposite to the particle movement. The formulae describing the gravitational, buoyancy and drag forces for a free falling sphere moving through a fluid are given in equation (4.1), (4.2) and (4.3) respectively.

$$F_g = \frac{\pi}{6} \cdot D_s^3 \cdot \rho_s \cdot g \quad (4.1)$$

$$F_b = \frac{\pi}{6} \cdot D_s^3 \cdot \rho_f \cdot g \quad (4.2)$$

$$F_D = \frac{1}{2} \cdot C_D \cdot \rho_f \cdot A \cdot (v_f - v_s) \cdot |v_f - v_s| \quad (4.3)$$

Where D_s is equal to the diameter of the stone, ρ_s and ρ_f represent the density of the solid and fluid material and g is the gravitational acceleration. C_D is the drag coefficient, v_s and v_f indicate the vertical velocity of both the solid and the fluid material, A is the surface area of the moving object in the direction of the flow. The drag coefficient is dependent on the Reynolds number, however for a spherical grain falling through water the drag coefficient is presumed equal to 1.0 (Battjes, 2002).

4.1.2 Penetration determination

Since all forces on a free falling stone falling through fluid are defined, a velocity profile can be created and thus the impact velocity on the seabed can be determined. This impact velocity is one of the

important factors influencing the penetration. If the velocity at impact is small, no dynamic effects have to be taken into account. This is the case for the impact speeds of normally deposited rock fill. As described in chapter 3 other important factors are the diameter of the particle and the strength as well as the consistency of the subsoil. The soil characteristics can vary to a large extent over the entire project area and may consist of weak materials such as very loose sands and soft clays to strong materials such as very dense sands and hard clays. However in this thesis only soft clay penetration will be modelled.

To model the penetration of individual rocks multiple kinematic methods can be used. Bijmagne & Luger (2005) describe a method using work and energy equations whereas Visser & van der Meer (2008) use an impulse balance. Since Van Oord has already set out using the impulse balance approach, this is preferred for further use. The impulse balance used is shown in (4.4). This impulse is valid for the whole trajectory of the stone including the free fall, however the penetration in soft soil is the main objective of this model and thus the following section will explain the use of this formula for the penetration determination only.

$$F_r = m \cdot a = m \cdot \frac{dv}{dt} \quad (4.4)$$

Here F_r is the net force acting on the rock, m is the mass of the rock which can be calculated using (3.4), a is the acceleration of the rock, dt is the time step, and dv is the change in the velocity of the stone during one time step. During penetration in the soil the velocity of the particle will decrease, this decrease in velocity can be calculated for each time step using:

$$dv = \frac{F_r(t)}{m} dt \quad (4.5)$$

When $v = 0$ m/s penetration stops and the final penetration depth is reached. The duration of the impact, (t_{imp}) and the total penetration (Δ) are therefore given by:

$$v_{imp} - \int_{t=0}^{t=t_{imp}} dv dt = 0 \quad (4.6)$$

$$\Delta = \int_{t=0}^{t=t_{imp}} v dt \quad (4.7)$$

Where v_{imp} is the rock velocity at $t = 0$ s, or in other words the impact velocity of the rock prior to hitting the seabed. Since the mass of the individual rock and the time step are known, (4.5) can be solved by determining the resultant force acting on the stone (F_r) for every time step. The resultant or net force on the stone is calculated using (4.8). This equation states that the net force can be found by subtracting the buoyancy, drag and resisting forces of the soil acting on the stone, from the gravitational force.

$$F_r(t) = F_g(t) - F_b(t) - F_D(t) - F_B(t) \quad (4.8)$$

Note: The difference between the buoyancy force (F_b) and soil resistance or bearing capacity force (F_B).

4.1.3 Bearing capacity

The ultimate load that can be supported by a soil before it fails is known as the bearing capacity. With this definition the penetration of a particle into the soft soil can be found. By calculating the position where the soil provides sufficient capacity to completely stop the decelerating stone, the penetration of the stone in the soil can be predicted. However the bearing capacity of a soil is uncertain. As described by Bowles (1997) there is currently no method to obtain the exact ultimate bearing capacity of a soil, there are however numerous theoretical models which can be used to estimate the soil's bearing capacity. Vesic (1973) describes these different methods in great detail. A short overview of the most popular formulae is given in Appendix 15.6.

In 1943 Terzaghi proposed a semi-empirical formula based on results of Prandtl, which suggests that the effect of self-weight, cohesion and surcharge forces could be separated and superimposed. Due to its convenience this equation is used frequently, however since this method is only applicable for shallow problems and rock penetration in soft soil can be described as a deep problem ($\Delta/B > 1$), this is not a suitable method. Here Δ is the foundation depth or penetration and B is the width of the foundation or in this particular case the diameter of the rock particle. Meyerhof (1963) slightly altered Terzaghi's equation by adding shape factor s_q and including depth factors d_i . For small depths ($\Delta \approx B$) Meyerhof's bearing capacity greatly resembles Terzaghi's value, for larger depths the difference between the two becomes more noticeable. For a deeper problem however Brinch Hansen (1970) and Vesić (1973) are recommended (Bowles, 1997). Since Brinch Hansen's formula is commonly applied and this equation implicitly allows any Δ/B ratio – and thus can be used for both shallow and deep problems – this method will form the basis for bearing capacity issues in this report. The formula which Brinch Hansen finally developed, distinguishes influences based on load and ground inclination, footing shape, depth and inclination and is shown below:

$$F_B = A_{eff} \left(c N_c s_c d_c i_c g_c b_c + \bar{q} N_q s_q d_q i_q g_q b_q + \frac{1}{2} \gamma B' N_\gamma s_\gamma d_\gamma i_\gamma g_\gamma b_\gamma \right) \quad (4.9)$$

Note: The full determination of all factors is provided in Appendix 15.7.

Here A_{eff} is the effective foundation area, B is the effective width of the foundation, N_i are bearing capacity factors, s_i are the shape factors for the effective foundation area, d_i are the depth factors, i_i are the inclination factors of the force on the foundation, b_i represents the inclination of the base of the foundation, g_i indicates the inclination of the ground, q is the effective surcharge acting upon the soil surface outside the foundation, γ is the effective unit weight of the soil and finally c is the apparent cohesion of the soil (Brinch Hansen, 1970). All these additional factors seem to create a rather complicated formula, however as shown in the previous paragraph the penetration of rock particles in soft clay can be described as undrained. Hence in case of undrained failure of clay due to the penetration of a spherical particle, the internal friction angle of the material (ϕ) goes to zero and the length and width of the foundation are equal. This greatly simplifies the equation. Moreover during penetration the forces on the soil are assumed to be vertical and the seabed is simplified as a horizontal surface. These assumptions reduce Hansen's equation to the following:

$$F_B = A_{eff} (s_c \cdot N_c \cdot c_u + \bar{q}) \quad (4.10)$$

Note: due to undrained behaviour cohesion c is altered to undrained shear strength c_u of the material

In which s_c is the cohesive shape factor and for undrained behaviour, this is equal to 1.2. Equation (4.10) provides an estimation for the bearing capacity during undrained penetration, but the discussion about this formula is not complete, since the development of the N_c factor is ambiguous. Skempton (1951) describes the development of this parameter with depth, depending on the shape of the foundation. He states that at the surface ($\Delta = 0$) N_c should be 6.0 for a circular footing. Moreover he distinguished three different depth stages used to determine the N_c . This depth dependent separation is also used in other literature ((Bijmagne & Luger, 2005), (SNAME, 2008)). Both sources also differentiate between non-gapping and gapping penetration or, in other words, penetration with or without back flow of material, as indicated in Figure 4.1. According to Bijmagne & Luger (2005) the resistance of the soil increases during non-gapping penetration since more material has to be deformed, leading to a smaller penetration. Controversially SNAME (2008) states the additional load from the back flowing material increases the maximum penetration. However during the laboratory testing all particles caused a fully gapping penetration independent from the soil strength. Therefore the bearing capacity factor N_c is fixed at 6.0, which indeed proved to provide the correct fit with the results (see chapter 11).

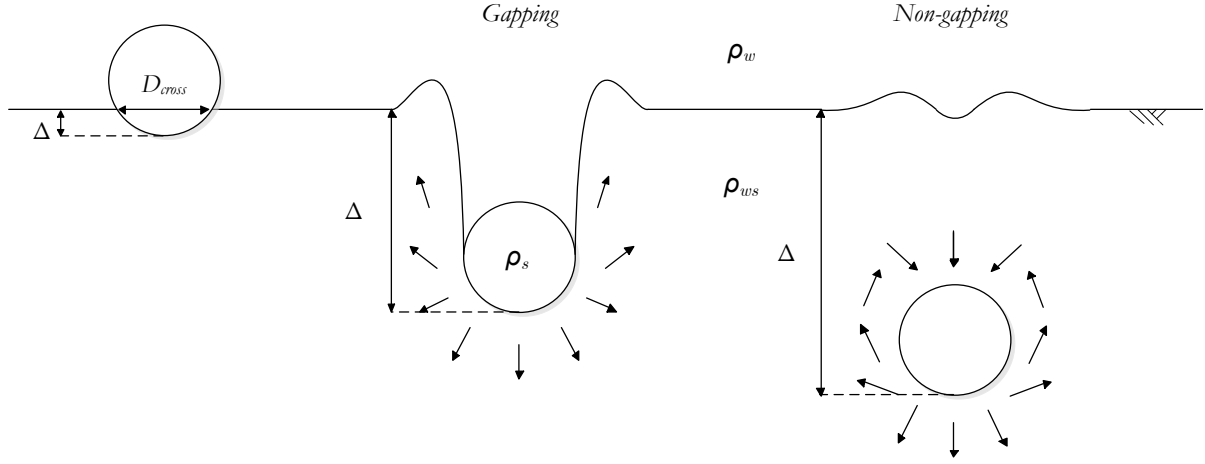


Figure 4.1: Gapping and non-gapping penetration

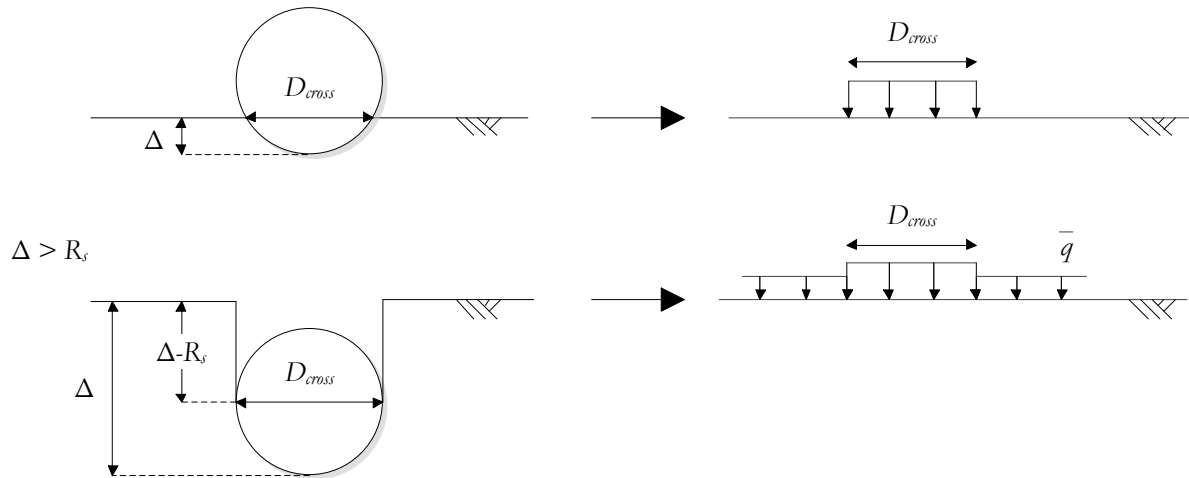
4.1.4 Soil resistance

In formula (4.8) $F_B(t)$ represents the resistance of the soil acting on the rock. The proposed formula creates the link between the hydraulic and geotechnical processes and is based on previous work done by Van Oord and Deltare (De Vries, et al., 2007), (Visser & Van der Meer, 2008) and (Bijnagte & Luger, 2005)). The latter states that since the velocities are small, no dynamic effects have to be taken into account and consequently the resistant force on the rock can be determined using a static loading case. Thus calculations for the soil resistance in this dynamic setting can be approached using common bearing capacity formulae. This central assumption greatly simplifies modelling, but can have significant influence on the results. As described in the previous paragraph Brinch Hansen developed a suitable formula to estimate the bearing capacity of a foundation in case of static loading, the simplified formula for undrained penetration the of a particle on a flat seabed is shown below:

$$F_B = A_{eff}(s_c \cdot N_c \cdot c_u + \bar{q}) \quad (4.11)$$

As mentioned before in this equation A_{eff} and q are penetration dependent (see Figure 4.2). In reality the undrained shear strength c_u is also penetration dependent, increasing with the average effective stress in the soil. However since both the penetration and the unit weight of the soil are relatively small, the average effective stress increase only a little with depth, hence the undrained shear strength is assumed to remain constant with depth.

$$0 \leq \Delta \leq R_s$$

Figure 4.2: Penetration dependent parameters A_{eff} and q

The development of the cross-sectional area A_{eff} can be expressed in the following way:

$$D_{cross} = \begin{cases} 2 \cdot \sqrt{R_s^2 - (\Delta - R_s)^2} & 0 \leq \Delta \leq R_s \\ 2 \cdot R_s & \Delta > R_s \end{cases} \quad (4.12)$$

$$A_{eff} = \frac{\pi D_{cross}^2}{4} \quad (4.13)$$

Here $D_{cross}(\Delta)$ is the diameter of the penetrated rock section, R_s is the radius of the sphere and Δ is the penetration. The development of the effective surcharge acting upon the soil surface outside the foundation \bar{q} is best described using:

$$\bar{q} = \begin{cases} 0 & 0 \leq \Delta \leq R_s \\ (\Delta - R_s)\bar{\gamma} & \Delta > R_s \end{cases} \quad (4.14)$$

Additional to this penetration dependent behaviour, one must realize that equation (4.11) is based on a flat foundation. In case of such a flat foundation in undrained conditions ($\varphi = 0^\circ$) the Prandtl wedges are symmetrical (Figure 4.3a) and wedge do not contribute to the bearing capacity. However with a spherical particle the wedges are no longer symmetrical and cause for overestimation of the wedge volume and hence underestimation of the soil resistance (Figure 4.3b). The added bearing capacity is related to the penetrated spherical volume (Figure 4.3c) and can be determined using:

$$F_{wedge_extra} = V_{wedge} \cdot \bar{\gamma} \quad (4.15)$$

Where:

$$V_{wedge} = \int_0^\Delta \pi \cdot (\sqrt{R_s^2 - (\Delta - R_s)^2}) d\Delta$$

$$V_{wedge} = \begin{cases} \pi \left(R_s \cdot \Delta^2 - \frac{1}{3} \Delta^3 \right) & 0 \leq \Delta \leq R_s \\ \frac{2}{3} \pi R_s^3 & \Delta > R_s \end{cases} \quad (4.16)$$

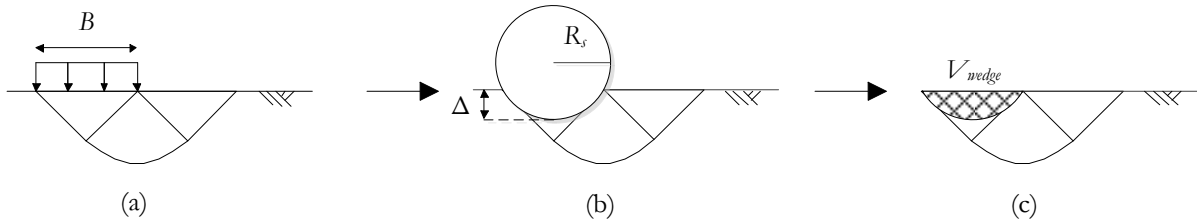


Figure 4.3: Additional soil resistance due to overestimation of the wedge volume

As a result in the particular case of the rock penetration, equation (4.11) has to be complemented with an additional wedge bearing capacity, completing the final soil resistance to be:

$$F_B(t) = F_{cohesion}(t) + F_{surcharge}(t) + F_{wedge_extra}(t) \quad (4.17)$$

$$F_B(t) = A_{eff}(s_c \cdot N_c \cdot c_u + \bar{q}) + V_{wedge} \cdot \bar{\gamma}$$

With the description of this extra bearing capacity and the penetration dependent bearing capacity factors, all unknowns in equation (4.8) are defined and the impulse balance can be solved, leading to a simple computation of the penetration depth of a rock particle in soft soil. This mathematical formulation for single stone penetrations is validated using laboratory experiments in chapter 11.

4.2 Impact velocity

In reality however production rates lie between 250 and 2000 tons per hour and not one but thousands of stones are dumped simultaneously. Since these stones all interfere with each other the impact velocity changes during dumping using a flexible fallpipe, which in turn effects the impulse balance equation defined in the previous paragraph. The following paragraph describes the hydraulic processes during the installation of multiple rocks through a fallpipe.

4.2.1 Fallpipe velocity

Several studies into the velocity development of a group of stones during the descent have been done. Richardson & Zaki (1997) describe the hindered settling of rock groups; Wal (2002) divides the trajectory of a group of rocks in five different stages based on literature and experimental research, as shown below:

- Acceleration of the group
- Deceleration of the group
- Formation of a rock front
- Single stone falling
- Radial run-off

More information about the different stages during the dumping of multiple rocks is provided in Appendix 15.8. The main difference between rocks falling through a flexible fallpipe versus rocks falling in stagnant water, is the movement of the surrounding water. In case of FFP installation the moving rocks will cause a downwards directed water flow because of shear forces on the surrounding water. As a result of this flow rocks are not falling in stagnant water, but in a constant moving stream. This water movement can significantly increase the final velocity of a rock up to the point where friction of the pipe equals the downward force. At the exit of the pipe a water jet will be present which will affect the velocity and spreading of the rocks (Ravelli, 2012). Especially the research done by Van Rhee (2002) and Van Oord (2002) prove useful since they describe the development of the exit velocity for different production rates, pipe lengths and stone parameters. Since the model created by Van Oord is proven accurate using scale experiments, this model is used to determine the exit velocity of rocks dumped via a flexible fallpipe. In this model the exit velocity of the rock water mixture is found iteratively. The steps used to compute the final velocity are given below:

1. Choose a certain water velocity (v_{water})
2. Calculate the equilibrium or terminal velocity of the individual stones ($v_{equilibrium}$)
This equilibrium is reached very rapidly. After $8D_s$ the stone has already reached 99% of its terminal velocity. Therefore in this model the terminal velocity is assumed to be instantaneous. $v_{equilibrium}$ for a sphere can be calculated using:

$$v_{equilibrium} = \frac{\sqrt{4D_{s50}(\rho_s - \rho_w)g}}{3\rho_w C_D} \quad (4.18)$$

3. Calculate the fall velocity of the rock mass through the fallpipe ($v_{fallpipe}$)

$$v_{fallpipe} = v_{equilibrium} + v_{water} \quad (4.19)$$

4. Calculate the stone concentration under the vltter (c_m)

$$c_m = \frac{\frac{P_r}{\rho_s}}{v_{fallpipe} \cdot A_{min}} \quad (4.20)$$

Note: P_r is the production rate of the installed rock material in [kg/s]

5. Calculate the density of the mixture (ρ_m)

$$\rho_m = c_m \cdot \rho_s + (1 - c_m) \rho_w \quad (4.21)$$

6. Calculate the estimate for the water velocity in the vltutter by equating the driving and frictional forces present in a fallpipe using the following formulae:

$$\begin{aligned} \Delta p_{driving} &= \Delta p_{loss, total} \\ (\rho_m - \rho_w) g \cdot h &= \frac{1}{2} (\zeta_{carnot} + \zeta_{wall}) \rho_m \cdot v_{water}^2 \\ v_{water} &= \sqrt{\frac{2(\rho_m - \rho_w) g \cdot L_{eff}}{(\zeta_{carnot} + \zeta_{wall}) \rho_m}} \end{aligned} \quad (4.22)$$

Note: More information about the derivation of the driving and frictional forces can be found in appendix 15.8.

7. Finally the correct approximation for the exit velocity of the mixture is found by repeating previous steps until the result of 6 equals 1 within an acceptable error ($1e^{-06}$).

More about the determination of the fall pipe velocity can be found in Appendix 15.9.

4.2.2 Jet characteristics

The previous iteration determines the final velocity of the rock water mixture at the end of the fallpipe, however between leaving the FFP and reaching the sea bottom, the mixture is subjected to changes. Since the impact velocity of the particles on the soft seabed is of particular importance to the extent of the penetration, additional attention is given to its derivation. Research performed by Van Oord ACZ (2002) and Ravelli (2012) indicates that the process determining the impact velocity is best described using jet theory. Rajaratnam (1976) divides the jet into three different regions (Figure 4.4):

- Free jet region
- Impinging jet region
- Wall jet region

In the free jet region the flow is not restricted by any boundaries. This free jet region can itself be subdivided into three zones (Figure 4.5): the zone of flow establishment (ZFE), the zone of established flow (ZEF) and the intermediate transition zone (Albertson, et al., 1948). In the ZFE the velocity is expected to remain the same as the jet exit velocity. In the ZEF region however the jet flow will start to expand, as a result of this expansion the flow velocity will decrease.

Solutions have been found in literature to describe the velocity profile and the expansion in vertical and horizontal direction for different kinds of jet nozzles ((Lee, et al., 2010), (Beltaos & Rajaratnam, 1974)). Since the vltutters used to create the flexible fallpipe are round, this jet can be regarded as a circular jet. In that case the jet spreads out radially, symmetrical to the centreline of the jet. As can be seen in Figure 4.5 the velocity profile of the cross section of a circular jet can best be described as a Gaussian distribution. The largest velocity is present in the centre of the jet flow, near the sides of the jet the velocity decreases towards the ambient vertical velocity. As a first estimate of the impact velocity the centre velocity of the jet is used. Although this might be a conservative assumption – since impact speed and hence penetration increases – it is fair to state that the centre of the ROV will hover over the whole berm. Rajaratnam (1976) describes the centreline velocity development of a circular turbulent jet using the following formula:

$$v_{centre} = \begin{cases} v_0 & 0 \leq x \leq x_{cb} \\ \frac{x_{cb}}{x} \cdot v_0 & x > x_{cb} \end{cases} \quad (4.23)$$

In which v_{centre} is the vertical velocity in the centre of the circular free jet region, v_0 the jet exit velocity, x is the distance from the orifice and x_{cb} the characteristic length where the flow is fully established. This can be calculated using:

$$x_{cb} = 6.11 \cdot D_{min} \left(\frac{v_{\infty} + v_0}{v_0} \right) \quad (4.24)$$

Here v_{∞} is the ambient flow velocity in the vertical direction and D_{min} equals the minimal diameter of the vltter at the end of the pipe. In the deep sea conditions the ambient horizontal velocity lies in the order of magnitude of 0.5 m/s, the vertical ambient flow velocity however is negligible. In that case equation (4.24) is slightly altered and becomes

$$x_{cb} = 6.3 \cdot D_{min} \quad (4.25)$$

Indicating that the centreline jet velocity starts to decay at a characteristic length of $6.3D_{min}$.

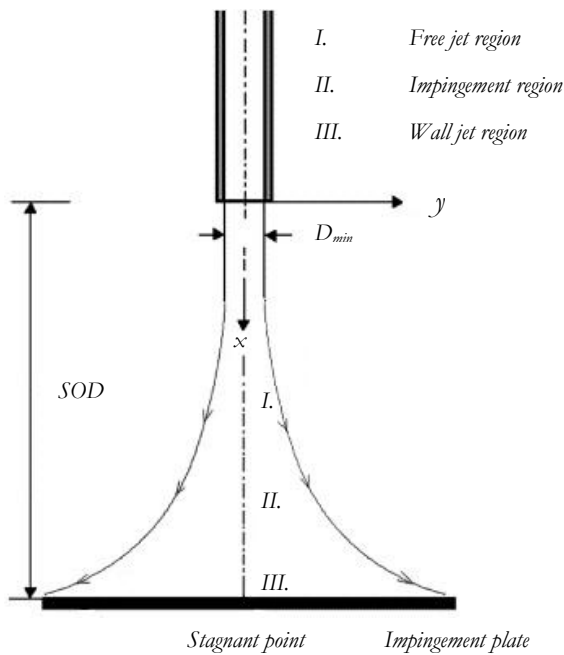


Figure 4.4: Circular jet regions (Karimipناه & Awbi, 2002)

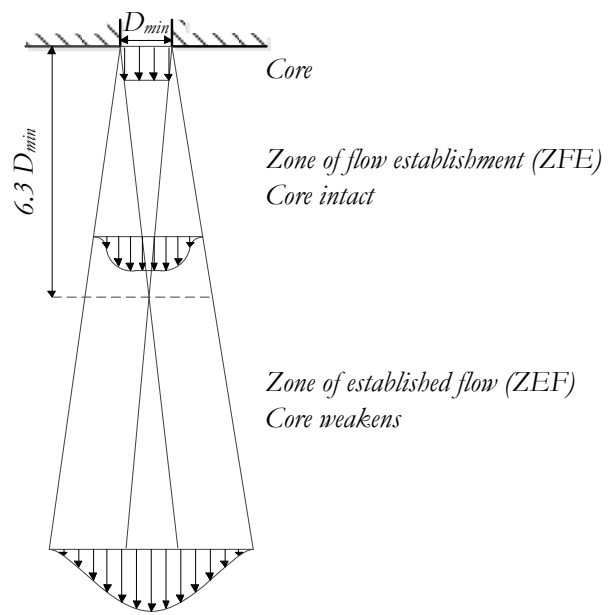


Figure 4.5: Subdivision of free jet regions

In the impinging jet region the jet starts to get affected by the presence of the sea bottom. The impinging region is dependent on the distance between the jet exit and the seabed, also known as the stand-off distance (SOD). Rajaratam (1976) describes the location where the jet becomes affected by the bottom using a dimensionless parameter (SOD/D_{min}). For large stand-off distances ($SOD/D_{min} > 8.3$) this will occur at $x/SOD = 0.86$. From this point on the velocity will start to decrease rapidly and differs from the previously described free flow region.

When the circular jet flow reaches a rigid surface the vertical velocity of the jet is deflected in horizontal direction and spreads out radially, forming a radial wall jet. In this region the vertical velocity drops. Horizontally the velocity distribution is axisymmetric around the stagnant point. With a completely rigid wall the vertical velocity of the jet is zero at this centre point. Theoretically this would imply that the impact velocity of the rock particle, in a mixture of rocks and water, is always equal to its equilibrium velocity with an impinging jet. This is unlikely to happen in reality. In the case of a soft seabed one can image that the water jet penetrates slightly into the soft sediment, keeping a vertical velocity. Moreover the stone itself also suffers from inertia, retaining its vertical velocity during descent.

In practice the ROV is always kept at a distance of minimal 10 m from the seabed. This is done to prevent damage to the ROV due to collisions with the surface. Obviously wave influences at the surface cause this distance to vary over time, but 10 m can be assumed average. This means that the stand-off distance is large and the vertical velocity of the jet is only influenced by the presence of the seabed when $x/SOD \geq 0.86$. As stated before the jet velocity decrease rapidly in the last part of the descent. This sudden decrease in water velocity is expected only to have a small effect on the impulse of the stone due to inertia effects. Therefore it is assumed that the rock particles are not slowed down by this decrease in water velocity and the impinging velocity profile is simplified as a free jet profile. Clearly this is not what happens in reality, but exploring the real vertical velocity of water at this point falls outside the scope of this thesis. Moreover modelling an impinging jet as a free jet will overestimate the water velocity causing a slight overestimation of the penetration which is conservative. Using the derived fallpipe exit velocity shown in section 4.2.1 combined with the free jet region velocity formula (4.23) for ambient water the following formulae are found:

$$v_{imp} = \begin{cases} v_{fallpipe} & 0 \leq x \leq x_{cb} \\ \left(\frac{x_{cb}}{x} \cdot v_{water} \right) + v_{equilibrium} & x > x_{cb} \end{cases} \quad (4.26)$$

$$x_{cb} = 6.3 \cdot D_{min} \quad (4.27)$$

When $x = SOD$ the impact velocity at the sea bottom, can be found using:

$$v_{imp} = \frac{6.3 \cdot D_{min}}{SOD} \cdot v_{water} + v_{equilibrium} \quad (4.28)$$

Bases on this formula the impact velocity of the stone is always at least equal to the equilibrium velocity and maximal when this stand-off distance falls within the zone of flow establishment. All previous assumptions cause this impact velocity to be rather high and hence conservative.

Moreover the water flow directed at the seabed caused by the falling of the stones through the water develops a water pressure between stone and seabed just before impact. As a consequence an excess pressure will develop, at the stagnation point of the flow this pressure is equal to:

$$p = \frac{1}{2} \cdot \rho_f \cdot v_{imp}^2 \quad (4.29)$$

This excess pressure will act on the falling stone in the upwards direction, slowing down the stone, resulting in a smaller penetration. In this thesis the existence of the stagnation point and its effect are not further investigated nor taken into account. Additional research into stone groups installed using a fall pipe and their effect on impact velocity is recommended.

4.3 Additional processes

Based on the previous paragraphs the impact velocity and resulting immediate penetration can be assessed. Depending on the specific rock, soil and production characteristics this single stone penetration is about 5 cm. The complete volume loss in soft clay however can be a lot larger. This is the result of additional processes, listed below, which will be described briefly in this paragraph.

1. Multi stone penetration
2. Loss of fine particles due to currents
3. Immediate deformation of the seabed
4. Long term settling of the berm due to consolidation
5. Flow of cohesive material into the pores of the installed rock fill

4.3.1 Multi stone penetration

During installation of an actual berm thousands of stones are dumped simultaneously. A single stone penetrating in the virgin seabed is therefore a very simplified version of the dumping process. After the first particles have penetrated into the soil, other particles will fall on top of the previous layers. Due to this process the penetrated particles will be pushed deeper into the seabed as indicated in Figure 4.6. The magnitude of this additional penetration can be derived using the conservation of momentum principle. The impulse added by the new stone is equal to the created momentum of both stones. The exact way the stones react after the collision depends on numerous factors, such as angle of impact, mass of both particles, impact velocity and the coefficient of restitution.

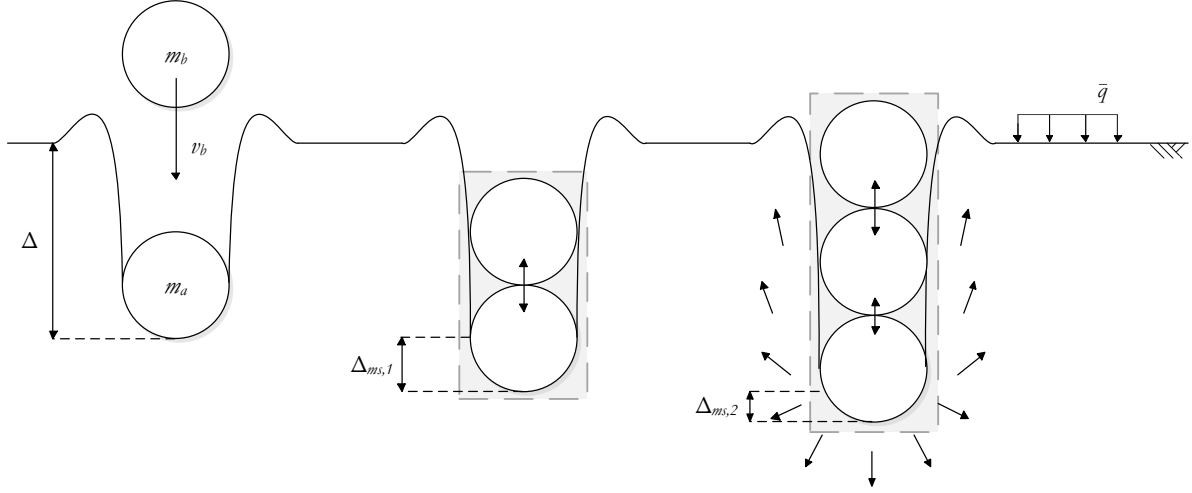


Figure 4.6: Schematic overview of multi stone penetration

In order to roughly assess the influence of multi stone penetration a few assumptions have to be made. First the impact velocity and mass of the additional particle are presumed equal to the previously derived single stone impact and mass (equation (4.31)). Secondly the impact is schematised as fully plastic without any loss of energy, i.e. after impact both particles form one combination of masses which both move in the same direction with an identical velocity. This is indicated by the grey rectangle surrounding the group of particles in Figure 4.6. Finally the collision is simplified as a central impact, which means that both masses collide with each other on a linear line of impact. In other words the centres of mass are situated on one straight line, preventing any skew impact forces. Based on these assumptions this following formulae can be used to determine the additional penetration:

$$\sum m_i(\vec{v}_i)_1 = \sum m_i(\vec{v}_i)_2$$

$$m_a(v_a)_1 + m_b(v_b)_1 = m_a(v_a)_2 + m_b(v_b)_2 \quad (4.30)$$

And since:

$$m_a = m_b$$

$$(v_a)_1 = 0 \text{ m/s}$$

$$(v_b)_1 = v_{imp} \quad (4.31)$$

The formula can be simplified to:

$$m \cdot v_{imp} = 2m \cdot v_{ms}$$

$$v_{ms} = \frac{1}{2} v_{imp} \quad (4.32)$$

And when the amount of impacting rocks increases:

$$m \cdot v_{imp} = i \cdot m \cdot v_{ms}$$

$$v_{ms} = \frac{1}{i} v_{imp} \quad (4.33)$$

Note: i is the number of subsequent stones colliding

Using the impact velocity for the coupled particles, the additional penetration can be derived with the existing single stone model. Here the mass of the particle is doubled and the impact velocity is cut in half. As a result the gravitational and buoyancy forces double due to the doubling of the mass. The drag and bearing forces are still calculated using the same cross-sectional area, since the stones are modelled to fall directly on top of each other, limiting the exposed effective cross-sectional area to one stone. Figure 4.7 shows the additional penetration as a result of multiple impacts on top of the previous stone, both in absolute and in relative values. Moreover the relation between the multi stone penetration and the undrained shear strength of the surrounding material is indicated. The absolute graph (Figure 4.7a) is self-explanatory; all subsequent impacts show a substantial increase, however with more resistance of the soil due to a higher undrained shear strength, the penetration becomes smaller. The relative graph (Figure 4.7b) however requires additional explanation. In this figure the initial single stone penetration is the reference plane (Δ_{ref}) forming 100%. The graph indicates that multiple impacts cause a smaller relative additional impact when the undrained shear strength of the seabed is larger. This can be explained by looking at the relative influence of gravitational forces. In low undrained shear strength conditions bearing capacity is small and hence the increase in gravity becomes increasingly important. If the bearing capacity is larger – due to the larger undrained shear strength – the influence of additional gravitational load is less severe. Moreover during the initial single stone penetration in a soft soil with a low undrained shear strength, the particle already penetrates more than its equivalent radius. Consequently the resistance on the particle will remain the same for increasing penetration depths. Whereas for a high undrained shear strength the particle barely penetrates into the soil and for increasing penetration the resisting area grows, increasing the total resistance of the soil.

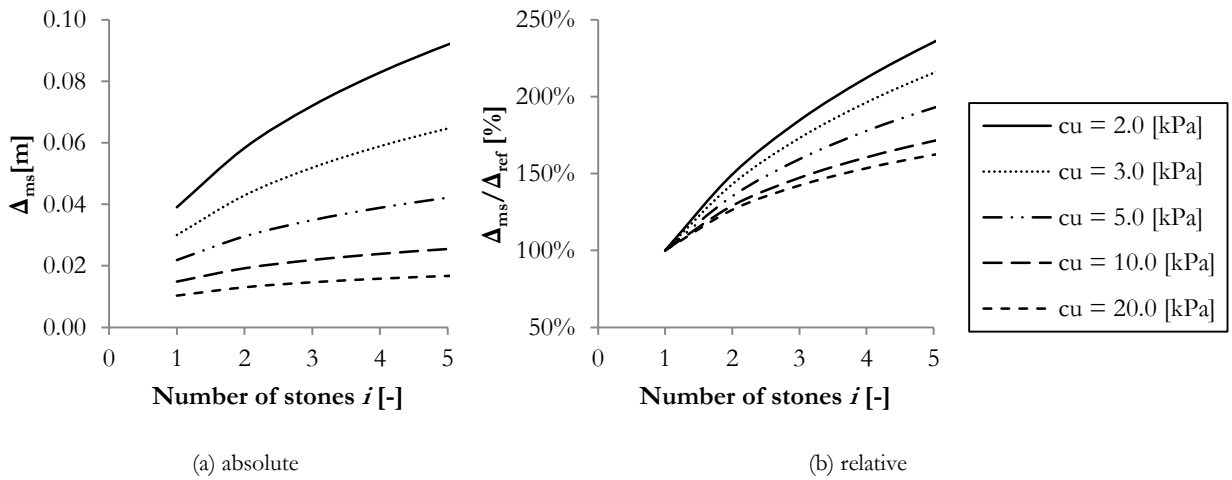


Figure 4.7: Additional penetration as a result of multi stone impact ($D_{50} = 0.05$ m, $\rho_s = 2680$ kg/m³)

According to the relation described in the figure above the penetration keeps increasing with additional stones impacting on the previous ones indefinitely. This simplified representation of the multi stone effect is not realistic and hence form the upper boundary of additional penetration for to a number of reasons. First of all during the dumping process hundreds of stones are dropped onto the seabed, these stones all penetrate into the soil up to certain extend. That is why the characteristics of the seabed start to change during dumping. Additional stone particles mixed in the soil increase the strength and stiffness of the soft clay. In addition to the change of soil properties during dumping, the surcharge on the seabed increases. The weight of all the rocks dumped on the seabed prevents the displacement of soil towards the top

during penetration. That is why this additional surcharge load on top of the seabed enlarges the bearing capacity of the soil and decreases possible penetration. Finally, after a certain amount of rocks are dumped, a layer of rock or berm is formed. From this moment on the new stones due not impact on one stone directly, but will spread their impulse over a number of stones. As a result the amount of energy added to one stone will drop and consequently the additional penetration will decrease as well.

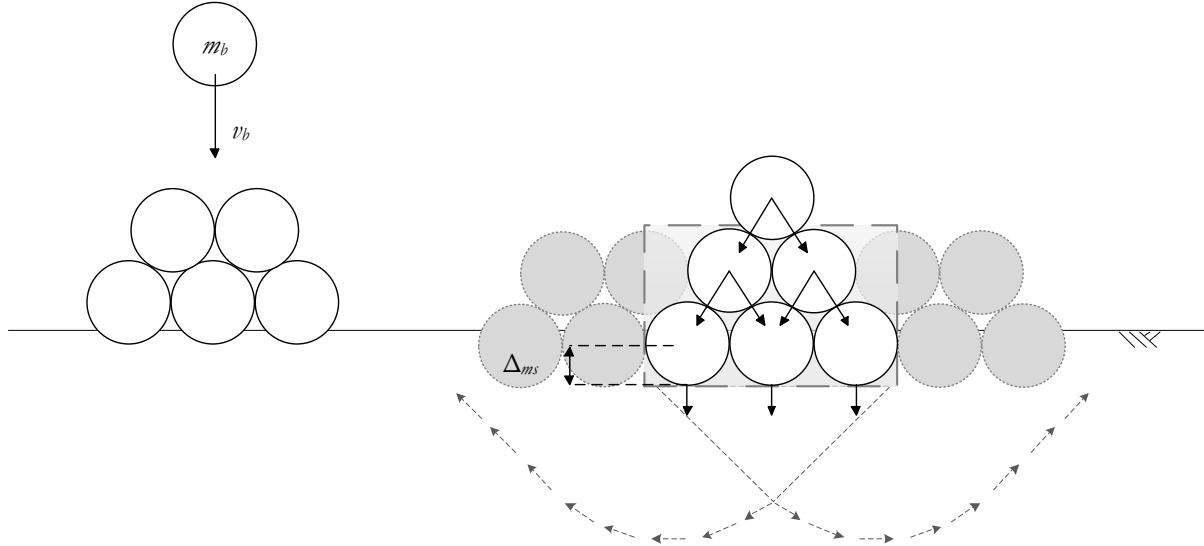


Figure 4.8: Schematic overview of multi stone penetration including force spreading

This is shown in a very simplified way in Figure 4.8. Based on this representation, where the impulse of one stone is distributed across a bed of already installed particles a lower boundary of the multi stone penetration effect is modelled. This model forms the lower boundary since it is unlikely that the particles are stacked on top of each other in a perfect rhombic way. Moreover in this model the installed rocks also form a surcharge load which hinders the displacement of clay towards the top of the seabed and consequently lowers penetration. Figure 4.8 shows the bed of particles in 2D however in reality the impulse is divided over stones in three dimensions. When using this approach the additional penetration is only 5% and does not increase any further after five subsequent stones drop directly on top of the stacked previous ones. For the increasing berm height the required mobilised mass is so large and the velocity so small, that the resulting force of this impulse is negligible.

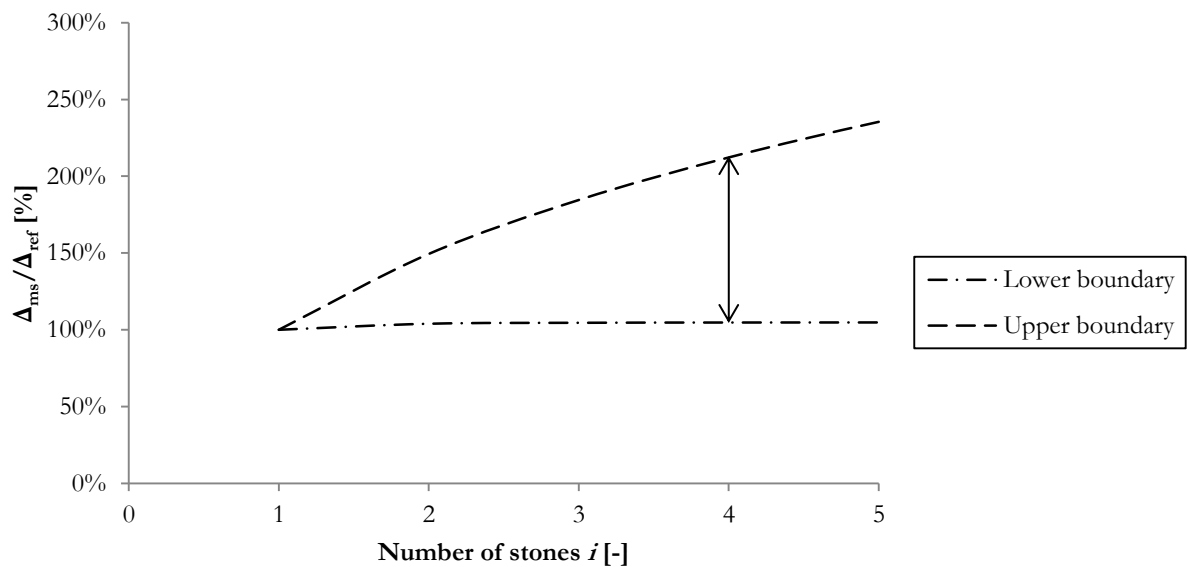


Figure 4.9: Upper and lower boundary of the multi stone penetration effect

The assumptions made in this paragraph greatly simplify the real process and form a possible first impression of multi stone impact both for the upper as for the lower bound values. In reality the chance that stones will fall perfectly vertical on top of each other and from a central collision is limited. Additionally the packing and shape of the particles will differ. Moreover the assumption that the impact is perfectly plastic and the stones move as one after impact has large implications for the additional penetration. Probably the real impact is slightly elastic which causes the stones to move in opposite direction after impact. In addition the impact velocity of the particles can change due to group effects of the large amount of particles being dumped at the same time. These stones all affect the trajectory and velocity of one another. These reasons combined make that the conservation of momentum for a string of stones dropped directly on top of each other overestimates the additional penetration and therefore forms a highly conservative upper limit for multi stone penetration. On the other hand the three dimensional distribution of the impulse combined with the surcharge increase forms the lower limit. In reality the behaviour is situated somewhere in between as indicated in Figure 4.9. The extent of the described processes such as soil strength increase, surcharge influence and diversion of energy over multiple stones is not been examined thoroughly and requires additional (experimental) research since the influence of this process on the volume loss is large. Additional tests on group effects during dumping and multi stone impact will have to be performed to validate the assumptions made and further improve the model for this effect.

4.3.2 Loss of fines

During dumping through the fallpipe the rocks are protected by the vlutters, however in the final descent between the mouth of the fallpipe and the seabed the rocks can be affected by subsea currents. These currents can carry the rock material and deposit it outside the theoretical perimeter of the project. The material is then accounted for as dumped material, but does not end up in the rock fill, as shown in Figure 4.10.

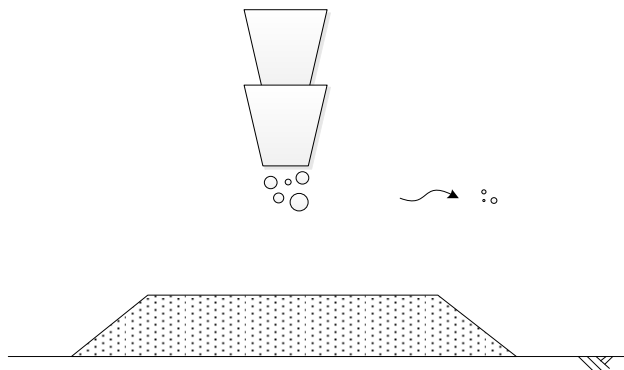


Figure 4.10: Loss of fine particle material

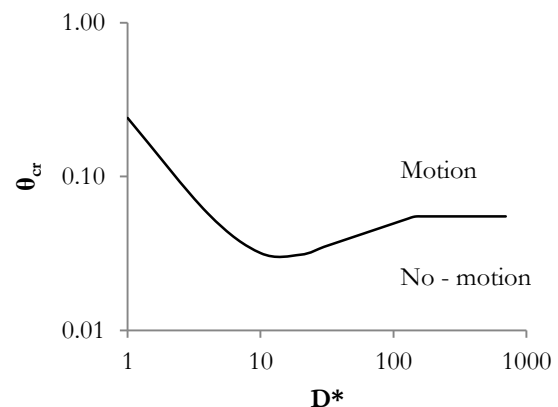


Figure 4.11: Initiation of motion according to Shields

The wash-out of fines can be estimated by assessing the grading curve of the rock material, combined with the local current circumstances and depth. By calculating a maximum grain size that can be transported away from the installation zone by deep sea current, a certain percentage of the installed material can be assumed lost. To determine this percentage a formula used for sand transport in hydraulic engineering is applied. Based on the experimental results of Shields (1936) – related to a flat bed – the critical conditions for initiation of motion are determined as shown in Figure 4.11. The curve represents a critical stage at which only part of the bed surface is moving. With help of formulae (15.12) to (15.16) in Appendix 15.10 created by Van Rijn a relation is established between the subsea current velocity and the particle size which is picked up from the seabed by this current (Van Rijn, 1993). Obviously the particles which descend from the mouth towards the fill are not lying on the seabed yet and will therefore be moved more

easily by the currents, however this influence is presumed small since the duration of this descent is small too. Moreover all floating particles are presumed lost. In reality part of the particles taken by the currents will drop inside the perimeter of the project and will still contribute to the creation of the berm.

4.3.3 Immediate deformation

Due to the weight of the installed rock fill the seabed will start to deform. This deformation can be separated in an immediate and a time dependent component (consolidation). In this paragraph the immediate deformation will be explained. Deformation due to consolidation will be discussed in the next paragraph.

Immediate deformation of the seabed due to loads on top is not caused by a change in volume or in soil structure, but by pushing away the surrounding material. Since this effect is immediate, water cannot dissipate from the pores resulting in undrained soil behaviour. Due to this undrained behaviour, volumetric change is prevented during the deformation. The material which is displaced underneath the rock fill will cause a swelling effect alongside the berm (shown in Figure 4.12 and Appendix 15.25). The volume of displaced material under the berm is equal to the volume of the lumps arising at the sides of the fill. These bulges can become rather large and have to be accounted for when determining the reference level surrounding the berm.

Immediate deformation will occur both in sand and clay. Because of the larger compressibility of clay however, this effect will be larger for this soil type. The magnitude of the immediate deformations depends on the support geometry, the soil type, the soil properties and the thickness of the soft layer. A high berm in combination with a thick layer of soft highly compressible soil results in a large immediate deformation (~ 5 cm). However research indicates that the support height is governing (Visser & Van der Meer, 2008). The immediate displacement of clay can be computed using finite element calculations in PLAXIS, for instance in combination with the Mohr – Coulomb linear elastic perfectly plastic material model. By allowing the development of excess pore pressures undrained behaviour is simulated.

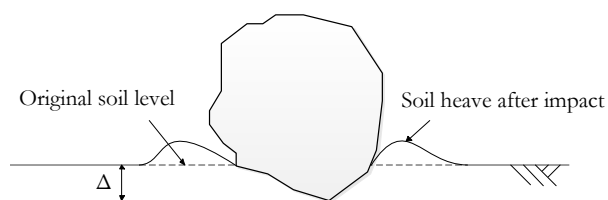


Figure 4.12: Soil heave effect during single stone penetration



Figure 4.13: Vertical deformations over the depth seabed

The thickness of clay layers influences the magnitude of the immediate deformation; the greater the thickness of the layer, the larger the settlement. The geometry of the support structure determines the loading on the seabed to occur. A higher support results in a larger load and hence causes greater deformations of the subsoil. An increase in length and/or a width of the structure will further result in an increase of the stress at deeper levels in the subsoil, resulting in a higher level of immediate deformations. Since the berms installed in SRI project can be rather large (~ 100 m) even the properties of the deeper layers will to some extent influence the immediate deformation on the surface. Figure 4.13 indicates that the course of the deformations over the different layers. As can be seen here the seabed deformation extends all the way down to layers at a depth of 24 m.

4.3.4 Consolidation

During installation of the rock fill the soil layer underneath is subjected to a stress increase equal to the submerged weight of the rock material. This increase in stress induces an increase in pore water pressure. Pore water drainage causes the effective stress in the soil to increase and is therefore associated with settlement. In highly permeable soils such as coarse sands, the excess pore water pressure dissipated

almost instantly. In fine grained material however the hydraulic conductivity is significantly smaller; here the drainage of pore water gradually dissipates over a long period. The associated volume change will continue long after the load is applied and the immediate settlement occurred. This prolonged settlement due to the hindered drainage of excess pore water pressures is known as consolidation (Das, 2002). In clay consolidation settlement may be several times greater than the immediate settlements. The theoretical volume necessary to fulfil the requirements is based on the original seabed present before dumping. Due to the settling of the seabed more material is necessary to complete the fill and that is why on-going deformation caused by consolidation effects volume loss (as shown in Figure 4.14). Although projects only last a short period of time – fluctuating between hours and several days – and the permeability of the clay material is very small, this process still plays a significant role.

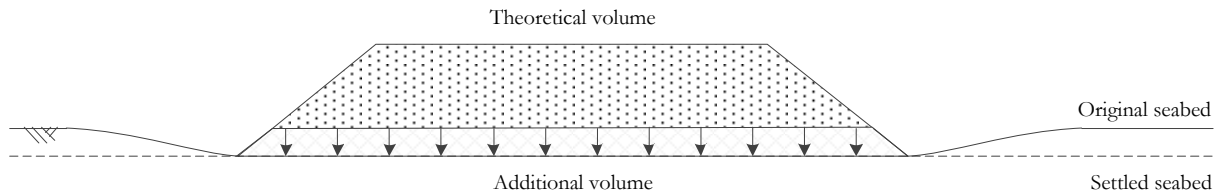


Figure 4.14: Additional volume necessary due to consolidation deformation of the seabed

The magnitude of this loss depends on the duration of the project, the soil properties and the fill geometry. Since the fill is often installed on very soft soil with a low permeability, the consolidation loss is typically a few centimetres. This is small compared to complete consolidation deformation of the seabed, but significant compared to the single stone penetration. The final settlement of the seabed due to consolidation can reach values of over a meter after 30 years or more. This value can be determined analytically, however if the relation between time and settlement needs to be obtained it is recommended to use more advanced software such as D-Settlement.

4.3.5 Material flow into rock pores

To finalize the considered processes which influence the volume loss during installation, the flow of material into the installed rock skeleton is described. Due to immediate rock penetration an interface layer is created between mixed soil and stones. Initially for small additional loads, this interface remains stable. During continuous rock dumping however the surcharge increases and the contact stresses at the interface continue to rise similarly. At a certain level of contact stress the cohesive material will penetrate into the rock skeleton as presented in Figure 4.15. This partial penetration will continue until a new equilibrium between the contact stresses at the interface is reached. Over time the stability of this interface level will increase due to consolidation.

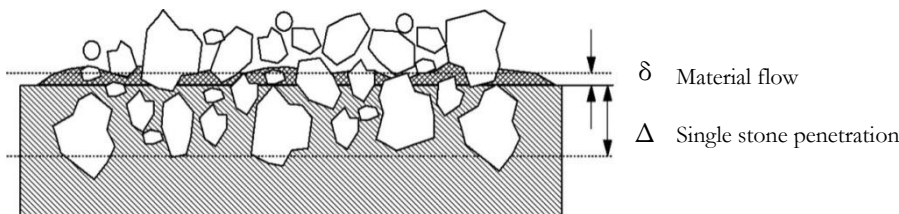


Figure 4.15: Penetration of cohesive material in rock fills (De Vries, et al., 2007)

Bijnagte & Luger (2005) presented a calculation method for the additional penetration (δ); the full derivation of the method is presented in Appendix 15.11. This rheological model is based on groundwater flow through a porous medium. The final result of this model is presented in equation (4.34)

$$\delta = n \cdot \left(\frac{p}{\alpha \cdot c_{u,r} \cdot \sqrt{\frac{n}{\kappa}}} \right) \quad (4.34)$$

Here p is the effective surcharge pressure, $c_{u,r}$ is the remoulded undrained shear strength, n is the porosity of the rock fill, κ is the intrinsic permeability of the rock fill, α is a constant between 0.6 and 0.9 based on the rate of strain (Bijmagne & Luger, 2005) and finally δ is the additional penetration depth due to material flow in the pores. The influence of this process is estimated to be rather small with an order of magnitude of only a couple of millimetres.

4.4 Remarks on the theory

The volume losses which occur during subsea rock dumping can roughly be estimated using the previous described formulae, however certain simplifying assumptions are made which will have influence on the result. Moreover some processes are more important than others. This thesis focuses especially on immediate rock penetration, however the influence of this process largely depend on the specific seabed conditions. In this paragraph the following limitations of the theory described are indicated:

- Surface erosion and difference in survey level
- Shape and roughness of the installed particles
- Strain rate dependency of shear strength
- Local consolidation
- Sensitivity of clay

4.4.1 Surface erosion and difference in survey level

Often the top of the seabed consist of a small layer of very soft soil or even floating particles which can best be described as thick water. This layer can be detected by the multi beam echo sounder (MBES) attached to the ROV, but will not show on the conventional CPT measurements performed in-situ. This weak material can be washed away during subsea rock installation since the jet velocity of the rock water mixture is quite high. At the seabed the jet will deflect from a vertical to a horizontal direction and the turbulence created during this movement will erode the soft material. The thickness of this mud depends on local conditions, but will affect the volume loss since more material is necessary to fulfil the height requirements based on the MBES surface profile. According to Deltares this weak layer often has a thickness of 0.10 to 0.15 m in the northern part of the North Sea, which is large compared to the estimated penetration of 0.03 m. Survey experts at Van Oord even speak of mud thicknesses of up to 0.5 m on certain locations with no horizontal currents (Koper, 2013). More about the accuracy of the MBES system can be found in chapter 9.

4.4.2 Shape and roughness of the installed particles

The shape of the penetrating body influences the generated soil resistance. A cubical particle penetrating with a corner pointing downwards will penetrate deeper into the soil compared to a particle hitting the soil with its flat side. In reality the particles can have all kinds of shapes and penetrate with different directions facing downward. In this thesis however all particles are modelled as spheres with no sharp edges. The effect of this simplification is expected to be limited. In the experiments performed the particles consisted of ball bearings which are completely smooth. The rough surface of an actual rock particle will generate a slightly larger resistance when penetrating, resulting in a smaller penetration. Research estimates that this shape effect together with the difference in roughness of the particles is about 5 to 10% (Bijmagne & Luger, 2005).

4.4.3 Strain rate and local consolidation

The shear strength of a clay material is strain rate dependent. That is to say, the resistance of clay increases with a larger rate of straining. A tremendous amount of research is performed to understand the influence of strain rate dependency of shear strength ((Chung, et al., 2006), (Einav & Randolph, 2004), (Lehane, et al., 2009), (Hossain & Randolph, 2009), (Zhou & Randolph, 2009), (2011)). Typically the resistance is assessed to increase by 7.5 to 20% for each order of magnitude increase in shear strain rate. In triaxial tests where the imposed strain rate is low, this value lies around 10% per log cycle and appears comparable for both intact and remoulded conditions (Hossain & Randolph, 2009). In situ soil characterization tests, such as field vane and full flow penetrometers strain rates involved are 3 to 5 orders of magnitude higher than standard laboratory tests and consequently provide higher degrees of strength. The torque or penetration resistance increases about 10 to 20% for every tenfold increase in rotation or penetration rate. However this occurs in fully undrained conditions. When penetration rates decrease below a certain point, resistance will start to increase again due to partial drainage and local consolidation as previously indicated in Figure 3.1 and Figure 4.16.

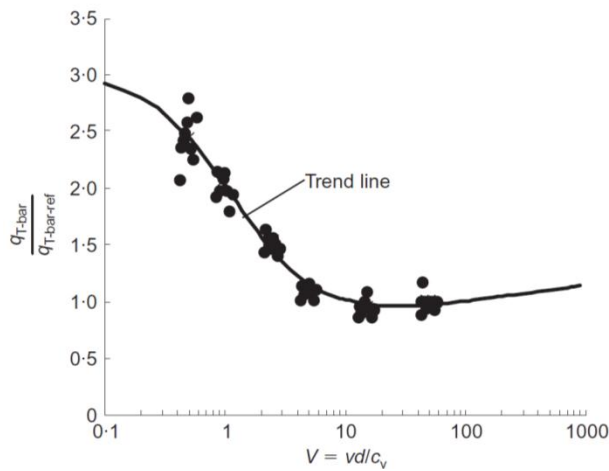


Figure 4.16: Rate dependency of shear strength (Lehane, et al., 2009)

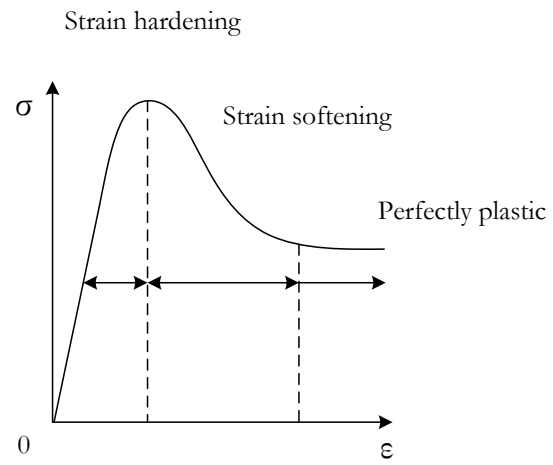


Figure 4.17: Strain hardening and softening of soil during continuous shearing

On top of this rate dependent behaviour clay is also known to exhibit strain softening defined as a gradual loss of shear resistance after a peak strength has been reached as shown in Figure 4.17 (Prevost & Hoeg, 1975). However this softening behaviour occurs in material such as rocks, dense sand and over-consolidated clays. In case of very soft normally consolidated this is unlikely to happen. Both strain rate dependency as well as strain hardening and softening are not considered in the Single Stone Model. The influence of this simplification in case of high speed impacts of particles on soft fine grained material is estimated to be about 10 to 25% (Lehane, et al., 2009). This resembles the estimation made by Bijmagne & Luger (2005) who base their assessment on a formula given by Briaud en Terry (1986):

$$\frac{c_{u,2}}{c_{u,1}} = \left[\frac{\left(\frac{v}{D} \right)_2}{\left(\frac{v}{D} \right)_1} \right]^A \quad \text{with } A \text{ between } 0.06 \text{ and } 0.10 \quad (4.35)$$

Where c_u is the undrained shear strength, D equals the diameter of the penetrating body and v is the penetrating velocity of the particle or body.

4.4.4 Sensitivity of clay

Sensitivity is defined as the ratio between the undisturbed and disturbed undrained shear strength:

$$St = \frac{c_u}{c_{u,r}} \quad (4.36)$$

Generally the remoulded undrained shear strength is a factor two lower than the undisturbed undrained shear strength. However values can range between 1 and 100 (quick clay) depending on the location. When a particle penetrates into the soil it disturbs the surrounding clay, changing the properties and hence the undrained shear strength. This effect, which creates a lower resistance during penetration of subsequent particles, has not been taken into account in the model. In the choice of different possible soil properties however a distinction is made between minimum, maximum and best estimate properties (as will be described in chapter 12). In case of penetration the remoulded shear strength is chosen as the maximum property. The lower remoulded shear strength increases the penetration of multiple particles, providing the most conservative estimation of possible losses.

Part II – Data gathering

5 Introduction

This thesis focuses on the volume loss of rock material during subsea rock installation using flexible fallpipe vessels. Particle penetration into the soft seabed is of particular interest to the contractor since penetrated particles do not contribute to the design and thus can be regarded as lost. To make up for this loss additional volumes of particles will have to be installed, increasing the amount of required material. For years contractors have been trying to accurately predict the penetration in order to create a precise estimation of the required material. In the previous part the theoretical background related to this problem is presented. To verify if the theory also resembles practice, a series of experiments is conducted. These experiments can be used to obtain better insights in the governing parameters influencing the rock penetration. Moreover using the data from the experiments, the created model for single stone rock penetration can be validated.

Since the penetration is affected by a large number of parameters and as it is impossible to vary all individual parameters, it is decided to simplify the problem by limiting amount of variables. Three significant parameters have been determined during the literature survey namely, fall speed, undrained shear strength and particle diameter. These parameters will be varied during different sets of laboratory test. The experiments provide an opportunity to isolate the effect of each individual parameter and since all tests are done in the same standardized environment, multiple tests can be compared with each other.

Chapter 6 provides a short the explanation of the scope of the test along with a description of the experimental setup used during the tests. In chapter 7 the results of the test will be presented. To investigate if the data obtained from the idealized laboratory experiment resembles the penetration found during SRI projects, a comparison between both laboratory results and in-situ penetration is made. A description of the compared project is given in chapter 8. The performed measurements are described in chapter 9 and the corresponding results in chapter 10. The validation of the created single stone model is presented in chapter 11. Finally chapter 12 gives a comparison between the measured complete height deficit in the field and the modelled height deficit. Here the influence of all processes is presented separately.

6 Experimental measurements

As indicated by the theory in chapter 3 and 4 there are many factors which can influence penetration. However since time is limited not all these factors can be tested. By varying certain parameters their influence on penetration and the model could be verified. During the tests the most important clay property was varied namely the undrained shear strength. Through creating a reconstituted clay sample a representative strength could be created. Moreover the different sizes and densities of particle were used to check their influence on the impulse balance. Finally the impact velocity was changed by varying the fall height. Table 6.1 shows all the values of parameters which have been varied during testing, more about the test setup is explained in paragraph 6.1.

Table 6.1: Experimental program

Verification	c_u [kPa]	D_s [mm]	ρ_s [kg/m ³]	v_{imp} [m/s]
Variety	3	2	2	5
Spread	$\sim 2, 4, 12$	15, 30	$\sim 2500, 7800$	2, 3, 4, 5, 6

Supplementary test were performed to assess the influence of boundary effects of the test setup and the effect of possible evaporation during testing on the clay parameters. All test are performed in triplo to increase the reliability of the result, moreover this allows for the results to be assessed statistically. Lastly specific test were conducted with a high speed camera which captured the deformation of the clay during penetration of a single particle. Altogether seven different experiments were executed. The key objective of the laboratory tests is to validate the penetration model and to check if the theory used, is suitable for this problem.

6.1 Setup

The setup used for the penetration test is schematically displayed in Figure 6.1a. This setup is used to drop a particle from different heights into clay with a known undrained shear strength. During the test steel ball bearings and marbles were used to resemble particles in reality. By varying the fall height (h) the impact velocity can be altered. To limit the boundary effects the diameter of the bucket containing the clay (D_{bucket}) should be $10D_s$ and the clay thickness beneath the penetrated particle should be at least $5D_s$ (Craig & Sabagh, 1994). After dropping the particle the penetration was determined by measuring the level between the top of the particle and a reference point, in this case the top of the bucket. Since the difference in height between the top clay level and this reference point is determined before the testing commences, the particle penetration can be derived. All lengths were accurately measured using a calliper. The testing is simple yet effective, images of the test setup and the experiments are attached in Appendix 15.12.

For the high speed camera (HSC) tests the setup was altered. The setup is shown in Figure 6.1b. Instead of a round bucket a strongbox was used to store the clay. One side of the strongbox is made out of elongated Plexiglas enabling the capture of the penetration using a camera. To ensure the particle would visibly penetrate at the desired position it had to remain in contact with the glass. That is why the wooden particle was cut in half and placed on a steel rod. This rod guided the particle during its fall and presses the particle against the Plexiglas wall. Obviously this contact with the glass causes additional resistance to occur which influences the fall speed of the sphere, however since the penetration is captured using a high speed camera the real impact velocity can accurately be determined. To minimize resistance and make sure no clay would be pushed between the particle and the glass, a soft sealing strip was attached to the particle. These strips and the guiding rod were sprayed with Teflon to further reduce resistance. By releasing the half sphere from a height, the particle will drop and penetrate at a predefined location and

the camera could capture the penetration. Using particle image velocimetry (PIV) the displacements of the clay during penetration can be determined. For PIV to work, the pictures need to contain sufficient amounts of contrast over the deformed area. Kaolin itself forms an even grey clay (Figure 6.3b), therefore contrast material had to be added on the Plexiglas to make sure the deformation between individual pictures could be determined by the PIV software. The results of the HSC test are shown in paragraph 7.2.

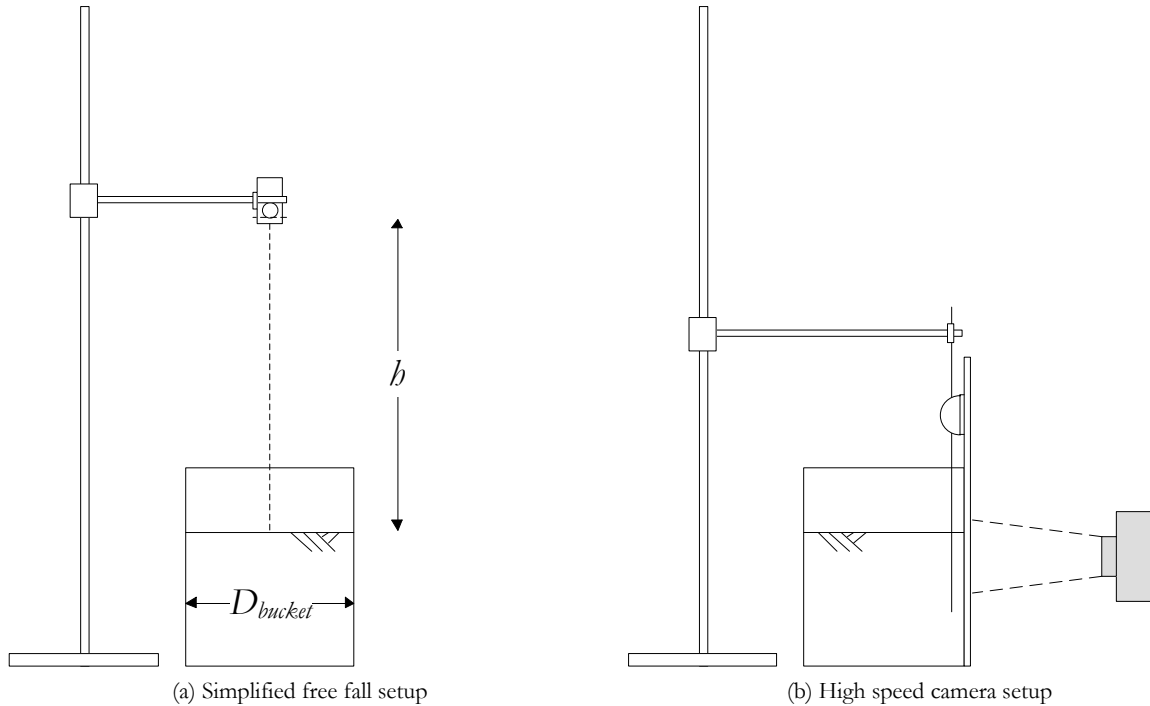


Figure 6.1: Simplified test setups

6.2 Clay properties

To create clay which resembles the strength characteristics of very soft deep sea clay, kaolin is used. Kaolin is often used for experiments to reconstitute soft soils since it is cheap, largely available and has positive testing characteristics. Among others kaolin exhibits almost no thixotropy, in other words the material expresses almost no strength increase over time after remoulding (Andersen & Jostad, 2002). Due to its frequent use for laboratory testing, lots of research into its properties is conducted ((Bol, 2012), (Rao & Sridharan, 1985), (1973)).

As described by Burland (1990) natural soils greatly differ from reconstituted soils, like kaolin clay, with regard to the soil structure. Soil structure is described as the combination of particle arrangement and inter particle bonding (Mitchell, 1976). The structure of natural clay depends on many factors such as depositional conditions, ageing, cementation and leaching, which all have a profound effect on the mechanical properties of the material. Since most of these effects cannot be recreated in reconstituted soils a difference in mechanical properties remains, possibly affecting the outcome of laboratory tests. However the intrinsic properties of corresponding reconstituted clay can provide a reference frame to assess the behaviour of natural clays in in-situ state and the effect of altering different properties. In other words the use of reconstituted clays provides the possibility to understand the behaviour of natural clays when using reconstructed clays with similar characteristics. The properties of these reconstituted clays are called ‘intrinsic’ since they are inherent to the soil and independent of the natural state (Burland, 1990). As a result the challenge lies in the creation of a sample that resembles the key properties of the natural clay found on the Norwegian seabed. In this thesis the undrained shear strength is such a key parameter.

To create clay samples with different undrained shear strengths different methods can be used, two different methods will be described. Firstly, one can start by adding a small amount of kaolin clay particles to a lot of water and stirring this mixture. A fully saturated kaolin slurry will be the result. This slurry can be poured into the bucket and by adding a weight on top of the sample the material will be compressed. This compression will cause an increase in strength and – depending on the specific weight on top – the strength can be brought to desired level. However due to the low permeability of kaolin clay and since the sample can only drain to the top, the complete consolidation of the large sample of will take a long time. This is one of the major downsides of this method. On the other hand the sample quality will be high since the amount of air inclusions is limited and therefore the sample properties will be nicely uniform.

The other possibility to create a sample, is to start off with dry kaolin clay particles and adding a specific amount of water (see Figure 6.2a). By adding different amounts of water the moisture content of the sample is changed. Since every clay has its own relationship between the moisture content and the undrained shear strength a sample with the desired shear strength can be created. One can understand that by adding more water to the mixture the strength of the sample will reduce until the clay mixture turns into a viscous fluid. More information about the relation between moisture content and undrained shear strength is found in the next paragraph.



Figure 6.2: Kaolin water mixing process

The water and particles are mixed thoroughly forming a clay (Figure 6.2b). This clay mixture is too strong to be poured into the testing bucket and is therefore scooped (Figure 6.3a). The material in the bucket is then remoulded until it perfectly fits the container (Figure 6.3b). This way of preparing a kaolin clay test sample is faster and therefore used in this experimental research. However the probability of an air inclusion during the scooping and remoulding of the clay is possible. In case a particle would drop directly on such an inclusion, the penetration will increase and distort the measurements. However since all experiments are done in triplo and it is highly unlikely that all three particles will fall on an inclusion these distorted measurements can be isolated.



Figure 6.3: Kaolin clay testing bucket

6.3 Undrained shear strength determination

Since the undrained shear strength of the clay is one of the governing parameters during the test (see chapter 3), it is important to accurately determine this variable. Undrained shear strength of a remoulded clay can be determined at any water content based solely on its consistency limits (Sharma & Bora, 2003). In 1911 Atterberg proposed the liquid and plastic limit as limits of consistency, also known as the Atterberg limits, to get a clear concept of the range of water contents of a soil in the plastic state. The liquid limit (w_L) is defined as the limiting water content (w) at which the soil is liquid enough to flow, in other word the water content above which soil behaves like a viscous liquid. The plastic limit (w_P) is reached when clay can no longer be rolled into a small thread without cracking (Nagaraj, et al., 2012). These limits are widely used to classify fine-grained soils. However the exact undrained shear strength values at liquid and plastic limit water contents are still part of a lively debate. Extensive research ((Casagrande, 1932), (Wroth & Wood, 1978), (Wood, 1985), (Sharma & Bora, 2003), (Kayabali & Tufenkci, 2010)) indicates that consistency limits are quite variable and both test and soil type dependent. Literature indicates that the liquid limit ranges from an undrained shear strength of 0.2 to 12.0 kPa where the plastic limit varies between a c_u of 20 and 230 kPa. This wide spread in literature clearly shows that soils cannot be described uniformly and all have a unique strength at different levels of water content. Although it might be misleading according to (Nagaraj, et al., 2012) most researchers have concluded that the undrained shear strength of remoulded soils at the liquid limit and plastic limit lies around 1.7 kPa and 170 kPa respectively (Kayabali & Tufenkci, 2010). This also agrees with a widely adopted correlation by Wroth & Wood (1978), stating that the undrained shear strength at the plastic limit can be found by multiplying the liquid limit with a factor of 100.

Not only the location (strength value) of the consistency limits is prone to debate, also the intermediate relation between water content and undrained shear strength greatly varies. Again different literature advocates different relations, but a commonly used relation is a linear relation between undrained shear strength and water content on a log-log plot (Sharma & Bora, 2003). This relation is shown in Figure 6.4 for the kaolin clay and used during testing. The undrained shear strength is determined using the Swedish fall cone method. The linear line on the log-log plot of water content versus undrained shear strength shows a nice fit, however as water content increases and shear strength reaches the liquid limit the spread in the results increases and more variation can be seen. Considering this variation at the liquid limit the relation based on multiple results, is preferred over single in-situ measurements at the liquid limit. The linear trend line is a conservative fit providing a higher undrained shear strength near the liquid limit. This conservative approach is chosen bearing in mind the final result of this thesis to estimate stone penetration. Due to a higher undrained shear strength, penetration might be slightly overestimated providing an additional buffer during volume estimation.

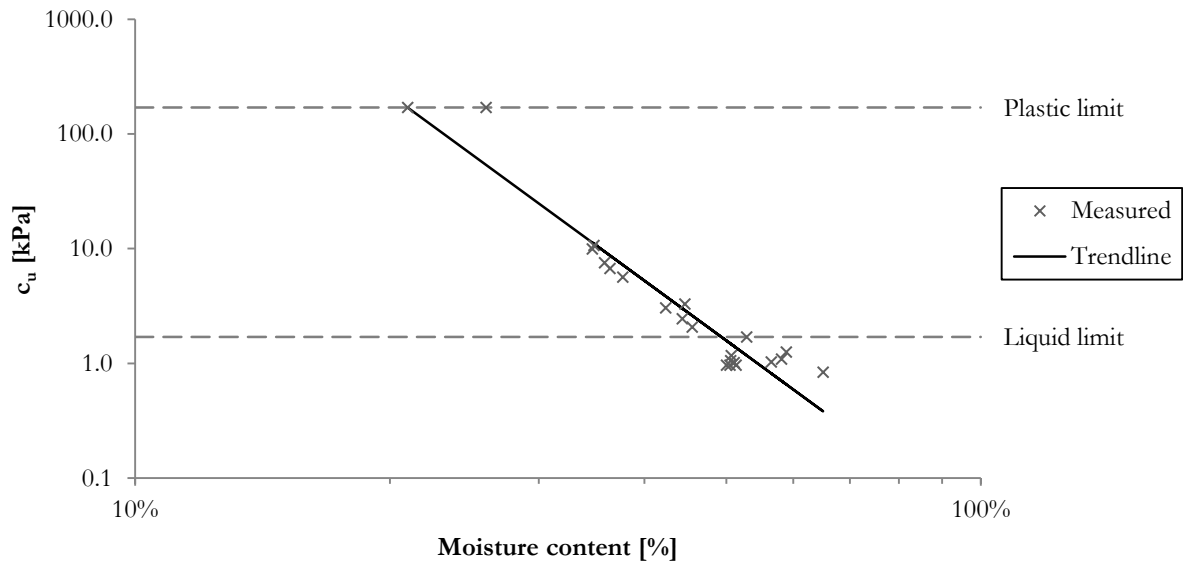


Figure 6.4: Linear relation between water content and undrained shear strength (log scale) for Kaolin

Besides the Swedish fall cone several other techniques exist to determine the undrained shear strength. Common methods are the field vane, laboratory vane and cone penetrometer tests. To improve the reliability of the shear strength determination additional field vane test were conducted. However the vane tests slightly overestimate the undrained shear strength at the liquid limit and thus care must be taken when comparing both results near the liquid limit (Kayabali & Tufenkci, 2010).

7 Experimental results

In this chapter the results of the previous described set of experiments are presented. Using these results the single stone penetration model presented in chapter 4 can be validated. Additionally, using high speed camera tests more insight in the processes involved in single stone penetration can be obtained.

7.1 Single stone penetration

Table 7.1 shows the result of the different undrained shear strength test methods performed on the weakest clay sample created. Contrary to the expectations the Swedish fall cone does not overestimate the shear strength but suggests the lowest undrained shear strength. This trend can also be seen for the strongest test sample (see Appendix 15.13). For the sample with an undrained shear strength of 3.6 kPa the fall cone indicates the highest strength. Because of this large spread in results and the fact that the fall cone becomes less accurate near the liquid limit, this result is not considered when defining the undrained shear strength of the samples. Accordingly the final undrained shear strength is solely based on the average between the in-situ vane and the previously defined moisture content relation.

Table 7.1: Undrained shear strength determination using different methods

Test method	Undrained shear strength [kPa]	Deviation from average [%]
Fall cone	1.0	-29%
In-situ vane	1.4	0%
Moisture content	1.4	0%
Average	1.4	0%

Note: The fall cone method is not taken into account and therefore crossed out

In Figure 7.1 the experimentally determined penetration is shown for different impact velocities in a clay with an undrained shear strength of 1.4 kPa. The measurement points are shown for two types of particles, the larger 30.00 mm diameter steel sphere and the smaller 15.00 mm steel sphere. These two sizes are chosen both practically and based on the particle sizes found in reality. Since experimental literature recommends a bucket which is $10D_s$ wide, it would become very unpractical to perform tests with a particle of 5". Moreover the particles used in the Norwegian SRI project (further described in chapter 8) are in the range of 1 - 3" for the first layers and 16 – 32 mm for the top layer.

In Figure 7.2 and Figure 7.3 the similar relation between single stone penetration and impact velocity is presented for undrained shear strength of 3.6 and 12.4 kPa, respectively. All graphs appear to show a linear relation, however as the model in chapter 11 will point out, this relation is in fact quadratic. The seeming linearity is the result of the low undrained shear stresses near the liquid limit. If the undrained shear stress rises the quadratic bend in the line will start to appear.

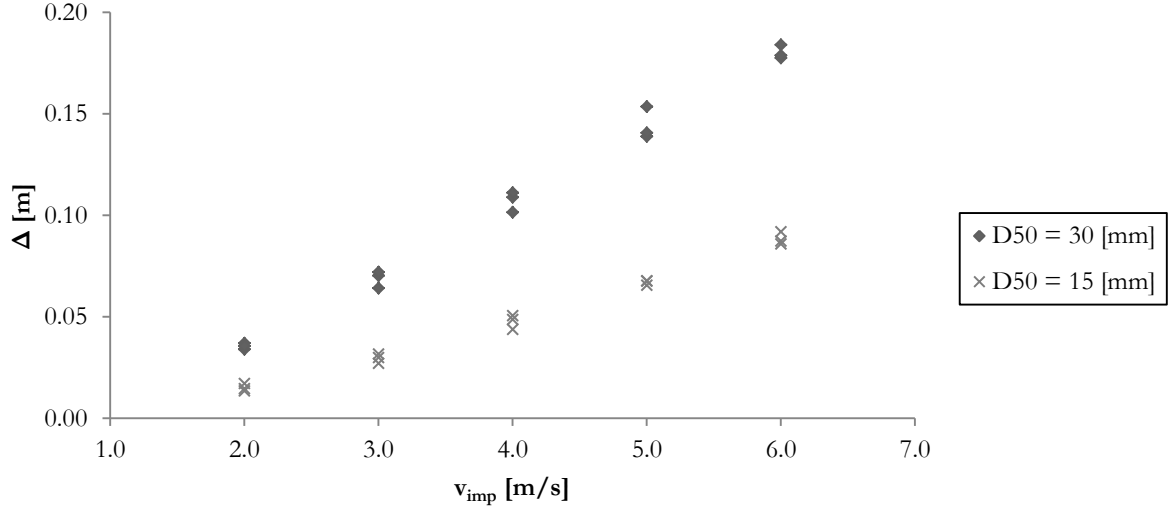


Figure 7.1: Particle penetration for different impact velocities ($c_u = 1.4$ kPa, $\rho_s = 7804$ kg/m³)

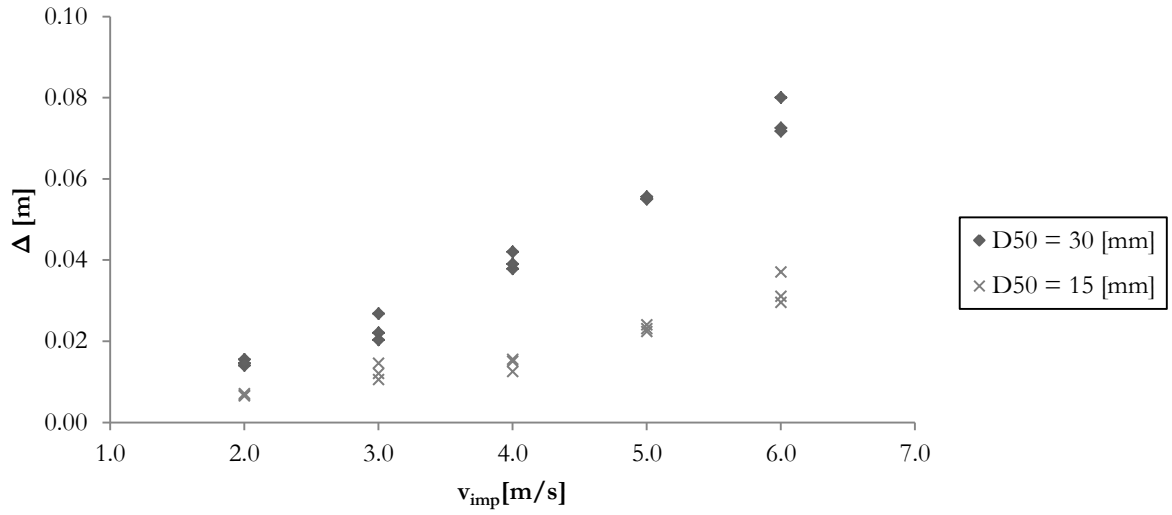


Figure 7.2: Particle penetration for different impact velocities ($c_u = 3.6$ kPa, $\rho_s = 7804$ kg/m³)

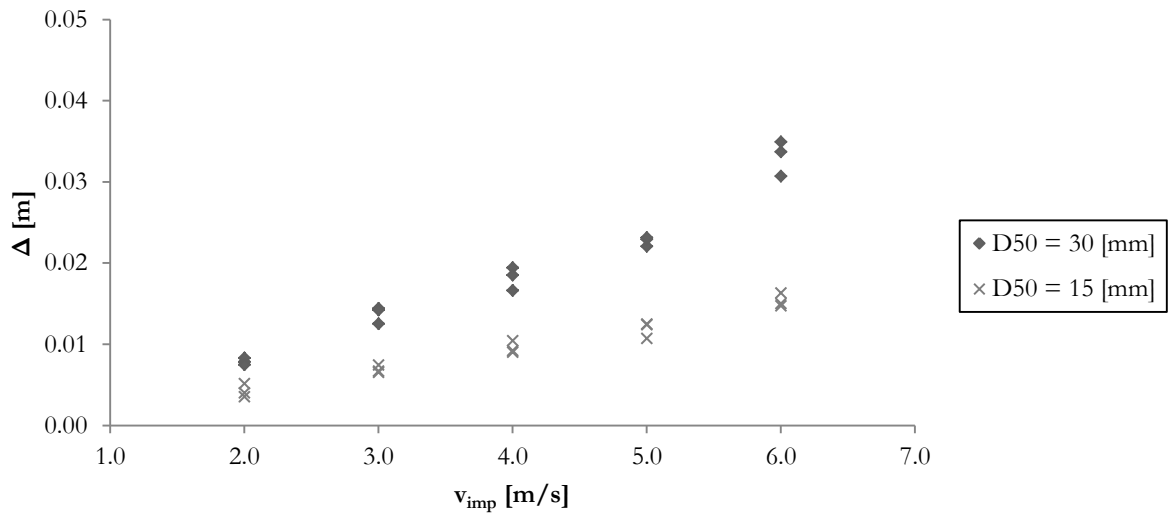


Figure 7.3: Particle penetration for different impact velocities ($c_u = 12.4$ kPa, $\rho_s = 7804$ kg/m³)

When searching for a common denominator the sphere diameter is found to give a relationship between the penetration and the impact velocity. Figure 7.4 shows the relation between dimensionless penetration (Δ/D_{50}) and the impact velocity. As can be seen by the trend line drawn through the results in the graph, a linear relation can be found with a slope depending on the undrained shear strength of the material.

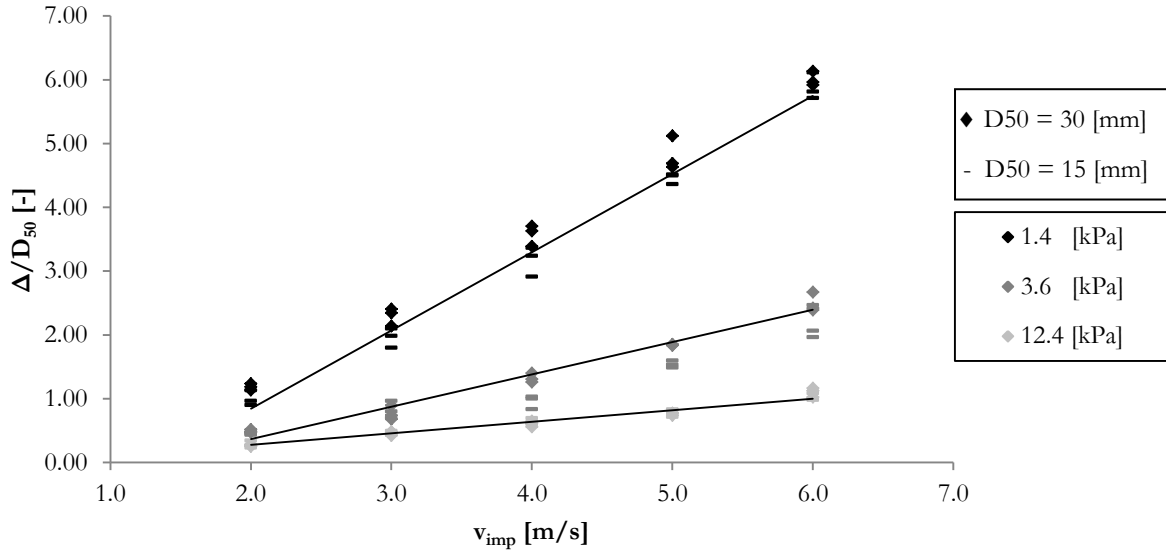


Figure 7.4: Dimensionless penetration versus impact velocity for different undrained shear strengths

After performing the penetration test for multiple clay strengths and different particle diameters, the density of the particle is varied. Since normal particles will have a specific density between 2300 and 3400 kg/m³, a material with a density of ~ 2500 kg/m³ is used. For both materials a small diameter particle of 15.00 mm is used. The results are shown in Figure 7.5.

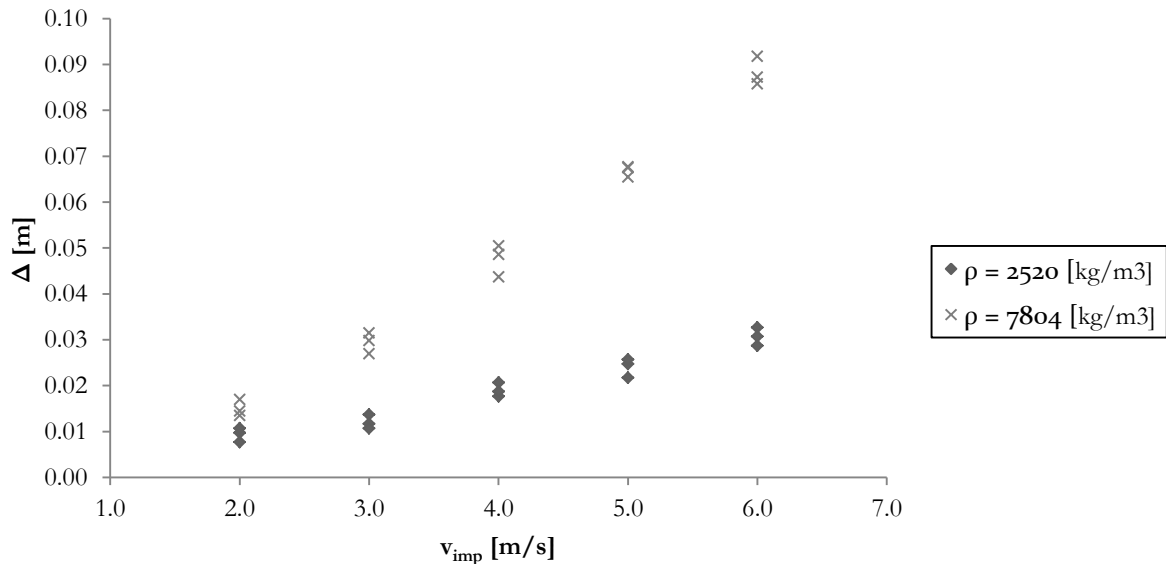


Figure 7.5: Relation between particle penetration and impact velocities for different densities ($D_s = 0.015$ m, $c_u = 1.5$ kPa)

Since the particles were dropped relatively close to the side of bucket, measurements might be influenced by this boundary. As indicated in the previous paragraph additional tests were performed to assess the possible boundary effects during testing. Due to the stiff behaviour of the bucket wall it is possible that the clay reacts stiffer at the sides than in the middle of the bucket. This is the result of additional

confinement at the sides of the bucket, which influences the strength of the soil. This fictive strength can cause lower penetration. By dropping the same size particle on different positions in the bucket, namely in the middle and on the sides and by comparing the penetration any possible deviations in the penetration could be noticed. Obviously all tests were performed on the same type of clay and with the same impact speed. The results are shown in Figure 7.6. As can be seen in this graph the penetrations resemble each other well. The particles that were dropped at the sides (1D from side) even seem to show a better match than the ones that have been dropped in the middle (5D from side). Moreover the relative influence of multiple particles being dropped at different positions after each other in the bucket is minim (Relative influence). All in all the boundary effect prove to be negligible.

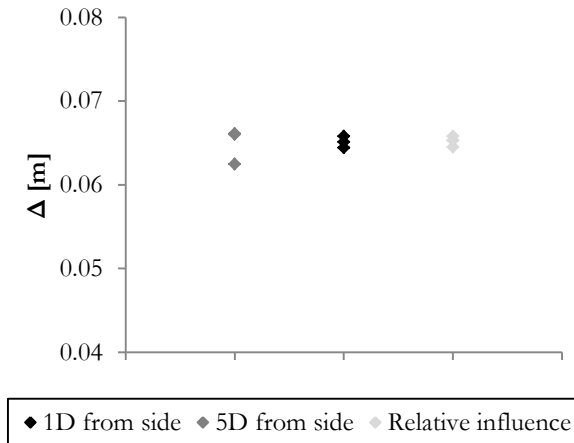


Figure 7.6: Boundary influences during testing ($v_{imp} = 3.0$ m/s, $c_u = 1.7$ kPa)

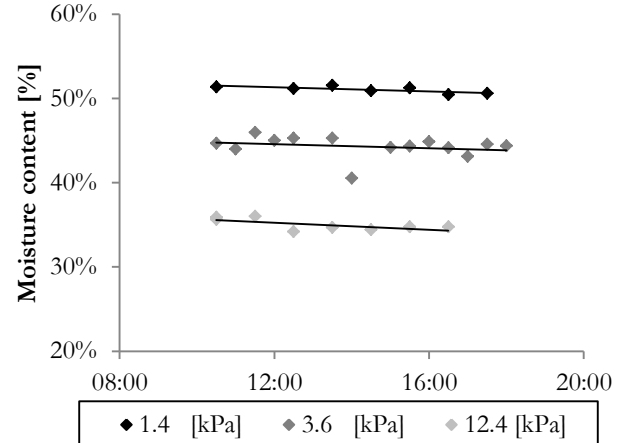


Figure 7.7: Moisture content over time during testing

Another important value to monitor during testing is the moisture content. This is especially important on the top layer of the clay where evaporation can cause crust forming, which can have a significant influence on the shear strength of the material. Therefore a small sample of the top of the container has been taken after each test and the moisture content is determined. Figure 7.7 shows the development of the crust's moisture content over the day. A slight decrease in moisture content can be observed. The influence of this decrease can be neglected, however future tests are performed in a climate controlled room to further prevent evaporation of the water at the top of the sample.

7.2 High speed camera tests

In Figure 7.8 five pictures of consecutive periods in the penetration process are shown. The half sphere penetrates into the soil with an initial velocity of 2.2 m/s, this lies in region of the expected real impact velocities. Initially during impact the velocity is still high and the incremental displacements between pictures are relatively large. As penetration continues kinetic energy of the sphere taken up by the soil and converted into elastic and plastic deformation, until it finally loses all its initial energy and stops.

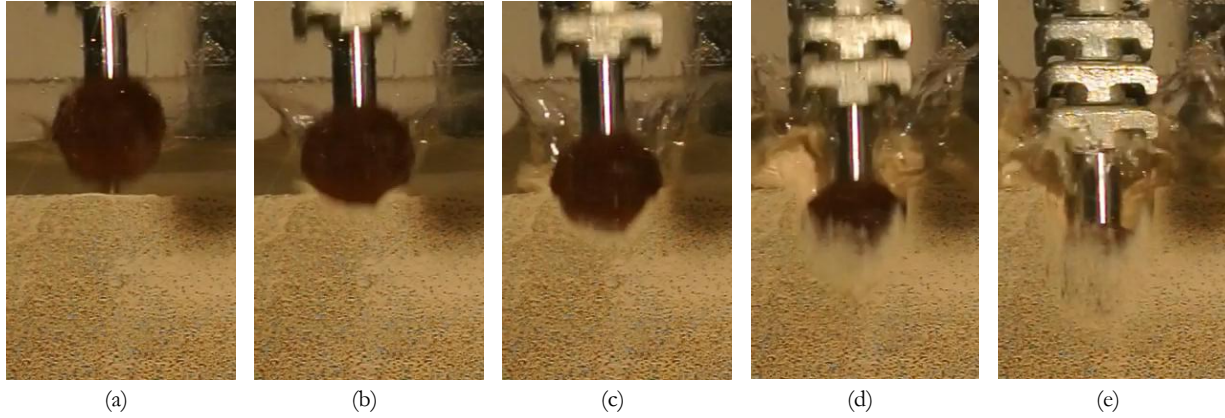


Figure 7.8: A selection of the high speed camera penetration pictures

Using a high speed camera this rapid impact (~ 50 ms) is caught on camera in multiple separate frames. The individual frames can be compared with each other using the open source particle image velocimetry software JPIV. This program determines the direction and magnitude of displacements of individual groups of pixels based on contrast values, an example of incremental displacements between two separate frames is shown in Figure 7.9.

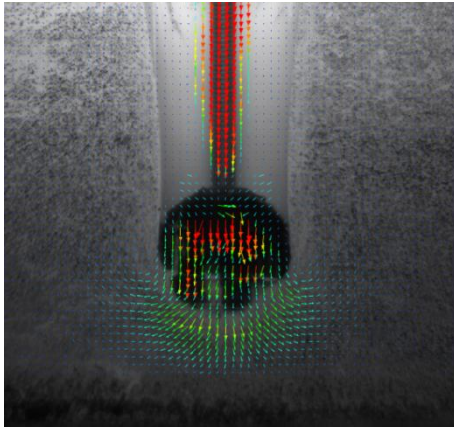


Figure 7.9: Incremental total displacements found using JPIV

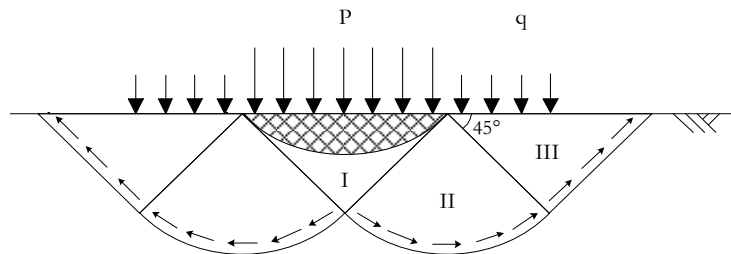


Figure 7.10: Slip surface for undrained conditions ($\psi = 0^\circ$) according to Prandtl

By adding the vectors of individual frames the total displacement during impact can be determined and plotted in a contour plot as shown in Figure 7.11. The plots are dimensionless since the vertical and horizontal axes are divided by the ball diameter. Both the position of the penetrating body as well as the displacements are indicated relative to the ball size. The resulting cumulative displacement of the high speed impact is shown in a contour plot in Figure 7.11a. In this plot the darker colour means a larger displacement. It is clearly visible that directly surrounding the sphere displacements are larger, further away from the particle displacements become smaller. However this total cumulative contour plot is not very clear, more can be seen when separating the vectors into horizontal and vertical displacements, Figure 7.11b and c respectively. In Figure 7.11b the Prandtl failure surfaces can vaguely been recognised since the blue colour shows the deformation of the clay towards the left and the red toward the right. Prandtl subdivided the soil deformed by the stresses into three different zones, based on the assumption

that in a certain region at the soil surface the stresses satisfy the equilibrium conditions and the Mohr-Coulomb failure criterion. In this entire region the soil then is on the verge of yielding. Prandtl's original slip surfaces are shown in Figure 7.10. In zone I the horizontal stress is larger than the vertical stress, which is equal to the surcharge load (q). In zone III the vertical normal stress is supposed to be the largest stress, and its value is equal to the unknown load (P). The transition is formed by the wedge shaped zone II (Prandtl's wedge), which is bounded below by a logarithmic spiral (Verruijt, 2005). Figure 7.11c clearly shows the displacement of material in upward direction at the sides of the particle. The material which is displaced by the particle is transported to the sides and up. Images of the penetration also show that this process is fully gapping, no back flow of material is present.

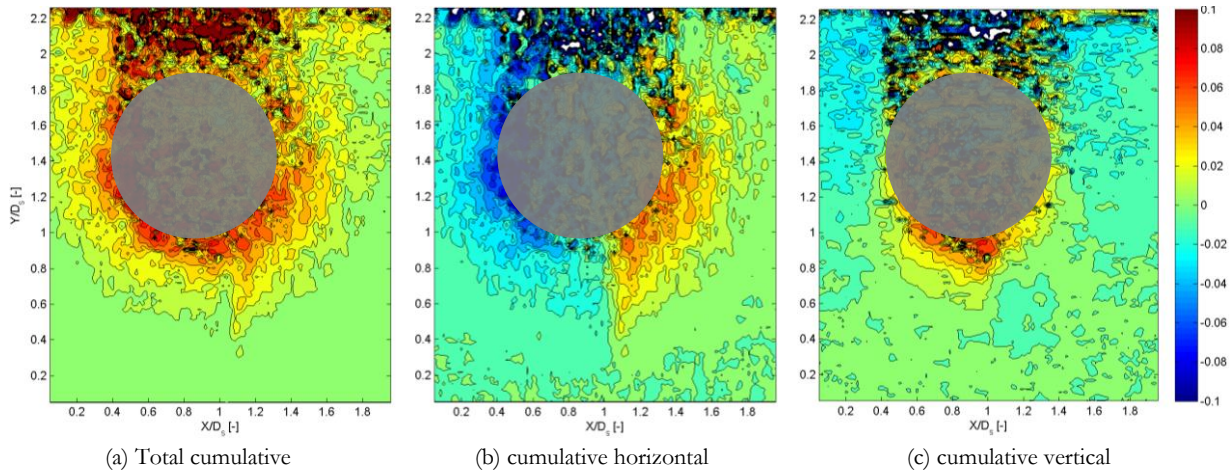


Figure 7.11: Dimensionless displacements contours of high speed impact

These images are still of low quality and troubled by noise. This is caused by the clay squeezed between the Plexiglas and the particle, clearly indicated in Figure 7.8e. This limits the processing of the results. Therefore an additional test is performed in which the particle is not dropped into the soil, but pushed using a threaded rod. With a fixed velocity of 1 mm/s the particle is pushed into the soil. This process is different from the free fall and high speed impact, since the penetration depth is not dependent on the initial velocity and the soil parameters but merely on the settings of the installing frame. Moreover the dynamic effects during the penetration will not occur. However this test does given better insight in the displacements of soft clay material during penetration and since the real velocities are small the difference due to dynamic effects are also presumed small (Bijmagne & Luger, 2005). Figure 7.12 shows a selection of the slow penetration pictures. This time no clay is squeezed between the particle and the Plexiglas and a clear contour plot can be created. Moreover the gap created by the penetrating particle is clearly visible, this would suggest no backflow occurs and hence contradicts the predicted process by (Bijmagne & Luger, 2005). Even after a full day in which drainage can occur no backflow is present. The fact that a half sphere is used might affects the backflow process as arching can occur between the gap and the Plexiglas, however gapping penetration is also observed during single stone free fall testing (see Appendix 15.12).

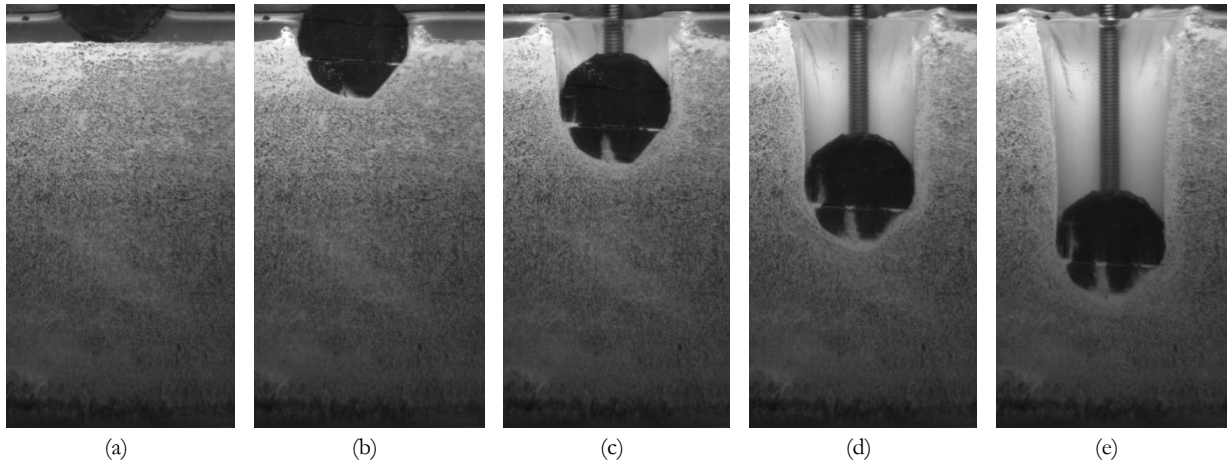


Figure 7.12: A selection of the slow penetration pictures

The result of the PIV analysis of this slow test is shown in the contour plots in Figure 7.13. Figure 7.13a shows the cumulative total displacement of the soil including the location of the penetrating particle. The gap created by the particle is clearly visible and indicated in red. Again the vertical and horizontal contour plots are more revealing, shown in Figure 7.13b and c respectively. The vertical plot shows the vertical transportation of clay material downwards right underneath the clay particle and upwards at the sides. Since the sides of the plot are completely blue this colour indicates that clay material has been transported towards the top during the complete trajectory of the particle. This is the effects of the undrained behaviour of the soil. In undrained behaviour no volumetric change is possible and hence all displaced material will have to shift towards the top. This induces significant heave at the top (see Figure 7.12e). The horizontal plot clearly shows the shape of the Prandtl wedge and indicates the failure shape of the material.

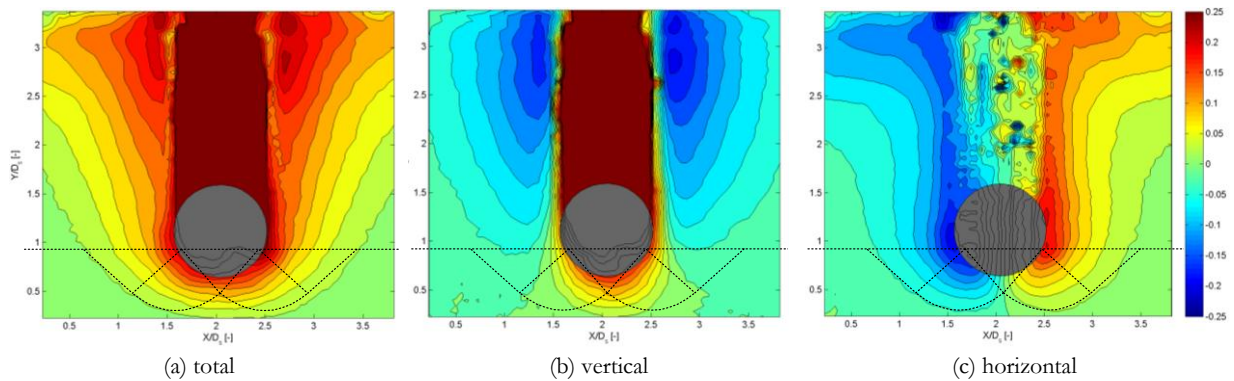


Figure 7.13: Final cumulative dimensionless displacements during slow penetration including particle

However by summing the displacements of all pictures a lot of information of the intermediate trajectory and its deformations is lost. That is why the result of the incremental deformation is also shown in Figure 7.14. In these plots the displacements between the 75th and 76th picture are shown. Again the Prandtl zones can be recognized. The total displacement shows the outward reduction of displacement; the vertical displacement indicates vertical transport of material and the horizontal incremental deformation largely fits the expected Prandtl deformations.

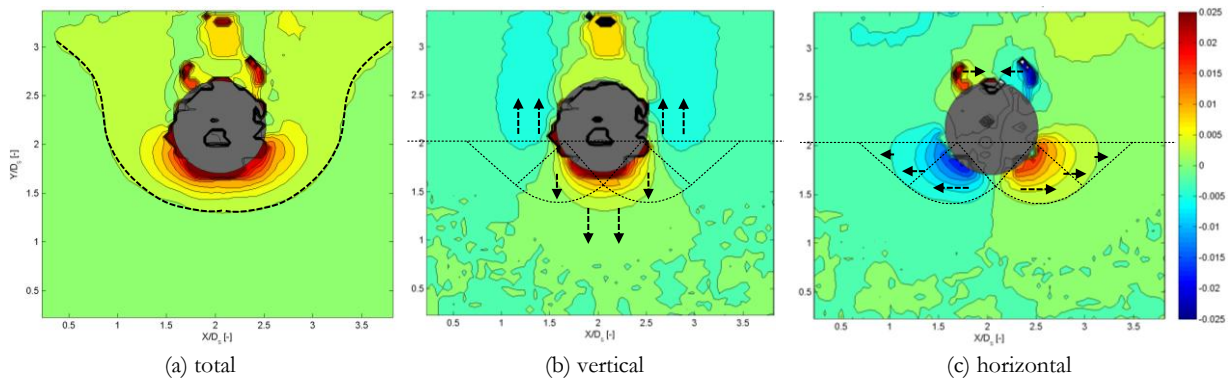


Figure 7.14: Dimensionless displacements during slow penetration including particle and Prandtl wedge

Note: the scale of incremental displacements is 10 times smaller than the cumulative displacement scale

What is striking in the last contour plot (Figure 7.14c) are the small displacements at the top of the particle pointed in the opposite direction. These displacements are not clearly visible when looking at the cumulative result of the penetration, but can indicate that the clay “flows” around the particle. The clay slightly sticks to the upper side of the ball and releases after about 80% of the circumference of the particle. This would imply that the visually gapping penetration is not fully gapping, but a slight back flow of the material occurs. This backflow is likely to increase the soil resistance - since extra energy is needed to deform the material - and decrease the penetration of the particle (Bijnagte & Luger, 2005). However this effect is limited.

These results indicate that a model based on the static bearing capacity formulation of Brinch Hansen, using the Prandtl wedge to describe failure, seems to correspond well with the observed failure mechanism. Even during high speed dynamic penetration of a spherical particle into soft soil. And although more sophisticated models (CET & FEM) might correspond even better with the shown displacements, the created model forms a nice and practical first reconnaissance.

8 Subsea rock installation project

In order to verify the modelled penetration with data from a real project and to assess the impact of stone penetration on the installation process, data from a SRI project in the North Sea is examined. During measurements on board of the FFPV Stormes, data on the project, the seabed, rock properties, installed volume and related penetration was gathered. This specific project provided an ideal test case, since the seabed on top of which the rocks had to be installed, consisted of very soft clays and thus corresponded well to the experiments conducted. Moreover the fill had to be completed according to strict requirements for which additional surveys were necessary, increasing the possible accuracy of interpretation. Subsequently, not only did the trip present an opportunity to get a glimpse of the used material and execution methods, it also caused for a better impression of accuracy in reality and the related influence of the thesis in practice. The result of this field data is presented in the chapters 9 and 10.

8.1 Project description

Approximately 100 km west of the Norwegian city Florø lays the Knarr field in the Norwegian sector of the North Sea (see Figure 8.1). This field is currently developed as a possible hub, to allow for future connections between nearby fields as they are currently developed.

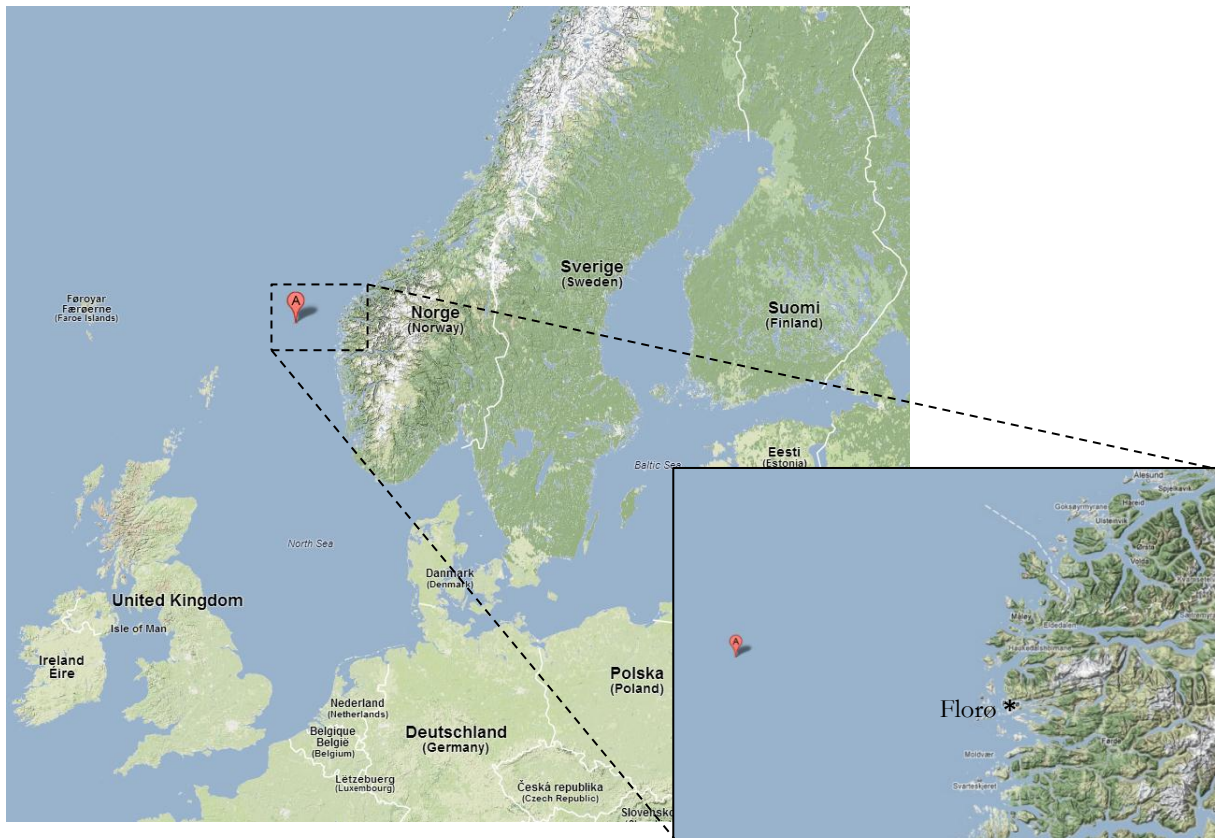


Figure 8.1: Knarr field located in the northern part of the North Sea (source: Google maps)

The Knarr reservoir will be provided with one production and one water injection installation. The water injection (WI) facility assists the extraction of hydrocarbons from the field and controls the pressure of the reservoir throughout the field's lifetime. The production facility will be connected to the Knarr FPSO (Floating Production, Storage and Offloading) facility using one pipeline bundle and flexible risers. The water injection facility will be connected to the bundle towhead located at the production template (PT) using one flexible flow line and static umbilical. The towhead is a complex rigid structure of pipes, pumps and valves especially designed to suit the requirement of the field. Export of the produced oil will take

place using a shuttle tanker from the Knarr FPSO. The field's gas will be exported using a dedicated pipeline, which connects the field to an existing subsea tie-in facility at the United Kingdom Continental Shelf. From here a pipeline runs to the mainland of Scotland. Figure 8.2 gives a schematic representation of the Knarr field layout when all systems are installed.

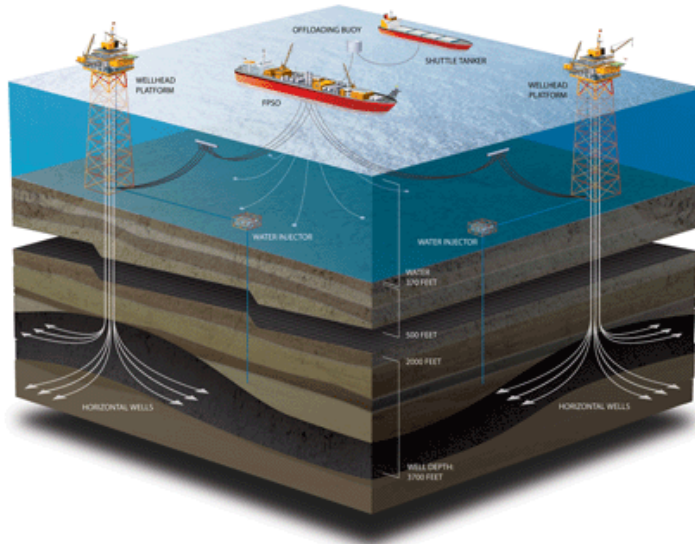


Figure 8.2: Possible layout of the Knarr field (Bradbury, 2011)

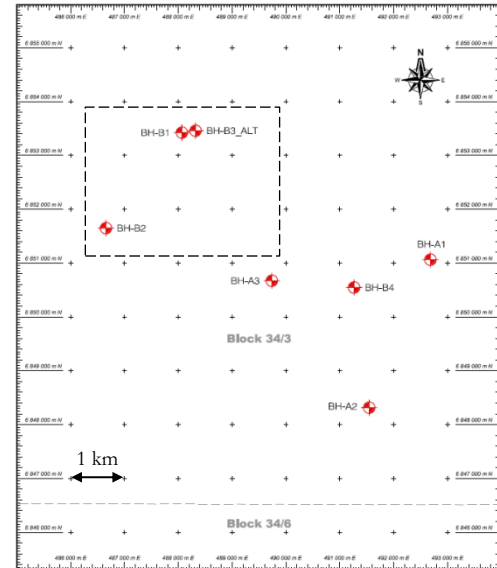


Figure 8.3: Location of geotechnical investigations. (Fugro Geoconsulting Ltd., 2012)

For this project Van Oord is contracted to install a rock berm on the Norwegian soft clayey seabed. This berm is installed as a support for the 500 ton heavy towhead. Due to large temperature difference during production the pipe bundle will start to expand. The resulting large expansion force will move the complete bundle system. To facilitate this movement the heavy towhead structure will have to be able to slide over the rock foundation. This provides the governing requirement for the level completion of the berm. Additionally the foundation has to be flat in order to prevent angular distortion of the towhead and buckling of the bundle. The installation tolerances of the top are -0.0 m to +0.2 m and the surface must be installed with horizontal tolerances of less than 1.5°. Each towhead foundation shall be installed with a ramp which gradually decreases in height towards to the seabed (slope 1:50). This ramp will support the pipe that will rest on top during completion of the project.

In total two large and four smaller rock fills will be constructed on three different project locations. A cross-section of the biggest rock foundations is given in Figure 8.4, the large towhead structure is shown on top of the completed berm. The remaining dimensions of the rock foundation as well as detailed drawing are enclosed in Appendix 15.14 and 15.15 respectively.

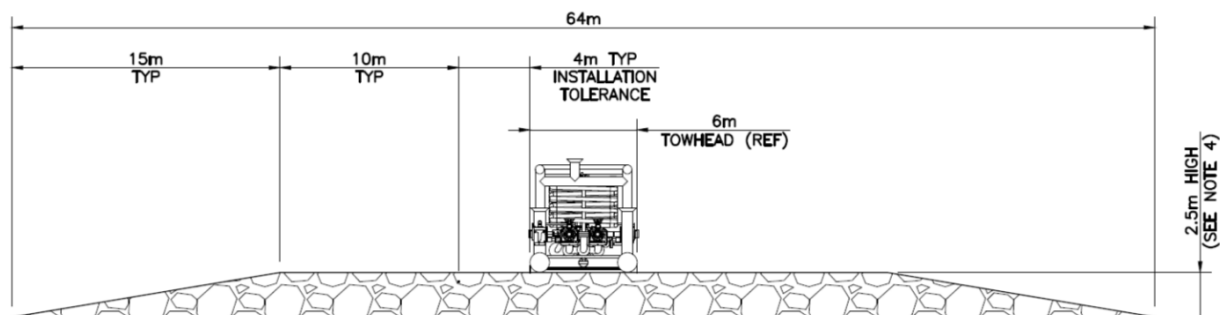


Figure 8.4: Cross section rock foundation towhead Knar FPSO location (Subsea 7, 2013)

8.2 Seabed properties

Before starting the rock berm installation an extensive soil investigation is carried out to determine the soil properties required to design best possible solution in this particular case. The location of the geotechnical investigation is given in Figure 8.3. As can be seen from this map the locations are a maximum of almost 6 km apart. Therefore the soil profile and corresponding parameters are not identical over the whole project area. Nonetheless the soil profile for the production template location (borehole BHB1) is taken as representative since all boreholes are situated in a zone with the same depositional environment and the individual differences prove to be small. Moreover the biggest berm will be installed at this location. The corresponding soil parameters needed for several calculations are determined by averaging the values for adjacent locations. These locations are indicated with the rectangle in the figure. The SI is used for the design of the rock berms and the installation of the seabed systems. The established soil layering and parameters are given in Table 8.1. Depending on the purpose of the calculation different parameters will be used. Since the penetration particularly involves the soft top layer an additional soil layer is introduced with different parameters, separating the very soft top layer from the deeper soft layers. A detailed overview of the soil layering and parameters is given in Appendix 15.16.

Table 8.1: Soil layering and description at the production template, taken as representative for the project

Layer number	Depth Range of Soil [m BSF]		Soil Description
	Top	Base	
Ia *	0.0	2.0	Very soft dark grey slightly sandy CLAY
Ib	2.0	10.0	Very soft dark grey slightly sandy CLAY
II	10.0	15.2	Very soft to firm dark grey slightly sandy CLAY
IIIa	15.2	17.0	Stiff to very stiff dark grey slightly sandy CLAY with traces of coarse sand- sized shell fragments
IIIb	17.0	24.5	Medium dense to very dense dark grey very silty fine SAND with traces of coarse sand-sized shell fragments – with a thick bed of hard slightly sandy clay at 22.9 m
IIIc	24.5	30.0	Stiff to very stiff slightly sandy CLAY with traces of coarse sand-sized shell fragments – with a medium bed of sand at 29.7 m

Note I: * = New created soft top layer

Note II: BSF = Below Sea Floor

What is particularly important in these determined properties is the undrained shear strength, since this defines the stone penetration to a large extent. In the graphs on the next page the relation between the undrained shear strength and the depth is shown. The graphs show that the Norwegian seabed is very soft especially the top parts, with undrained shear strengths between 2 and 25 kPa. The different methods used to determine the undrained shear strength are also indicated. The laboratory vane stands out with values which are smaller than the other methods. Based on the different methods for different depth a profile is created for the minimum, maximum and best estimate relation of the undrained shear strength with depth. This relation deviates from the values prescribed by Fugro (see Appendix 15.17). The c_u values used in the penetration calculation are often taken lower. This difference is especially large in the, for this problem relevant, the top layers. The lower undrained shear strength makes the penetration determination slightly conservative and hence takes into account the unreliability of laboratory test on disturbed low stress soil samples.

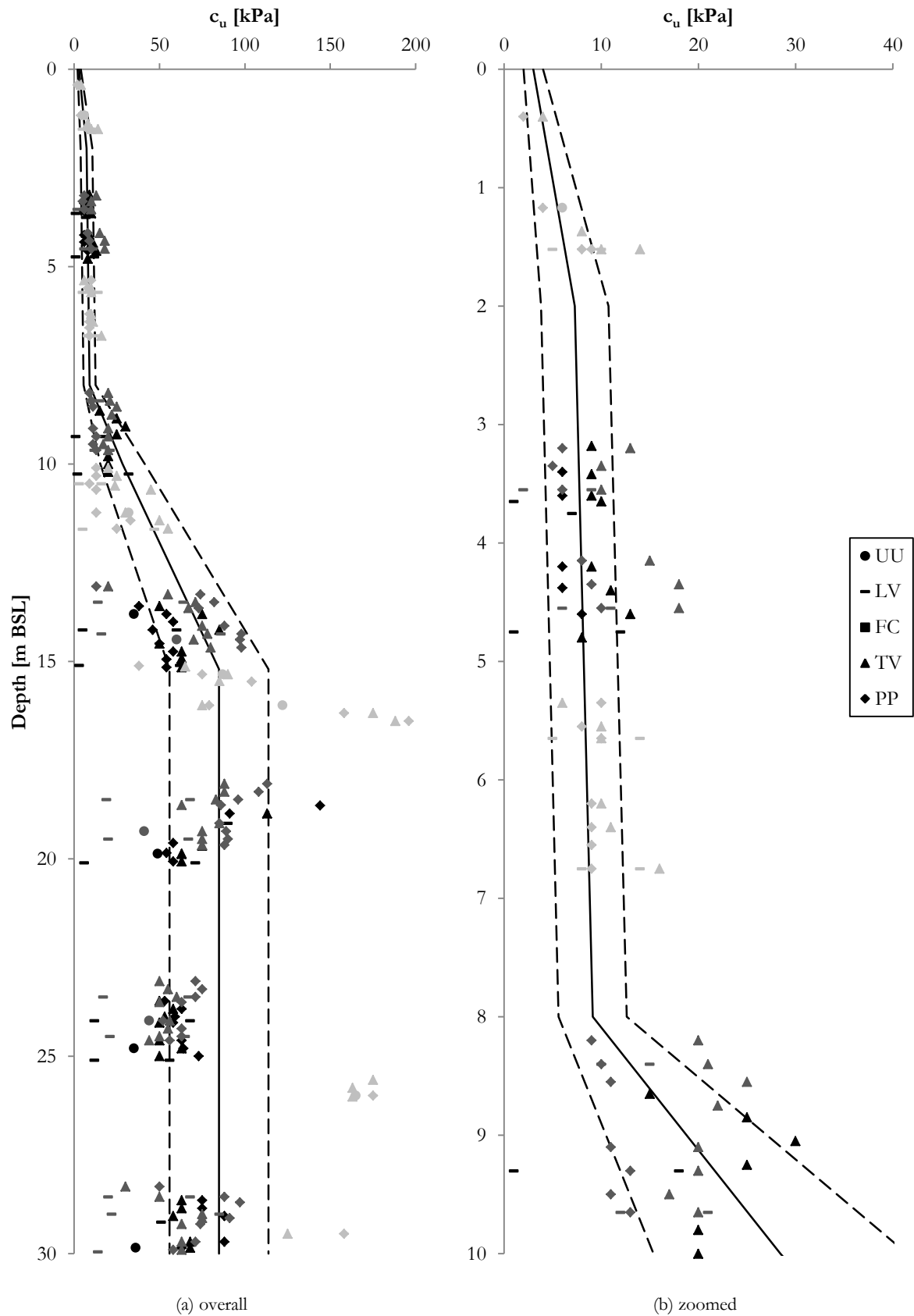


Figure 8.5: Undrained shear strength relation with depth for the Knarr Surf project

UU = Unconsolidated undrained triaxial
TV = Torvane

LV = Laboratory vane
PP = Pocket penetrometer

FC = Fall cone

One major issue with offshore site investigation is the reliability of the results in low stress soil behaviour. In the top part of the soil, where the confining pressures are small, the classical site investigation using a CPT often provides insufficient accuracy. Moreover laboratory tests on samples with low stress levels are difficult to perform due to the huge influence of boundary friction effects, let alone the significant disturbances when acquiring samples (Randolph & Gourvenec, 2011). That is why, in an attempt to improve the ability to estimate shear strength directly from field penetrometer tests, alternative ‘full-flow’ penetrometers are now sometimes used (see Figure 8.6). These penetrometers have the advantage that the soil flows around the device, ensuring a higher accuracy in soft deposits like the ones present in the top layers of the Norwegian seabed. In SRI projects to come it is therefore recommended to use these full flow penetrometers instead of conventional CPT tests, especially when soft soil conditions are expected. More information regarding this recommendation can be found in chapter 14.

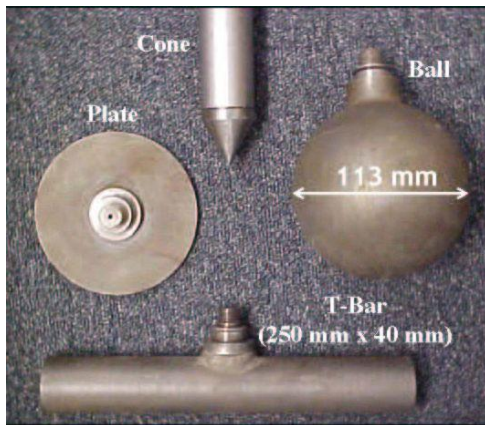


Figure 8.6: Full flow penetrometers (Ball cone and T-Bar) (Randolph, et al., 2005)

8.3 Rock properties

The rocks used for this project come from two local Norwegian quarries situated along the coast, in Jelsa and Sløvåg. Both quarries provide rock material with a different composition. The quarry in Jelsa provides rocks composed of granodiorite, a material similar to granite with a density of 2760 kg/m^3 . The quarry in Sløvåg provides Gneiss rock particles which differ in density ranging from $2600 - 2900 \text{ kg/m}^3$. Both quarries provide crushed rocks of a size 25 to 76 mm (1 – 3”) for the first layers. Since vertical tolerances are critical in this project, the top 0.5 m will consist of smaller rock particles with a size of 16 – 32 mm. The sieve curves for both sizes are shown in Figure 8.7. Here the dotted lines indicate the grading curve for the sieved samples; the continuous line shows the boundaries between which the sieve curve should be located in order to fulfil the grading requirements.

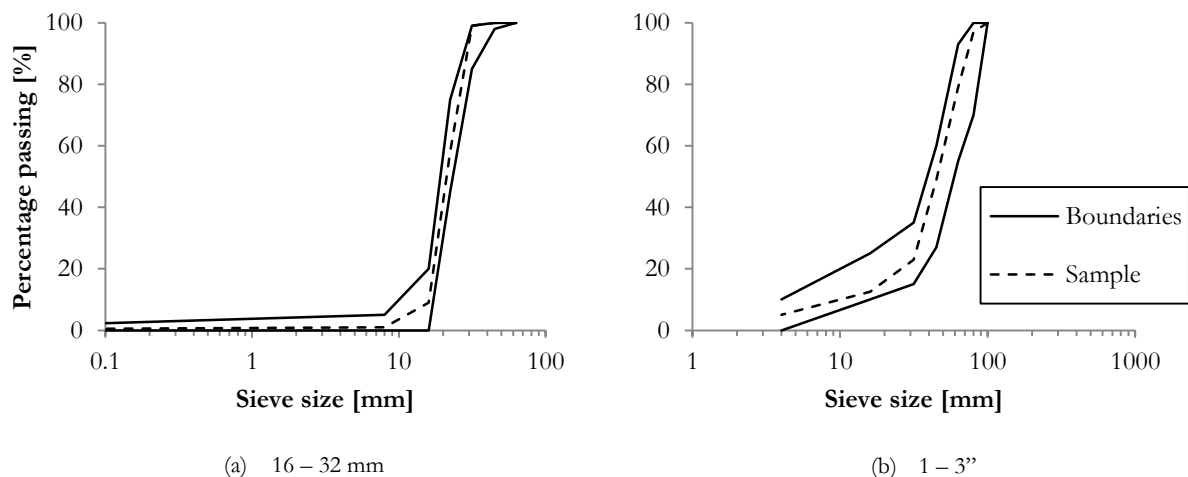


Figure 8.7: Particle size distributions for the Knarr Surf project

The rock material has a bulk density varying between 1460 and 1600 kg/m³. This value is often referred to as dry bulk density when it is determined from an oven dried soil sample. However in the case of the Norwegian quarries this bulk density is determined without drying the sample, hence a small natural percentage of moisture content will be remain in the samples during testing. That is why the term dry bulk density is not appropriate and bulk density will be used instead. As will later be described in chapter 10, it is not the rock density which leads to a large uncertainty in the volume loss determination, but the derivation of the bulk density of the material after installation.

9 Field measurements

As described in chapter 2 the flexible fallpipe vessel and specifically the ROV are equipped with several instruments to thoroughly measure a variety of different properties, such as position, wave height, wind, water temperature, etc. Using these systems the bathymetry of the seabed can be determined before subsea rock installation and afterwards. These so called pre and post surveys respectively are used to validate the work provided and to determine the theoretical volume of rocks required to complete the berm. In this thesis however the surveys are used to determine the complete volume loss during installation. The first paragraph of this chapter will explain the way the measurements are obtained and the procedure used to determine the volume loss. The accuracy of the essential multi beam echo sounder instrument is described in detail in paragraph 9.2. Multi beam echo sounder (MBES) determines bathymetry of the seabed by transmitting a range of acoustic pulses. The depth and shape of the seabed can be determined based on the reception angle and the two-way travel time of an acoustic pulse.

9.1 Approach

Figure 9.1 indicates the processed bathymetric data from the multi beam echo sounder attached to the ROV. Figure 9.1a shows the virgin seabed of a large area. This is obtained by combining several independent pre surveys. As can be seen the bathymetry of the deep sea bottom is not entirely flat, over a length of 450 m the average slope is about 0.2° . Moreover large holes are present in the seabed; in this case the gap is about 5 m deep and has a size of almost 35 x 20 m. Figure 9.1b however, indicates the final result after dumping. This series of combined post surveys clearly indicates the completed rock berm in orange.

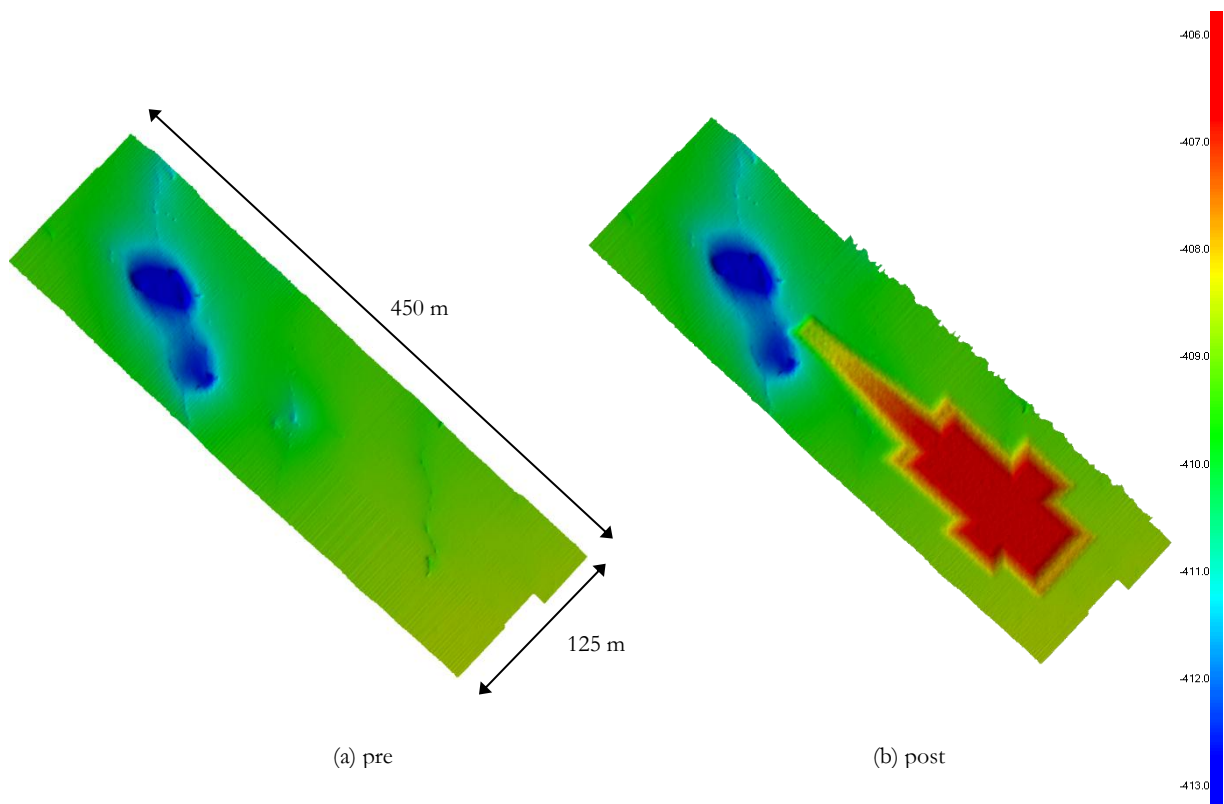


Figure 9.1: Knarr Surf bathymetry at the FPSO location

In Figure 9.2 a cross section of the same fill is shown. This time the pre survey is shown in red, the post survey in purple and the planned design in light green. It can be seen that the installed volume is slightly

larger than the intended design to fulfil the client requirement on all positions of the fill. By determining the difference in height between the pre and the post survey for the complete rock fill area, the total installed volume can be determined. This can be derived automatically using Van Oord's in house software VOSS.net (see Appendix 15.18).

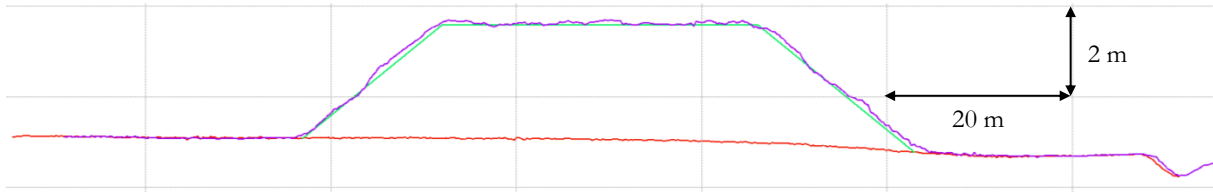


Figure 9.2: Cross section of the multi beam echo sound data for the FPSO location

Note: The vertical and horizontal scale differ, creating a distorted image of the real berm dimensions

On the other hand using the mass of installed stones measured aboard the vessel the total theoretical volume can be determined using equation (9.1). Where $m_{s,m}$ indicates the installed mass of stone measured using the instruments on board, ρ_s is the stone density and n represent the porosity of the installed material. The estimation of this porosity strongly affects the reliability of this volume calculation as will be discussed in the following chapter.

$$V_{s,m} = \frac{m_{s,m}}{\rho_s \cdot (1 - n)} \quad (9.1)$$

During a large project as Knarr Surf more than two surveys (pre and post) are made. These so called intermediate surveys can also be used to determine penetration throughout the works. It is expected that the initial penetration is larger than the penetration of subsequent layers, due to a stronger soil reaction when the soil is completely covered with rocks, as indicated in the graphs added in the Appendix 15.19. The difference in volume determined using the cross sections and the installed volume based on the installed mass of the rock material is described as the volume deficit. This difference in measured and installed volume can partially be explained by multi stone immediate penetration, but washout of fine material and consolidation during measurements also affect these results. That is why these measurements can be used to validate the current processes described.

9.2 Accuracy

Although the precise operation of a MBES system falls outside of the scope of this thesis, the accuracy with which measurements of the seabed are done is very important to determine the losses of material during penetration. That is why additional attention is given to this subject.

Figure 9.3 shows the real-time feed directly from the multi beam echo sounder attached to the ROV. To precisely determine the transmit and receive angle of each beam, a multi beam echo sounder requires accurate measurement of the motion of the ROV. These measured values are typically heave, pitch, roll, yaw, and heading which are compensated for by the instruments software. Moreover the speed of sound under water will have to be monitored continuously, since this can change from location to location based on water temperature, pressure and salinity. Figure 9.3a schematically shows the width of a swath and the unprocessed measurements. The influence of the waves is visible through the sinusoidal movement at the sides as indicated. Additionally the figure indicates the difference in measurement density and size for altering locations. Right underneath the MBES the pixel density is high and the size of each measurement – also known as footprint – is small. At the edges of the measurement range the density decreases whereas the footprint of one measurement increases. Figure 9.3b shows the flat virgin Norwegian seabed before dumping during a survey again this image shows real-time unprocessed data. The white dots indicate one single pulse reflecting on the sea bottom.

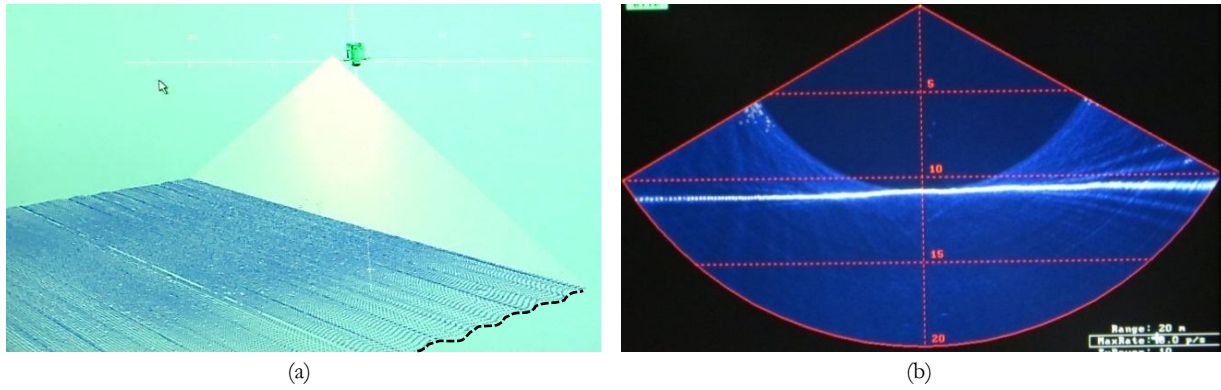


Figure 9.3: Real-time multi beam echo sound data

Depending on the stand-off distance and settings of the MBES a difference in accuracy can be achieved. The amount of measurements per linear meter can change, here a higher measurement density obviously relates to a higher accuracy. By increasing the frequency of the pulse the resolution of the measurements increase, i.e. smaller objects can be seen. On the other hand, the penetration of the pulse into the seabed decreases. High frequency instruments only indicate the top of the seabed. When the density of the material increases above the water density of 1025 kg/m^3 a reflection of the sound wave will be measured. This means that clay particles in suspension with no bearing capacity whatsoever are indicated as the seabed according to these measurements. Obviously the installed rock material will penetrate right through this mud. By using low frequency sound waves, the energy per pulse increases making it possible to penetrate into the soil and reflect on material with a density of 1200 kg/m^3 . This density resembles the so called nautical bottom density. Downside of this low frequency system is the lower resolution. Moreover currently the ROV is not fitted with such a device. In case of the Knarr Surf project high frequency pulses were used with a frequency of about 400 kHz . These pulses will not penetrate into the seabed at all and possibly indicate the layer of sludge as the top of the seabed (Koper, 2013).

Not only the density and frequency of the pulse, but also the footprint of each measurement influences its accuracy. The size of the acoustic footprint (shown in Figure 9.4a) affects the intrusion of the signal into the rock berm (indicated in Figure 9.4b). If the seabed is fine grained this intrusion of the signal is negligible. However in the case of large particles, commonly used for SRI projects, this is an aspect which has to be taken into account. Literature indicates that the acoustic signal penetrates into the porous rock fill depending on the position of the signal. In the centre, the footprint is small and the penetration is therefore bigger, whereas at the sides the footprint is bigger and the top of the particles is more likely to be hit and reflect the signal. On average the deviation of the acoustic signal can be found using:

$$\sigma = c_1 + c_2 \cdot D_{n50} \quad (9.2)$$

Where c_1 is 0.035 m and c_2 is 0.3 based on a full scale test (VKBO, 2000). This indicates that there is a systematic error in the acoustic measurements and an error which is based on the roughness of the seabed. In case of the Knarr Surf project ($D_{n50} = 0.049$) this error is about 0.05 m . When comparing the pre and post surveys this inaccuracy causes a structural underestimation of the berm height (Figure 9.5). This is the result of the fact that the acoustic signal does not penetrate into clayey seabed, but does penetrate into the installed rock berm. Consequently the installed volume is underestimated, which in turn leads to an overestimation of the volume loss.

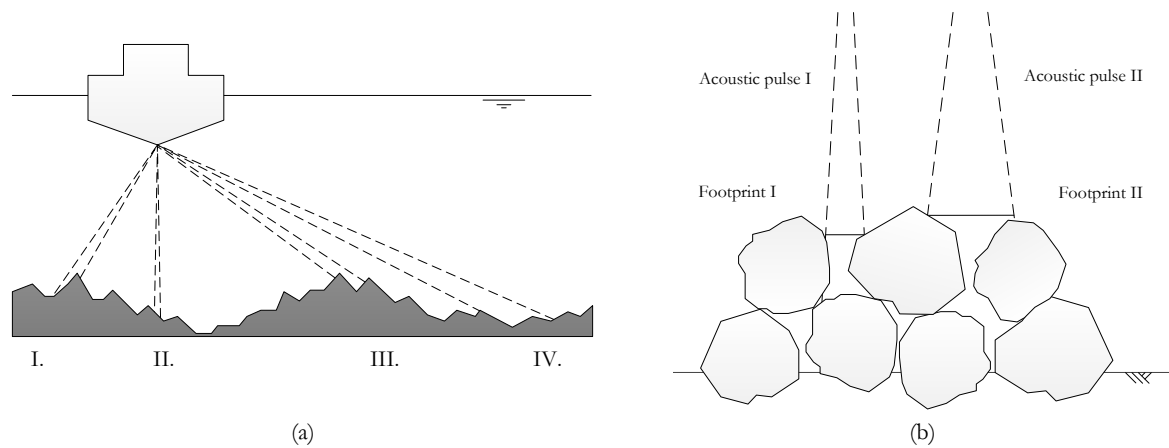


Figure 9.4: Bathymetric measurements using multi beam echo sounders

Besides the processes described before changes in the position of the original seabed also influence the reliability of the volume estimation. Figure 9.5 shows the difference between the installed layer thickness and the measured layer thickness. Previously described processes such as stone penetration and seabed deformation influence the derivation of the layer thickness and hence form an uncertainty in the volume determination. However during SRI the reference level of the seabed can also change due to heave and volumes of rock which are dumped outside the perimeter or undrained response of the seabed, that is why the reference plane for the pre survey has to be located at least 15 m beyond the perimeter of the rock fill.

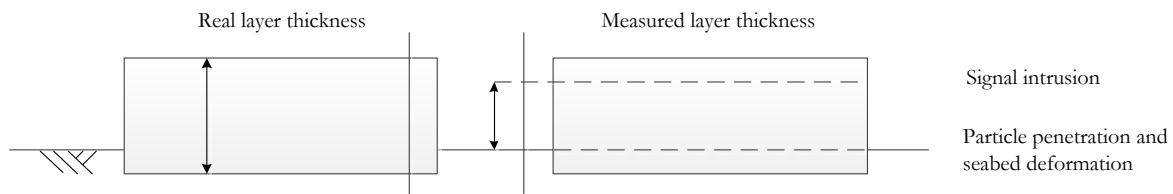


Figure 9.5: Signal distortion

When performing absolute measurements using MBES instruments the vertical achieved accuracy lies in the order of 0.1 - 0.2 m. However with clients demanding an equivalent accuracy over the complete project a higher precision is necessary. This is found by using relative measurement. Instead of fixing the seabed to a certain known position, all surveys are fitted on top of each other as shown in Figure 9.6. By using the large reference plane a good fit can be achieved, moreover water or installation influences will be very small beyond 15 m outside the perimeter. Based on this relative approach the accuracy of these measurements are experienced to be in the order of 3 - 5 cm (Scheermakers & Koper, 2013), which equals the precision found in literature (VKBO, 2000).

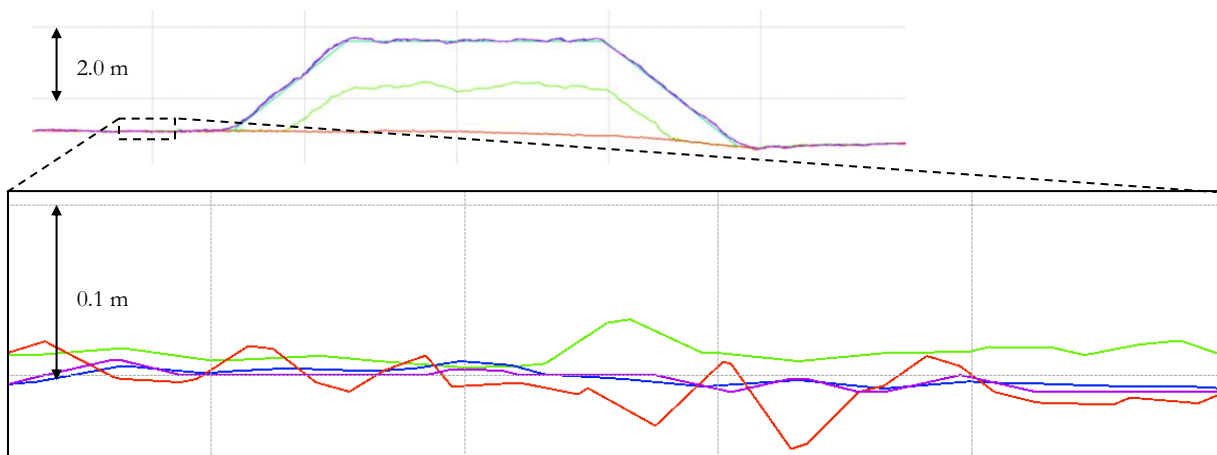


Figure 9.6: Relative fitting of surveys

The final inaccuracy during survey measurements of the seabed and installed rock material arises in the comparison between the offshore site investigation and the pre survey. As described the latter is performed relatively, since the absolute accuracy is too low. The geophysical part of the SI is often performed in the same relative way using the same type of multi beam echo sounding equipment on a ROV. However to determine the geotechnical properties of the seabed at great depths a so called seabed system is used (Lunne, 2010). The system consists of a small independent rig which is placed on the seabed. This steel seabed frame will itself penetrate into the soil under its own weight. During this initial deformation the drill string is retracted. After installation of the system the drill string is pushed down to perform alternating CPTs, vane tests and take samples. As soon as the cone hits material which provides sufficient resistance, this level is defined as the top of the seabed (Woldringh, 2013). Obviously this plane is subject to a lot of variance since this definition of the “sufficient resistance” is very vague and largely depends on the accuracy of the used instruments and the judgment of the engineer on board of the vessel. Often when soft material is expected, cones with an accuracy of 0.01 MPa are used. These devices are capable of determining the presence of a material with an undrained shear strength of roughly 1.5 kPa, and hence can – in theory – determine the difference between seawater and mud. However this is also dependent on how you process the CPT results (Bol, 2013).

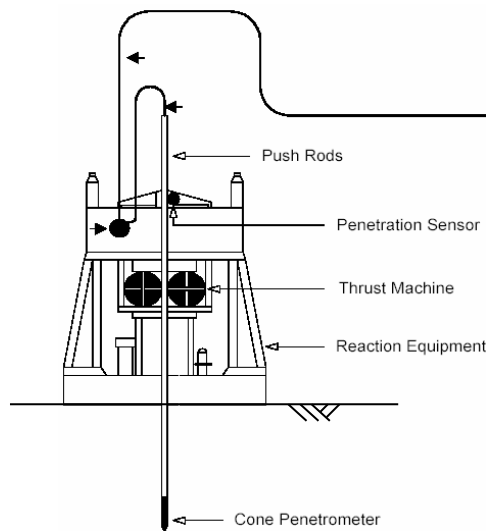


Figure 9.7: Seabed system (Randolph, et al., 2005)

Besides the described difficulty to accurately assess the in-situ properties of soil in low stress condition, this system also has difficulty to determine the exact location of the top of the seabed. If the demarcation of the mudline is known a water depth will have to be coupled to this location. That is why a number of different measurements are performed in order to determine the depth of the seabed system. This is done using a CTD (Conductivity, temperature and depth) probe and a drill string reading. The CTD probe is attached to the seabed system and measures the absolute pressure on the seafloor. Since the atmospheric pressure is recorded using a barometer on the vessel, the water pressure and hence the installation depth of the seabed system can be derived. On the other hand a physical measurement is made by the drilling personnel on board by adding up the length of pipe used to reach the seabed. Though when operating in deep water errors can occur in this measurement, due to effects of currents on the drill string. Based on these two methods a certain depth is assigned to the mudline. This depth often does not correspond to the water depth found using the MBES. In some cases this difference can be as large as 0.5 m. Therefore the possibility arises that the first decimetres of material are observed by the multi beam equipment, but not characterized in the soil investigation. In case of the Knarr Surf project this undefined layer is estimated to be 0.10 m, which causes the undrained shear strength determination to be missing for these first decimetres. This difference has to be taken into account since this uncharacterised top layer probably consists of even softer material.

10 Field results

In this chapter the results of the fieldwork using the method described in the previous chapter are shown, together with their reliability. As previously indicated the in-situ density of the rock material forming the berm is important and forms a vital consideration in the determination of the total volume loss. That is why additional effort is put into the thorough description of this property.

10.1 Volume loss

Table 10.1 shows the derived volume loss and corresponding height deficit for the five different berms installed during the Knarr Surf project. As indicated in the last column the height deficit ranges between 0.1 and 0.4 m. This is determined for all individual locations by first defining the total area in which the material will be installed. The border of this area is kept constant for all intermediate measurements. The fourth column indicates the assumed in-situ density of the rocks installed on the soft seabed. This density is based on tests performed by the quarry. Since one berm can contain multiple rock batches a weighted average based on the relative installed volume per batch and corresponding density, is taken. The fifth column shows the volume of installed material. This value is obtained by dividing the installed mass by the assumed bulk density. The mass of installed rock material is accurately measured using equipment installed in the conveyor belt of the vessel. This found volume is compared with the volume determined using the MBES equipment, as shown in the sixth column. The difference between these volumes and hence the volume loss, is shown in the seventh column. By dividing this loss over the measured area, the average height deficit is found as indicated in the eighth and final column. The unit for this height deficit is m (m^3/m^2). In case no other process would influence the volume loss, this height would be equal to the average penetration.

Table 10.1: Field results indicating the total volume loss per location

Berm location	Berm height [m]	Measured area [m ²]	Bulk density [t/m ³]	Installed volume [m ³]	Measured volume [m ³]	Volume loss [m ³]	Height deficit [m]
FPSO Wet storage	0.50	1448	1.56	910	758	152	0.10
PT Wet storage	0.55	6266	1.60	5050	3942	1108	0.18
WI Wet storage	0.60	2261	1.46	1500	1203	297	0.13
PT Towhead	2.00	10564	1.55	17216	13877	3339	0.32
FPSO Towhead	2.65	14384	1.53	30563	25082	5481	0.38

However as discussed in chapter 9 the penetration of the MBES acoustic signal in the rock berm forms a consequent underestimation of the field measurement. This is caused by the fact that the acoustic wave does not penetration in the fine grained seabed, but does penetrate in the installed granular berm. This leads to an underestimation of the installed volume and hence to an overestimation of the height deficit (VKBO, 2000). In case of the Knarr Surf project this error is 0.05m, depending on the size of the installed particles. Table 10.2 shows the spread in height deficit if this measurement error is incorporated in the measurement results. These values will be used in the remainder of the thesis as the height deficit per location.

Table 10.2: Modified field results taken into account the measurement deviation

Berm location	Berm height [m]	Height deficit [m]
FPSO Wet storage	0.50	0.05
PT Wet storage	0.55	0.13
WI Wet storage	0.60	0.08
PT Towhead	2.00	0.27
FPSO Towhead	2.65	0.33

10.2 In-situ density

The large assumption made here is the fact that the bulk density provided by the quarry, is considered the same as the installed in-situ density on the seabed. Consequently the packing of rock material on the seabed equals the packing determined at the quarry. This assumption is prone to discussion, since the particles might be packed in a denser state due to the increase in energy during the descent through the fallpipe. This on-going addition impact energy might compact the berm and increase the in-situ density of the material. On the other hand, the fines might wash out of the installed aggregate, creating a more uniform grain distribution. Consequently the pores of the rock fill will not be filled with small particles resulting in a lower in-situ density. The relative influence of both these processes on the in-situ density is not exactly known but proves to be very important. Therefore additional research into this topic is advised. In Figure 10.1 the absolute and relative influence of the in-situ bulk density on the volume loss determined is given. The relative influence is found by dividing the calculated volume loss by a reference loss. This reference volume loss is in turn based on the bulk rock density derived by the quarry. These graphs indicate the sensitivity of this quantity; for in-situ densities larger than 1800 kg/m³ no volume loss remains, whereas for densities smaller than 1400 kg/m³ the volume loss increases by 50%.

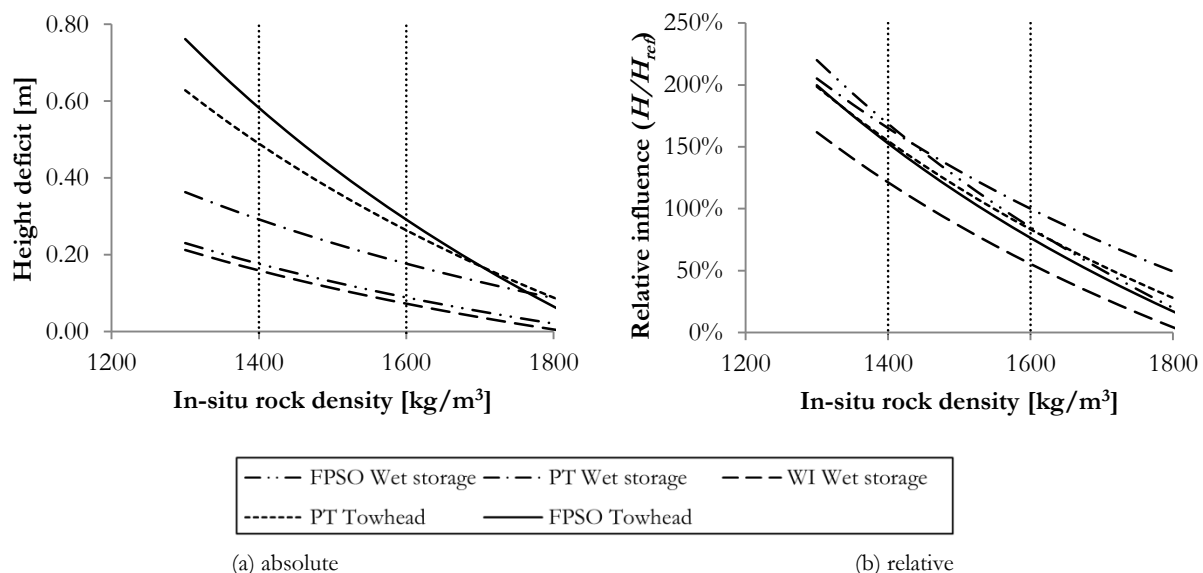


Figure 10.1: Influence of assumed in-situ density on the total height deficit per Knarr Surf location

Figure 10.2 indicates the spread in bulk densities found in the two quarries used to supply the rock material for the Knarr Surf project based on historical data for rock material of the same size. Since the Sløvåg quarry produces rock material with a larger spread of bulk density (Figure 10.2a) and it provides the majority of the rock material during the installation, the densities of this quarry are presumed governing. Figure 10.2b shows the detailed probability density function of the Sløvåg quarry including the standard deviation. Based on this figure the spread of bulk density is derived to lie between 1400 and 1600 kg/m³ which is also indicated in the graphs of Figure 10.1.

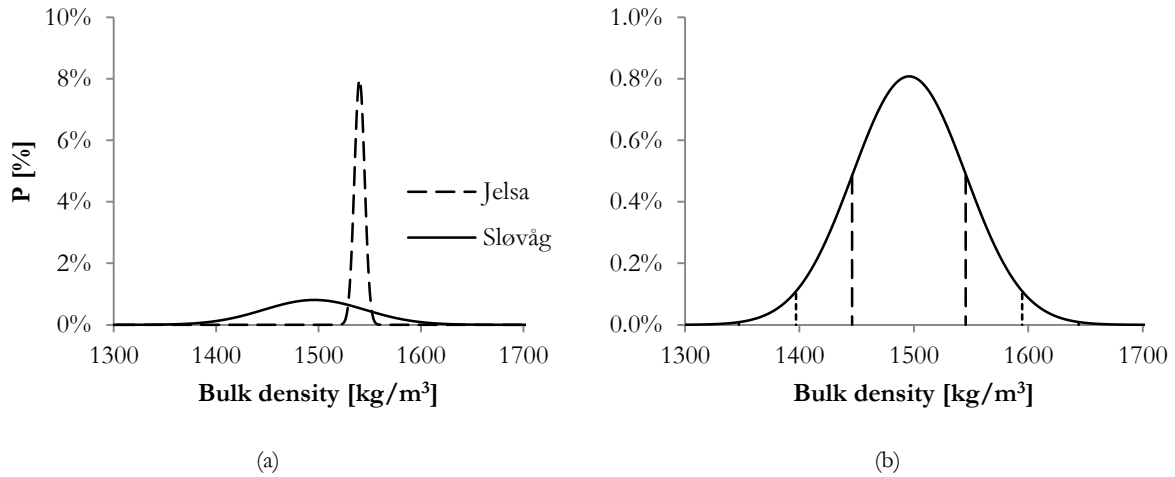


Figure 10.2: Probability density function for the addressed quarries

These values correspond well to the average spread in bulk densities of rock material produced in quarries on the Norwegian coast, based on research performed presented in Appendix 15.20. A comment has to be made when comparing these bulk densities since the determination of this value has not been standardised, i.e. the way of determining the in-situ densities slightly varies from quarry to quarry possibly influencing the obtained results. Moreover the porosity of the material and thus the grading curve influence the bulk density to a large extent. Therefore only material with the same size can be compared. In this case all grading curves of material with a size between 1 - 5" are used.

Contradictory, Figure 10.3 shows the back calculated in-situ density found for different locations during the Knarr Surf project. These densities are derived by dividing the installed tons during installation of one layer by the measured increase in volume between the corresponding intermediate surveys. As a result this determination does include the total volume loss due to all previously described installation processes. That is to say, the loss of volume distorts the presentation of the densities. Because of the volume losses during installation an increased amount of material is installed which does not lead to an increase in measured volume. This partially explains the relatively high measured density. The spread of these measurements lie between the 1500 and 2300 kg/m³. The historic measurements performed by Van Oord for the Ormen Lange project are also indicated in this figure using open circles. It can be seen these measurement coincide with the lower limit of the back calculated densities.

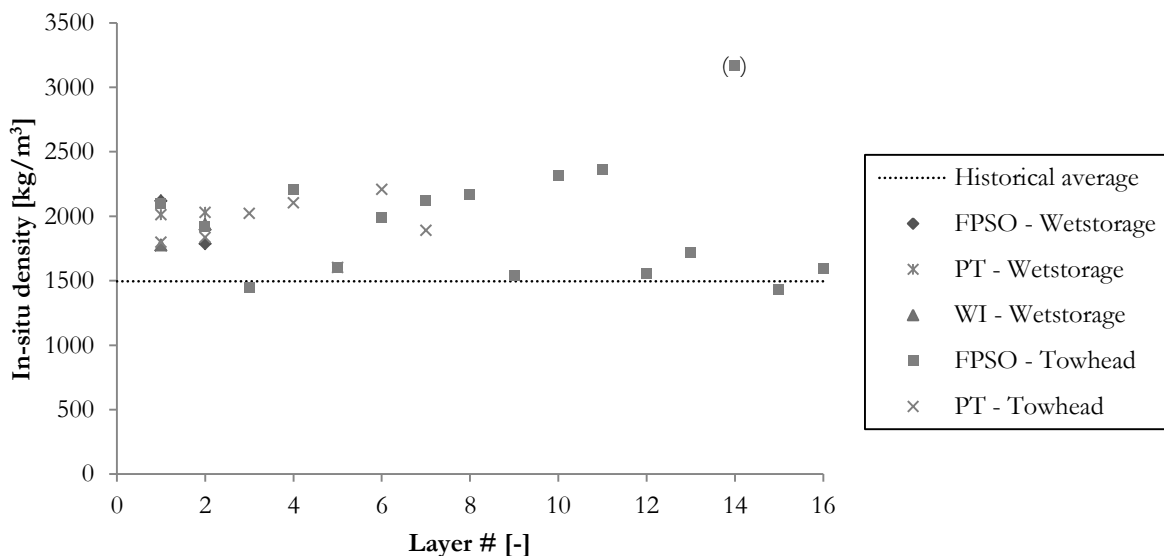


Figure 10.3: In-situ densities back calculated during the Knarr Surf project for different locations and layers

Figure 10.3 shows no apparent decrease in measured in-situ rock density with increasing layers. This is unlike what was initially expected. As described in paragraph 9.1 initial penetration is estimated to be larger for the first layers and – assuming a constant influence of other processes – this would presume that the measured in-situ density would start high and decrease to a constant value over time. However this cannot be seen in Figure 10.3, in fact no real trend can be seen at all. If these measurements were to be correct, this would suggest that penetration is either a small influence factor of the complete volume loss or the penetration does not reduce for subsequent layers. However the uncertainty in the survey results is thought to be governing in this case. As described in the previous chapter, the relative MBES measurements provide readings with an accuracy of 3 to 5 cm. This small height difference can have a significant influence on the in-situ density back calculation, especially since Figure 10.3 has been created by comparing intermediate surveys of different rock layers with each other. These surveys are sometimes performed after dumping only 10 cm of rock. In this case the relative error of the MBES system becomes very significant for the in-situ density determination and may provide a distorted result.

The final spread of possible volume losses for different in-situ rock densities is indicated in Table 10.3. Here the minimal, maximal and best estimate values are given for different location of the project. The minimal value is based on an in-situ density of 1600 kg/m³, whereas the maximal value is based on 1400 kg/m³. The best estimate is based on the relative installed volume per rock grading and corresponding bulk density found at the quarry. At the moment this is the best assumption; choosing a different density would be arbitrary. Additional research on this topic is recommended since its influence is large, especially research into the influence of the added energy during subsea rock installation using a fallpipe vessel on the packing and in-situ density of the rock material.

Table 10.3: Spread in height deficit for different in-situ bulk densities

Berm location		Bulk density [t/m ³]	Min [m]	BE [m]	Max [m]
FPSO	Wet storage	1.56	0.09	0.10	0.18
PT	Wet storage	1.60	0.18	0.18	0.29
WI	Wet storage	1.46	0.07	0.13	0.16
PT	Towhead	1.55	0.26	0.32	0.49
FPSO	Towhead	1.53	0.29	0.38	0.59

Note: min and max are situated two standard deviations from the mean ($\mu \pm 2\sigma$), resulting in a range of 95% probability

10.3 Consolidation

During the Knarr Surf project the possibility arose to perform an intermediate survey directly after having dumped one shipment of rocks and an additional one right after getting back from the harbour. During this time, at which the vessel got resupplied with new rock material, the seabed would continue to settle due to consolidation. The height difference between the two surveys therefore equals the consolidation settlement over a period of two days. The results of these surveys are shown in Table 10.4 and would later be used to validate the order of magnitude of the consolidation obtained using the D-Settlement calculation. Since these additional surveys take time and provide limited benefits for the installation process only two surveys of this sort could be performed. Similar measurements during a later stage where unfortunately not possible.

Table 10.4: Consolidation measurements in the field after two days

Location		Settlement [m]	
FPSO	Towhead	0.023	0.021

Part III – Modelling

11 Single stone penetration model

As explained in chapter 4 the single stone penetration depth depends, among others, on the diameter of the particle, its velocity at impact, and the strength as well as the consistency of the subsoil. Using the explained impulse balance the penetration of rock particles into soft soils can be determined. The bearing capacity equation of Brinch Hansen determines the resistance of the soft soil during penetration. This resistance is based on the soil properties gathered from an offshore site investigation. The properties of the rock installed together with the production rate and vessel specification define the impact velocity of the rocks onto the seabed. The approach used to model this process is schematically presented in Figure 11.1.

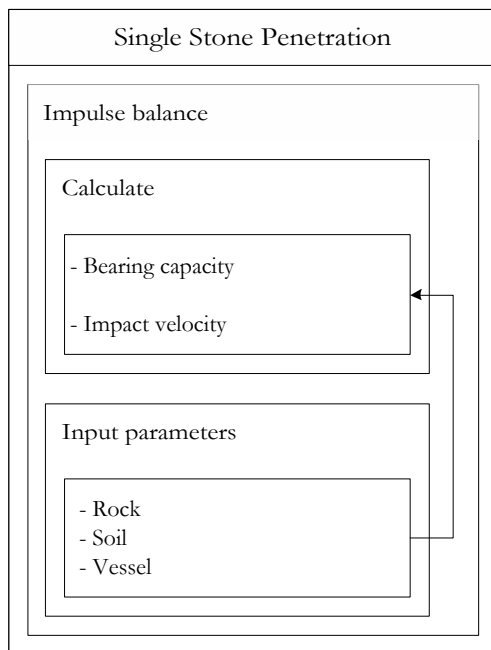


Figure 11.1: Flowchart used for the single stone penetration model

The input file for this model is provided in Appendix 15.21. Only the orange coloured fields can be changed during usage, all other properties remain fixed. In the following chapter this model is validated using the results of laboratory tests as shown in paragraph 7.1. Moreover a sensitivity analysis of the validated model is provided, indicating the influence of each parameter. Based on this sensitivity analysis a prediction can be made of the effect of implementing a wrong estimation. This analysis tells something about the reliability of the model and the consequence of being wrong.

11.1 Validation

Figure 11.2 shows the results of the single stone penetration for clay with an undrained shear strength of 1.4 kPa. These results have already been described, however this time calculated value determined using the created model for single stone penetration is shown as a solid line in the same graph. The lines follow the experimental results almost exactly with an average discrepancy of only 4.6 % and -2.4 % for the large and small ball respectively.

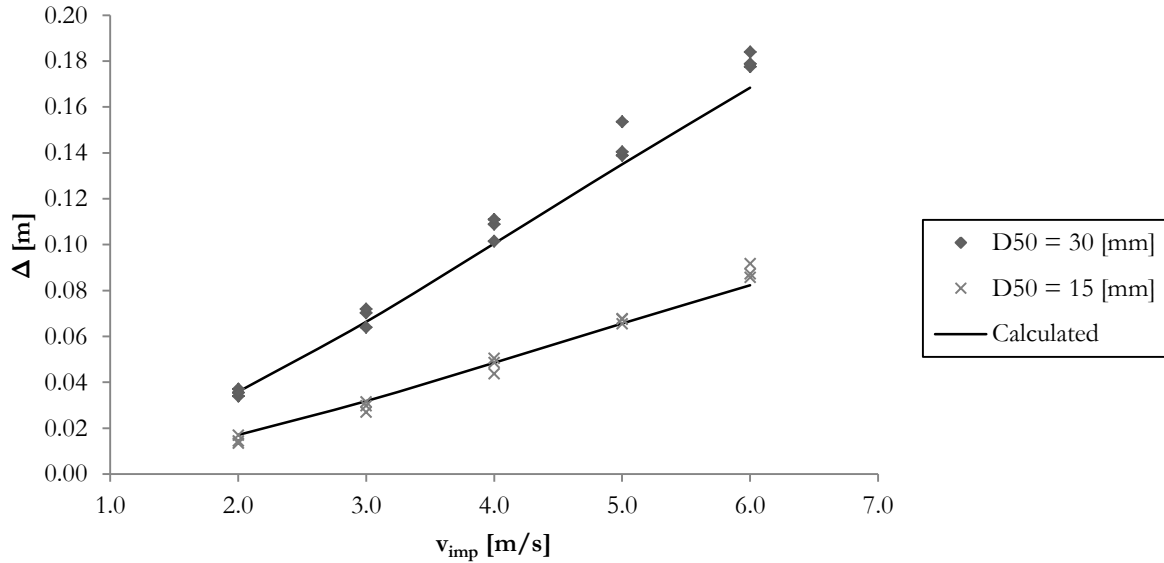


Figure 11.2: Modelled particle penetration for different impact velocities ($c_u = 1.4$ kPa, $\rho_s = 7804$ kg/m³)

Figure 11.3 indicates the same type of data only in this figure the undrained shear strength of the tested clay is 3.6 kPa. The difference between the measured penetration and the calculated model penetration is noticeably larger. With an overestimation of 17.1% and 26.2% of the penetration for the large and small particle this fit is less accurate than for the previous weaker clay. This might suggest an error in the data or the way of experimenting. However that is considered highly unlikely, since all measurements correspond nicely with each other with an average coefficient of variation of 8%. Another reason for the overestimation is an error in the model. Yet when comparing the results of other experiment the model seems correct. Hence it is believed that this difference is caused by an underestimation of the undrained shear strength. As explained explicitly before (chapter 6), the undrained shear strength determination is a delicate part of penetration modelling. A slight underestimation in the shear strength causes an overestimation in the penetration. Although the different methods indicate that the created clay has an undrained shear strength of 3.6 kPa, this value is assumed to be larger in reality. Modelling the single stone penetration of an equivalent particle in clay with an undrained shear strength of 4.6 kPa provides a perfect fit.

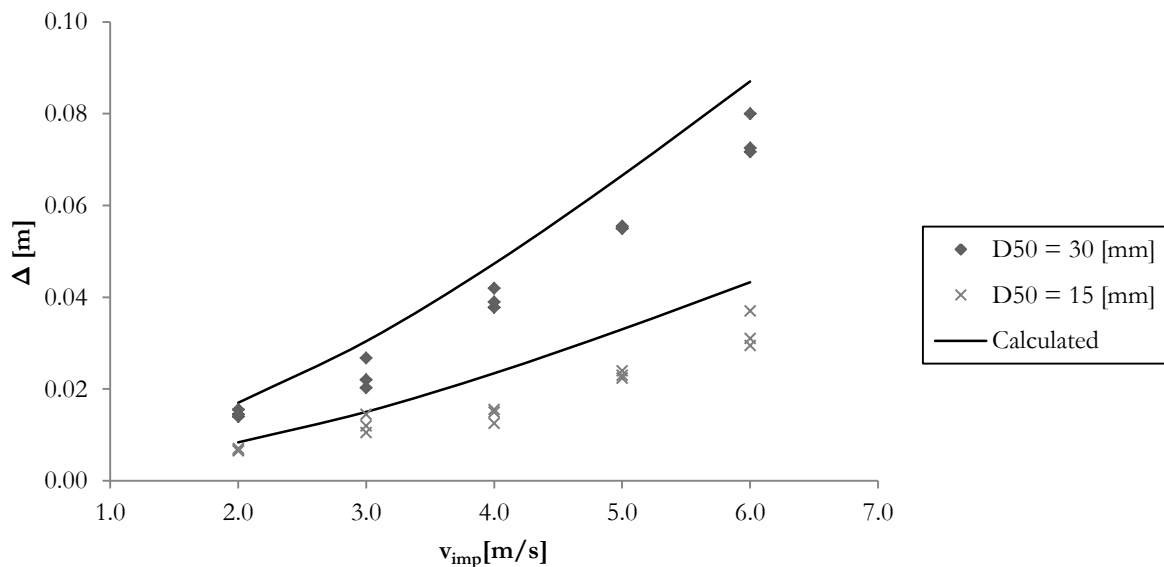


Figure 11.3: Modelled particle penetration for different impact velocities ($c_u = 3.6$ kPa, $\rho_s = 7804$ kg/m³)

The results of the single stone penetration test for the strongest clay in the testing regime, with an undrained shear strength of 12.4 kPa is shown in Figure 11.4. The calculated graphs show a fit of -0.5% and 1.0% for the large and small particle respectively. The slight curvature of the model results seems to follow the measured results nicely.

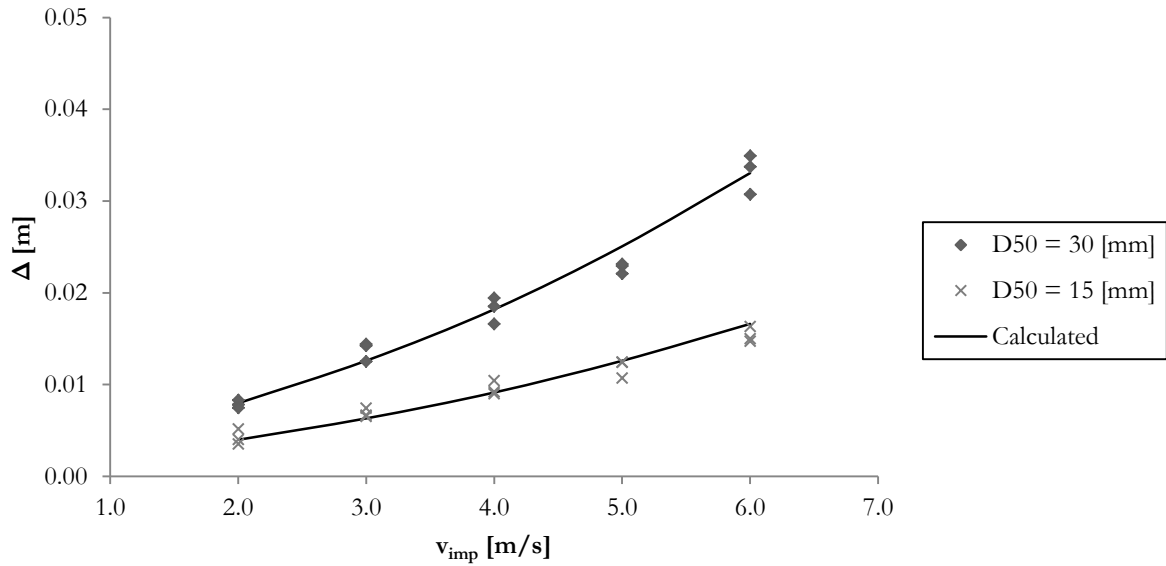


Figure 11.4: Modelled particle penetration for different impact velocities ($c_u = 12.4$ kPa, $\rho_s = 7804$ kg/m³)

Figure 11.5 shows the results for the experimental and modelled outcome of the penetration test using different densities. This time the penetration is slightly underestimated with an average difference of 2.4% and 23.6% for the steel and glass particles respectively.

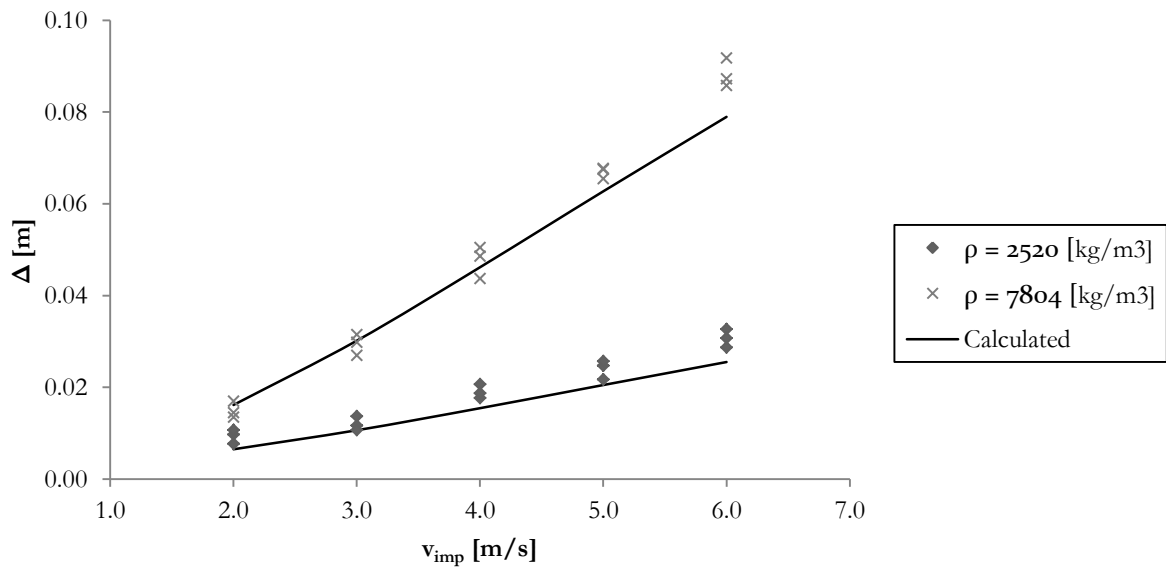


Figure 11.5: Modelled relation between particle penetration and impact velocities for different densities ($D_s = 0.015$ m, $c_u = 1.5$ kPa)

Figure 11.6 shows the interesting difference between the forces working on the stone in soft and stronger clay, with an undrain shear strength of 1.4 kPa and 12.4 kPa respectively. These forces are derived from the created model and have been split up in different parts which all contribute in equation (4.8). Because the forces are shown for the complete duration of the penetration, the area underneath each line is equal

to absorbed impulse by that force. Since in both cases the particle parameters (D_s and ρ_s) are identical no difference is found in the gravity and buoyancy forces (F_d and F_g). The large increase in cohesive forces is clearly visible in the graphs. This is caused by the difference in undrained shear strengths and its corresponding influence on the bearing capacity force of the penetration (F_B). The larger bearing capacity of the stronger soil results in a larger resistance of the soil and thus a smaller penetration depth and time. The calculated penetration in soft soil is 8.2 cm, whereas the particle only penetrates 1.7 cm the stronger soil. Moreover the penetration time is 33 ms versus only 5 ms for the soft and stronger soil respectively. Since the timescale of the graph is show in percentages of the full penetration time the cohesion forces seem to rise more rapidly in the soft clay test, however this is slightly distorted by the use of relative time scales. The maximum cohesive force is reached when the full effective area of the particle is mobilised. This happens nearly at the same time for both cases.

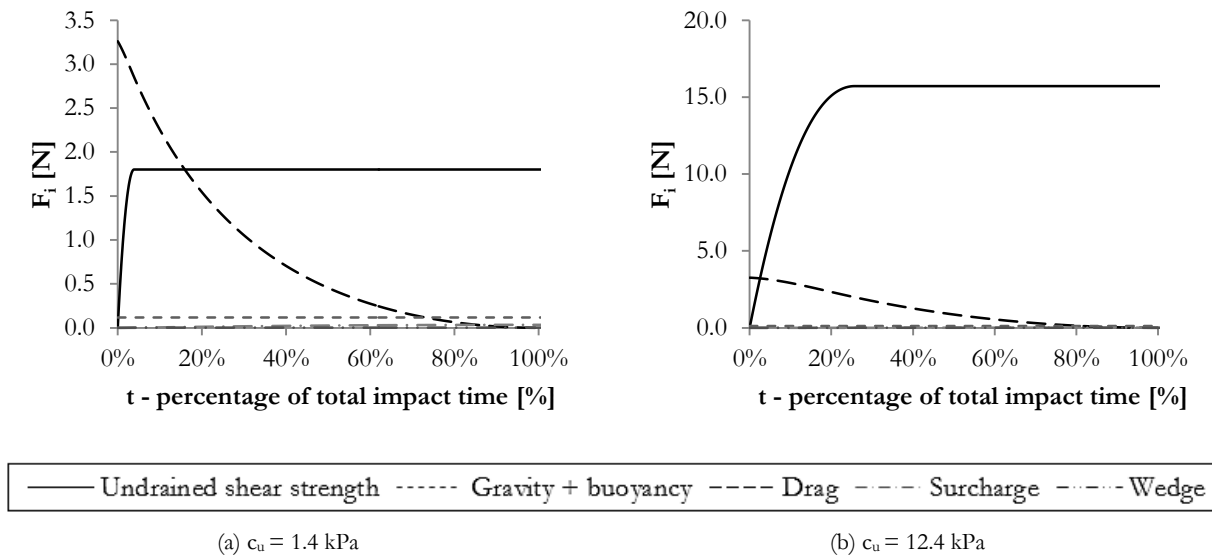


Figure 11.6: Force development during penetration divided in different components for different undrained shear strengths ($D_s = 0.015$ m, $v_{imp} = 6.0$ m/s, $\rho_s = 7804$ kg/m³)

11.2 Sensitivity analysis

Since several simplifications and assumptions that have been made, the model will still deviate from reality. However in the ideal laboratory environment, where conditions can be controlled are well defined, the test can be performed to achieve the highest resemblance with the model. With an average deviation between the model and the experimental results of 9.7%, the results are satisfying. Based on the previous results one can conclude that the impulse balance with soil resistance based on Brinch Hansen's theory can very well be used to determine immediate penetration of a single stone. For different sizes, impact velocities, shear strengths and densities the model has been validated and the theory seems to be able to predict the penetration well. To estimate the influence of different parameters used in the model an analysis of the effect of the input variables on the final penetration is made. This sensitivity analysis indicates which variables can greatly affect the outcome of the calculated penetration. The variables will have to be implemented carefully. Moreover one has to be aware that all processes that have not been implemented into the model, cannot affect the result. To determine the influence of each separate variable all individual variables must be changed within a suitable range, while all other variables remain the same. The fixed input parameters are given in Table 11.1. The range of possible input variables is given in Table 11.2. These values are likely to be found in reality, clarification of the applied range can be found in Appendix 15.22.

11. Single stone penetration model

Table 11.1: Input variables for the sensitivity analysis, based on the real Norwegian circumstances

Sieve size	D_{50}	0.030	[m]
Drag coefficient	C_D	1.00	[-]
Density water	ρ_w	1025	[kg/m ³]
Rock density	ρ_s	2650	[kg/m ³]
Saturated density	ρ_{sat}	15	[kN/m ³]
Velocity at impact seabed	v_{imp}	3.3	[m/s]
Undrained shear strength	c_u	3.0	[kPa]

Note: others do not vary.

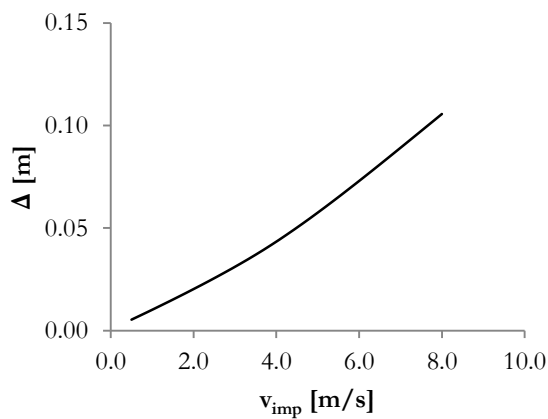
Table 11.2: Range of possible input variables

Sieve size	D_{50}	0.01	-	0.25	[m]
Drag coefficient	C_D	0.40	-	1.40	[-]
Density water	ρ_w	998	-	1050	[kg/m ³]
Rock density	ρ_s	2400	-	3400	[kg/m ³]
Saturated density	ρ_{ws}	11.0	-	18.0	[kN/m ³]
Velocity at impact seabed	v_{imp}	0.5	-	7.5	[m/s]
Undrained shear strength	c_u	0.0	-	20.0	[kPa]

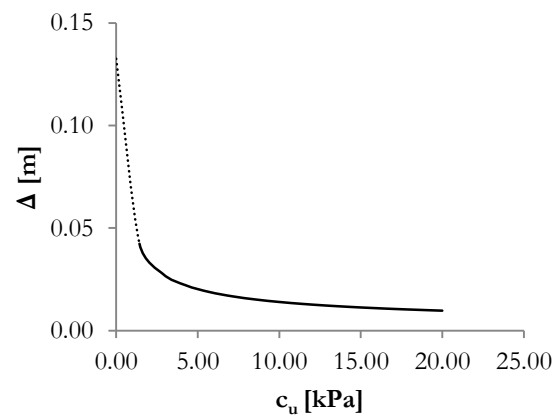
Based on these input parameters and possible spread for different parameters the penetration was determined. As a result of these runs the following parameters proved to be of a big influence for the single stone penetration (shown in Figure 11.7)

- Impact velocity v_{imp}
- Particle diameter D_{50}
- Undrained shear strength of the seabed c_u

One must realize that the impact velocity is in itself related to several separate variables such as stone diameter, production rate and stand-off distance. These variables are therefore very important as well, however indicating the influence of these variables is the same as showing the influence of the impact velocity.

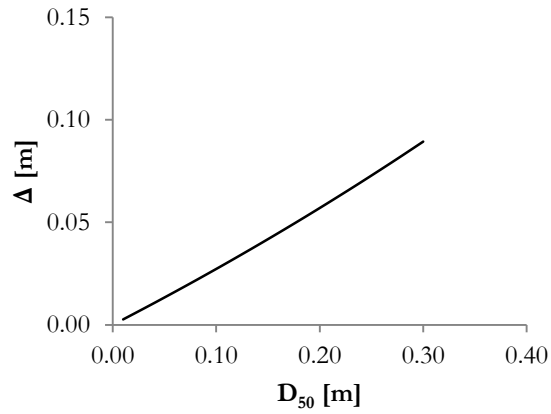


(a) Particle impact velocity



(b) Undrained shear strength

Note: the first part of the graph b is dotted since these low values of undrained shear strength would presume viscous behaviour, in which penetration goes to infinity.



(c) Particle diameter

Figure 11.7: Results of the sensitivity analysis for the three most important parameters of single stone penetration

Obviously these parameters were assumed to be of a significant influence from the start, since these parameters control the impulse balance. The results for all other less important parameters are shown in Appendix 15.23.

12 Volume loss determination

Based on the validated single stone model and the described supplementary processes, the total volume loss is modelled. A fit between the field results and the modelled penetration is determined to check if all processes are described and to validate their magnitude. Based data retrieved from the site investigation; provided by the quarry and experience obtained during the fieldwork, parameters are determined. For each process a minimum, maximum and best estimate (BE) of the volume loss is provided, here the maximum values of the properties are the properties which relate to a largest volume loss. Moreover an indication of reliability of the determination is given. This is based on the experience with the model, the possibility to confirm the process and the reliability of the input parameters. Finally the results of the different processes are indicated in relation to the measured height deficit.

12.1 Single stone penetration

Using the validated model the single stone penetration can be determined. The parameters presented in Table 12.1 have been implemented to derive the immediate penetration. The rock berms are installed using multiple batches all with their corresponding grading curves and derived bulk densities. That explains why different properties can be chosen. The lowest values in stone diameter and density provide the smallest penetration. Noteworthy is the use of the remoulded undrained shear strength ($c_{u,r} = 1.5$ kPa) for the maximum penetration value. Using these parameters the penetration presented in Table 12.2 is found for different locations.

Table 12.1: Single stone penetration input parameters

	Min.	BE	Max.	
D_{50}	0.045	0.049	0.049	[m]
ρ_s	2660	2680	2760	[kg/m ³]
c_u	5.0	3.0	1.5	[kN/m ²]
$\rho_{wet\ soil}$	1530	1500	1430	[kg/m ³]

Table 12.2: Derived single stone penetration in m

Item	Location	Min.	BE	Max.
FPSO	Wet storage	0.02	0.03	0.05
PT	Wet storage	0.02	0.03	0.05
WI	Wet storage	0.02	0.03	0.05
PT	Towhead	0.02	0.03	0.05
FPSO	Towhead	0.02	0.03	0.05

Since this model has been validated using laboratory experiments which provided an accurate fit with an average deviation of less than 10%, these results are thought to be reliable. Moreover most input parameters, such as rock diameter and specific density are well known. However the soil parameters obtained during the offshore site investigation are still dubious, as explained in chapter 8. That is why care must be taken when using this model.

12.2 Multi stone penetration

To determine the influence of multiple stones falling on top of each other, the in chapter 4 described conservation of momentum is used. As explained this is a very simplified representation of reality which can represent both the upper and lower limit for multi stone penetration. To be conservative the upper limit is used to determine the multi stone influence. Based on the same input parameters as the single stone penetration, shown in Table 12.1, the multi stone penetration is obtained. The result of this analysis is shown in Table 12.3. Here the additional penetration is based on five stones colliding on top each other. This amount is chosen based on the lower limit model, which indicated that only five subsequent layers of stone influence further penetration. Although only additional research can prove that this assumption is correct, for now it seems more reasonable than the infinite increase of penetration which is represented by the upper boundary model. To accurately determine the influence of multiple stones on top of each other more research is necessary. Not only in the conservation of motion, but also in the elastic behaviour of two particles colliding. This will make the determination of the amount of rocks still influencing the first particle less arbitrary and verifiable.

Table 12.3: Multi stone penetration results in m

Item	Location	Min.	BE	Max.
FPSO	Wet storage	0.02	0.03	0.08
PT	Wet storage	0.02	0.03	0.08
WI	Wet storage	0.02	0.03	0.08
PT	Towhead	0.02	0.03	0.08
FPSO	Towhead	0.02	0.03	0.08

12.3 Loss of fines

With the help of the Shields parameter and the formulae determined by Van Rijn, the diameters of the particles influenced by deep sea current can be determined. Based on the input parameters shown in Table 12.4 and the formulae described in Appendix 15.10, Figure 12.1 is created. This graph shows the particle diameter which is picked up by the horizontal deep sea currents.

Table 12.4: Parameters used to determine the loss of fines

k	0.22	[m]
R	10.00	[m]
c_f	4.0E-03	[-]
$(\rho_s \rho_f) / \rho_f$	1.60	[-]
D^*	22.70	[-]
ν	1.0E-06	[m/s ²]
θ_{cr}	0.03	[-]
ν^*	0.019	[-]
v	0.3	[m/s]
D_s	0.0008	[m]

Note: difference between viscosity (ν) and velocity (v)

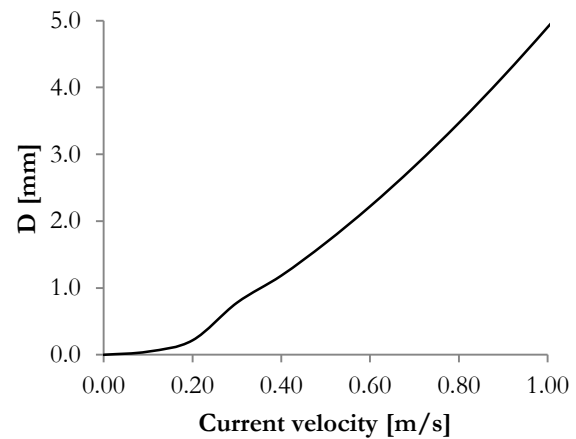


Figure 12.1: Relation between deep sea currents and particle size

The horizontal currents existing on the sea bottom is the governing parameter for this relation. With a best estimate deep sea current of 0.3 m/s at the northern part of the North Sea (Nio, 1991), particles with a diameter of 0.8 mm will be picked up by the currents and possibly be dropped far outside the perimeter of the fill. Based on the sieve curves of the installed material this means that about 1% of the rock is dumped outside the scope. However deep sea currents greatly fluctuate from location to location. With bottom currents ranging between 0 and 1 m/s the minimal and maximal influence of this process differ greatly (Koper, 2013). With a horizontal velocity of 1 m/s almost 4% of the installed aggregate will be picked up by the currents. However if the bottom current is this strong the soft clay layer forming the top of the seabed will probably erode, increasing the strength of this top layer and changing all previous calculations. That is why the maximal value is chosen at 0.5 m/s. The result of this process influence is indicated in in Table 12.5. As can be derived from this table the influence of this process remains small.

Table 12.5: Additional height deficit due to loss of fine material in m

Item	Location	Min	BE	Max
FPSO	Wet storage	0.00	0.01	0.01
PT	Wet storage	0.00	0.01	0.01
WI	Wet storage	0.00	0.01	0.01
PT	Towhead	0.01	0.02	0.02
FPSO	Towhead	0.01	0.02	0.03

12.4 Immediate deformation

To determine the immediate deformation of the seabed under the loading of the berm, the undrained behaviour of the clay layer is implemented in the geotechnical finite element program PLAXIS. The same stratification as described in paragraph 8.2 has been used. The created fine mesh is shown in Figure 12.2a. A detailed overview of the implemented layer properties and calculated deformation is shown in Appendix 15.24 and 15.25.

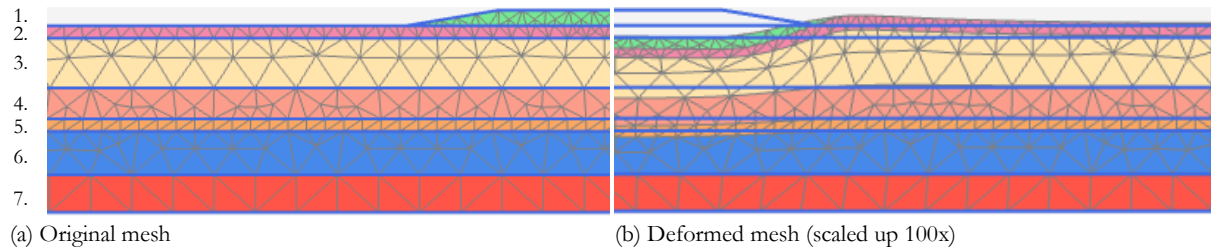


Figure 12.2: Plaxis meshes

For this calculation the Mohr-Coulomb material model is used. The layers 1 and 6 consist of a granular material with a substantial larger permeability than the other clay layers, therefore these layers are considered as drained. The remaining layers are modelled using the undrained C drainage type. This drainage type enables undrained effective stress simulations using a total stress analysis with all parameters specified as undrained (PLAXIS, 2012). For these layers the Poisson's ratio (ν) is set to be 0.495 in order to model immediate undrained behaviour without volumetric change. This model type requires the implementation of the undrained elasticity modulus (E_u) for all layers. This parameter has been derived from the secant modulus gained from consolidated undrained triaxial test performed on samples taken from the project location. The range of elasticity moduli is shown in Table 12.6.

Table 12.6: Range of stiffness input parameters

Material			Elevation [m]			E_u [kPa]		
						min	BE	Max
1	Rock	Drained	0.0	-	2.65	80000	80000	80000
2	Clay_Top	Undrained	0.0	-	-2.0	1600	1000	900
3	Clay_Middle	Undrained	-2.0	-	-10.0	4300	2750	1200
4	Clay_Low	Undrained	-10.0	-	-15.0	9100	8350	7600
5	Stiff_Clay	Undrained	-15.0	-	-17.0	19000	12300	7400
6	Sandy_clay	Drained	-17.0	-	-24.0	14200	14200	14200
7	Very_Stiff_Clay	Undrained	-24.0	-	-30.0	27200	20400	10300

Based on these values the immediate deformations presented in Table 12.7 have been found for different project locations. Obviously the elevation of the rock berm is altered to the installed height at the corresponding location. This table indicated the largest vertical deformation which occurs in the middle of the berm.

Table 12.7: Height deficit due to immediate deformation in m

Item	Location	Min	BE	Max
FPSO	Wet storage	0.01	0.01	0.01
PT	Wet storage	0.01	0.01	0.01
WI	Wet storage	0.01	0.01	0.02
PT	Towhead	0.02	0.03	0.05
FPSO	Towhead	0.03	0.04	0.07

Since these results are smaller than expected from previous research (De Vries, et al., 2007), additional PLAXIS calculations are performed to assess the robustness and reliability of this modelled result. Not only the layer stiffness is changed, other drainage types, material models and grid refinements have also been used to confirm the correct order of magnitude of the immediate deformations.

Besides the Mohr Coulomb model the Hardening Soil model has been used to model the immediate deformations. In contrast to the more simplified Mohr-Coulomb model, this material model also accounts for stress-dependency of stiffness moduli. In other words, it incorporates the increase of stiffness for an increase in pressure. Based on the consolidated undrained triaxial test the secant stiffness moduli (E_{50}) as shown in Table 12.8 were determined. Using equation (12.1) the oedometric stiffness can be determined based on the secant stiffness. Here the Poisson's ratio is assumed to be 0.3, which is suitable for clayey soils. In all soil layers the triaxial tests are performed with a cell pressure of 400 kPa. This pressure is the reference pressure at which the stiffness is defined.

$$E_{oed} = \frac{(1 - \nu)E}{(1 + \nu)(1 - 2\nu)} \quad (12.1)$$

The best estimate results of these different material models are shown in Table 12.9. As can be derived from these results, the immediate deformation remains the same order of magnitude for different drainage and material models.

Table 12.8: Hardening Soil input stiffness parameters

Material	E_{50} [kPa]	E_{oed} [kPa]	p_{Ref} [kPa]
1 Rock	80000	-	-
2 Clay_Top	1000	1300	400
3 Clay_Middle	2750	3700	400
4 Clay_Low	8350	11200	400
5 Stiff_Clay	12300	16600	400
6 Sandy_clay	14200	-	-
7 Very_Stiff_Clay	20400	27500	400

Table 12.9: Best estimate immediate deformations for different material models in m

Item	Location	MC	HS
FPSO	Wet storage	0.01	0.00
PT	Wet storage	0.01	0.00
WI	Wet storage	0.01	0.01
PT	Towhead	0.03	0.02
FPSO	Towhead	0.04	0.03

Note: MC = Mohr-Coulomb HS = Hardening Soil

Since all results indicate the same degree of immediate deformations even when important parameters such as stiffness moduli are varied, the model seems robust and is presumed to provide the correct magnitude of this process. Obviously a difference with reality is always present, but since real behaviour is almost impossible to measure, these models provide the best indication of the immediate deformation. The process itself can be modelled reliably and forms an important contributor to the total height deficit.



Figure 12.3: Total displacements in y-direction, showing squeezing mechanism ($y_{max} = 0.02$ m, $y_{min} = -0.04$ m)

Since no volume change can occur during undrained deformation, the material pushed away by the weight of the berm will cause a squeezing effect as described in paragraph 4.3.3. The forming of clay bulges alongside the rock berms is also observed in the models results as can be seen in Figure 12.2b and Figure 12.3. The latter shows the deformation in vertical direction directly underneath the berm. As can be seen the seabed rises directly alongside the rock berm. This rise of the seabed can distort the reference measurements done to determine deformation in between two installation runs by the vessel. That is why

the surveys have to be extended at least 15 m outside the perimeter of the berm. At this distance from the berm the rise of the surface is still about 0.01 m which is small, but has to be accounted for.

12.5 Consolidation

Using Deltares' software package D-Settlement the settlement due to consolidation of the soft clay layers can be assessed. For this calculation the project duration and installed berm height per day are important. The latter controls the amount of pressure on top of the soft layers. Table 12.10 shows the amounts of time spend on the berm per location including the height of material dumped during that day. Some days indicate that no material is dumped; during these days the vessel sailed back to the harbour to refill its cargo with a new batch of rock material. Consolidation can proceed during this time.

Table 12.10: Daily progress per location

Item	Location	Total height [m]	Dump duration [day]	Dump height per day [m]						Consolidation after [day]
				1	2	3	4	5	6	
FPSO	Wet storage	0.50	1	0.50						2
PT	Wet storage	0.55	2	0.35	0.20					3
WI	Wet storage	0.60	1	0.60						2
PT	Towhead	2.00	5	0.35	0.50	0.00	0.65	0.50		6
FPSO	Towhead	2.65	6	1.00	0.70	0.00	0.30	0.50	0.15	7

D-Settlement allows for the use of different calculations models. For this project the NEN-Bjerum method is used in combination with the Darcy flow model. The Bjerum model uses isotache formulation to determine the compression based on linear strain soil parameters, i.e. the compression (C_c), reloading/swelling (C_r) and secondary compression index (C_α). The first two parameters can easily be determined from common oedometer test and are provided in the SI report as indicated in Table 12.11. The latter is determined using a correlation by Mesri (1973) between the moisture content of the soil layer and its coefficient of secondary compression. The SI report presents the compression indexes as fixed values. In reality however these values can fluctuate severely and hence influence the outcome of the calculations. Unfortunately the spread of these parameters is not known.

Darcy's storage equation is used to determine the influence of excess pore pressures on settlements of combined soil layers. The Darcy method calculates the excess pore pressure distributions at different times and derives the deformation during consolidation from the development of the true effective stress. The Darcy model is the preferred consolidation model (Deltares, 2012). The implemented parameter to determine the settlement over time is the vertical consolidation coefficient (c_v). This parameter is determined from permeability test performed in the lab, its variation is shown in Table 12.11.

Table 12.11: D-Settlement input parameters

Material	γ_{sat}	Min	c_v [m ² /s]			C_c	C_r	C_α	e_0	OCR
	[kN/m ³]		BE	Max		[-]	[-]	[-]	[-]	[-]
Clay_Top	14.7	6.66E-08	8.15E-08	1.74E-07		0.66	0.02	0.009	2.12	1.10
Clay_Middle	16.4	6.66E-08	8.15E-08	1.74E-07		0.66	0.02	0.006	1.56	1.10
Clay_Low	20.3	3.17E-08	7.71E-08	1.35E-07		0.17	0.01	0.002	0.58	1.45
Stiff_Clay	20.5	4.12E-08	6.22E-08	6.98E-08		0.17	0.01	0.002	0.77	1.60
Sandy_clay	20.5	-	-	-		-	-	-	0.53	1.00
Very_Stiff_Clay	20.7	5.37E-07	5.37E-07	5.37E-07		0.15	0.01	0.002	0.57	2.25

Note I: the sandy clay layer is presumed to be fully drained

Based on these parameters, the described loading steps and project duration, a prediction is made for the consolidation. This is shown for the largest berm in Figure 12.4 and Appendix 15.26. Figure a displays the effective stress on the top layer of the seabed. Notice that the effective stress already starts around 10 kPa, this is caused by the installation of 1.0 m of rock berm on the first day and hence the effective load on the seabed is equal to the submerged weight of the rocks. Based on the density tests provided this load equals 9.7 kN/m³. Figure b indicates the full development of settlement over time. Based on this model the final settlement is estimated to be almost 1.20 m after 30 years' time. This large settlement is no problem for the effectiveness of the berm as long as the settlement is uniformly distributed.

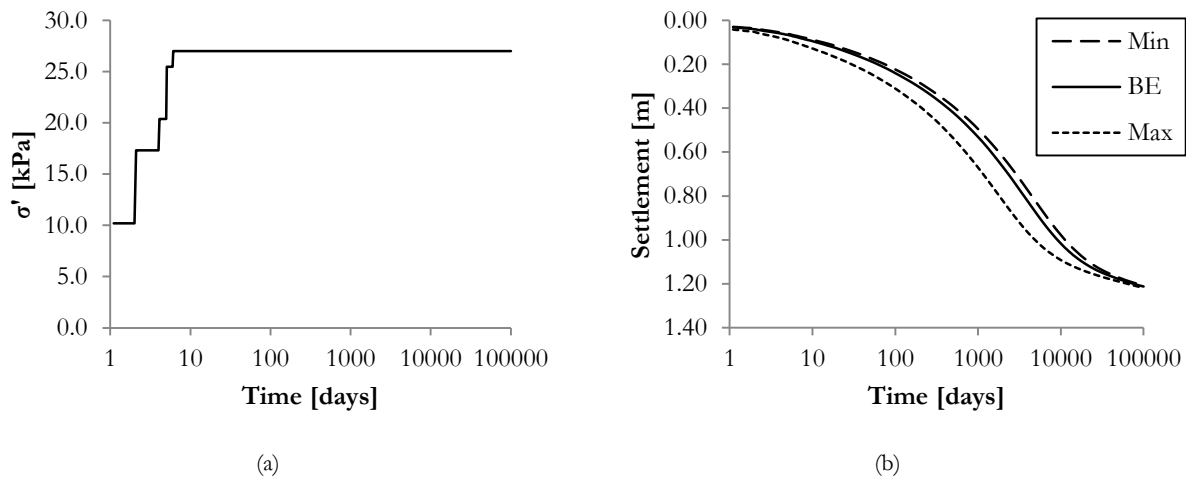


Figure 12.4: Consolidation for the FPSO towhead location

What is more important however is the consolidation settlement during and directly after installation. This development is shown in Figure 12.5. Again three lines represent the minimal, maximal and best estimate for the described process. Figure a shows the incremental settlement between days two and five of the dumping process. Here the settlement after two days is set as the origin of this graph. The two field measurements are added in this figure indicated by crosses. As described these measurements are done by comparing the intermediate survey performed directly after dumping with an additional survey performed right before installing a new batch of rocks. During this time, at which the vessel got resupplied with new rock material, consolidation could continue as shown in figure b. The two measurements are used to validate the chosen parameters and modelling type. Since the measurements are situated between the best estimate and the maximal consolidation settlement some confidence in this model is created. More measurements during a later stage of the project would further increase this thrust. Unfortunately this was not possible. This is why only one comparison could be performed.

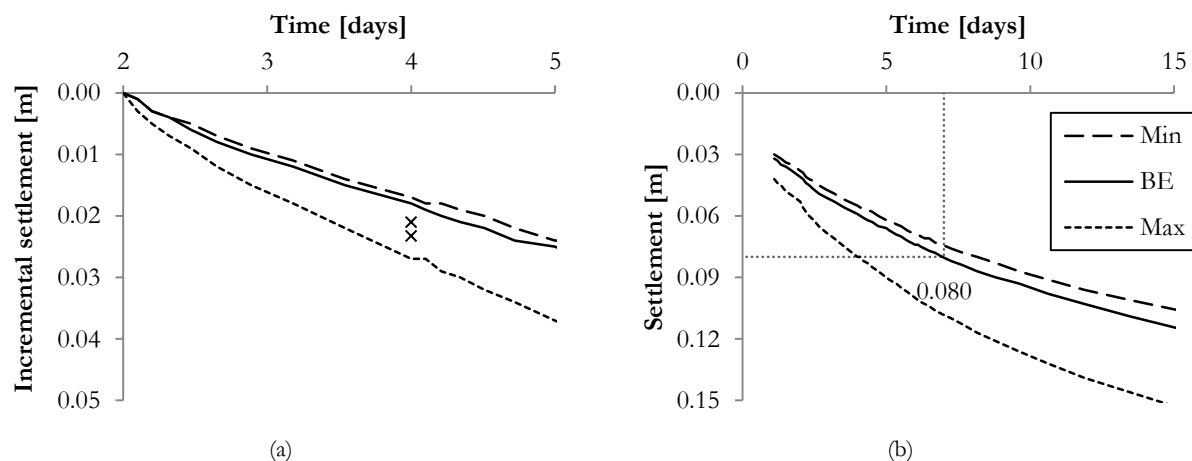


Figure 12.5: Short term consolidation for the FPSO towhead location

Based on this model the settlement due to consolidation can be derived for different locations, as shown in Table 12.12. The numbers presented are thought to be reliable, since the method is commonly used, validated in numerous other projects and the field measurements agree with the obtained modelled values.

Table 12.12: Consolidation results for different location in m

Item	Location	min	BE	max
FPSO	Wet storage	0.03	0.03	0.05
PT	Wet storage	0.04	0.04	0.05
WI	Wet storage	0.03	0.04	0.05
PT	Towhead	0.06	0.07	0.09
FPSO	Towhead	0.07	0.08	0.11

12.6 Material flow into pores

As described in paragraph 4.3.5 the material flow of cohesive material into the pores of the rock fill can be determined using equation (4.34):

$$\delta = n \cdot \left(\frac{p}{\alpha \cdot c_{u,r} \cdot \sqrt{\frac{n}{\kappa}}} \right)$$

Based on data provided by the quarry and the soil investigation Table 12.13 shows the set of parameters implemented to solve in this equation. Here the remoulded undrained shear strength is used. These values are derived by dividing the best estimate undrained shear strength value by the sensitivity of the very soft upper clay layer. The intrinsic permeability of the rock fill is determined using the Kozeny-Carman permeability equation (Verruijt, 2005). Factor α is based on previous estimations done by Deltares for similar project along the Norwegian coast (Bijnagte & Luger, 2005). Based on these parameters the values presented in Table 12.14 of are found as additional penetration per locations of the project.

Table 12.13: Parameters used for material flow through pores

	Min	BE	Max	
D_{50}	45.1	49.0	49.0	[mm]
n	0.40	0.40	0.43	[-]
p	8.50	9.70	9.70	[kN/m]
$c_{u,r}$	2.30	1.50	1.00	[kPa]
κ	1.8E-06	2.9E-06	3.9E-06	[m ²]
α	0.90	0.75	0.60	[-]

Note: the sensitivity of the very soft upper clay layer ranges between 1.3 and 3.0

Table 12.14: Additional penetration due to material flow through pores in m

Item	Location	Min.	BE	Max.
FPSO	Wet storage	0.00	0.00	0.01
PT	Wet storage	0.00	0.01	0.01
WI	Wet storage	0.00	0.01	0.01
PT	Towhead	0.01	0.02	0.04
FPSO	Towhead	0.01	0.02	0.06

Based on these small values the process proves to be minor. However the model as presented in Appendix 15.11 is not validated for such an application. Therefore additional experimental research in the applicability of this formula is recommended.

12.7 Results

Figure 12.6 indicates the relative influence of all previous described processes for different berm locations. These values reflect the calculated best estimate results. The sum of all processes is set to be 100%. As will later be described, a difference remains between the calculated volume loss and the measured volume loss. However based on the average calculated results (indicated by the black line), one can conclude that consolidation still plays an important role even though the project duration is relatively short. Moreover combined stone penetration – both single and multi stone – proves to form almost half of the calculated volume loss. Yet the flow of material into the pores of the rock fill seems to have a small effect on the complete loss of material during installation. This is also counts for the loss of fine material.

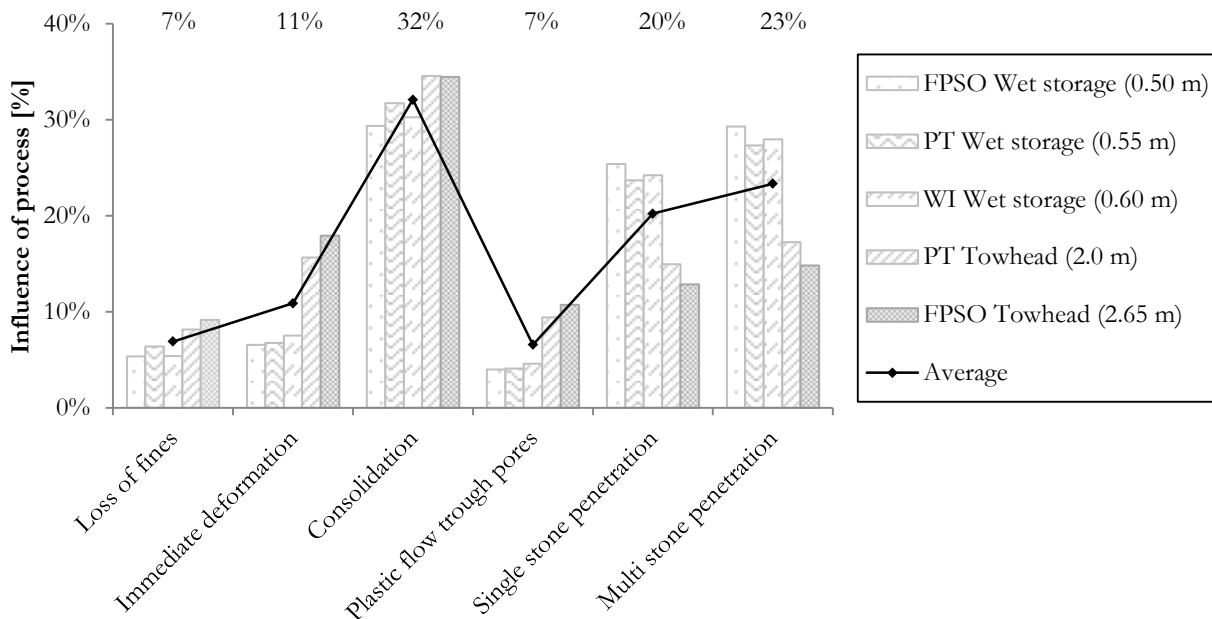


Figure 12.6: Relative influence of described processes for different locations

In Figure 12.7 on the next page, the absolute influence of all separated processes is indicated for the FPSO towhead location. At this location the largest berm is installed and the largest height deficit is observed. This figure shows the minimum, maximum and best estimate results for the different processes. The width of the bar indicates the uncertainty of the results. This uncertainty can be the result of a large possible spread in the input parameters, as well as a low confidence in the methods used for calculating or modelling.

Striking in Figure 12.7 is difference in uncertainty between the measured height deficit and the calculated processes. The uncertainty in this measured result – obtained from the fieldwork – is to a large extent caused by the determination of the in-situ density and the applied survey method. The spread in bulk density and the assumption that the cargo density is equal to the in-situ berm density (as presented in Figure 10.1), remain uncertain and will have to be investigated further. Moreover the fact that the location of the seabed is unclear and hence the properties of the first decimetres might be unknown, cause for an additional uncertainty. If the uncertainty of the field measurements is compared with the uncertainty of the calculated processes, the error margin of the measurements is on average almost 7 times higher. This indicates that the measurement precision in field is governing. Moreover it clearly shows the importance of a correct determination of the in-situ bulk density.

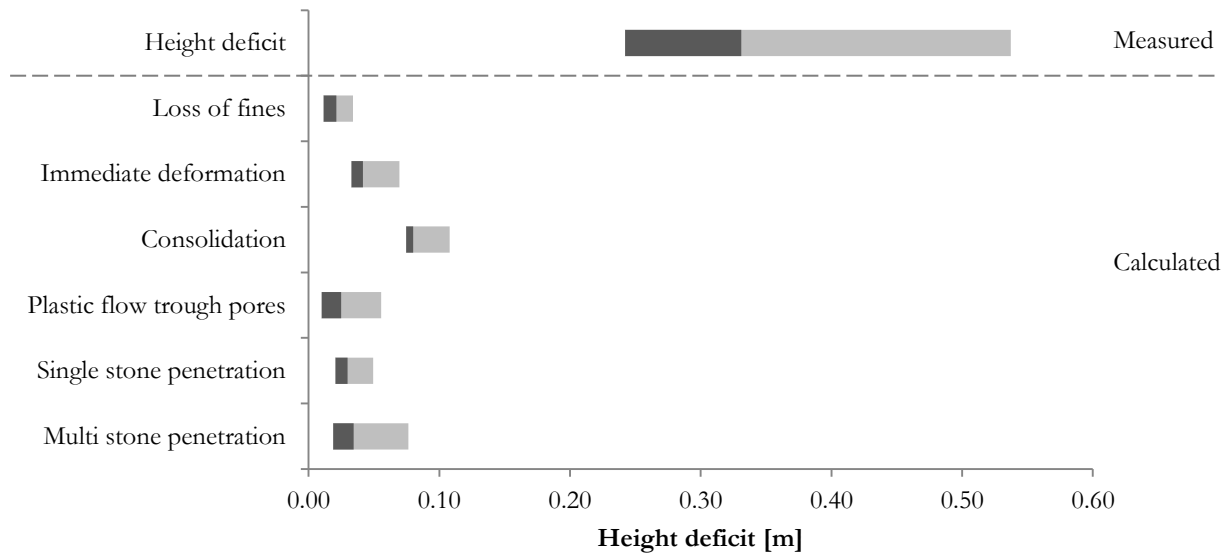


Figure 12.7: Influence of different processes on the total loss of material for the FPSO towhead location (2.65 m)

Note: the calculated best estimate result is located on the transition between the two bars.

The calculated results are a lot smaller and their uncertainty is equally small, in absolute terms. The multi stone penetration shows the largest spread which indicates that this process is still the most uncertain. Similarly the single stone penetration also shows a spread in the results. However this is not due to the fact that the model is unreliable, after all, the experiments indicate that the model is accurate. In this case the determination of the soil parameters and the uncertainty in obtaining these values is the cause of the large uncertainty. A detailed overview of the influence per process per location both relative and absolute is provided in Appendix 15.27. In these tables a similar comparison is made between the measured and calculated results. Again the sum of the calculated results is set to be 100%.

Figure 12.8 shows the measured versus the calculated results including their uncertainty for all different locations. The error bars indicate the possible spread of the result; the markers indicate the best estimate. The graph displays the absolute values. From this graph it can be derived that if the berm size increases, the uncertainty and difference between the measured and modelled values increase. This is caused by the increase in installed volume of material, hence the bulk density assumption becomes more important. Moreover some processes are height dependent, such as consolidation and immediate deformation, for these processes the uncertainty increases with an increasing berm height. Whereas the other processes, such as single stone penetration, show the same uncertainty independent from the berm height. However even though the total volume loss determination is dependent on a large amount of assumptions, all with their own influence on the reliability of the result, an overlap between the calculated and measured volume loss is found. This would presume that all processes influencing the volume loss during subsea rock installation have been incorporated.

From the graph it can also be derived that the calculated best estimates (indicated by the diamonds) underestimate the height deficit for high berms, while overestimating the loss for small berms. This can be caused by the following reasons. Either the height independent processes are too large and/or the height dependent effects are modelled too small. Since the effect of the multi stone penetration is still largely uncertain, the underestimation of this height independent process can be rather large, even though a conservative upper boundary is used for this determination. More research is necessary to confirm the accuracy of this effect.

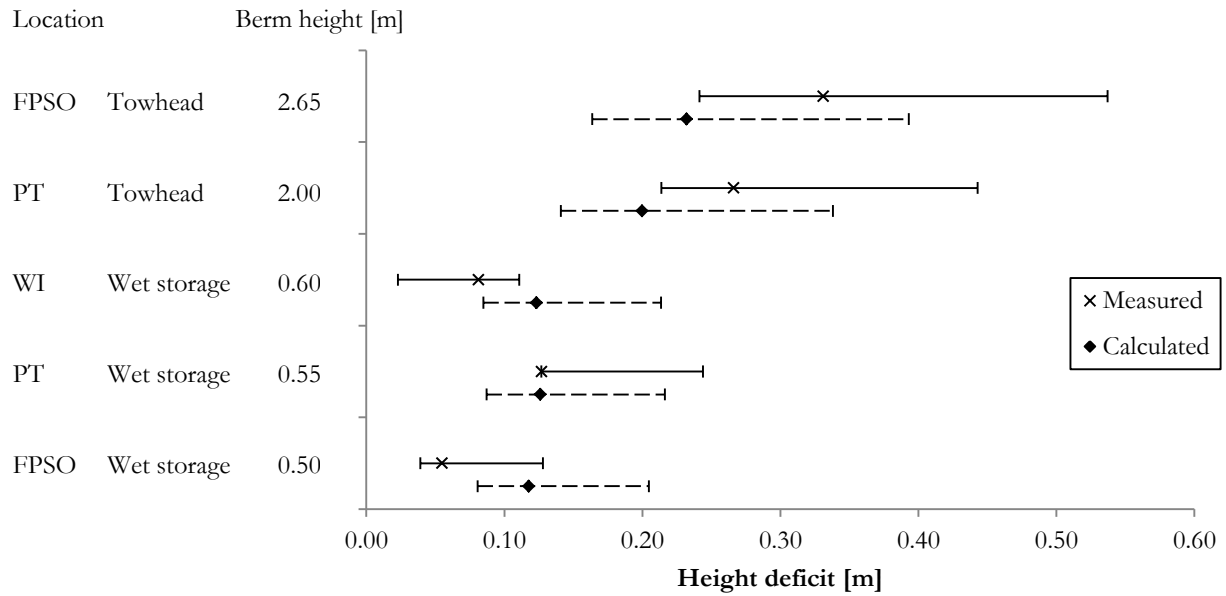


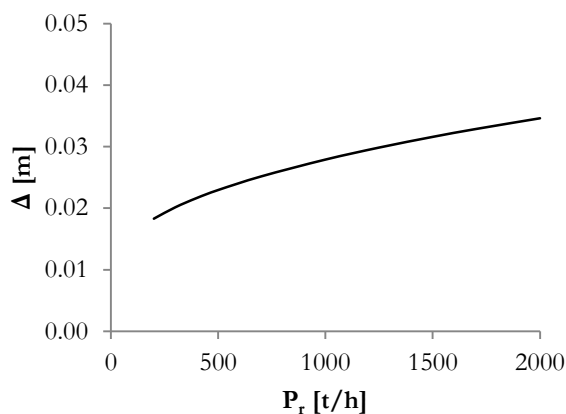
Figure 12.8: Measured versus calculated volume loss for different location of the Knarr Surf project

The berm installed at production template on wet storage location shows a remarkable result. Here the measured result equals the minimum height deficit, i.e. the error bar only extends towards a larger height deficit. This is the result of the bulk density of 1600 kg/m^3 which equals the maximum possible bulk density based on historical research. A high in-situ density causes the installed rock volume to decrease (when the weight of installed rock remains constant). Due to the smaller installed volume, the difference between the measured and installed volume reduces, in turn resulting in a smaller height deficit. This might be the case in reality or be a distortion of the results.

Intermezzo - Operational costs

As described in the problem description, accurate knowledge of the amount of material required to complete a rock fill according to its original design is needed to ensure proper project management and cost estimation. This paragraph forms a short side step indicating the relative influence of particle penetration on the complete project. For this paragraph a fictional project is used with soil conditions similar to the Knarr Surf location.

Figure 12.9 shows the relation between production rate and single stone penetration, based on the created model. This figure shows that a higher production rate causes a larger penetration depth. This is the result of a higher impact velocity. Due to the larger production rate the mixture density of water and rocks rises which increases the fall velocity and hence the impact velocity. This in turn results in a larger penetration depth. Not only single stone but also multi stone impact increases. Based on this relation one can conclude that to minimize penetration losses the production speeds will have to remain as low as possible.



$$D_{50} = 0.049 \text{ m}, c_u = 3.0 \text{ kPa}, \rho_s = 2680 \text{ kg/m}^3, \rho_{ws} = 1500 \text{ kg/m}^3$$

Figure 12.9: Influence of production rate on single stone penetration

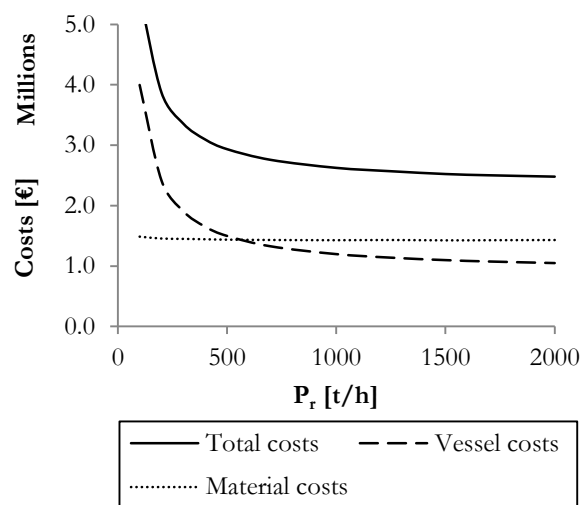


Figure 12.10: Influence of production rate on project costs

In reality however project duration is more important than material usage. With a vessel expense of almost € 150.000,- per day and an installed material price of about € 30,- per ton, the breakeven point of this relation is always limited by the duration of the project. This is also presented in Figure 12.10 here one can see that the total costs go down rapidly when the production rate increases and the project duration drops. However if penetration is unexpected and proves to be large, the vessel might need to sail back to the quarry and refill its cargo. This possible additional tour results in a longer project duration and consequently significantly increases operational costs.

In this simple example consolidation has been taken into account, i.e. if project duration increases so will the settlement due to consolidation. Multi stone influence has not been taken into account and neither has the growth of possible operational volume loss due to the increase in production rate (seabed erosion, particles dropped outside the designed perimeter). However the example does clearly indicate that based on costs it is better to maximize production, rather than minimising volume loss.

Part IV – Conclusions

13 Conclusions

The main objective of this thesis is to get more insight in the governing processes which influence the rock volume loss during subsea rock installation (Ch. 1). The total volume of rock used during installation can be determined by summing the geometrical volume, the operational losses and the displacements of the seabed. Specific attention is given to the impact of immediate particle penetration. Accurate knowledge of the volume loss during installation is needed to ensure proper project management and cost estimation. The following processes prove to be important with regard to the volume loss during subsea rock installation:

- Immediate deformation of the seabed
- Loss of fine particles due to deep sea currents
- Immediate particle penetration in the seabed
- Flow of cohesive material in to the pores of the rock fill
- Long term settling of the berm due to consolidation
- Possible erosion of the seabed
- Stones deposited outside the theoretical perimeter of the construction

Using different existing modelling techniques the influence of the described processes is obtained. Complemented with the developed and validated single stone penetration model, the total rock volume loss is determined. This calculated volume loss excludes possible influences of seabed erosion and material deposited outside the perimeter of the construction. The sum of this volume loss calculation is set to be 100% and is compared with loss measured during field work in the northern part of the North Sea on board of Van Oord's FFPV Stornes. The obtained measurements are used to verify the magnitude and extent of the calculated results (Ch. 12). However the large amount of assumptions and used acoustic measurement technique influences the reliability of the field measurements.

Based on the calculated process influence, it can be concluded that seabed deformation due to consolidation forms the largest factor of volume loss. This is a surprising result since the project duration is only limited and hence this effect was presumed to be small. However on average the influence of this process forms almost one third of the height deficit, based on best estimate properties of both the installed material and the seabed. With one fifth of the calculated volume loss, single stone penetration forms another important factor. However with an average magnitude of 0.03 m this process is smaller than initially expected. Multi stone penetration causes the particles to penetrate even deeper into the soft soil. In this thesis only the upper and lower boundaries of this effect are indicated. Even though the spread between both limits is large, the multi stone process causes a significant increase in volume loss. With an average effect of 23% of the total loss this is even larger than the single stone effect. Combined these immediate particle penetration processes form almost half of the calculated volume loss. The exact extent of this additional penetration requires additional research (Ch. 14).

The overlap between the measured and calculated processes suggests that the current approach does take all the right processes into account. However to be able to predict the volume loss, the accuracy of each process will have to be optimised. So far no unambiguous volume loss estimation can be obtained. The large amount of assumptions combined with the uncertainty and inability to accurately measure occurring processes and properties, make the determination of the volume loss an uncertain procedure. By assessing this uncertainty and indicating the range of possible solutions it can be concluded that the field measurements require the most attention. The measurement accuracy of the survey system and the relative location of the seabed will have to be optimised. Currently the measurement accuracy of the survey systems installed on the ROV proves to lack the required accuracy to be able to conclude the exact

magnitude of different processes. The MBES system provides measurements with an accuracy of 0.03 to 0.05 m (Ch. 9). This is the same order of magnitude as the immediate single stone penetration of installed rock particles in soft clay. Furthermore some assumptions made during the back calculation will have to be verified. Especially the assumption that the in-situ density of the installed material equals the bulk density could have a large impact on the volume loss determination (Ch. 10). More about this optimisation can be found in the next chapter, recommendations.

For the single stone model, which has been the main focus of this thesis, the existing model based on Brinch Hansen's theory seems to be applicable to properly estimate single stone penetration (Ch. 4). Based on experimental research (Ch. 6) performed this model is slightly altered. With an average deviation 9.7% the adjusted model shows a good fit with the experimental results (Ch. 11). This reflects that the static bearing capacity equation can very well be used to determine the extent of the highly dynamic stone penetration (Ch.7). As expected impact velocity, particle size and undrained shear strength of the clay prove to be governing in the determination of the single stone penetration. The impact velocity of the particle onto the seabed can best be determined using the impinging jet theory. The direct undrained shear stress determination remains difficult, since the offshore soil investigation in low stress conditions provides properties with limited reliability (Ch. 8). Moreover if the top layer of the seabed is very soft, it is possible that this layer is not characterised at all. Certain simplifying assumptions are made which will have their influence on the modelled result; however this influence is regarded small.

14 Recommendations

This thesis has indicated the influence of different processes on the volume loss during subsea rock installation projects. Special attention has been given to the single stone penetration effects, since these were believed to be the largest. During this research however a lot of simplifications and assumptions have been made, which allow for improvement of the results in future studies. This chapter is subdivided into three paragraphs. First future research subjects are described which can contribute to a higher level of confidence in the results and extend the application of the model. This is followed by a few recommendations to optimise data gathering. These optimizations will increase the accuracy of the modelled results. Lastly a measurement plan is added, in order to develop a database with case studies, containing the volume losses for different projects. This approach will help to develop a uniform database with comparable quantities for a variety of project characteristics and subsoils. If measurements are performed in the same uniform way, also for projects on very hard soils, over time this can increase the reliability of the current method.

14.1 Future research

In this thesis not all questions and uncertainties have been solved. In fact after finishing the thesis the problem itself proves to be even more complicated than expected at first and more questions remain unanswered. The following subjects are thought to be relevant for future research and can help to create part of the solution.

- *Perform experimental tests on sandy soils*

Using an impulse balance between the impacting and resisting force the particle penetration is modelled and later validated using experimental tests. However this validation is only performed for clay. In these conditions the model proves to be able to predict single stone penetration. However for sandy soils this might not be the case. Various other processes will influence the penetration in this soil type. By performing experimental tests on sandy soils and incorporating the results of these test into the model the effectiveness can be expanded.

- *In-situ density determination*

In this thesis the important assumption is made that the bulk density of the rock material equals the installed in-situ density on the seabed. However the particles might be packed in a denser state due to the increase in kinetic energy during the descent through the fallpipe. The addition of energy during on-going particle impact might compact the berm and increase the in-situ density of the material. On the other hand, the fines might wash out of the installed aggregate, creating a more uniform grain distribution. Consequently the pores of the rock fill will not be filled with small particles resulting in a lower in-situ density. The relative influence of both these processes can be determined using (full) scale tests in Van Oord's testing facility in Moerdijk.

- *Impact velocity testing in practice and modelling seabed erosion*

Velocity of a particle proves to be very important when installing rock on the seabed, not only for penetration of the particle but also for possible erosion due to jet effects, yet little is known about this (impact) velocity in practice. By equipping the ROV with two sets of magnetic sensors and dropping steel warped particles into the fallpipe, the exit velocity of the water-rock mixture can be determined in reality. Creating a hydrodynamic impinging jet model based on this exit velocity enables the verification of the presumed impact velocity. Moreover possible seabed erosion can also be modelled in this way. During the creation of this hydrodynamic model one should not forget the presence of the splitter, located at the end of the fallpipe.

As described the sludge layer forming the top of the seabed can sometimes be as thick as 0.5 m in certain deep sea environments. Identifying the location and the extent of this extremely soft layer, and modelling the surface erosion caused by SRI, forms a valuable extension of the results presented in this thesis.

- *Determine the influence of multiple stones dropping on top of each other*

This study provides an upper and lower boundary for the multi stone penetration effects. Using experimental research more information can be gathered about the real influence of multiple stone dropping on top of each other. The effect of soil strength increase during penetration, corresponding surcharge influence and diversion of energy over multiple stones might be modelled and validated. The influence of this effect during dumping is expected to be large. Test performed using groups of particles and their influence on penetration can further improve the model.

- *Determine flow of clay into rock skeleton experimentally*

Despite the fact that the material flow into the pores of the rock fill only forms as a small part of the complete volume loss, additional research into this subject is recommended. The formulae that are currently used for this derivation have not been validated for clay and different processes might change the magnitude of this process in reality. A setup where a bonded rock fill is pushed into soft clay while measuring the required force, can be used to experimentally determine and describe the relevant processes to model this plastic flow into pores.

14.2 Data gathering

By optimising data acquisition for future SRI projects, the measured volume deficit and stone penetration can be obtained more accurately. The following recommendation can help in this process:

- *Use full flow penetrometers to accurately determine the properties of the top layers of the seabed.*

Classical site investigation by means of CPT is insufficient for low stress soil conditions. The current method of offshore soil investigation using alternating CPTs, vane tests and taking samples is not suited to accurately determine low stress seabed properties. Yet precisely these shallow depth properties are relevant for stone penetration. Cone penetration tests up to a depth of 30 m now provide information about the soft top layer, while the obtained values lie within the measurement range of the system and hence lack reliability. Full flow penetrometers such as the ball cone and T-bar would be more suitable in these low stress conditions, since they provide higher sensitivity in soft deposits. If possible this type of SI should be added to the existing approach, this way both the properties of the soft seabed as the deeper layers are obtained as accurate as possible.

Additionally when performing laboratory test on low stress samples, boundary friction has a huge influence on the results. Furthermore these samples are often highly disturbed and hence can provide distorted soil properties. Therefore one should be careful when using the results of laboratory test performed on samples taken from shallow depths.

- *Combine low frequency measurements with high frequency multi beam echo sound survey data*

The accuracy of the bathymetric measurements is very important in this study. The MBES system provides a large number of measurements capable of indicating the position and shape of the virgin bathymetry with an accuracy that is satisfactory for its offshore purposes. However for this thesis the reflections of the top of the soft seabed alone are not sufficient. By attaching a low frequency single beam echo sounder to the survey arm of the ROV the survey data can be improved, providing valuable new data.

In a dual frequency system, both frequencies reflect on material of a different density. If the reflection density of both frequencies is known, a profile of the density of the depth can be created. Since the density increases with the strength of the material, with the right adjustments the extent of the soft sludge layer floating on top of the seabed can be determined. Moreover the influence of the strength increase on the stone penetration can be modelled. In deep conditions with almost no horizontal current the thickness of this soft layer can be large (0.5 m), significantly increasing volume loss during installation due to erosion and particle penetration.

– *Increase focus on bulk density determination*

As accurately described in chapter 10 the influence of the bulk density is large when assuming the bulk density resembles the in-situ density after installation. Therefore the determination of the bulk density becomes important. Currently the bulk density determination is often done by the quarry itself and varies per quarry. It is therefore advised to standardise the test according to the in Appendix 15.20 described testing procedure for all quarries. Strict monitoring of the frequency and execution of this procedure by an independent third party is advised. Examples of results of density tests performed by the two quarries investigated in this thesis (Jelsa and Sløvåg) have been added in Appendix 15.28.

14.3 Future data gathering

1. Obtain the soil investigation data.
 - Determine soil type and when relevant the undrained shear strength.
 - Bear in mind that the undrained shear strength determination based on CPT tests in shallow depth low stress conditions is based on an inaccurate relation.
2. For each batch of installed rock particles determine its properties (particle grading/material type/bulk density).
 - Make sure the data provided corresponds to the material installed.
 - Record the method used to determine the bulk density.
3. Obtain the initial bathymetry from pre survey.
 - If possible the survey should extend at least 15 m beyond the perimeter of construction. This way a suitable undisturbed reference plane can be used to compare the surveys with each other.
4. Determine the amount of tons installed during installation. Accurately record date, time and location of the installation in order to later compare the results correctly.
 - Use the revised tonnage (after the correction factor of the Ramsey has been applied).
Note: Ramsey is the weighing machine installed in the conveyor belt of the FFPVs
5. Determine the volume installed by dividing the measured tonnage by the provided bulk density.
 - If multiple batches of rock are used on one location, keep track of the amount of rock installed per batch and divide by the corresponding bulk density.
6. Obtain the bathymetry after installation using the post survey. Accurately record date, time and location of survey to be able to compare the results with the corresponding installation.
 - Make sure the (intermediate) surveys are all conducted in the same way as the pre survey.

7. Use VOSS.net to determine volume between post and the pre survey.
 - Preferably use surface models instead of point clouds for this volume determination
 - Make sure the polygon forming border of the volume calculation follows the perimeter of the designed rock berm and that this boundary remains constant throughout the project.
8. Difference between installed and surveyed volumes is caused by loss of material and measurement inaccuracies.
 - Total loss consist of:
 - Possible seabed erosion
 - Immediate penetration of stones into the seabed
 - Immediate (undrained) seabed deformation
 - Consolidation
 - Flow of cohesive material in to the pores of the rock fill
 - Washout of fines
 - Operational losses associated with stone deposited outside the perimeter of the construction
 - Inaccuracy of in-situ density
 - Inaccuracy of survey data
 - Assuming the losses due to the last bullet points (indicated in [Blue](#)) proportionally remain the same during further installation, the immediate losses can be isolated and determined accurately.
9. It is possible to repeat step 3 to 7 between each intermediate installation and survey to obtain more data and reference material to calculate installation losses due to penetration.
 - The immediate penetration during the first installation is likely to be the biggest, since the soil will become stronger during installation of subsequent layers of rock.
 - With more reference material the average in-situ density and losses can be determined more accurately.

Part V – Appendices

15 Appendices

15.1 Bibliography

- Albertson, M., Dai, Y., Jensen, R. & Rouse, H., 1948. Diffusion of submerged jets. *Transactions of the American Society of Civil Engineers*, Volume 2409, pp. 639-664.
- Andersen, K. H. & Jostad, H. P., 2002. *Shear Strength Along Outside Wall of Suction Anchors in Clay after Installation*. Kyushu, International Society of Offshore and Polar Engineers.
- Battjes, J., 2002. *Vloeistofmechanica*. Delft: Delft university press.
- Beltaos, S. & Rajaratnam, N., 1974. Impinging circular turbulent jets. *Journal of hydraulic division*, 100(10), pp. 1313-1328.
- Bernard, R. S., 1978. *Depth and motion prediction for earth penetrators*, Washington: U.S. Army.
- Bijnagte, J. & Luger, H., 2005. *Rock fill penetration in a soft soil seabed - Impact penetration and plastic flow through a stone skeleton*, Delft: GeoDelft.
- Bol, J., 2012. *Floating piles - An investigative study into the behaviour of friction piles installed within a settling soil profile*, Delft: Delft University Press.
- Bol, J., 2013. *Offshore geotechnical engineer* [Interview] (9 september 2013).
- Bowles, J. E., 1997. *Foundation analysis and design*. 5th ed. New York: McGraw-Hill Companies.
- Bradbury, J., 2011. <http://www.offshore.no/>. [Online] Available at: http://www.offshore.no/international/article/Bentley_set_for_2012_start [Accessed 30 July 2013].
- Brinch Hansen, J., 1970. A revised and extended formula for bearing capacity. *Geoteknisk Institut*, Volume 28, pp. 5-11.
- Brinkgreve, R., 2007. *Materiaalmodellen voor grond en gesteente*. Delft: Delft University Press.
- Burland, J., 1990. On the compressibility and shear strength of natural clays. *Geotechnique*, 40(3), pp. 329-378.
- Casagrande, A., 1932. Research on the Atterberg limits of soil. *Public Roads*, 13(3), pp. 121-130.
- Chung, S. F., Randolph, M. F. & Schneider, J. A., 2006. Effect of penetration rate on penetrometer resistance in clay. *Journal of geotechnical and geoenvironmental engineering*, Volume 132, pp. 1188-1196.
- Craig, W. H. & Sabagh, S. K., 1994. Stress-level effects in model tests on piles. *Canadian Geotechnical Journal*, 31(1), pp. 28-41.
- CUR, 1995. *The Rock Manual - The use of rock in hydraulic engineering*. Rotterdam: CUR.
- Das, B. M., 2002. *Principles of geotechnical engineering*. 5th ed. Bangalore: Eastern press.
- De Vries, G., van der Meer, J., Brennodden, H. & Wendel, S., 2007. *Ormen Lange gas field - Immediate settlement of offshore rock supports*. San Diego, Offshore Mechanics and Arctic Engineering.
- Deltares, 2012. *D-SETTLEMENT - Manual*. Delft: Deltares.

- Einav, I. & Randolph, M. F., 2004. Combining upper bound and strain path methods for evaluating penetration resistance. *International journal for numerical methods in engineering*, Volume 63, p. 1991–2016.
- Fugro Geoconsulting Ltd., 2012. *Knarr Geotechnical Site Investigation*, Leidschendam: s.n.
- Hill, R., 1950. *The mathematical theory of plasticity*. London: Oxford university press.
- Hossain, M. S. & Randolph, M. F., 2009. Effect of Strain Rate and Strain Softening on the Penetration Resistance of Spudcan Foundations on Clay. *International journal of geomechanics*, Volume 9, pp. 122-132.
- Kayabali, K. & Tufenkci, O., 2010. Shear strength of remolded soils at consistency limits. *Canadian Geotechnical Journal*, Volume 47, pp. 259-266.
- Koper, J., 2013. *Offshore surveying* [Interview] (3 September 2013).
- Kumano, A. & Goldsmith, W., 1982. *An experimental investigation of the projectile penetration into soft, porous rock under dry and liquid-filled conditions*. Berkeley, American Rock Mechanics Association.
- Lee, J., Lu, T., Sun, H. & Miao, G., 2010. A novel formula to describe the velocity profile of free jet flow. *Archive of applied mechanics*, 81(2), pp. 397-402.
- Lehane, B. M., O'Loughlin, C. D., Gaudin, C. & Randolph, M. F., 2009. Rate effects on penetrometer resistance in kaolin. *Geotechnique*, 59(1), pp. 41-52.
- Lunne, T., 2010. *The CPT in offshore soil investigations - a historic perspective*. Huntington Beach, 2nd International Symposium on Cone Penetration Testing.
- Mesri, G., 1973. Coefficient of secondary compression.. *Journal of the soil mechanics and foundations division*, 99(1), pp. 123-137.
- Meyerhof, G., 1951. The ultimate bearing capacity of foundations. *Geotechnique*, 2(4), pp. 301-331.
- Mitchell, J. K., 1976. *Fundamentals of soil behavior*. New York: Wiley.
- Nagaraj, H., Sridharan, A. & Mallikarjuna, H., 2012. Re-examination of undrained strength at Atterberg limits water contents. *Geotechnical and Geological Engineering*, Volume 30, pp. 727-736.
- Nio, S., 1991. *Holocene Marine Sedimentation in the North Sea Basin*. 1st ed. London: John Wiley & Sons.
- Palmer, A. C. & King, R. A., 2008. *Subsea Pipeline Engineering*. 2nd ed. Tulsa: PennWell Corporation.
- Peuchen, L. & Raap, C., 2007. *Logging, sampling and testing for offshore geohazards*. Houston, s.n.
- PLAXIS, 2012. *Material models manual*, Delft: Plaxis.
- Prevost, J.-H. & Hoeg, K., 1975. Analysis of Pressuremeter in Strain-Softening Soil. *Journal of the geotechnical engineering division*, 101(8), pp. 717-732.
- Quinn, T. & Brown, M., 2011. Effect of strain rate on isotropically consolidated kaolin over a wide range of strain rates in the triaxial apparatus. In: C. Chung, et al. eds. *Deformation characteristics of geomaterials*. Seoul: IOS Press, pp. 607-613.
- Rajaratnam, N., 1976. *Turbulent jets*. Amsterdam: Elsevier scientific publishing company.

- Randolph, M., Cassidy, M., Gourvenec, S. & Erbrich, C., 2005. Challenges of Offshore Geotechnical Engineering. *Proceedings of the international conference on soil mechanics and geotechnical engineering*, 16(1), pp. 123-177.
- Randolph, M. & Gourvenec, S., 2011. *Offshore geotechnical engineering*. New York: Spon Press.
- Rao, S. & Sridharan, a., 1985. Mechanism controlling the volume change behavior of kaolinite. *Clays and Clay Minerals*, 33(4), pp. 323-328.
- Ravelli, F. D. C., 2012. *Improving the efficiency of a flexible fallpipe vessel - An experimental study on the spreading of rock in an impinging plane jet*, Delft: Delft University Press.
- Richardson, J. & Zaki, W., 1997. Sedimentation and fluidisation: Part I. *Chemical Engineering Research and Design*, Volume 75, pp. 82-100.
- Rise, L., Rokoengen, K., Skinner, A. & Long, D., 1984. *Northern north sea quaternary geology map*, Trondheim: Institutt for kontinentalsokkelundersøkelser.
- Russell, A. R. & Khalili, N., 2006. On the problem of cavity expansion in unsaturated soils. *Computer Mechanics*, Volume 37, pp. 311-330.
- Scheermakers, R. & Koper, J., 2013. *Offshore surveying during subsea rock instalation* [Interview] (2 September 2013).
- Sejrup, H. P., Nagy, J. & Brigham-Grette, J., 1989. Foraminiferal stratigraphy and amino acid geochronology of Quaternary sediments in the Norwegian Channel, northern North Sea. *Norsk geologiske Tidsskrift*, 69(2), pp. 111-124.
- Sharma, B. & Bora, P. K., 2003. Plastic limit, liquid limit and undrained shear strength of soil - Reappraisal. *Journal of Geotechnical and Geoenvironmental engineering*, 129(8), pp. 774-777.
- Skempton, A. W., 1951. *The bearing capacity of clays*. London, s.n.
- SNAME, 2008. *Guidelines for Site Specific Assessment of Mobile Jack-up Units - Technical & Research Bulletin 5-5A*, New Jersey: Society of Naval Architects and Marine Engineers.
- Sridharan, A. & Rao, S., 1973. Mechanisms controlling volume change of saturated clays and the role of the effective stress concept. *Geotechnique*, Volume 23, pp. 359-382.
- Subsea 7, 2013. *Rockdump - Scope of work document*, London: Subsea 7.
- Terzaghi, K., 1943. *Theoretical soil mechanics*. New York: John Wiley & Sons.
- Van Oord ACZ, 2002. *Technical Note - Flexible Fallpipe Vessel - Calculation of equilibrium velocity in semi-closed fallpipe without using chain calculation*, Rotterdam: s.n.
- Van Oord, 2004. *Technical note - Rock Penetration*, Rotterdam: s.n.
- Van Rhee, C., 2002. *On the sedimentation process in a trailing suction hopper dredger*. Delft: Delft university press.
- Van Rijn, L., 1993. *Principles of sediment transport in rivers, estuaries and coastal seas*. 1st ed. Amsterdam: Aqua Publications.
- Verruijt, A., 2005. *Grondmechanica*. 7th ed. Delft: VSSD.
- Verruijt, A., 2006. *Offshore soil mechanics*. Delft: s.n.

- Vesić, A., 1973. Analysis of ultimate loads of shallow foundations. *Journal of soil mechanics and foundation devision*, Volume 99, pp. 45-73.
- Visser, R. & Van der Meer, J., 2008. Immediate displacement of the seabed during subsea rock installation (SRI). *Terra et Aqua*, Issue 110, pp. 3-8.
- VKBO, 2000. *Maak- en meetnaam/keurigheden bij uitvoering van baggerwerken en steenbestortingen*, Leidschendam: Vereniging van waterbouwers in Bagger-, Kust- en Oeverwerken.
- Vrijling, J., Manni, R. & Wilde, D., 1995. *Prediction of the deposition mound of dumped rubble*. Rio de Janeiro, s.n.
- Wal, J. v. d., 2002. *Het valgedrag van steengroepen - Modelonderzoek ter vergroting van het inzicht in het valgedrag van breuksteen*, Delft: Delft university press.
- Woldringh, B., 2013. *Fugro offshore survey methods* [Interview] (02 07 2013).
- Wood, 1985. Some fall-cone tests. *Geotechnique*, 35(1), pp. 64-68.
- Wroth, C. & Wood, D., 1978. The correlation of index properties with some basic engineering properties of soils. *Canadian Geotechnical Journal*, 15(2), pp. 137-145.
- Young, C., 1981. An Empirical Equation for Predicting Penetration Depth into Soft Sediments. *OCEANS 81*, pp. 674-677.
- Zhou, H. & Randolph, M. F., 2009. Resistance of full-flow penetrometers in rate-dependent and strain-softening clay. *Geotechnique*, 59(2), pp. 79-86.
- Zhou, H. & Randolph, M. F., 2011. Numerical analysis of a cylinder moving through rate-dependent undrained soil. *Ocean Engineering*, 38(7), pp. 943-953.

15.2 Nomenclature

Variables

η	Dynamic viscosity	[Ns/m ²]
ν	Kinematic viscosity	[Nms/kg]
τ	Shear stress	[N/m ²]
A	Area	[m ²]
a	Acceleration	[m/s ²]
B	Width	[m]
b_{\dots}	Base inclination factor	[-]
c	Cohesion	[N/m ²]
C	Compression index	[-]
C_D	Drag coefficient	[-]
c_m	Mixture concentration	[kg/m ³]
c_u	Undrained shear strength	[N/m ²]
c_v	Consolidation coefficient	[m ² /s]
D	Diameter	[m]
d_{\dots}	Depth factor	[-]
E_{50}	Secant stiffness	[MPa]
F	Force	[N]
g	Gravitational acceleration	[m/s ²]
g_{\dots}	Ground inclination factor	[-]
i	Hydraulic gradient	[-]
i_{\dots}	Force inclination factor	[-]
k	Permeability	[m/s]
m	Mass	[kg]
n	Porosity	[-]
N	Bearing capacity factor	[-]
p	Pressure	[N/m ²]
Pr	Production rate	[kg/s]
q	Discharge	[m/s]
\bar{q}	Effective surcharge	[N]
R	Radius	[m]
S	Shear rate	[s ⁻¹]
s_{\dots}	Shape factor	[-]
St	Sensitivity	[-]
t	Time	[s]
v	Velocity	[m/s]
V	Volume	[m ³]
x, y	Location coordinates	[-]
γ	Unit weight	[N/m ³]
Δ	Penetration depth	[-]
δ	Penetration of cohesive material	[m]
ζ	Friction loss coefficient	[-]
θ	Shields parameter	[-]
ν	Poisson's ratio	[-]
ρ	Density	[kg/m ³]
σ	Stress	[N/m ²]
φ	Internal friction angle	[°]

Subscripts

<i>B</i>	Bearing
<i>b</i>	Buoyancy
<i>c</i>	Cohesion
<i>cb</i>	Characteristic
<i>D</i>	Drag
<i>eff</i>	Effective
<i>f</i>	Fluid
<i>g</i>	Gravitational
<i>imp</i>	Impact
<i>min</i>	Minimal
<i>ms</i>	Multi stone
<i>n</i>	Nominal
<i>r</i>	Resultant
<i>s</i>	Stone
<i>u</i>	Undrained
<i>w</i>	Water
<i>ws</i>	Wet soil
γ	Unit weight
<i>q</i>	Surcharge
<i>sat</i>	Saturated
<i>cross</i>	Cross-sectional
∞	Ambient
<i>m</i>	Mixture
<i>u,r</i>	Remoulded undrained
<i>0</i>	Exit
<i>50</i>	Median

Abbreviations

BP	Before present
BSF	Below sea floor
CPT	Cone penetration test
DP	Dynamic positioning
DTM	Digital terrain model
FFPV	Flexible fallpipe vessel
FPSO	Floating production, storage and offloading
HSC	High speed camera
MBES	Multi beam echo sounder
MSM	Multi stone model
PIV	Particle image velocimetry
PT	Production template
ROV	Remotely operated vehicle
SI	Soil investigation
SOD	Stand of distance
SRI	Subsea rock installation
SSM	Single stone model
WI	Water injection
ZEF	Zone of flow establishment
ZFE	Zone of established flow

15.3 List of tables

Table 6.1: Experimental program	36
Table 7.1: Undrained shear strength determination using different methods	41
Table 8.1: Soil layering and description at the production template, taken as representative for the project	51
Table 10.1: Field results indicating the total volume loss per location	60
Table 10.2: Modified field results taken into account the measurement deviation	61
Table 10.3: Spread in height deficit for different in-situ bulk densities	63
Table 10.4: Consolidation measurements in the field after two days	63
Table 11.1: Input variables for the sensitivity analysis, based on the real Norwegian circumstances	69
Table 11.2: Range of possible input variables	69
Table 12.1: Single stone penetration input parameters	71
Table 12.2: Derived single stone penetration in m	71
Table 12.3: Multi stone penetration results in m	72
Table 12.4: Parameters used to determine the loss of fines	72
Table 12.5: Additional height deficit due to loss of fine material in m	72
Table 12.6: Range of stiffness input parameters	73
Table 12.7: Height deficit due to immediate deformation in m	73
Table 12.8: Hardening Soil input stiffness parameters	74
Table 12.9: Best estimate immediate deformations for different material models in m	74
Table 12.10: Daily progress per location	75
Table 12.11: D-Settlement input parameters	75
Table 12.12: Consolidation results for different location in m	77
Table 12.13: Parameters used for material flow through pores	77
Table 12.14: Additional penetration due to material flow through pores in m	77
Table 15.1: Stornes properties	101
Table 15.2: Bearing capacity equations according to different authors	103
Table 15.3: α values for different shear strain rate functions	114
Table 15.4: Designed berm dimensions	123
Table 15.5: Soil profile with corresponding best estimate property values	127
Table 15.6: Soil profile [Continued]	127
Table 15.7: Summary of recommended spoil parameters - BH-B1 (Fugro Geoconsulting Ltd., 2012)	128
Table 15.8: Range of possible input variables	134
Table 15.9: Soil profile used for PLAXIS calculations – Mohr Coulomb	136
Table 15.10: Soil profile used for PLAXIS calculations – Hardening Soil	136
Table 15.11: Absolute influence of individual processes per location (minimum input parameters)	139
Table 15.12: Relative influence of individual processes per location (minimum input parameters)	139
Table 15.13: Absolute influence of individual processes per location (best estimate input parameters)	140
Table 15.14: Relative influence of individual processes per location (best estimate input parameters)	140
Table 15.15: Absolute influence of individual processes per location (maximum input parameters)	141
Table 15.16: Relative influence of individual processes per location (maximum input parameters)	141
Table 15.17: Results of bulk density tests for the Sløvåg quarry	142
Table 15.18: Results of bulk density tests for the Jelsa quarry	145

15.4 List of figures

Figure 1.1: Processes that affect the volume installed during the subsea rock installation	1
Figure 1.2: Boundaries of the research (Visser & Van der Meer, 2008)	3
Figure 1.3: Flowchart indicating the approach of this thesis	4
Figure 2.1: Different rock installation vessels (CUR, 1995)	6
Figure 2.2: Applications of subsea pipelines (Palmer & King, 2008)	7
Figure 2.3: Different reasons for subsea rock installation (Visser & Van der Meer, 2008)	7
Figure 2.4: Cross section FFPV Stornes	8
Figure 2.5: Moon pool and fallpipe installation	9
Figure 2.6: Composition of the flexible fallpipe system	9
Figure 2.7: Self-propelled remotely operated vehicle	10
Figure 3.1: Curve showing the idealized variation of rate effect with strain rate (Quinn & Brown, 2011)	12
Figure 3.2: Mohr circles for undrained shear strength (Verruijt, 2005)	12
Figure 3.3: Schematic representation of different types of stress strain behaviour	13
Figure 3.4: Particle size distributions for the Knarr Surf project	14
Figure 3.5: Particle shape measurement system (CUR, 1995)	14
Figure 3.6: Marine zones (Fugro Geoconsulting Ltd., 2012)	15
Figure 4.1: Gapping and non-gapping penetration	19
Figure 4.2: Penetration dependent parameters A_{eff} and q	19
Figure 4.3: Additional soil resistance due to overestimation of the wedge volume	20
Figure 4.4: Circular jet regions (Karimipناه & Awbi, 2002)	23
Figure 4.5: Subdivision of free jet regions	23
Figure 4.6: Schematic overview of multi stone penetration	25
Figure 4.7: Additional penetration as a result of multi stone impact ($D_{50} = 0.05$ m, $\rho_s = 2680$ kg/m ³)	26
Figure 4.8: Schematic overview of multi stone penetration including force spreading	27
Figure 4.9: Upper and lower boundary of the multi stone penetration effect	27
Figure 4.10: Loss of fine particle material	28
Figure 4.11: Initiation of motion according to Shields	28
Figure 4.12: Soil heave effect during single stone penetration	29
Figure 4.13: Vertical deformations over the depth seabed	29
Figure 4.14: Additional volume necessary due to consolidation deformation of the seabed	30
Figure 4.15: Penetration of cohesive material in rock fill (De Vries, et al., 2007)	30
Figure 4.16: Rate dependency of shear strength (Lehane, et al., 2009)	32
Figure 4.17: Strain hardening and softening of soil during continuous shearing	32
Figure 6.1: Simplified test setups	37
Figure 6.2: Kaolin water mixing process	38
Figure 6.3: Kaolin clay testing bucket	39
Figure 6.4: Linear relation between water content and undrained shear strength (log scale) for Kaolin	40
Figure 7.1: Particle penetration for different impact velocities ($c_u = 1.4$ kPa, $\rho_s = 7804$ kg/m ³)	42
Figure 7.2: Particle penetration for different impact velocities ($c_u = 3.6$ kPa, $\rho_s = 7804$ kg/m ³)	42
Figure 7.3: Particle penetration for different impact velocities ($c_u = 12.4$ kPa, $\rho_s = 7804$ kg/m ³)	42
Figure 7.4: Dimensionless penetration versus impact velocity for different undrained shear strengths	43
Figure 7.5: Relation between particle penetration and impact velocities for different densities ($D_s = 0.015$ m, $c_u = 1.5$ kPa)	43

Figure 7.6: Boundary influences during testing ($v_{imp} = 3.0$ m/s, $c_u = 1.7$ kPa)	44
Figure 7.7: Moisture content over time during testing	44
Figure 7.8: A selection of the high speed camera penetration pictures	45
Figure 7.9: Incremental total displacements found using JPIV	45
Figure 7.10: Slip surface for undrained conditions ($\varphi = 0^\circ$) according to Prandtl	45
Figure 7.11: Dimensionless displacements contours of high speed impact	46
Figure 7.12: A selection of the slow penetration pictures	47
Figure 7.13: Final cumulative dimensionless displacements during slow penetration including particle	47
Figure 7.14: Dimensionless displacements during slow penetration including particle and Prandtl wedge	48
Figure 8.1: Knarr field located in the northern part of the North Sea (source: Google maps)	49
Figure 8.2: Possible layout of the Knarr field (Bradbury, 2011)	50
Figure 8.3: Location of geotechnical investigations. (Fugro Geoconsulting Ltd., 2012)	50
Figure 8.4: Cross section rock foundation towhead Knar FPSO location (Subsea 7, 2013)	50
Figure 8.5: Undrained shear strength relation with depth for the Knarr Surf project	52
Figure 8.6: Full flow penetrometers (Ball cone and T-Bar) (Randolph, et al., 2005)	53
Figure 8.7: Particle size distributions for the Knarr Surf project	53
Figure 9.1: Knarr Surf bathymetry at the FPSO location	55
Figure 9.2: Cross section of the multi beam echo sound data for the FPSO location	56
Figure 9.3: Real-time multi beam echo sound data	57
Figure 9.4: Bathymetric measurements using multi beam echo sounders	58
Figure 9.5: Signal distortion	58
Figure 9.6: Relative fitting of surveys	58
Figure 9.7: Seabed system (Randolph, et al., 2005)	59
Figure 10.1: Influence of assumed in-situ density on the total height deficit per Knarr Surf location	61
Figure 10.2: Probability density function for the addressed quarries	62
Figure 10.3: In-situ densities back calculated during the Knarr Surf project for different locations and layers	62
Figure 11.1: Flowchart used for the single stone penetration model	65
Figure 11.2: Modelled particle penetration for different impact velocities ($c_u = 1.4$ kPa, $\rho_s = 7804$ kg/m ³)	66
Figure 11.3: Modelled particle penetration for different impact velocities ($c_u = 3.6$ kPa, $\rho_s = 7804$ kg/m ³)	66
Figure 11.4: Modelled particle penetration for different impact velocities ($c_u = 12.4$ kPa, $\rho_s = 7804$ kg/m ³)	67
Figure 11.5: Modelled relation between particle penetration and impact velocities for different densities ($D_s = 0.015$ m, $c_u = 1.5$ kPa)	67
Figure 11.6: Force development during penetration divided in different components for different undrained shear strengths ($D_s = 0.015$ m, $v_{imp} = 6.0$ m/s, $\rho_s = 7804$ kg/m ³)	68
Figure 11.7: Results of the sensitivity analysis for the three most important parameters of single stone penetration	70
Figure 12.1: Relation between deep sea currents and particle size	72
Figure 12.2: Plaxis meshes	73
Figure 12.3: Total displacements in y-direction, showing squeezing mechanism ($y_{max} = 0.02$ m, $y_{min} = -0.04$ m)	74
Figure 12.4: Consolidation for the FPSO towhead location	76
Figure 12.5: Short term consolidation for the FPSO towhead location	76
Figure 12.6: Relative influence of described processes for different locations	78
Figure 12.7: Influence of different processes on the total loss of material for the FPSO towhead location (2.65 m)	79
Figure 12.8: Measured versus calculated volume loss for different location of the Knarr Surf project	80
Figure 12.9: Influence of production rate on single stone penetration	81

Figure 12.10: Influence of production rate on project costs	81
Figure 15.1: Cross section Stornes	101
Figure 15.2: Top view Stornes	102
Figure 15.3: Flexible fallpipe vessel Stornes	102
Figure 15.4: Flexible fallpipe composition (Ravelli, 2012)	102
Figure 15.5: Expressions for the pressure inside and outside the fall pipe	107
Figure 15.6: Flow pattern through the vltters	107
Figure 15.7: Carnot losses	108
Figure 15.8: Flow through a medium	110
Figure 15.9: Flow through the pores	110
Figure 15.10: Constant shear rate over the volume	111
Figure 15.11: Penetration depth of a clay in rock fill	114
Figure 15.12: Atterberg limit determination using the Casagrande cup	115
Figure 15.13: Tools required for test preparation	115
Figure 15.14: Water kaolin mixture	115
Figure 15.15: Clay mixing	115
Figure 15.16: Resulting clay	115
Figure 15.17: Test setup single stone fall experiment	115
Figure 15.18: Steel bearings in different sizes ranging from 15 mm to 38 mm diameter	116
Figure 15.19: Marbles and steel bearing with a diameter of 15 mm	116
Figure 15.20: Particle penetration $\Delta = 0.036$ m ($D_s = 30$ mm, $\rho_s = 7821$ kg/m ³ , $v_{imp} = 2.0$ m/s)	117
Figure 15.21: Particle penetration $\Delta = 0.069$ m ($D_s = 30$ mm, $\rho_s = 7821$ kg/m ³ , $v_{imp} = 3.0$ m/s)	117
Figure 15.22: Particle penetration $\Delta = 0.107$ m ($D_s = 30$ mm, $\rho_s = 7821$ kg/m ³ , $v_{imp} = 4.0$ m/s)	117
Figure 15.23: Particle penetration $\Delta = 0.144$ m ($D_s = 30$ mm, $\rho_s = 7821$ kg/m ³ , $v_{imp} = 5.0$ m/s)	117
Figure 15.24: Particle penetration $\Delta = 0.180$ m ($D_s = 30$ mm, $\rho_s = 7821$ kg/m ³ , $v_{imp} = 6.0$ m/s)	117
Figure 15.25: Particle penetration $\Delta = 0.015$ m ($D_s = 30$ mm, $\rho_s = 7821$ kg/m ³ , $v_{imp} = 2.0$ m/s)	118
Figure 15.26: Particle penetration $\Delta = 0.023$ m ($D_s = 30$ mm, $\rho_s = 7821$ kg/m ³ , $v_{imp} = 3.0$ m/s)	118
Figure 15.27: Particle penetration $\Delta = 0.040$ m ($D_s = 30$ mm, $\rho_s = 7821$ kg/m ³ , $v_{imp} = 4.0$ m/s)	118
Figure 15.28: Particle penetration $\Delta = 0.055$ m ($D_s = 30$ mm, $\rho_s = 7821$ kg/m ³ , $v_{imp} = 5.0$ m/s)	118
Figure 15.29: Particle penetration $\Delta = 0.075$ m ($D_s = 30$ mm, $\rho_s = 7821$ kg/m ³ , $v_{imp} = 6.0$ m/s)	118
Figure 15.30: Particle penetration $\Delta = 0.008$ m ($D_s = 30$ mm, $\rho_s = 7821$ kg/m ³ , $v_{imp} = 2.0$ m/s)	119
Figure 15.31: Particle penetration $\Delta = 0.014$ m ($D_s = 30$ mm, $\rho_s = 7821$ kg/m ³ , $v_{imp} = 3.0$ m/s)	119
Figure 15.32: Particle penetration $\Delta = 0.018$ m ($D_s = 30$ mm, $\rho_s = 7821$ kg/m ³ , $v_{imp} = 4.0$ m/s)	119
Figure 15.33: Particle penetration $\Delta = 0.023$ m ($D_s = 30$ mm, $\rho_s = 7821$ kg/m ³ , $v_{imp} = 5.0$ m/s)	119
Figure 15.34: Particle penetration $\Delta = 0.033$ m ($D_s = 30$ mm, $\rho_s = 7821$ kg/m ³ , $v_{imp} = 6.0$ m/s)	119
Figure 15.35: Experimental strongbox	120
Figure 15.36: Half sphere particle preparation	120
Figure 15.37: Fully saturated kaolin clay sample	120
Figure 15.38: Additional contrast material added on the Plexiglas strongbox wall	120
Figure 15.39: Speed up consolidation under own weight using the geotechnical centrifuge	120
Figure 15.40: Extended Plexiglas wall to ensure sufficient fall height	120
Figure 15.41: Final high speed camera test setup	120
Figure 15.42: Penetrate with a set velocity using the loading frame in the geotechnical centrifuge	121
Figure 15.43: The half sphere pressed against the Plexiglas right before slow penetration into the Kaolin clay	121

Figure 15.44: Slow penetration into normally consolidated clay with constrast material	121
Figure 15.45: Dimensionless displacements contours of high speed impact	123
Figure 15.46: Cumulative dimensionless displacement contours of slow penetration	123
Figure 15.47: Field layout (Subsea 7, 2013)	124
Figure 15.48: Production template towhead rock berm design (Subsea 7, 2013)	125
Figure 15.49: FPSO towhead rock berm design (Subsea 7, 2013)	126
Figure 15.50: Undrained shear strength versus depth - BH-B1 (Fugro Geoconsulting Ltd., 2012)	128
Figure 15.51: Phased subsea rock installation	130
Figure 15.52: Berm development indicated using intermediate surveys	130
Figure 15.53: Average bulk density of surrounding quarries with standard deviation	132
Figure 15.54: PDF for the bulk density of material obtained from different quarries on the Norwegian coast	132
Figure 15.55: Influence of drag coefficient on single stone penetration	134
Figure 15.56: Influence of rock density on single stone penetration	134
Figure 15.57: Influence of water density on single stone penetration	134
Figure 15.58: Influence of wet soil density on single stone penetration	134
Figure 15.59: Influence of bearing capacity factor on single stone penetration	135
Figure 15.60: Plaxis input geometry	137
Figure 15.61: Original fine mesh	137
Figure 15.62: Deformed mesh (scaled up 100 times)	137
Figure 15.63: Vertical deformations	137
Figure 15.64: Horizontal deformations	137
Figure 15.65: Vertical deformation over the length of the berm	137
Figure 15.66: Vertical deformations over the depth seabed	137
Figure 15.67: D-Settlement input soil layers	138
Figure 15.68: D-Settlement development of effective pressures and consolidation results at section 5	138
Figure 15.69: Sieves curve provided by the Sløvåg quarry	144
Figure 15.70: Density tests provided by the Jelsa quarry	148

15.5 Flexible Fallpipe Vessel – Stornes

Table 15.1: Stornes properties

Name	Stornes		
Type	Flexible fallpipe vessel		
Classification	American Bureau of Shipping		
Year of construction	2011		
Dimensions	Length overall	175.00	m
	Breadth moulded	26.00	m
	Depth moulded	14.50	m
	Draught	10.57	m
Deadweight	27500 tons		
Loading capacity	25500 tons		
Speed loaded	14.0 kn		
Propulsion	8000 kW		
Bow thrusters	Tunnel	3 x 1500	kW
Retractable thrusters	Azimuth	2 x 2200	kW
Total power installed	16572 kW		
Dynamic positioning	DP Class 2		
Accommodation	51 persons		
Bunkers	Heavy fuel oil	1012	m
	Marine diesel oil	551	m
	Fresh water	389	m
Stern thrusters	Tunnel	1 x 1000	kW
Flexible fallpipe system	ø 1.1 m		
	Dumping depth 2200 m		
	Dumping capacity up to 3000 t/h		
Survey equipment	HIPAP, bathymetric systems, multi beam and mechanical scanning profilers, scanning sonar, underwater cameras and lights & other options		

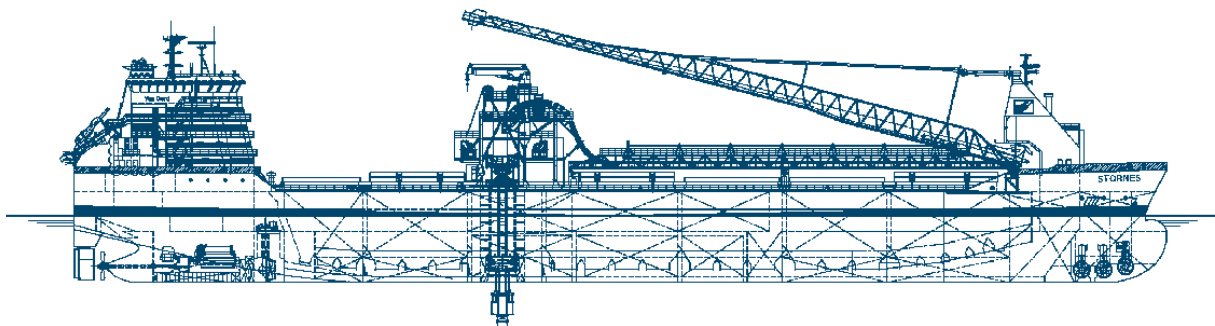


Figure 15.1: Cross section Stornes

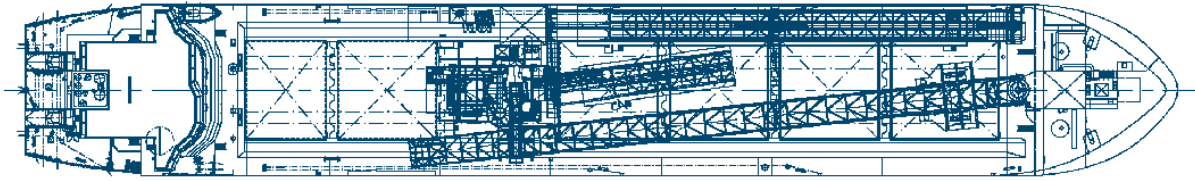


Figure 15.2: Top view Stornes



Figure 15.3: Flexible fallpipe vessel Stornes

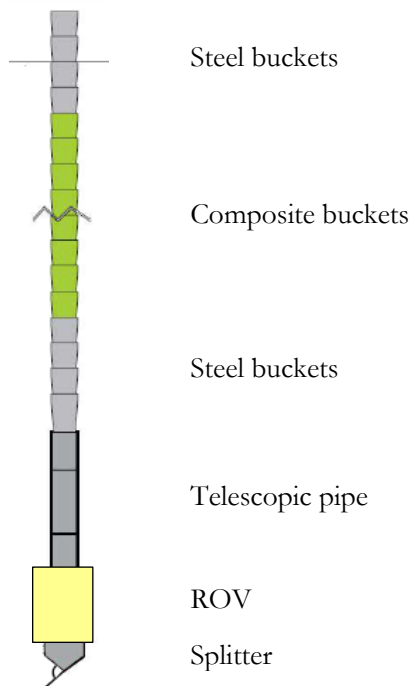


Figure 15.4: Flexible fallpipe composition (Ravelli, 2012)

15.6 Bearing capacity models

In the past decades several methods have been created in order to estimate the maximum force which can be applied on a strip foundation. All methods are closely related to each other. A short overview of the different approaches is given in Table 15.2.

Table 15.2: Bearing capacity equations according to different authors

Terzaghi		$\frac{F_B}{A_{eff}} = cN_c s_c + \bar{q}N_q + \frac{1}{2}\gamma B N_\gamma s_\gamma$	(15.1)
		$N_q = \frac{a^2}{a \cdot \cos^2(45 + \varphi / 2)}$	
		$N_c = (N_q - 1) \cot \varphi$	
		$N_\gamma = \frac{\tan \varphi}{2} \left(\frac{K_{p\gamma}}{\cos^2 \varphi} - 1 \right)$	
	In which:		
		$a = e^{\left(0.75\pi - \frac{\varphi}{2}\right) \tan \varphi}$	
Meyerhof	Vertical load	$\frac{F_B}{A_{eff}} = cN_c s_c d_c + \bar{q}N_q s_q d_q + \frac{1}{2}\gamma B' N_\gamma s_\gamma d_\gamma$	(15.2)
	Inclined load	$\frac{F_B}{A_{eff}} = cN_c d_c i_c + \bar{q}N_q d_q i_q + \frac{1}{2}\gamma B' N_\gamma d_\gamma i_\gamma$	(15.3)
		$N_q = e^{\pi \tan \varphi} \tan^2(45 + \varphi / 2)$	
		$N_c = (N_q - 1) \cot \varphi$	
		$N_\gamma = (N_q - 1) \tan 1.4\varphi$	
Hansen		$\frac{F_B}{A_{eff}} = cN_c s_c d_c i_c g_c b_c + \bar{q}N_q s_q d_q i_q g_q b_q + \frac{1}{2}\gamma B' N_\gamma s_\gamma d_\gamma i_\gamma g_\gamma b_\gamma$	(15.4)
		$N_q = \text{same as Meyerhof}$	
		$N_c = \text{same as Meyerhof}$	
		$N_g = 1.5(N_q - 1) \tan \varphi$	
Vesic		$\frac{F_B}{A_{eff}} = cN_c s_c d_c i_c g_c b_c + \bar{q}N_q s_q d_q i_q g_q b_q + \frac{1}{2}\gamma B' N_\gamma s_\gamma d_\gamma i_\gamma g_\gamma b_\gamma^*$	(15.5)
		$N_q = \text{same as Meyerhof}$	
		$N_c = \text{same as Meyerhof}$	
		$N_\gamma = 2(N_q + 1) \tan \varphi$	

* = Same as Hansen, but with different shape, depth and inclination factors

s = shape factor

d = depth factor

i = inclination factor

b = base inclination factor

g = ground inclination factor

Based on early work by Prandtl, Terzaghi (Terzaghi, 1943) created a solution for the bearing capacity of a shallow strip foundation. Terzaghi only uses shape factors with the cohesion (s_c) and base (s_y) terms. The method is only applicable for shallow foundations where $D \leq B$.

Meyerhof (Meyerhof, 1951) slightly modified the formula by adding a shape factor (s_q) for the depth term (N_q) and by including depth and inclination factors d_b , i_b , respectively. The inclination factors are applied in cases where the loading direction is not vertical.

Brinch Hansen further extends the formula by including supplementary factors for base (b_i) and ground (g_i) inclination. Moreover the Brinch Hansen equation is also applicable for deeper cases, for instance in case of piles or caissons (Brinch Hansen, 1970). This depth dependency is implicitly included in the depth factors d_c and d_q , as shown in here:

$$\left. \begin{aligned} d_c &= 1 + 0.4 \frac{D}{B} \\ d_q &= 1 + 2 \tan \varphi (1 - \sin \varphi)^2 \frac{D}{B} \end{aligned} \right\} \frac{D}{B} \leq 1$$

$$\left. \begin{aligned} d_c &= 1 + \tan^{-1} 0.4 \frac{D}{B} \\ d_q &= 1 + 2 \tan \varphi (1 - \sin \varphi)^2 \tan^{-1} \frac{D}{B} \end{aligned} \right\} \frac{D}{B} > 1$$

Finally Vesić (Vesić, 1973) creates a method which greatly resembles Brinch Hansen's formula, however the way in which the base factor (N_y) is determined is different. Other changes can be found in the way the i_b , b_i and g_i terms are computed.

15.7 Brinch Hansen

$$\hat{F} = cN_c s_c d_c i_c g_c b_c + \bar{q}N_q s_q d_q i_q g_q b_q + \frac{1}{2}\gamma B' N_\gamma s_\gamma d_\gamma i_\gamma g_\gamma b_\gamma \quad (15.6)$$

In which:

$$N_q = e^{\pi \tan \varphi} \tan^2 \left(45 + \frac{\varphi}{2} \right)$$

$$N_c = (N_q - 1) \cot \varphi$$

$$N_\gamma = 1.5(N_q - 1) \tan \varphi$$

$$s_q = 1.0 + \frac{B'}{L} \cdot \sin \varphi$$

$$s_c = 1.0 + \frac{N_q}{N_c} \cdot \frac{B'}{L}$$

$$s_\gamma = 1.0 - 0.4 \frac{B'}{L}$$

$$d_q = 1 + 2 \tan \varphi (1 - \sin \varphi) \frac{D}{B};$$

$$\text{for } \frac{D}{B} \leq 1$$

$$= 1 + 2 \tan \varphi (1 - \sin \varphi) \tan^{-1} \frac{D}{B}$$

$$\text{for } \frac{D}{B} > 1$$

$$d_c = 1.0 + 0.4 \frac{D}{B}$$

$$\text{for } \frac{D}{B} \leq 1$$

$$= 1.0 + 0.4 \tan^{-1} \frac{D}{B}$$

$$\text{for } \frac{D}{B} > 1$$

$$d_\gamma = 1.0$$

$$i_q = \left(1 - \frac{0.5H}{V + A_f c_a \cot \varphi} \right)^{\alpha_1}$$

$$i_c = i_q - \frac{1 - i_q}{N_q - 1}$$

$$i_\gamma = \left(1 - \frac{0.7H}{V + A_f c_a \cot \varphi} \right)^{\alpha_2}$$

$$g_c = 1 - \frac{\beta^\circ}{147^\circ}$$

$$g_q = g_\gamma = (1.0 - 0.5 \tan \beta)^\circ$$

$$b_q = \exp(-2\eta \tan \varphi)$$

$$b_c = 1 - \frac{\eta^\circ}{147^\circ}$$

$$b_\gamma = \exp(-2.7\eta \tan \varphi)$$

15.8 Staged descent of a group of rock through water

Based on (Ravelli, 2012)

Acceleration of the group

The velocity of the group increases during the first phase. Water is trapped within the group (added-mass), which result in a slower acceleration than predicted by (van Mazijk, 1982) for a single stone. The water is added to the group from the rear. By the entrainment of water by the group, the size of the group, and thus the drag force, increases with depth. At a certain point in time, the acceleration of the group is reduced to zero while the size of the group is still increasing. This is the start of the second phase of the fall process. This phase is characterized by the total mass of the group and no longer by the individual stones. The acceleration, deceleration and trajectory of the group increases with the mass of the group. Groups with a constant mass, but with a different rock diameter, have the same maximum group speed and acceleration profile. For groups that consist of more than 100 rocks, the shape and diameter of the individual rocks does not affect the maximal velocity of the group.

Deceleration of the group

When the maximum group velocity is reached, the group starts to decelerate. The volume of the group, which is increasing with depth, causes an increased drag. This process continues until the equilibrium fall velocity of the largest rocks within the group is reached. At this point the larger rocks start to fall out of the group at the front of the group. During the first and second phases of the group fall process, rocks will circulate through the group. Rocks will progress from the rear of the group towards the front, where their speed is reduced by an increased drag. The rock is then forced towards the side of the group where a return flow forces them back to the rear of the group. This process indicates that the individual velocity of a rock in a rock group is higher than the group velocity itself. When the group consist of rocks of different grading, bigger rocks will spend more time in front of the group compared to smaller rocks.

Formation of a rock front

When the fall velocity of the rock group is equal to the equilibrium fall velocity of the largest rocks, these rocks start to leave the group at the front. This process intensifies itself because the added mass water stays behind. The energy of the added mass is dissipated by the surrounding water. The rocks will now fall through the water without the additional (water) mass. In the wake of the larger rocks the small rocks will follow. At a certain point the small rocks cannot keep up with the bigger rocks and will eventually leave the wake. This is where the fourth phase starts.

Single stone model

At a certain moment, when the distance between the rocks keeps increasing, the rocks will not 'feel' the presence of other rocks any more. Then their fall process will continue as if they started as a single stone. This fall behaviour can then be described by the Single Stone Model (Vrijling et al., 1995). The start of phase four will be influenced by the density of the group. Stones in groups with a larger total mass will influence each other till a lower density compared with groups with a lower total mass. This is caused by a larger inertia of the group with the larger mass due to the added mass.

Radial runoff

When the group approaches the bottom before the third phase starts, the energy accompanied with the added mass is still present. The water will be deflected by the seabed and a radial runoff, as of the middle of the rock group, takes place. Rocks are transported away from the group centre by this flow. The horizontal distance that a single rock will travel depends on the diameter, mass, flow speed and roughness of the seabed. The radial runoff is governed by the total mass of the group and the velocity at which the group reach the seabed.

15.9 Flexible fallpipe forces

Based on (Van Oord ACZ, 2002):

To calculate the equilibrium flow velocity the pressure just above and underneath the vltter is considered. Here equilibrium velocity ($U_{equilibrium}$) is present. The pressure outside and just underneath the vltter is used as a reference pressure, called $p_{outside}$ and can be derived using Bernouilli's law combined with the fact that no water may go into and out of the vltter if the flow velocity remains constant (Figure 15.5). Water will not enter nor exit through the gaps between the vltters if p_{inside} and $p_{outside}$ are equal. This results in the following equilibrium equations:

$$\begin{aligned} p_{outside} &= p_{inside} + \frac{1}{2}\rho U_{eq}^2 \\ p_{outside} - \rho_w g h &= p_{inside} + \frac{1}{2}U_{eq}^2 - \rho_m g h + \Delta p_{friction} \\ p_{friction} &= (\rho_m - \rho_w) g h \end{aligned} \quad (15.7)$$

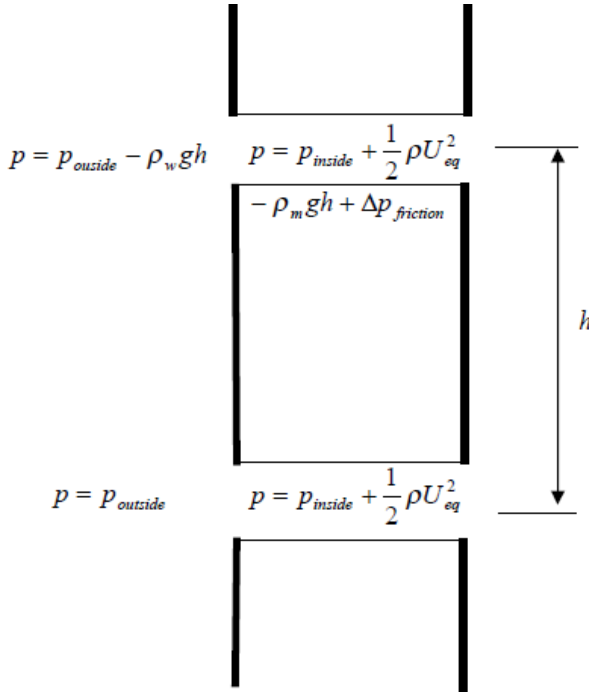


Figure 15.5: Expressions for the pressure inside and outside the fall pipe

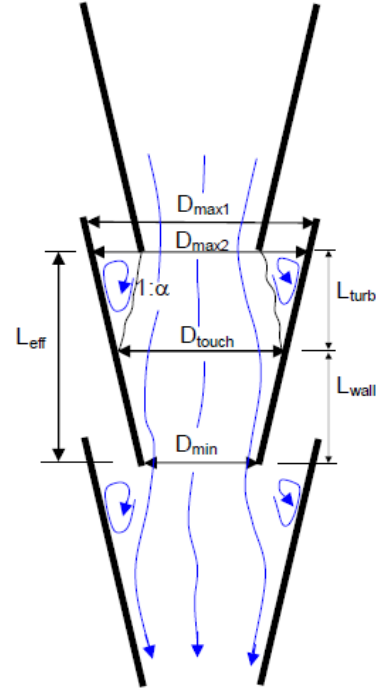


Figure 15.6: Flow pattern through the vltters

Inside a flutter the pressure decreased as result of friction. Two types of friction occur:

- Wall friction inside the vltter
- Energy dissipation through turbulence in the deceleration zone called Carnot losses (Figure 15.6)

When the water leaves a vltter it will decelerate when entering the next flutter, which is wider at that the top end. The expression for the pressure drop due to widening of a round tube is given by Carnot for 2 tubes each having a constant diameter \mathcal{A} , as shown in Figure 15.7

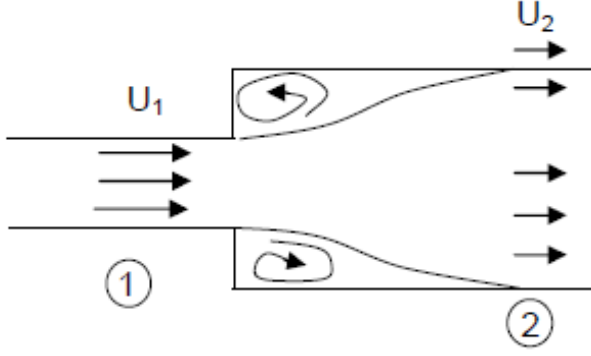


Figure 15.7: Carnot losses

Based on this the following equations can be applied:

$$\begin{aligned}\Delta H_{carnot} &= \zeta_{carnot} \cdot \frac{U^2}{2g} = \frac{U_1 - U_2}{2g} \cdot \frac{U_1^2}{2g} \\ \zeta_{carnot} &= \left(1 - \frac{A_1}{A_2}\right)^2 \\ \Delta p_{carnot} &= \rho g \cdot \Delta H_{carnot} = \zeta_{carnot} \cdot \frac{1}{2} \rho U^2\end{aligned}\tag{15.8}$$

And:

$$\begin{aligned}\Delta H_{wall} &= f \cdot \frac{L}{D} \cdot \frac{U^2}{2g} \\ f &= \frac{8g}{C^2} \\ C &= 18 \log \left(12000 \frac{R}{k} \right) \\ \Delta p_{wall} &= \rho_m g \Delta H_{wall} = \zeta_{wall} \cdot \frac{1}{2} \rho_m U_{eq}^2\end{aligned}\tag{15.9}$$

Where:

$$\begin{aligned}\zeta_{wall} &= \frac{8g}{C^2} \cdot \frac{L_{wall}}{D_{wall,av}} \\ C_{wall} &= 18 \log \left(12000 \frac{R_{wall,av}}{k} \right) \\ R_{wall,av} &= \frac{\frac{1}{4} \pi D_{wall,av}^2}{\pi D_{wall,av}} \\ D_{wall,av} &= \frac{D_{touch} + D_{min}}{2}\end{aligned}\tag{15.10}$$

Which finally results in:

$$\Delta p_{loss,total} = (\zeta_{carnot} + \zeta_{wall}) \cdot \frac{1}{2} \rho_m U_{eq}^2\tag{15.11}$$

15.10 Shield parameter

$$\theta = \frac{v_*^2}{((\rho_s - \rho_f / \rho_f)gD)} \quad (15.12)$$

Where:

$$v_* = v \cdot \sqrt{c_f} \quad (15.13)$$

And:

$$\begin{aligned} \frac{1}{\sqrt{c_f}} &= 5.75 \cdot \log \frac{12R}{k} \\ R &= SOD \\ k &= 3 \cdot D_{90} \end{aligned} \quad (15.14)$$

$$D_* = \left(\frac{((\rho_s - \rho_f) / \rho_f)g}{v^2} \right)^{\frac{1}{3}} D \quad (15.15)$$

$$\theta_{cr} = \begin{cases} \frac{0.24}{D_*} & \text{for } 1 < D_* \leq 4 \\ \frac{0.14}{D_*^{0.64}} & \text{for } 4 < D_* \leq 10 \\ \frac{0.04}{D_*^{0.1}} & \text{for } 10 < D_* \leq 20 \\ 0.013D_*^{0.29} & \text{for } 20 < D_* \leq 150 \\ 0.055 & \text{for } D_* > 150 \end{cases} \quad (15.16)$$

15.11 Derivation of clay penetration in a rock fill

Based on (Bijnagte & Luger, 2005)

Consider a volume of rock fill with a cross-section $B \cdot H$ and a length L . A fluid flow with a specific discharge q in direction L can be described using Darcy:

$$q = k \cdot i \quad (15.17)$$

Where:

q	= discharge	[m/s]
k	= permeability	[m/s]
i	= hydraulic gradient	[-]

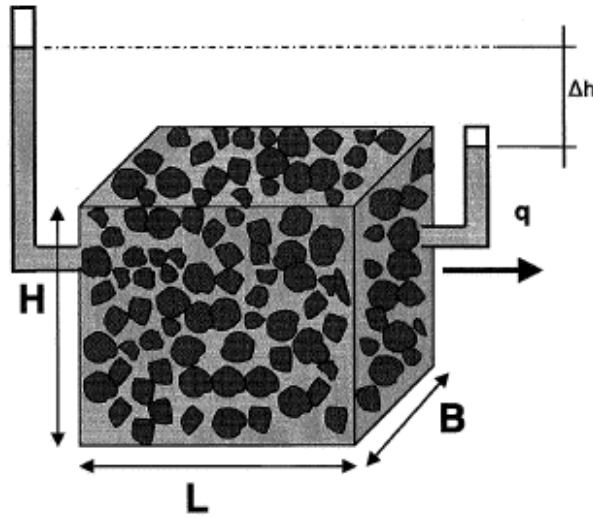


Figure 15.8: Flow through a medium

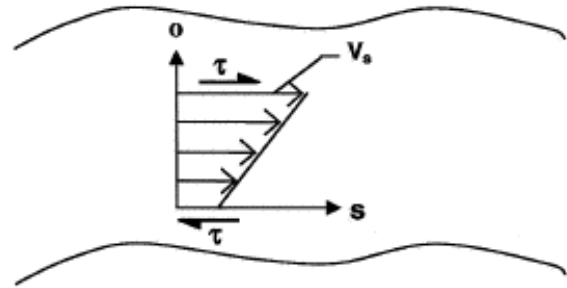


Figure 15.9: Flow through the pores

If one multiplies the hydraulic gradient i with the length L over which the flow is considered one finds the head loss; $\Delta h = i \cdot L$. The pressure loss over the distance L can be determined using the formula:

$$\Delta p = \Delta h \cdot \rho \cdot g = i \cdot L \cdot \rho \cdot g \quad (15.18)$$

The energy needed for this flow (per second) is:

$$W_{in} = B \cdot H \cdot q \cdot \Delta p \quad (15.19)$$

Inserting equation (15.18) and equation (15.19) gives:

$$W_{in} = B \cdot H \cdot q \cdot i \cdot L \cdot \rho \cdot g = B \cdot H \cdot L \cdot \frac{q^2}{k} \cdot \rho \cdot g = V \cdot \frac{q^2}{k} \cdot \rho \cdot g \quad (15.20)$$

The shear stress in the fluid in the pores in volume V is related to the velocity gradient by the viscosity of the fluid as indicated in Figure 15.9. This gives:

$$\frac{dv_y}{dx} \cdot \eta = \tau \quad (15.21)$$

With

$$\eta = \nu \cdot \rho$$

Here:

v_y	= the velocity through the pore	[m/s]
x	= the direction perpendicular to the (local) velocity direction	[-]
η	= dynamic viscosity	[kNs/m ²]
ρ	= density	[kg/m ³]
ν	= kinematic viscosity	[kNms/kg]
τ	= the shear stress	[kN/m ²]
S	= the shear rate	[s ⁻¹]

For a more general description one can write:

$$\frac{dv_s}{do} = S \quad (15.22)$$

Where:

v_s	= the velocity in the flow direction (direction of the pore channel) [m/s]
o	= the direction perpendicular to the flow direction [-]

Figure 15.10 shows the shear stresses for a shear rate that is constant over the water volume.

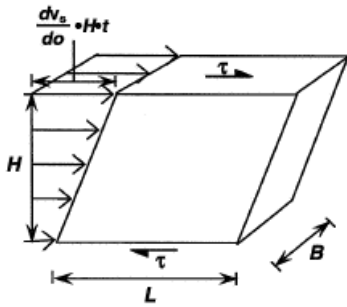


Figure 15.10: Constant shear rate over the volume

In this case the energy which is dissipated, per volume of fluid, is equal to:

$$E_{dis} = F \cdot distance \quad (15.23)$$

With

$$F = \tau \cdot B \cdot L$$

$$\tau = \frac{dv_s}{do} \cdot \eta$$

$$distance = \frac{dv_s}{do} \cdot H \cdot t$$

This gives:

$$E_{dis} = \frac{dv_s}{do} \cdot \eta \cdot B \cdot L \cdot \frac{dv_s}{do} \cdot H \cdot t = B \cdot H \cdot L \cdot \left(\frac{dv_s}{do} \right)^2 \quad (15.24)$$

Considering that the volume of fluid in the cube of Figure 15.8 is $B \cdot H \cdot L \cdot n$ (n = porosity) this gives per unit of time (see also equation (15.20)):

$$W_{in} = E_{dis} = B \cdot H \cdot L \cdot \frac{q^2}{k} \cdot \rho \cdot g = B \cdot H \cdot L \cdot n \cdot \left(\frac{dv_s}{do} \right)^2 \cdot \eta \quad (15.25)$$

This gives:

$$V \cdot \frac{q^2 \cdot \rho \cdot g}{k} = V \cdot n \cdot \left(\frac{dv_s}{do} \right)^2 \cdot \eta \quad (15.26)$$

Where

V = the volume of the cube [m³]

The viscous dissipation per unit of time over the fluid volume is found by integration:

$$\frac{E_{dis}}{t} = n \cdot \int_V S^2 \cdot \eta dV \quad (15.27)$$

NOTE: the total volume is V and that the fluid volume is given as $n \cdot V$

With

n	= porosity	[-]
V	= volume	[m ³]
S	= shear rate	[s ⁻¹]
η	= dynamic viscosity	[Ns/m ²]
t	= time	[s]

This energy dissipation should (for a fluid flow which can be described by the Darcy formulation) be equal to (see also equation (15.25)):

$$\frac{E_{dis}}{t} = \int_V \frac{q^2 \cdot \rho \cdot g}{k} dV \quad (15.28)$$

With:

q	= specific discharge	[m/s]
k	= permeability	[m/s]
ρ	= fluid density	[kg/m ³ = Ns ² /m ⁴]
g	= gravity	[m/s ²]

Using $\eta = \nu \cdot \rho$ and $k = \frac{\kappa \cdot g}{\nu}$ (where κ = intrinsic permeability \approx [m²] $10^{-7} \cdot k$) and inserting this in (15.28)

and (15.27), realizing that (15.28) and (15.27) should be equal for a fluid, one finds:

$$n \cdot S^2 \cdot \int_{V=0}^V dV = \frac{q^2}{\kappa} \cdot V \quad (15.29)$$

This is valid for a fluid. In case of a clay flowing through pores, also with a constant strain rate, the work done equals:

$$F \cdot \Delta = (B \cdot L \cdot \tau) \cdot \left(\frac{dv_s}{do} \right) \cdot H = B \cdot L \cdot H \cdot \tau \cdot \left(\frac{dv_s}{do} \right) \quad (15.30)$$

With $\tau = c_u$ and $V = B \cdot L \cdot H$ the work done is then:

$$V \cdot c_u \cdot \left(\frac{dv_s}{do} \right) = V \cdot c_u \cdot S \quad (15.31)$$

This means the dissipated energy (per second) in a volume V is:

$$\frac{E_{dis}}{t} = \int_V c_u \cdot S \cdot dV = n \cdot c_u \cdot \frac{q}{\sqrt{n \cdot \kappa}} \frac{q^2 \cdot \rho \cdot g}{k} \cdot V = c_u \cdot \sqrt{\frac{n}{\kappa}} \cdot q \cdot V \quad (15.32)$$

The effect of a variable shear rate over the volume can be incorporated with a factor α :

$$E = \alpha \cdot c_u \cdot \sqrt{\frac{n}{\kappa}} \cdot g \cdot V \quad (15.33)$$

So, in order to determine the resistance of a plastic (cohesive) material the value of α should be known. An estimation of this value can be obtained by assuming a certain distribution of S over the volume. It is then possible to use (15.28) to determine the magnitude of S and hence α . Assume that the shear strain rate distribution over the volume is given as:

$$S = C_m \cdot V^m \quad (15.34)$$

For different values of m this results in a whole range of distributions. Combining (15.29) and (15.34) realizing that the fluid volume equals $n \cdot V$ gives:

$$\int_{v=0}^1 (C_m \cdot v^m)^2 dv = \frac{q^2}{\kappa \cdot n} \quad (15.35)$$

This equals:

$$\int_{v=0}^1 C_m^2 \cdot v^{2m} dv = \frac{q^2}{\kappa \cdot n} \quad (15.36)$$

This gives:

$$C_m^2 \cdot \frac{1}{2m+1} = \frac{q^2}{\kappa \cdot n} \quad (15.37)$$

and so:

$$C_m = \sqrt{\frac{2m+1}{\kappa \cdot n}} \cdot q \quad (15.38)$$

The possible general distributions of S over the volume is:

$$S = C_m \cdot v^m = \sqrt{\frac{2m+1}{\kappa \cdot n}} \cdot q \cdot v^m. \quad (15.39)$$

Now in order to obtain the plastic work done within a volume V by a cohesive material following these shear rate distributions the dissipated energy per unit time (realising that the fluid volume equals $n \cdot V$), is:

$$\frac{E_{dis}}{t} = n \cdot V \cdot \int_{v=0}^1 c_u \cdot \sqrt{\frac{2m+1}{\kappa \cdot n}} \cdot q \cdot v^m dv \quad (15.40)$$

This gives:

$$\frac{E_{dis}}{t} = n \cdot V \cdot c_u \cdot q \cdot \sqrt{\frac{2m+1}{\kappa \cdot n}} \cdot \left[\frac{1}{m+1} \cdot v^{m+1} \right]_0^1 \quad (15.41)$$

Which is equal to:

$$\frac{E_{dis}}{t} = V \cdot c_u \cdot q \cdot \sqrt{\frac{n}{\kappa}} \cdot \frac{\sqrt{2m+1}}{m+1} \quad (15.42)$$

or:

$$\frac{E_{dis}}{t} = \alpha \cdot c_u \cdot q \cdot \sqrt{\frac{n}{\kappa}} \cdot V \quad (15.43)$$

With:

$$\alpha = \frac{\sqrt{2m+1}}{m+1}$$

Values of α can now easily be calculated:

Table 15.3: α values for different shear strain rate functions

m	α
0	1.00
1	0.87
2	0.75
3	0.66
4	0.60

Now the work done, per unit of time, by the driving force is the force (pressure times area = $p \cdot B \cdot H$) times the velocity (which equals q per unit of time) should be equal to the energy dissipated in the flow (15.43):

$$p \cdot B \cdot H \cdot q = \alpha \cdot c_u \cdot \sqrt{\frac{n}{\kappa}} \cdot q \cdot V \quad (15.44)$$

Or, after simplifying this equation (realizing that $V = B \cdot H \cdot L$):

$$p = \alpha \cdot c_u \cdot \sqrt{\frac{n}{\kappa}} \cdot L \quad (15.45)$$

Finally resulting in:

$$L = \frac{p}{\alpha \cdot c_u \cdot \sqrt{\frac{n}{\kappa}}} \quad (15.46)$$

with L = the penetration depth of the clay into the rock (see also Figure 15.11). In order to determine the penetration of the rock into the clay δ , L has to be multiplied with the porosity of the rock.

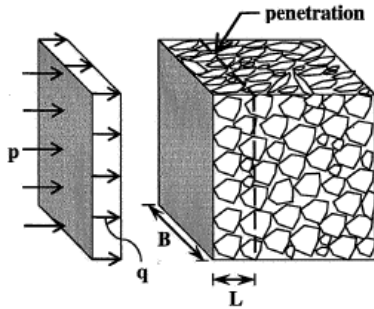


Figure 15.11: Penetration depth of a clay in rock fill

15.12 Images of experiments

Test preparation



Figure 15.12: Atterberg limit determination using the Casagrande cup



Figure 15.13: Tools required for test preparation



Figure 15.14: Water kaolin mixture



Figure 15.15: Clay mixing



Figure 15.16: Resulting clay



Figure 15.17: Test setup single stone fall experiment
($v_{imp} = 2 \text{ m/s}$)



Figure 15.18: Steel bearings in different sizes ranging from 15 mm to 38 mm diameter



Figure 15.19: Marbles and steel bearing with a diameter of 15 mm

Fall test ($c_u = 1.4$ kPa)



Figure 15.20: Particle penetration $\Delta = 0.036$ m ($D_s = 30$ mm, $\rho_s = 7821$ kg/m³, $v_{imp} = 2.0$ m/s)



Figure 15.21: Particle penetration $\Delta = 0.069$ m ($D_s = 30$ mm, $\rho_s = 7821$ kg/m³, $v_{imp} = 3.0$ m/s)



Figure 15.22: Particle penetration $\Delta = 0.107$ m ($D_s = 30$ mm, $\rho_s = 7821$ kg/m³, $v_{imp} = 4.0$ m/s)



Figure 15.23: Particle penetration $\Delta = 0.144$ m ($D_s = 30$ mm, $\rho_s = 7821$ kg/m³, $v_{imp} = 5.0$ m/s)



Figure 15.24: Particle penetration $\Delta = 0.180$ m ($D_s = 30$ mm, $\rho_s = 7821$ kg/m³, $v_{imp} = 6.0$ m/s)

Fall test ($c_u = 3.6$ kPa)


Figure 15.25: Particle penetration $\Delta = 0.015$ m ($D_s = 30$ mm, $\rho_s = 7821$ kg/m³, $v_{imp} = 2.0$ m/s)



Figure 15.26: Particle penetration $\Delta = 0.023$ m ($D_s = 30$ mm, $\rho_s = 7821$ kg/m³, $v_{imp} = 3.0$ m/s)



Figure 15.27: Particle penetration $\Delta = 0.040$ m ($D_s = 30$ mm, $\rho_s = 7821$ kg/m³, $v_{imp} = 4.0$ m/s)



Figure 15.28: Particle penetration $\Delta = 0.055$ m ($D_s = 30$ mm, $\rho_s = 7821$ kg/m³, $v_{imp} = 5.0$ m/s)



Figure 15.29: Particle penetration $\Delta = 0.075$ m ($D_s = 30$ mm, $\rho_s = 7821$ kg/m³, $v_{imp} = 6.0$ m/s)

Fall test ($c_u = 12.4$ kPa)



Figure 15.30: Particle penetration $\Delta = 0.008$ m ($D_s = 30$ mm, $\rho_s = 7821$ kg/m³, $v_{imp} = 2.0$ m/s)



Figure 15.31: Particle penetration $\Delta = 0.014$ m ($D_s = 30$ mm, $\rho_s = 7821$ kg/m³, $v_{imp} = 3.0$ m/s)



Figure 15.32: Particle penetration $\Delta = 0.018$ m ($D_s = 30$ mm, $\rho_s = 7821$ kg/m³, $v_{imp} = 4.0$ m/s)



Figure 15.33: Particle penetration $\Delta = 0.023$ m ($D_s = 30$ mm, $\rho_s = 7821$ kg/m³, $v_{imp} = 5.0$ m/s)



Figure 15.34: Particle penetration $\Delta = 0.033$ m ($D_s = 30$ mm, $\rho_s = 7821$ kg/m³, $v_{imp} = 6.0$ m/s)

High speed penetration test

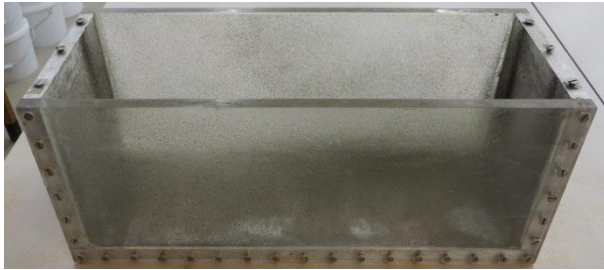


Figure 15.35: Experimental strongbox



Figure 15.36: Half sphere particle preparation



Figure 15.37: Fully saturated kaolin clay sample



Figure 15.38: Additional contrast material added on the Plexiglas strongbox wall

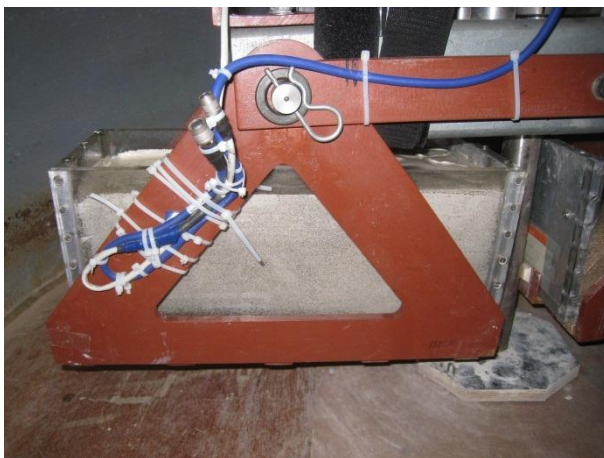


Figure 15.39: Speed up consolidation under own weight using the geotechnical centrifuge

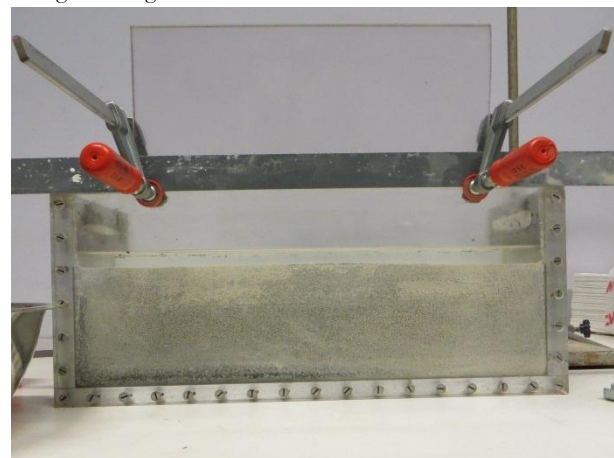


Figure 15.40: Extended Plexiglas wall to ensure sufficient fall height

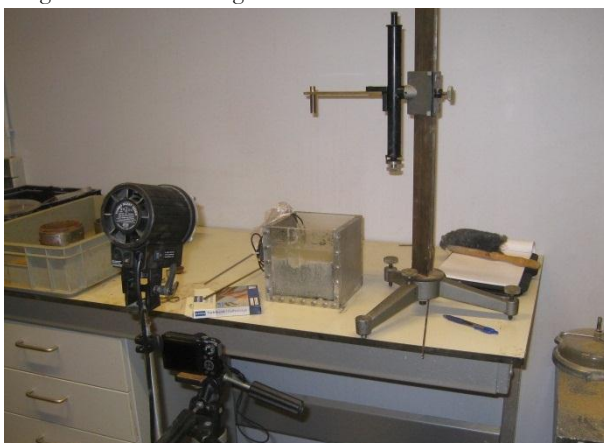


Figure 15.41: Final high speed camera test setup

Slow penetration test

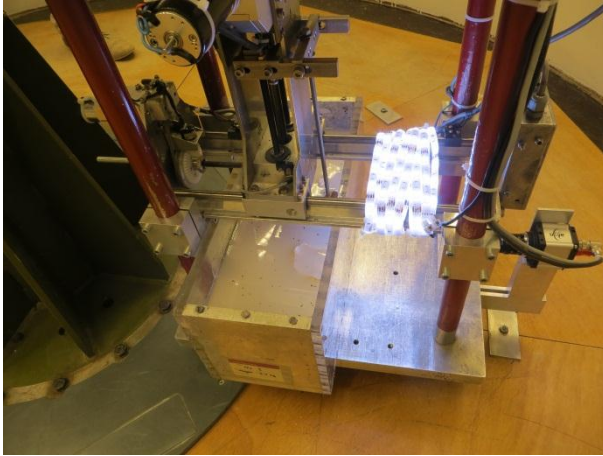


Figure 15.42: Penetrate with a set velocity using the loading frame in the geotechnical centrifuge

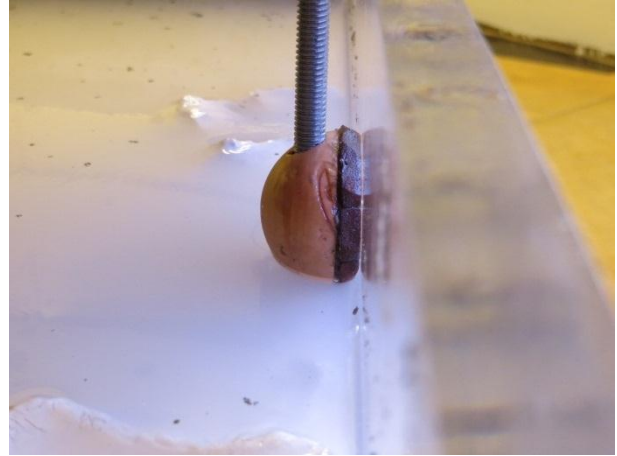


Figure 15.43: The half sphere pressed against the Plexiglas right before slow penetration into the Kaolin clay



Figure 15.44: Slow penetration into normally consolidated clay with contrast material

15.13 Additional experimental results

Undrained shear strength

Test method	Undrained shear strength [kPa]	Deviation from average [%]
Fall Cone	1.0	-29%
In-situ Vane	1.4	0%
Moisture content	1.4	0%
Average	1.4	

Test method	Undrained shear strength [kPa]	Deviation from average [%]
Fall Cone	4.3	21%
In-situ Vane	4.1	15%
Moisture content	3.0	-15%
Average	3.6	

Test method	Undrained shear strength [kPa]	Deviation from average [%]
Fall Cone	8.7	-29%
In-situ Vane	13.9	13%
Moisture content	10.8	-13%
Average	12.4	

Contour plots of high speed impact

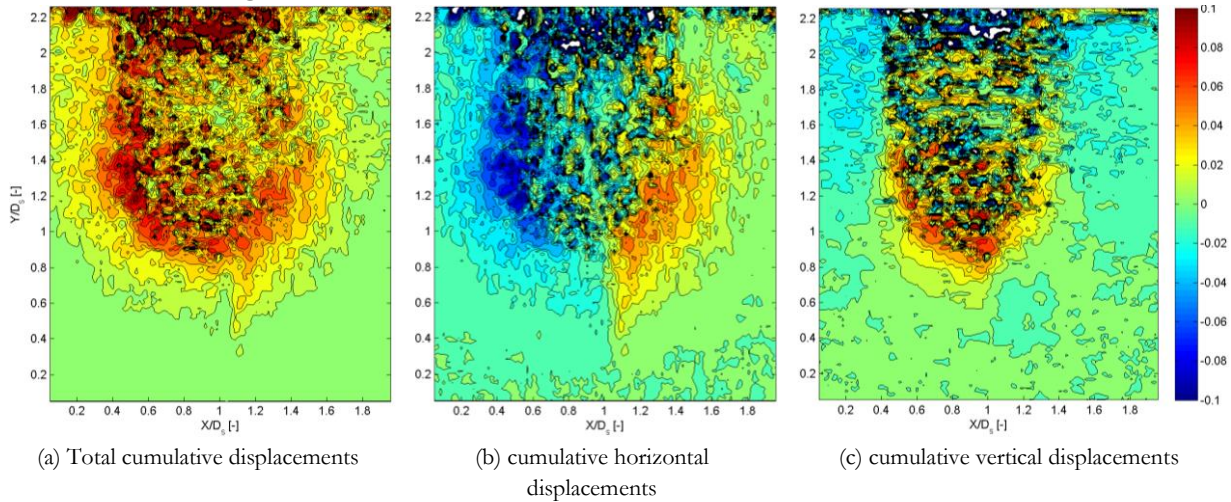


Figure 15.45: Dimensionless displacements contours of high speed impact

Contour plots of slow penetration

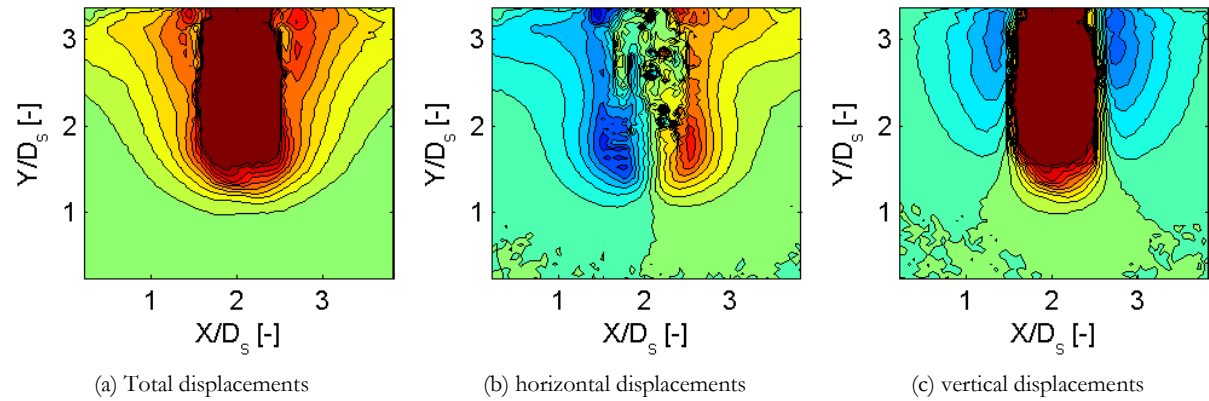


Figure 15.46: Cumulative dimensionless displacement contours of slow penetration

15.14 Berm dimensions

Table 15.4: Designed berm dimensions

Location	Description	Crest Length [m]	Crest Width [m]	Cover Height [m]	Slope
Knarr FPSO	Towhead	107	34	2.5	1:6
	Ramp	125	10	0 - 2.5	1:6
	Wet storage	50	25	0.5	1:3
Production template	Towhead	85	34	2	1:6
	Ramp	125	10	0 - 2.0	1:6
	Wet storage	65	90	0.5	1:3
Water injection template	Wet storage	50	50	0.5	1:3

15.15 Construction drawing Knarr project

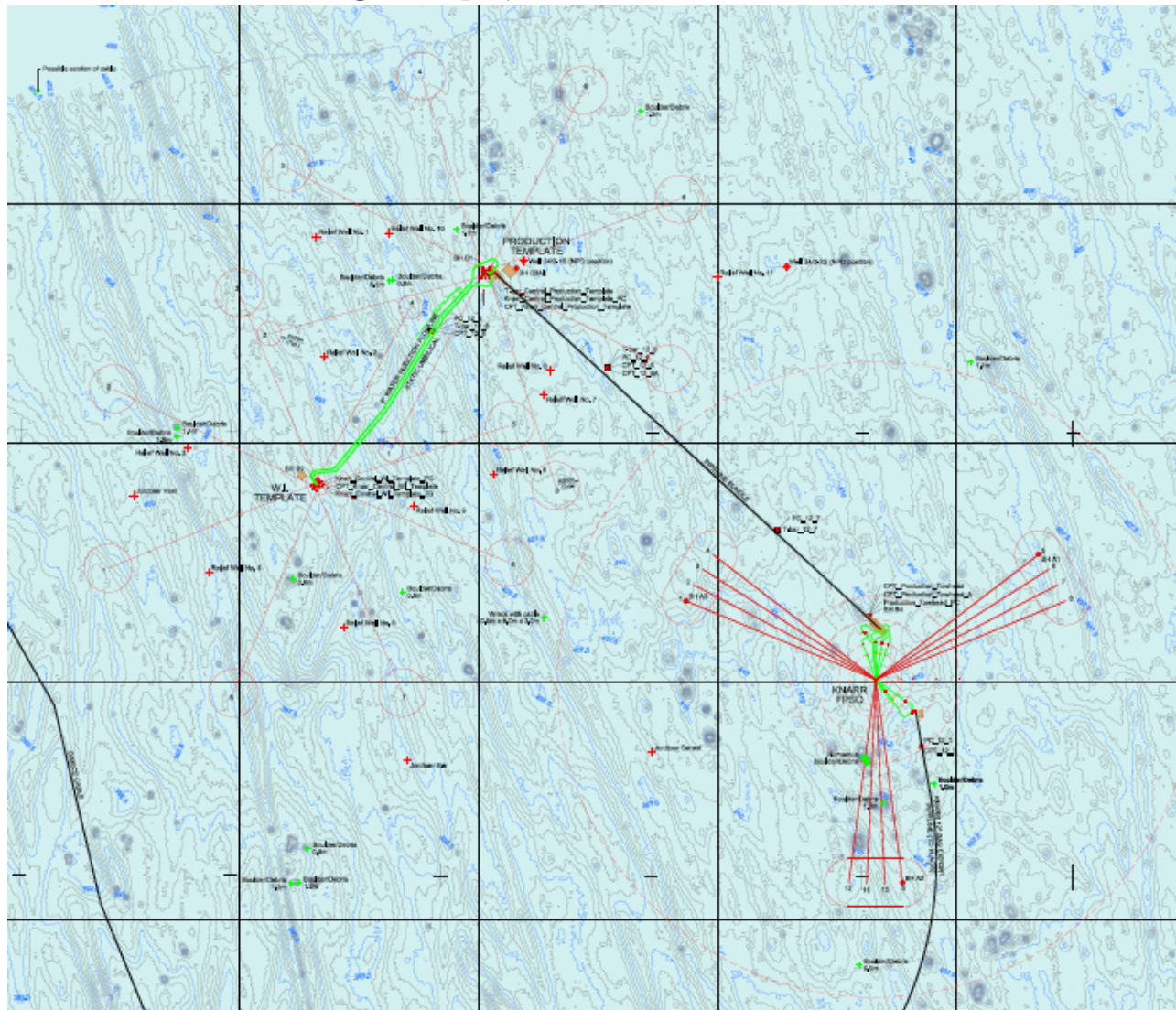
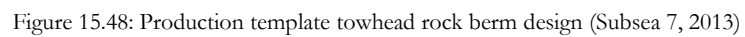


Figure 15.47: Field layout (Subsea 7, 2013)



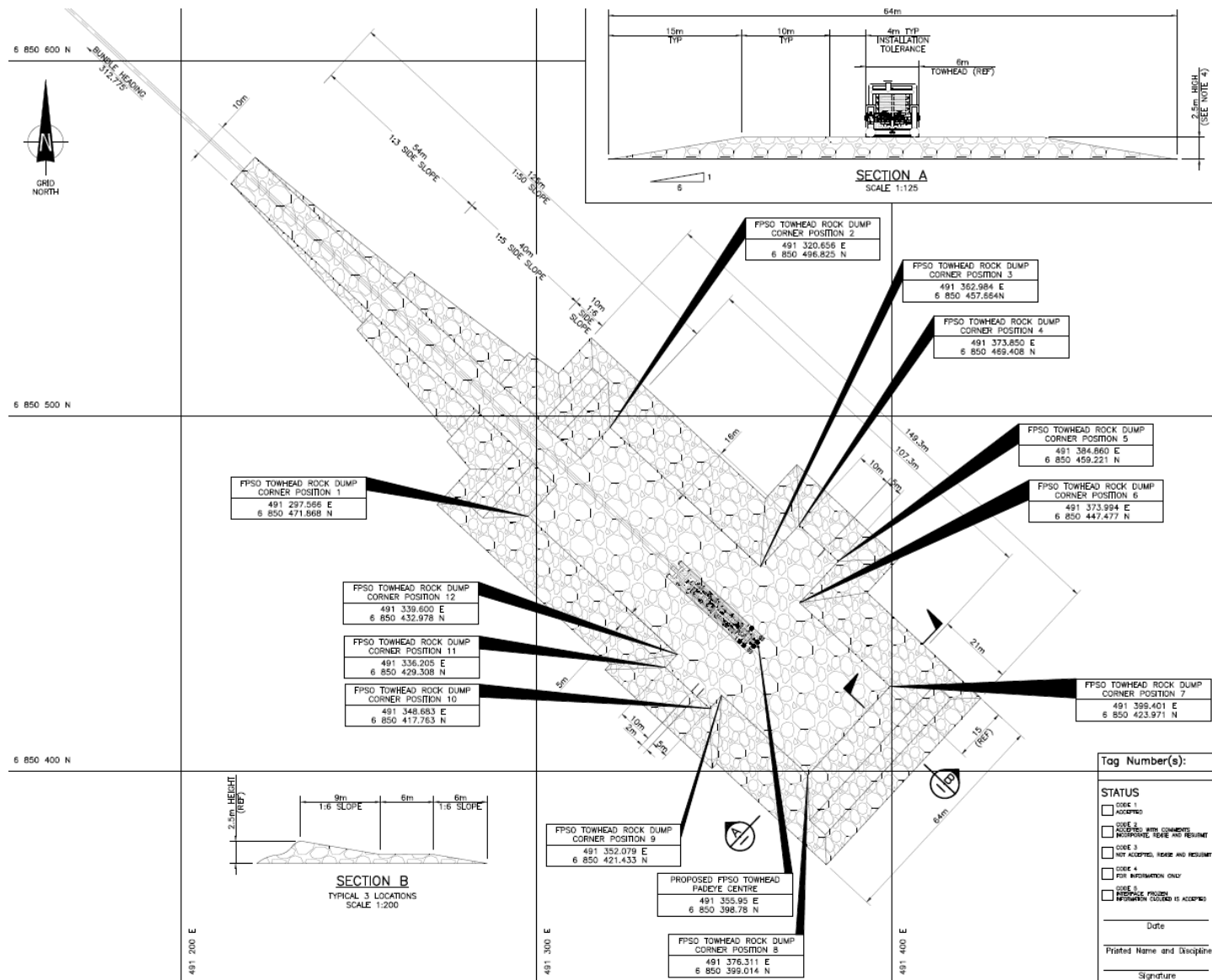


Figure 15.49: FPSO towhead rock berm design (Subsea 7, 2013)

15.16 Soil profile

Table 15.5: Soil profile with corresponding best estimate property values

Layer number	Depth range of soil [m BSF]		Soil Description	w	γ	w_p	w_L	I_p
	Top	Base		[%]	[kN/m ³]	[%]	[%]	[%]
Ia	0.0	2.0	Very soft dark grey slightly sandy CLAY	89.3	14.7	30.7	81	50.3
Ib	2.0	10.0	Very soft dark grey slightly sandy CLAY	59.9	16.4	27.2	64	36.8
II	10.0	15.2	Very soft to firm dark grey slightly sandy CLAY	22.8	20.3	15.8	35.4	19.6
IIIa	15.2	17.0	Stiff to very stiff dark grey slightly sandy CLAY with traces of coarse sand- sized shell fragments	20.9	20.5	15.8	35.5	19.7
IIIb	17.0	24.5	Medium dense to very dense dark grey very silty fine SAND with traces of coarse sand-sized shell fragments – with a thick bed of hard slightly sandy clay at 22.9 m	16.9	20.5	-	-	0.0
IIIc	24.5	30.0*	Stiff to very stiff slightly sandy CLAY with traces of coarse sand-sized shell fragments – with a medium bed of sand at 29.7 m	22.5	20.7	16.1	35	19.0

Note: BSF = Below Sea Floor

Table 15.6: Soil profile [Continued]

	c_u	$c_{u,r}$	q_c	M	ε_{50}	G_{max}	c_v	C_c	C_s	C_a	e_0	OCR
	[kPa]	[kPa]	[MPa]	[MPa]	[%]	[MPa]	[m ² /s]	[-]	[-]	[-]	[-]	[-]
Ia	3.0	1.5	0.0 – 0.1	1.0	0.65	0.4 – 5.3	8.15E-08	0.66	0.02	0.009	2.12	1.10
Ib	8.0	2.7	0.1 – 0.3	2.2	1.65	0.4 – 5.4	8.15E-08	0.66	0.02	0.006	1.56	1.10
II	30	20	0.3 – 0.8	5.8	1.23	19.80	7.71E-08	0.17	0.01	0.002	0.58	1.45
IIIa	100	77	0.8 – 1.6	9.7	1.33	54.40	6.22E-08	0.17	0.01	0.002	0.77	1.60
IIIb	-	-	1.6 – 50	96	-	117.6 – 172.9	-	-	-	0.000	0.53	1.00
IIIc	160	123	2.75 – 3.0	26	1.65	112.0 -125.8	8.78E-08	0.15	0.01	0.002	0.57	2.25

15.17 Fugro soil profile

Table 15.7: Summary of recommended spoil parameters - BH-B1 (Fugro Geoconsulting Ltd., 2012)

Soil Unit	Depth Range [m BSF]	s_u		$s_u(R)$		S_t	C_v	M	q_c	ε_{50}	D_r	G_{max}
		LE [kPa]	HE [kPa]	LE [kPa]	HE [kPa]	BE	BE [m ² /year]	BE [MPa]	BE [MPa]	BE [%]	BE [%]	BE [MPa]
I	0.0 – 10.0	2 – 14	6.0 – 19.0	1 – 8	2 – 10	3.0	2.57	1 – 2.2	0.0 – 0.3	0.65	–	0.4 – 5.3
II	10.0 – 15.2	14 – 30	19.0 – 50.0	8 – 16	10 – 26	1.5	2.43	5.8	0.3 – 0.8	1.23	–	19.8
IIIa	15.2 – 17.0	80	120.0	76	119	1.3	1.96	9.7	0.8 – 1.6	1.33	–	54.4
IIIb	17.0 – 24.5	–	–	–	–	–	–	65.5 – 119.8	1.6 – 50.0	–	40 – 90	117.6 – 172.9
IIId	24.5 – 30.0*	140 – 150	160	46 – 60	160	1.3	16.92	20.0 – 25.6	2.8 – 3.0	1.65	–	112.0 – 125.8

Notes:
 See Section A.6.1 for explanation of symbols and abbreviations
 * = Denotes end of the borehole and is not necessarily the end depth of the soil unit
 - = Data type not applicable for soil type

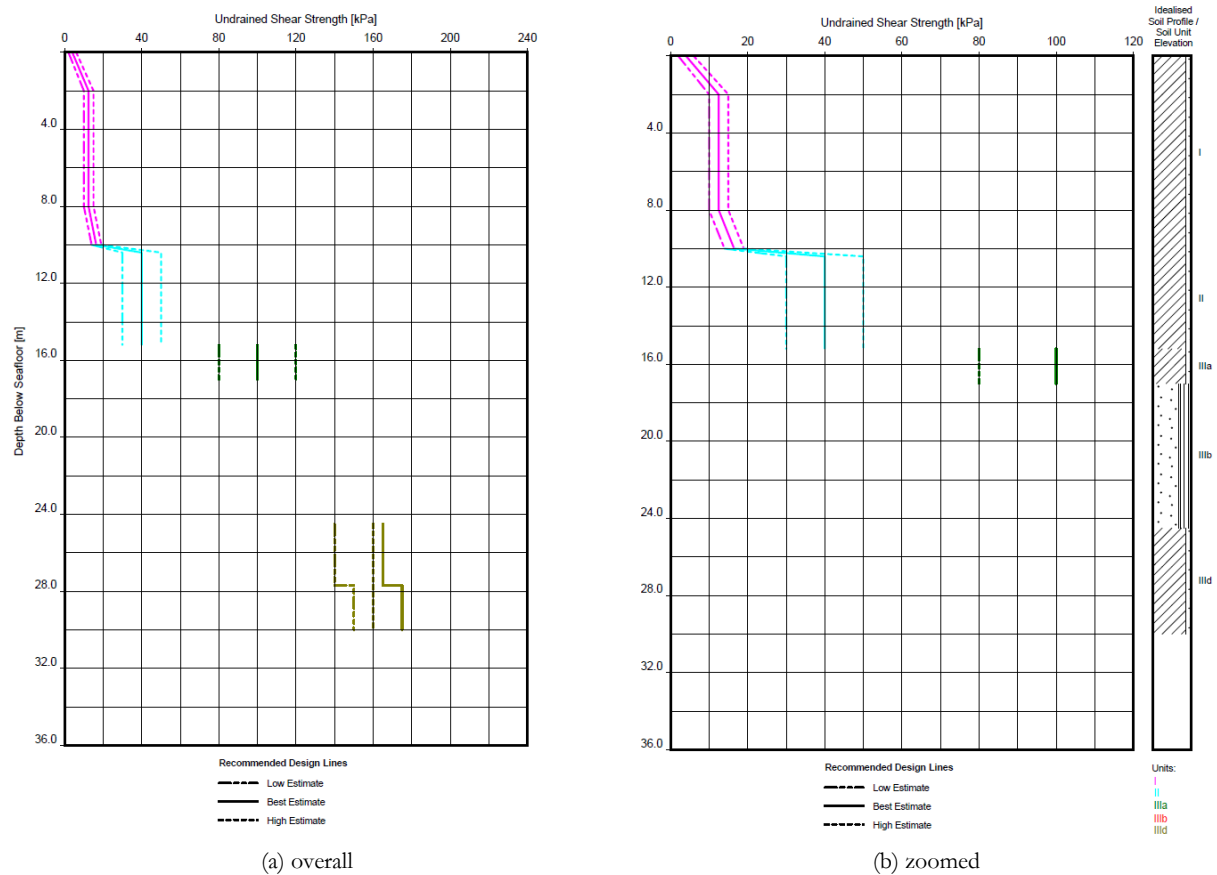


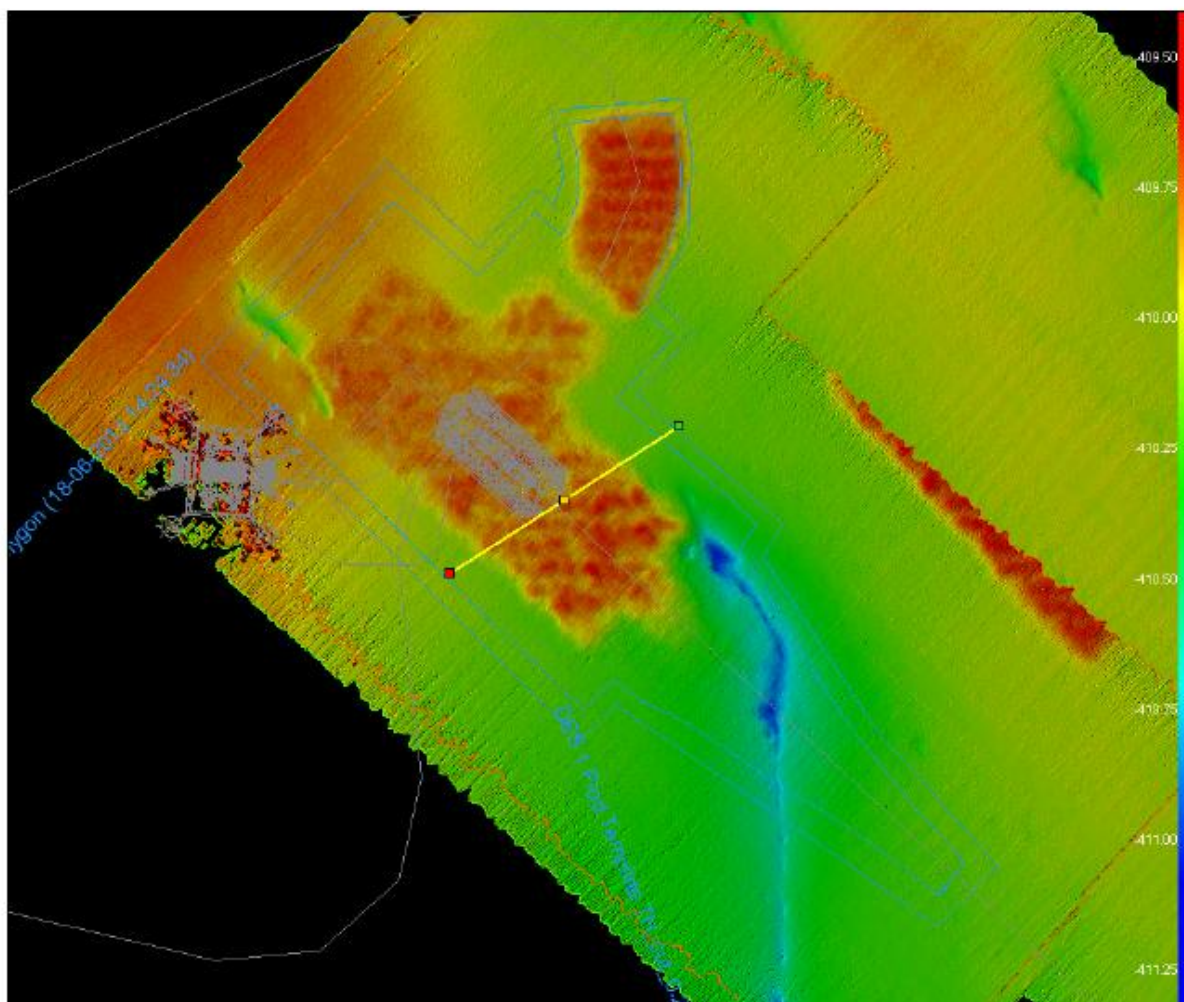
Figure 15.50: Undrained shear strength versus depth - BH-B1 (Fugro Geoconsulting Ltd., 2012)

15.18 Volume calculation

VOSS.NET - Volume Calculation

Project: BG Knarr Surf (10.4548)
 Date: 04-07-2013 15:09:42
 Model: Int 054-053-052 - Progress - CLD
 Reference Model: Pre Total Production - In Survey - CLD
 Reference Offset: 0.000
 Polygon Set: Dirk_Volume Calc Production Template

Polygon	Polygon Area	Volume Above Reference	Volume Below Reference	Area Above Reference	Area Below Reference	Average Layer Above / Below / Combined
Temporary Polygon	13,646 m ²	1,907 m ³	17 m ³	12,226 m ²	690 m ²	0.16 / 0.02 / 0.15 m



15.19 Phased subsea rock installation

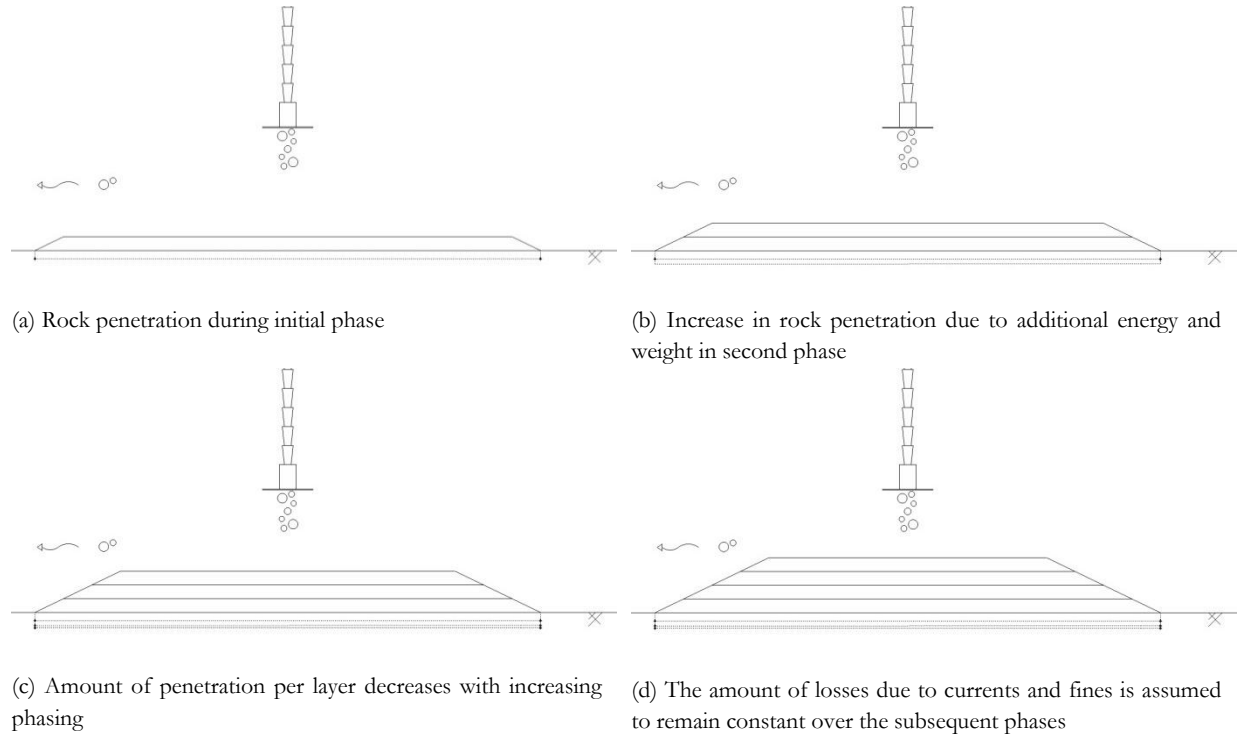


Figure 15.51: Phased subsea rock installation

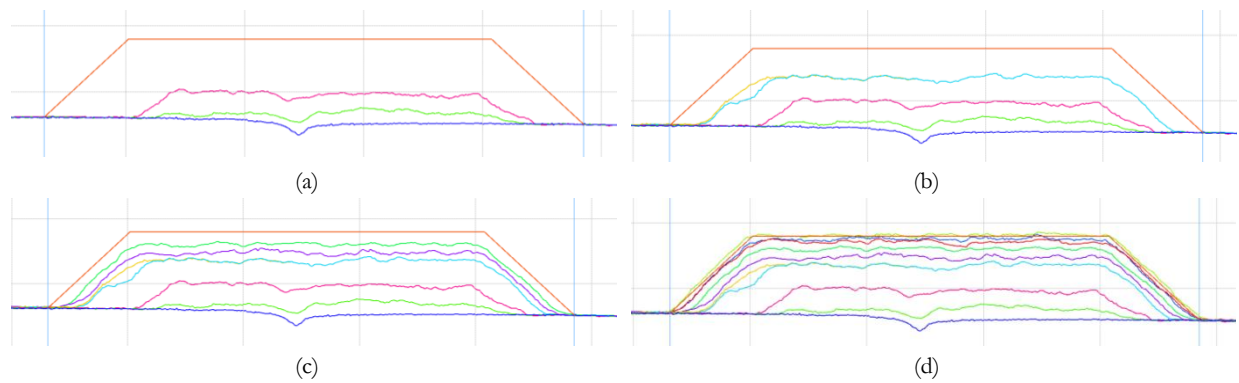


Figure 15.52: Berm development indicated using intermediate surveys

15.20 In-situ densities of Norwegian rock material

Testing method

First of all a large box is to be used. As a minimum 1.0 m³ is required, but the advised box size is 1.20x1.20x1.30 = 1.87m³ for a rock sample of 1 – 5". A large box is likely to results in more robust results. Considering the method of testing it is recommended to use the following procedure:

1. Weigh the empty box using an accurate scale (accuracy within approximately 0.2% of capacity)
2. Fill the box with water and weight the combination
3. Empty the box
4. Fill the box to the edge using a wheel loader. The rock should be dumped from a given height of approximately 2.0 m.
5. Level the top plane of the box.
6. Weigh the box
7. Fill the box to the edge with fresh water.
8. Weigh the box again

Calculation

Input variables:

– Weight of the empty box:	M_B	[kg]
– Weight of the box filled with water:	M_{BW}	[kg]
– Weight of the box filled with rock:	M_{BR}	[kg]
– Weight of the box filled with rock and water:	M_{BRW}	[kg]
– Unit Weight of fresh water:	ρ_w	[kg/m ³]

Output variables

– Porosity	[-]	$n = \frac{M_{BRW} - M_{BR}}{M_{BW} - M_B}$
– Bulk density	[kg/m ³]	$\rho_{bd} = \frac{M_{BR} - M_B}{M_{BW} - M_B} / \rho_w$
– Specific gravity	[kg/m ³]	$\rho_{sd} = \frac{\rho_{bd}}{1 - n}$
– Submerged unit weight	[kg/m ³]	$\rho' = 1 - n \cdot \rho_s - \rho_w$

Using this method, the average specific gravity of the rock in the box is measured. This is a very strong benefit of this testing method. In contrast with the specific gravity determined by weighing individual rocks, this average specific gravity per box has a reasonably small inherent standard deviation.

Results

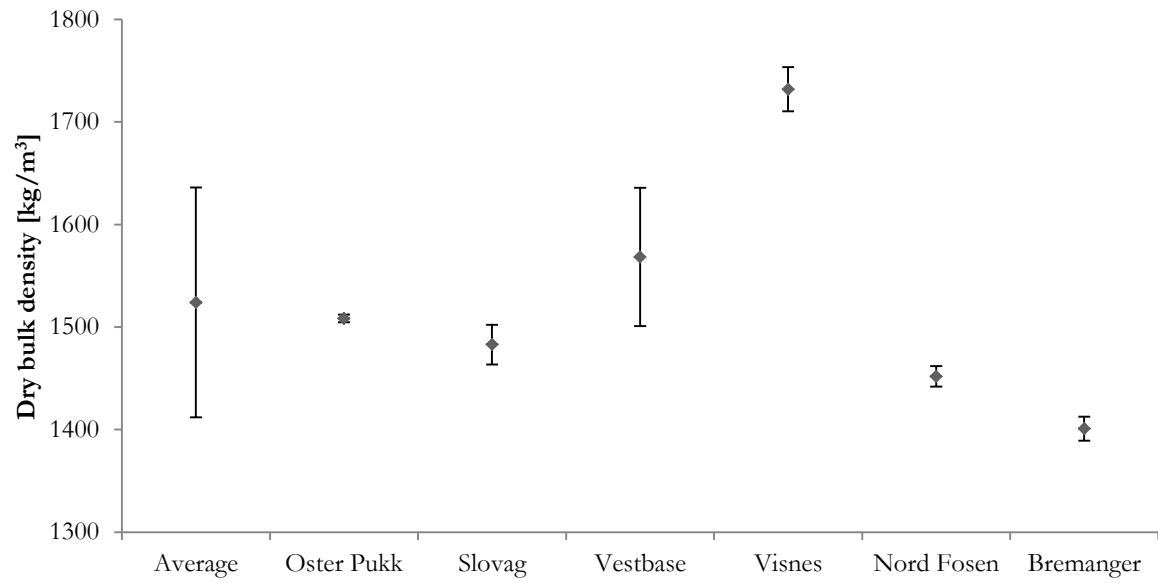


Figure 15.53: Average bulk density of surrounding quarries with standard deviation

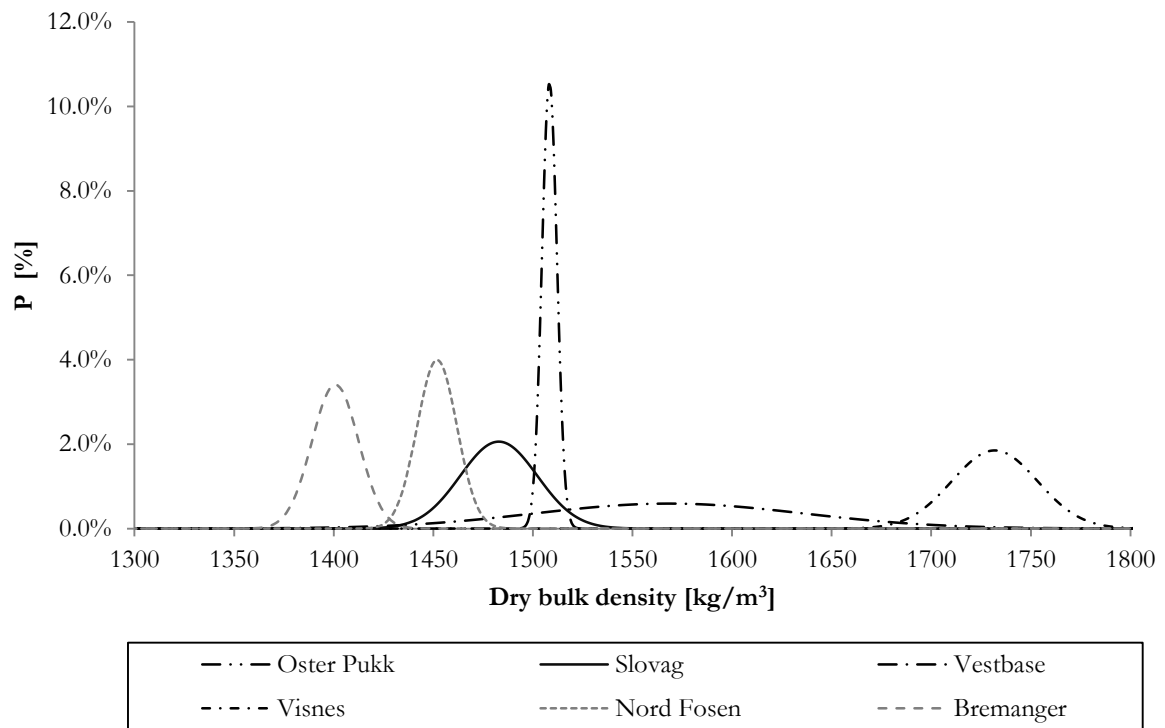


Figure 15.54: PDF for the bulk density of material obtained from different quarries on the Norwegian coast

Note: PDF = probability density function

15.21 Input file for Single Stone Penetration model

Design time step	Dt	=	3.00E-05	[s]
Proposed minimum time step	Dt_{min}	=	7.91E-06	[s]
Installation				
Fall pipe (Y/N)			Y	
Ship			Stornes	
Production	P_r	=	1250	[ton/h]
Length of fallpipe	L_{pipe}	=	400	[m]
Standoff distance	$H_{standoff}$	=	10	[m]
Characteristics gravel/rock				
Sieve size	D_{50}	=	0.049	[m]
Rib length (cube) (Rock Manual par. 3.4.2.)	D_{n50}	=	0.041	[m]
Rock mass (cube D_{n50})	m_{50}	=	0.192	[kg]
Equivalent sphere diameter from cube D_{n50}	D_{s50}	=	0.051	[m]
Equivalent sphere radius	R_s	=	0.026	[m]
Drag coefficient (= 1 for a sphere)	C_D	=	1.000	[-]
Gravity	g	=	9.81	[m/s ²]
Density water	ρ_w	=	1025	[kg/m ³]
Rock density	ρ_s	=	2760	[kg/m ³]
Equilibrium velocity falling stone	v_{equil}	=	0.95	[m/s]
Velocity of water	v_{water}	=	4.79	[m/s]
Velocity mass flow fall pipe	$v_{fallpipe}$	=	5.74	[m/s]
Velocity at impact	v_{imp}	=	3.52	[m/s]
Concentration of the mixture	c_m	=	3.9%	[%]
Mixture density	$\rho_{mixture}$	=	1092	[kg/m ³]
Minimal water velocity	$v_{water[min]}$	=	4.76	[m/s]
Check	$v_{water[check]}$	=	0.03	[m/s]
Duration in pipe	$t_{fall pipe}$	=	70	[s]
	h_{equi}	=	0.05	[m]
Characteristics sub-soil				
Undrained shear strength	c_u	=	3.0	[kN/m ²]
Saturated density	$\rho_{wet soil}$	=	1500	[kg/m ³]

Solve

Velocity at impact seabed	=	3.5	[m/s]
Max. penetration	=	0.031	[m]
Duration impact	=	0.016	[s]

15.22 Sensitivity analysis input

Table 15.8: Range of possible input variables

					Ranging from:
Sieve size	D_{50}	0.01	-	0.25 [m]	A very coarse sand to a small bolder. 10'' is practical limit of the FFPV
Drag coefficient	C_D	0.40	-	1.40 [-]	A half sphere to a plate perpendicular to the flow
Density water	ρ_w	998	-	1050 [kg/m ³]	Warm fresh water to cold salt water
Rock density	ρ_s	2400	-	3400 [kg/m ³]	Shale to Peridotite
Saturated density	ρ_{ws}	11.0	-	18.0 [kN/m ³]	Very soft to a compacted clay
Velocity at impact seabed	v_{imp}	0.5	-	7.5 [m/s]	The terminal velocity of a coarse sand particle to the jet impact of a bolder
Undrained shear strength	c_u	0.0	-	20.0 [kPa]	The demarcation of the research

15.23 Factors with negligible influence

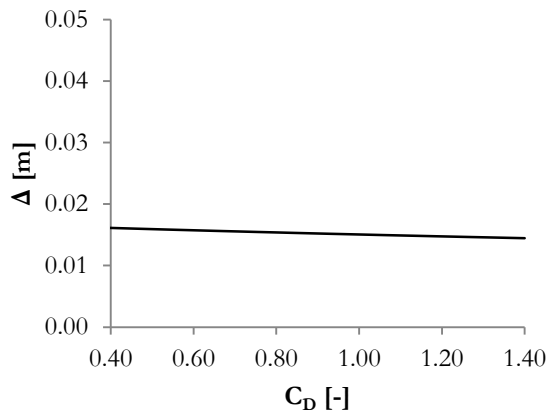


Figure 15.55: Influence of drag coefficient on single stone penetration

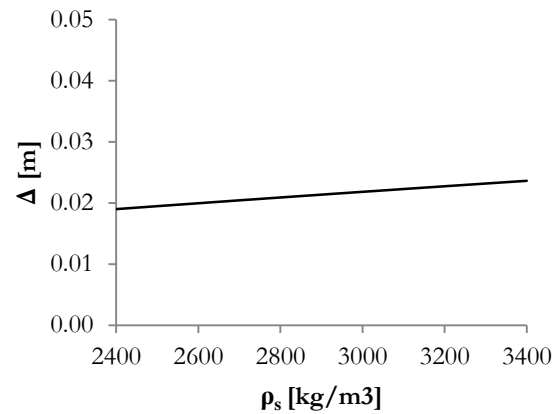


Figure 15.56: Influence of rock density on single stone penetration

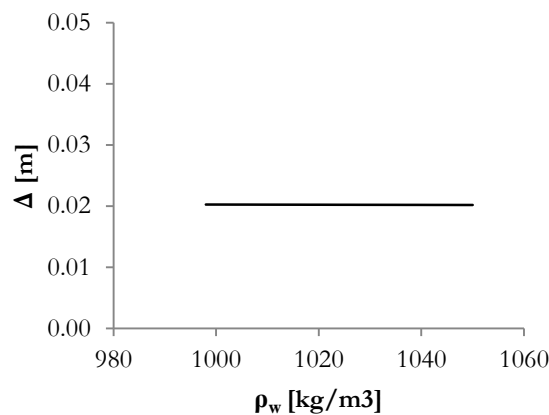


Figure 15.57: Influence of water density on single stone penetration

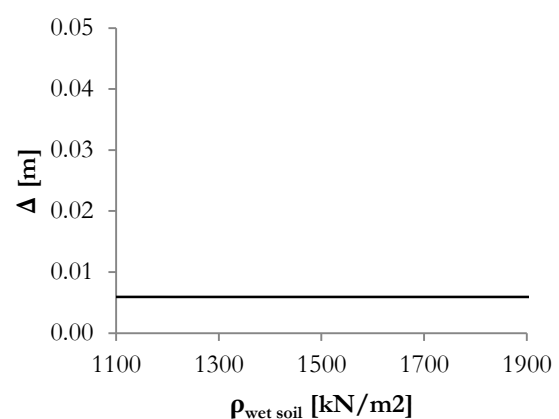


Figure 15.58: Influence of wet soil density on single stone penetration

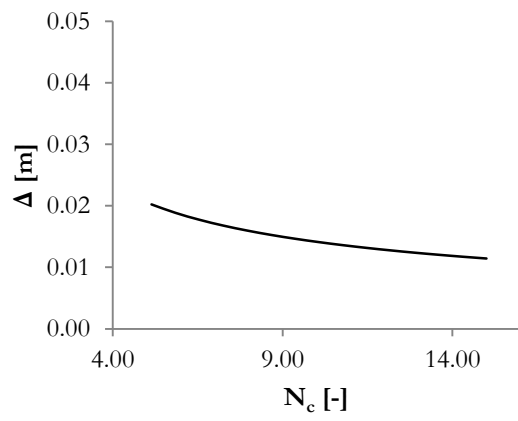


Figure 15.59: Influence of bearing capacity factor on single stone penetration

15.24 Plaxis input parameters

Table 15.9: Soil profile used for PLAXIS calculations – Mohr Coulomb

Material			Elevation			γ_{sat}	e_{init}	ν		E_u [kPa]		c_u	ϕ	ψ
						[kN/m ³]	[-]	[-]	min	BE	Max	[kPa]	[°]	[°]
1	Rock	Drained	0.0	-	2.5	20.0	0.65	0.250	80000	80000	80000	0.0	35.0	0.0
2	Clay_Top	Undrained	0.0	-	-2.0	14.7	2.12	0.495	1600	1000	900	3.0	0.0	0.0
3	Clay_Middle	Undrained	-2.0	-	-10.0	16.4	1.56	0.495	4300	2750	1200	8.0	0.0	0.0
4	Clay_Low	Undrained	-10.0	-	-15.0	20.3	0.58	0.495	9100	8350	7600	30.0	0.0	0.0
5	Stiff_Clay	Undrained	-15.0	-	-17.0	20.5	0.77	0.495	19000	12300	7400	100.0	0.0	0.0
6	Sandy_clay	Drained	-17.0	-	-24.0	20.5	0.53	0.350	14200	14200	14200	0.0	35.0	0.0
7	Very_Stiff_Clay	Undrained	-24.0	-	-30.0	20.7	0.57	0.495	27200	20400	10300	160.0	0.0	0.0

Table 15.10: Soil profile used for PLAXIS calculations – Hardening Soil

Material			Elevation			γ_{sat}	e_{init}	ν	E_{50}	E_{oed}	E_{ur}	p_{Ref}	c_u	ϕ	ψ
						[kN/m ³]	[-]	[-]	[kPa]	[kPa]	[kPa]	[kPa]	[kPa]	[°]	[°]
1	Rock	Drained	0.0	-	2.5	20.0	0.65	0.250	80000	-	-	-	0.0	35.0	0.0
2	Clay_Top	Undrained	0.0	-	-2.0	14.7	2.12	0.495	1000	1300	2000	400	3.0	0.0	0.0
3	Clay_Middle	Undrained	-2.0	-	-10.0	16.4	1.56	0.495	2750	3700	5500	400	8.0	0.0	0.0
4	Clay_Low	Undrained	-10.0	-	-15.0	20.3	0.58	0.495	8350	11200	16700	400	30.0	0.0	0.0
5	Stiff_Clay	Undrained	-15.0	-	-17.0	20.5	0.77	0.495	12300	16600	24600	400	100.0	0.0	0.0
6	Sandy_clay	Drained	-17.0	-	-24.0	20.5	0.53	0.350	14200	-	-	-	0.0	35.0	0.0
7	Very_Stiff_Clay	Undrained	-24.0	-	-30.0	20.7	0.57	0.495	20400	27500	40800	400	160.0	0.0	0.0

15.25 Plaxis mesh

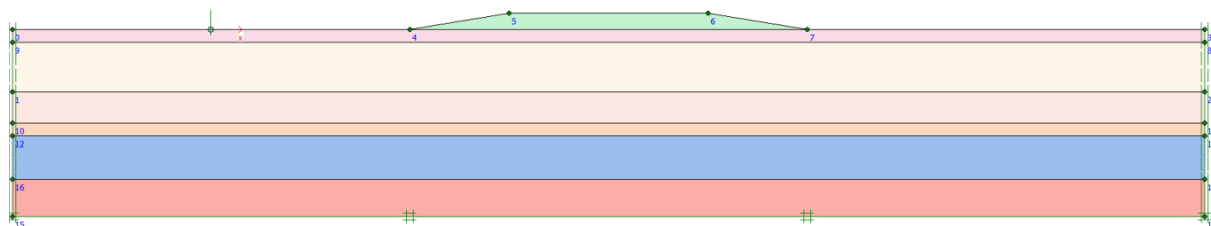


Figure 15.60: Plaxis input geometry

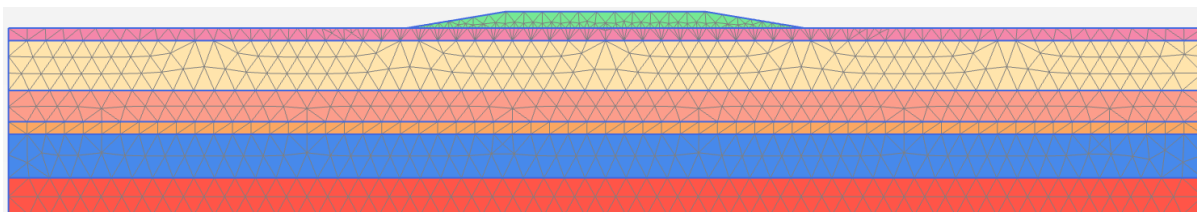


Figure 15.61: Original fine mesh

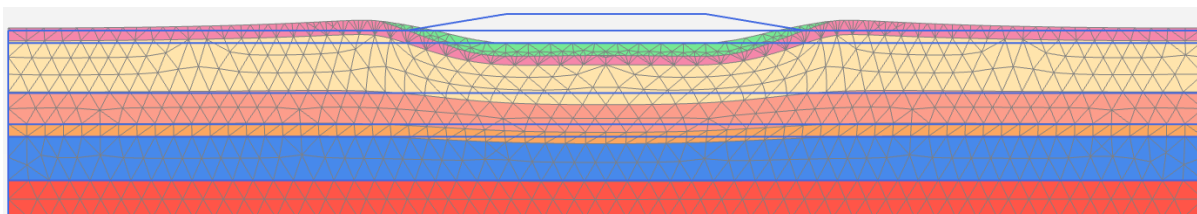


Figure 15.62: Deformed mesh (scaled up 100 times)

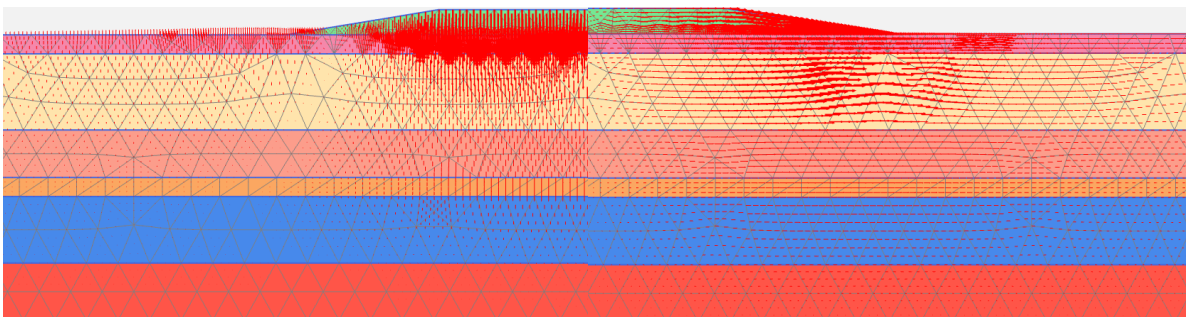


Figure 15.63: Vertical deformations

Figure 15.64: Horizontal deformations

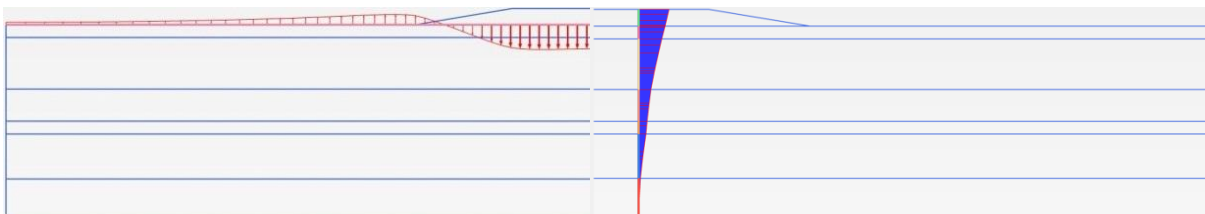


Figure 15.65: Vertical deformation over the length of the berm



Figure 15.66: Vertical deformations over the depth seabed berm

15.26 D-settlement calculation

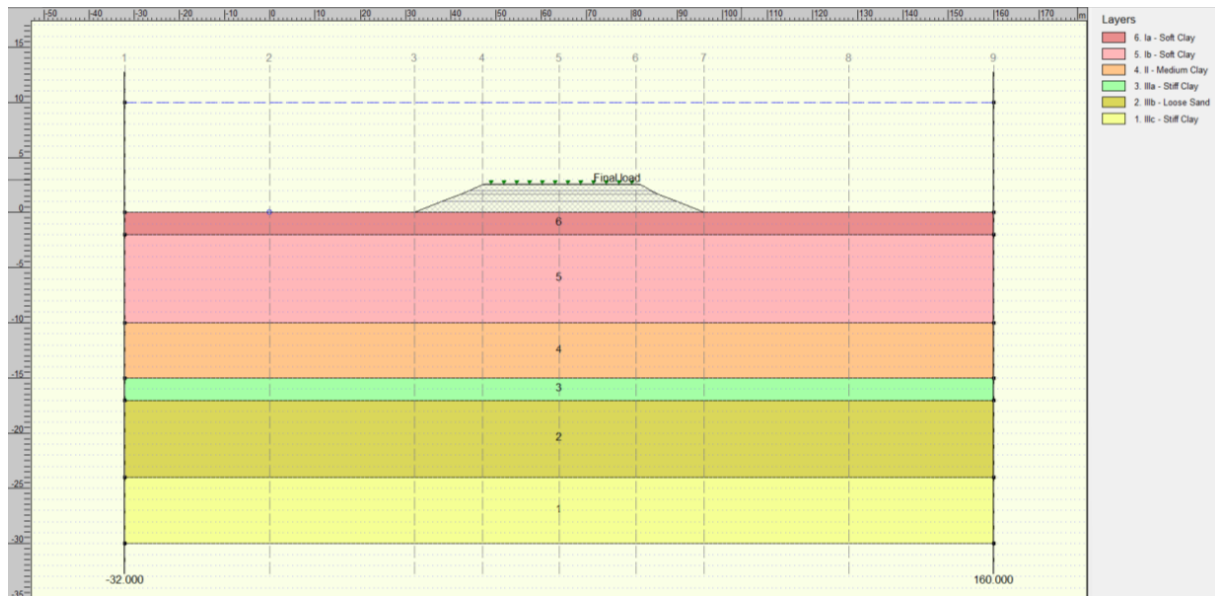


Figure 15.67: D-Settlement input soil layers

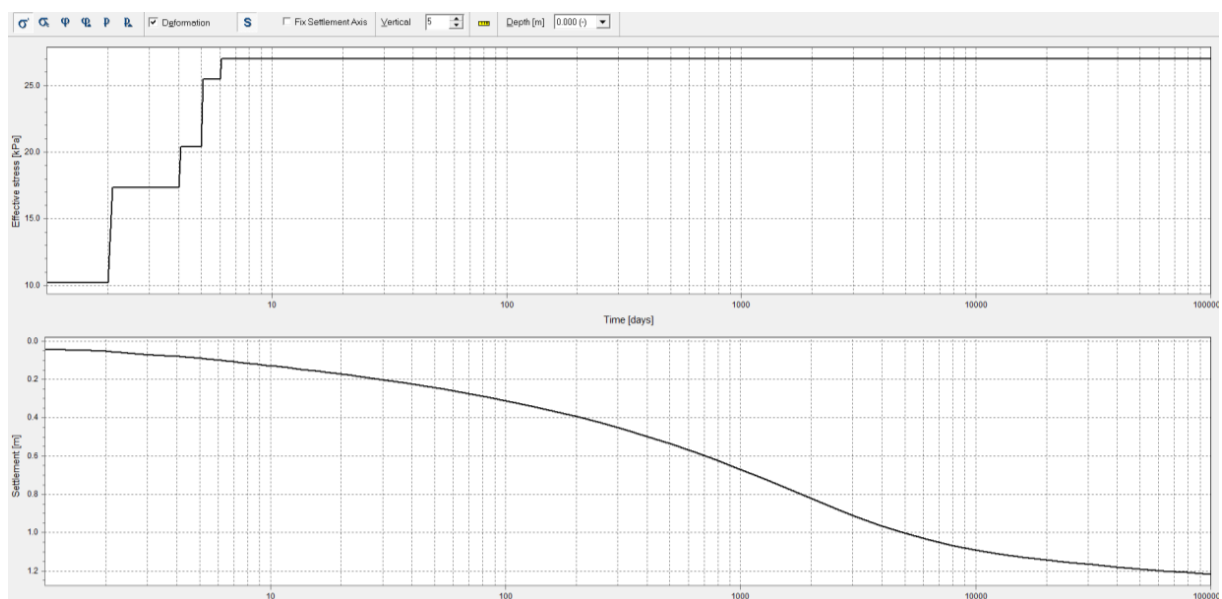


Figure 15.68: D-Settlement development of effective pressures and consolidation results at section 5

15.27 Volume determination results

The following tables indicate the influence of all individual processes separately for all locations, both absolute and relative. The tables are organised by minimum, maximum and best estimate input parameters. The relative values are determined with respect to the sum of the individual processes. The last column indicates the difference between the calculated the height deficit and the height deficit obtained from field measurements.

Minimum

Table 15.11: Absolute influence of individual processes per location (minimum input parameters)

Item	Location	Height deficit	Loss of fines	Immediate deformation	Consolidation	Plastic flow	SSM	MSM	Difference	
		[m]	[m]	[m]	[m]	[m]	[m]	[m]	[m]	[%]
FPSO	Wet storage	0.04	0.00	0.01	0.03	0.00	0.02	0.02	-0.04	-107%
PT	Wet storage	0.13	0.00	0.01	0.04	0.00	0.02	0.02	0.04	31%
WI	Wet storage	0.02	0.00	0.01	0.03	0.00	0.02	0.02	-0.06	-272%
PT	Towhead	0.21	0.01	0.02	0.06	0.01	0.02	0.02	0.07	34%
FPSO	Towhead	0.24	0.01	0.03	0.07	0.01	0.02	0.02	0.08	32%

Table 15.12: Relative influence of individual processes per location (minimum input parameters)

Item	Location	Loss of fines	Immediate deformation	Consolidation	Plastic flow	SSM	MSM
		[%]	[%]	[%]	[%]	[%]	[%]
FPSO	Wet storage	8%	15%	83%	4%	50%	46%
PT	Wet storage	3%	5%	29%	2%	16%	14%
WI	Wet storage	15%	31%	151%	9%	86%	79%
PT	Towhead	4%	11%	30%	3%	9%	8%
FPSO	Towhead	4%	13%	31%	4%	8%	7%
Average		7%	15%	65%	4%	34%	31%

Note: SSM = single stone model

MSM = multi stone model

Best estimate

Table 15.13: Absolute influence of individual processes per location (best estimate input parameters)

Item	Location	Height deficit	Loss of fines	Immediate deformation	Consolidation	Plastic flow	SSM	MSM	Difference	
		[m]	[m]	[m]	[m]	[m]	[m]	[m]	[m]	[%]
FPSO	Wet storage	0.05	0.01	0.01	0.03	0.00	0.03	0.03	-0.06	-115%
PT	Wet storage	0.13	0.01	0.01	0.04	0.01	0.03	0.03	0.00	1%
WI	Wet storage	0.08	0.01	0.01	0.04	0.01	0.03	0.03	-0.04	-51%
PT	Towhead	0.27	0.02	0.03	0.07	0.02	0.03	0.03	0.07	25%
FPSO	Towhead	0.33	0.02	0.04	0.08	0.02	0.03	0.03	0.10	30%

Table 15.14: Relative influence of individual processes per location (best estimate input parameters)

Item	Location	Loss of fines	Immediate deformation	Consolidation	Plastic flow	SSM	MSM
		[%]	[%]	[%]	[%]	[%]	[%]
FPSO	Wet storage	11%	14%	63%	9%	55%	63%
PT	Wet storage	6%	7%	32%	4%	24%	27%
WI	Wet storage	8%	11%	46%	7%	37%	42%
PT	Towhead	6%	12%	26%	7%	11%	13%
FPSO	Towhead	6%	13%	24%	8%	9%	10%
Average		8%	11%	38%	7%	27%	31%

Note: SSM = single stone model

MSM = multi stone model

Maximum

Table 15.15: Absolute influence of individual processes per location (maximum input parameters)

Item	Location	Height deficit	Loss of fines	Immediate deformation	Consolidation	Plastic flow	SSM	MSM	Difference	
		[m]	[m]	[m]	[m]	[m]	[m]	[m]	[m]	
FPSO	Wet storage	0.13	0.01	0.01	0.05	0.01	0.05	0.08	-0.08	-60%
PT	Wet storage	0.24	0.01	0.01	0.05	0.01	0.05	0.08	0.03	11%
WI	Wet storage	0.11	0.01	0.02	0.05	0.01	0.05	0.08	-0.10	-93%
PT	Towhead	0.44	0.03	0.05	0.09	0.04	0.05	0.08	0.10	24%
FPSO	Towhead	0.54	0.03	0.07	0.11	0.06	0.05	0.08	0.14	27%

Table 15.16: Relative influence of individual processes per location (maximum input parameters)

Item	Location	Loss of fines	Immediate deformation	Consolidation	Plastic flow	SSM	MSM
		[%]	[%]	[%]	[%]	[%]	[%]
FPSO	Wet storage	8%	10%	36%	8%	39%	60%
PT	Wet storage	5%	6%	21%	5%	20%	31%
WI	Wet storage	10%	14%	44%	11%	45%	69%
PT	Towhead	6%	12%	21%	9%	11%	17%
FPSO	Towhead	6%	13%	20%	10%	9%	14%
Average		7%	11%	28%	9%	25%	38%

Note: SSM = single stone model

MSM = multi stone model

15.28 Quarry density tests

Sløvåg quarry

Table 15.17: Results of bulk density tests for the Sløvåg quarry

Particle size	Porosity [-]	Bulk density [kg/m ³]	Submerged unit weight [kN/m ³]	Specific gravity [t/m ³]
1 - 5"	0.45	1482	9.0	2.70
1 - 5"	0.46	1464	9.0	2.72
1 - 5"	0.45	1503	9.2	2.72
1- 3"	0.40	1600	9.7	2.68
1- 3"	0.45	1440	8.9	2.69
1- 3"	0.46	1440	9.0	2.71
1- 3"	0.45	1480	9.3	2.73
16 – 32 mm	0.42	1540	9.6	2.71
16 – 32 mm	0.43	1530	9.5	2.71
16 – 32 mm	0.44	1480	9.2	2.70

Ref. job Halsvik - H29513 - Sample report page 1 of 1



Yeoman Halsvik

Sløvåg
N-5960 DalsøyraYeoman Halsvik AS.
5960 Dalsøyra
Norway
+47 57781446

GRADATION ANALYSIS TEST REPORT for Product: HLT.00091/ 1'-3' offshore blend

Supplier/ source: Yeoman Halsvik
Material type: Drystone aggregate Test method: Dry grading to EN 933-1:1998**SAMPLE INFORMATION****Sample number** H29513

Sampled from	Blending results	Time sampled	-
Plant/Customer	loko	Weather conditions	-
Sampled by	Lilly	Aggregate type	Gneiss
Remarks 1	-	Remarks 2	-

Sampled/ tested må 06 mai 2013/ 06-05-13 at 1500 hrs
--

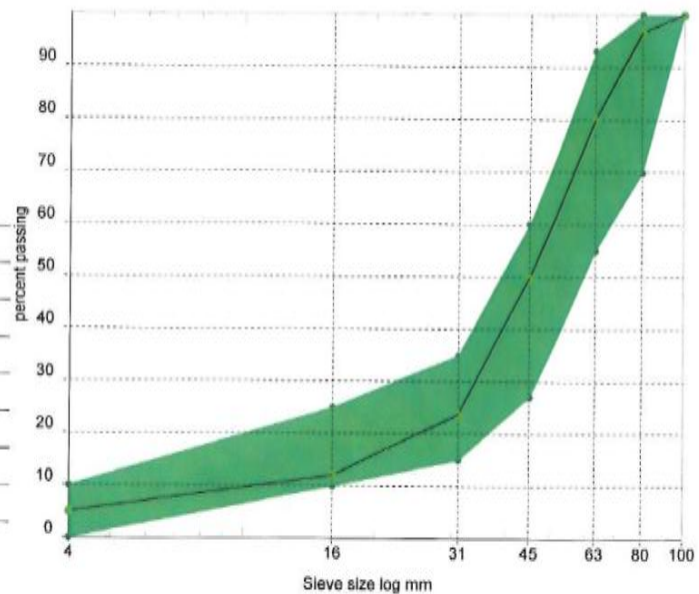
SAMPLE ANALYSIS

Sieve size	Percent passing	Specification limits	Complies ?
100mm	100	100 - 100	yes
80mm	97	70 - 100	yes
63mm	80	55 - 93	yes
45mm	50	27 - 60	yes
31mm	24	15 - 35	yes
16mm	12	10 - 25	yes
4mm	5	0 - 10	yes
Moisture content %	not determined	not specified	-

Parameters are evaluated to the accuracy of spec. limits

REMARKS**Compliance status ok****Category A of A-B includes secondary parameters**

Spesification:
D10 4-16 sendt mail abdulle van o. 0805013
D50 40-60
D90 60-90

Signed Jelly SttDate 16 / 5 / 2013

Ref. job Halsvik - H29597 - Sample report page 1 of 1



Yeoman Halsvik

Sløvåg
N-5960 DalsøyraYeoman Halsvik AS.
5960 Dalsøyra
Norway
+47 57781446

GRADATION ANALYSIS TEST REPORT

for Product: HLT.00091/ 1'-3' offshore blend
Supplier/ source: Yeoman Halsvik

Material type: Drystone aggregate Test method: Dry grading to EN 933-1:1998

SAMPLE INFORMATION

Sample number H29597

Sampled from stock
Plant/Customer -
Sampled by Lilly
Remarks 1 -Time sampled -
Weather conditions overcast
Aggregate type Gneiss
Remarks 2 -Sampled/ tested
to 09 mai 2013/ 09-05-13
at 1300 hrs

SAMPLE ANALYSIS

Sieve size	Percent passing	Specification limits	Complies ?
100mm	100	100 - 100	yes
80mm	97	70 - 100	yes
63mm	80	55 - 83	yes
45mm	50	27 - 60	yes
31mm	24	15 - 35	yes
16mm	12	10 - 25	yes
4mm	5	0 - 10	yes

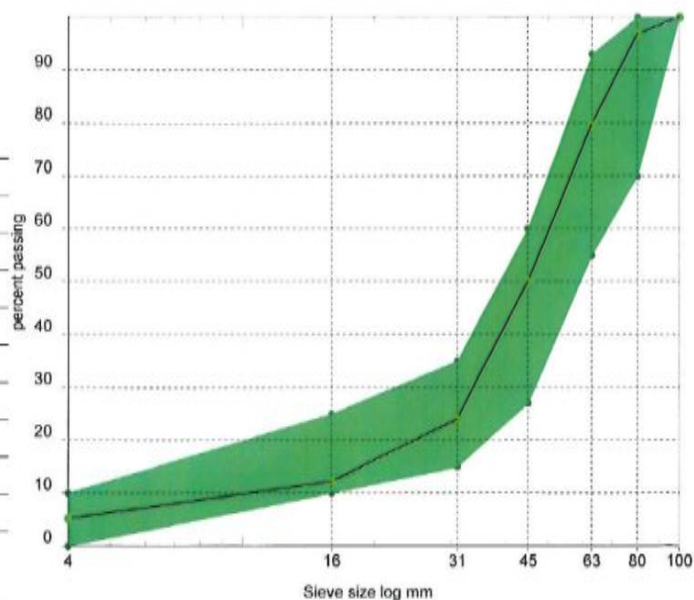
Moisture content % not determined

not specified

-

Parameters are evaluated to the accuracy of spec. limits

REMARKS

Compliance status ok
Category A of A-B includes secondary parametersSigned LillyDate 16/5/2013

Gradlab GDS v36708.00 © Hugh Lerwill THIS IS DEMONSTRATION SOFTWARE AND IS UNLICENSED AND UNSUPPORTED. email hugh@gradlab.com, phone 01531-822782

Figure 15.69: Sieves curve provided by the Sløvåg quarry

Jelsa quarry

Table 15.18: Results of bulk density tests for the Jelsa quarry

Date	Test volume [m ³]	Weight [kg]	Void volume [m ³]	Porosity [-]	Bulk density [kg/m ³]	Submerged unit weight [kN/m ³]	Specific gravity [t/m ³]
28-09-2012	1000	1540	440	0.44	1540	9.5	2.75
27-10-2012	1000	1540	440	0.44	1540	9.5	2.75
31-10-2012	1000	1540	440	0.44	1540	9.5	2.75
03-11-2012	1000	1540	440	0.44	1540	9.5	2.75
05-11-2012	1000	1540	440	0.44	1540	9.5	2.75
09-11-2012	1000	1540	440	0.44	1540	9.5	2.75
12-11-2012	1000	1540	440	0.44	1540	9.5	2.75
19-11-2012	1000	1540	440	0.44	1540	9.5	2.75
23-11-2012	1000	1540	440	0.44	1540	9.5	2.75
30-11-2012	1000	1540	440	0.44	1540	9.5	2.75
06-12-2012	1000	1540	440	0.44	1540	9.5	2.75
26-12-2012	1000	1540	440	0.44	1540	9.5	2.75
07-03-2013	1000	1540	440	0.44	1540	9.5	2.75
17-03-2013	1000	1540	440	0.44	1540	9.5	2.75

Note: all tests are performed on aggregate with a size between 1 and 5”



Density of crushed rock

Date: 28.09.2012
Project:
Material: 1-5" Norsk Stein

RESULTS

Parameter	Value	Unit
Density of solid rock:	2.75	t/m ³
Volume test box	1000	l
Correction, K	1.0	
Weight sample	1540	kg
Void volume	440.0	l
Porosity	0.44	
Void ratio	0.79	
Sea water density	1.025	t/m ³
Bulk dry density	1.54	t/m ³
Bulk submerged density	0.97	t/m ³
Dry unit weight	15.1	kN/m ³
Submerged unit weight	9.5	kN/m ³

Prepared by: (date and signature) 28.09.2012 Alfred Langenberg



Density of crushed rock

Date: 26/27.12.2012
Project:
Material: 1-5" Norsk Stein

RESULTS

Parameter	Value	Unit
Density of solid rock:	2.75	t/m ³
Volume test box	1000	l
Correction, K	1.0	
Weight sample	1540	kg
Void volume	440.0	l
Porosity	0.44	
Void ratio	0.79	
Sea water density	1.025	t/m ³
Bulk dry density	1.54	t/m ³
Bulk submerged density	0.97	t/m ³
Dry unit weight	15.1	kN/m ³
Submerged unit weight	9.5	kN/m ³

Prepared by: (date and signature) 26/27.12.2012 Alfred Langenberg



Density of crushed rock

Date: 17.03.2013
 Project:
 Material: 1-5" Norsk Stein

RESULTS

Parameter	Value	Unit
Density of solid rock:	2.75	t/m ³
Volume test box	1000	l
Correction, K	1.0	
Weight sample	1540	kg
Void volume	440.0	l
Porosity	0.44	
Void ratio	0.79	
Sea water density	1.025	t/m ³
Bulk dry density	1.54	t/m ³
Bulk submerged density	0.97	t/m ³
Dry unit weight	15.1	kN/m ³
Submerged unit weight	9.5	kN/m ³

Prepared by: (date and signature) 17.03.2013 Alfred Langenberg

Figure 15.70: Density tests provided by the Jelsa quarry

Note: the exact similarity in test results for a number of different investigations.